UNIVERSIDAD DE LA REPÚBLICA ORIENTAL DEL URUGUAY
UNIVERSITÉ DE LIMOGES (FRANCE)

CO-ADVISED THESIS
For the degree

DOCTOR EN INGENIERÍA QUÍMICA
de la Facultad de Ingeniería de MONTEVIDEO

DOCTEUR DE L'UNIVERSITÉ DE LIMOGES
Spécialité: Matériaux Céramiques et Traitements de Surface

Gustavo SÁNCHEZ MATHON

February the 12th 2009, Montevideo, Uruguay

PIEZOELECTRIC ALUMINUM NITRIDE THIN FILMS BY PECVD

Advisors: Aldo BOLOGNA ALLES / Pascal TRISTANT,
Christelle DUBLANCHE-TIXIER

Jury :

President :	Prof. Jean Claude LABBE	SPCTS, Limoges (France)
Revisors:	Prof. Miriam CASTRO	UNMDP, Mar del Plata (Argentina)
	Prof. Abdou DJOUADI	IMN, Nantes (France)
Members:	Prof. Ismael PIEDRA-CUEVA	FING, Montevideo (Uruguay)
	Prof. Enrique DALCHIELE	FING, Montevideo (Uruguay)
	Dr. Christelle DUBLANCHE-TIXIER	SPCTS, Limoges (France)
	Prof. Pascal TRISTANT	SPCTS, Limoges (France)
	Prof. Aldo BOLOGNA ALLES	FING, Montevideo (Uruguay)

Acknowledgments

I want to express my sincere gratitude to my thesis advisors, Dr. Aldo Bologna Alles, Dr. Pascal Tristant and Dr. Christelle Dublanche-Tixier for their friendship and guidance throughout the course of this work.

I also gratefully acknowledge Dr. Jean Claude Labbe, Dr. Ismael Piedra-Cueva, Dr. Abdou Djouadi, Dr. Miriam Castro, and Dr. Enrique Dalchiele for serving on my committee.

I would also like to thank to several members of the SPCTS laboratory at Limoges for their support: Daniel Tetard, Thérèse Merle, Valérie Coudert, Phillippe Thomas, Alexandre Boulle, René Guinebretiere, Bernard Soulestin, Fabrice Rossignol, Daniel Merle and Cédric Jaoul. I would like to give a special acknowledge in this sense to Hervé Hidalgo.

I want to acknowledge to Jaume Esteve and Joseph Montserrat from the Instituto de Microelectrónica de Barcelona for their assistance in the cleanroom fabrication of SAW devices, as well as to Aurelian Crunteanu from X-LIM (Limoges) for his assistance in the cleanroom fabrication of BAW devices as well in the device characterizations.

Furthermore, I would like to thank Florent Tetard (Université Paris XIII) as well as Bassam Abdallah, Eric Gautron, Vincent Fernandez and Jonathan Ahmon (Institut des Matériaux de Nantes) by their assistance in other characterizations.

I would like to remember the rest of the PhD students at Limoges for their friendship and their hospitality: Salman Asad, Christophe Cibert, Sébastien Menessier, Béatrice Sourd, Hamid Belghazi, Claire Tendero, Aure Arcondeguy, Cécile Marchand, Olivier Tingaud and Fabrice Goutier.

I want to remember Dr. Jean Desmaison, who was my advisor at the beginning of this work, and acknowledge his wife, Dr. Martine Desmaison-Brut for her friendship during my stages at Limoges.

I want to express my gratitude to all the institutions that have support this work in different ways: the University of Limoges, the University of the Republic (Uruguay) and the French Embassy in Uruguay. Particularly, I want to thank some persons of these institutions by their special disposition: Gaëlle Peyrat and Graciela Vigo.

Lastly and most importantly, I would like to thank my family. I thank my wife Isabel and my son Daniel for their role in helping me attain this goal.

Abstract

Polycrystalline aluminum nitride thin films were produced with a microwave-plasma enhanced chemical vapor deposition technique. The plasma-injector distance, the substrate temperature and the RF bias were the main variables which allowed achieving this objective. At the time, it was possible to control the preferential orientation as <0001> or <10$\underline{1}$0>, both interesting for piezoelectric applications. The growth mechanisms that conducted to film microstructure development under different process conditions were explained, enriched by the comparison with a physical vapor deposition sputtering technique. The obtained films were characterized in their piezoelectric performance, including the construction of surface acoustic wave devices and bulk acoustic wave devices. Adequate piezoelectric response and acoustic velocities were obtained for <0001> oriented films, while <10$\underline{1}$0> oriented films did not show piezoelectric response under the configurations essayed. An extensive analysis was done in order to explain these behaviors.

Keywords: aluminum nitride, thin films, PECVD, film microstructure, piezoelectricity, SAW devices, BAW devices.

Resumen

Películas delgadas policristalinas de nitruro de aluminio fueron producidas empleando una técnica de deposición química en fase vapor asistida por plasma de microondas. La distancia plasma - inyector, la temperatura de substrato y la polarización RF del porta-substrato fueron las principales variables que permitieron alcanzar ese objetivo. Al mismo tiempo, fue posible controlar la orientación preferencial como <0001> o <10$\underline{1}$0>, ambas de interés para aplicaciones piezoeléctricas. Los mecanismos de crecimiento que condujeron al desarrollo de la microestructura en las diferentes condiciones fueron explicados. Esta explicación fue enriquecida por la comparación con una técnica de deposición física en fase vapor por pulverización catódica. Las películas obtenidas fueron caracterizadas en su desempeño piezoeléctrico, incluyendo la construcción de dispositivos electroacústicos de onda de superficie y de onda de volumen. Las películas orientadas <0001> mostraron respuesta piezoeléctrica y velocidad de onda acústica adecuadas. Por otro lado, las películas orientadas <10$\underline{1}$0> no mostraron respuesta piezoeléctrica para las configuraciones ensayadas. Un análisis extenso fue efectuado para explicar las posibles razones de estos comportamientos.

Palabras clave: nitruro de aluminio, películas delgadas, PECVD, microestructura de películas delgadas, piezoelectricidad, dispositivos SAW, dispositivos BAW.

Résumé

Des couches minces polycristallines de nitrure d'aluminium ont été produites en utilisant une technique de dépôt chimique en phase vapeur assisté par plasma micro-onde. La distance plasma - injecteur, la température du substrat et la polarisation RF du porte - substrat ont été les principales variables pour arriver à ce but. Dans un même temps, il a été possible de contrôler l'orientation préférentielle comme <0001> ou <10$\underline{1}$0>, intéressantes pour des applications piézoélectriques. Les mécanismes de croissance qui ont conduit au développement des microstructures dans les différentes conditions ont été expliqués, la comparaison avec une technique de dépôt physique en phase vapeur par pulvérisation cathodique a permis d'enricher la discussion. Les performances piézoélectriques des couches obtenues ont été caractérisées par construction des dispositifs électroacoustiques d'onde de surface et d'onde de volume. Les couches orientées <0001> ont montré une réponse piézoélectrique et une vitesse acoustique adéquates. Par contre, les couches orientées <10$\underline{1}$0> n'ont pas montré de réponse piézoélectrique dans les configurations testées. Une analyse exhaustive a été conduite pour expliquer les possibles raisons de ces comportements.

Mots-clés : nitrure d'aluminium, couches minces, PECVD, microstructure, piézoélectricité, dispositifs SAW, dispositifs BAW.

Contents

List of Tables

List of Figures

INTRODUCTION

At the beginning of the 21st century the world of communications has become extremely important, and every time the access to information is key to the development of society. Each day more information is demanded, where the need for time is a limiting factor in all human activities. An element that has shown a significant impact on society, in this regard, has been the mobile cell phone, which has given more independence and security to people everywhere.

The above facts have led to the constant search thereof for higher communication rates that has derived in the need of higher transmission frequencies. The transmission and reception of information through electromagnetic waves requires controlling and filtering frequencies in a precise way. Simultaneously, the use of portable devices demands the minimization of size as well as energy consumption at a time that the complexity demand is always on the rise. Then, the integration of the frequency control technology with Integrated Circuits technology (IC) is a must, since this combination allows for simpler, more cost effective, manufacturing.

There are a number of ways to attain control over the operating frequency of communication devices, however frequency control components based on the piezoelectric effect, and particularly those based on piezoelectric thin films, have acquire widespread acceptance over the traditional means based on inductive-capacitive (LC) resonant systems because of their manufacturing compatibility with IC technology.

BAW (Bulk Acoustic Wave) and SAW (Surface Acoustic Wave) devices based on piezoelectric thin films have attained crucial importance in this sense. Particularly, aluminum nitride thin films have been showed as optimal for these applications, associated mainly with AlN adequate piezoelectric response and high acoustic velocity. Among the possible techniques to obtain these AlN films, the PECVD (Plasma Enhanced Chemical Vapor Deposition) shows several advantages to optimize film microstructure and, simultaneously, it has not been very investigated in the past for these applications. Consequently, the optimization of a microwave-

PECVD technique to obtain piezoelectric AlN films for SAW and BAW applications was conducted in this work.

Therefore, the content of this manuscript is organized as follows:

A general review of the fundamentals and state of the art of piezoelectric aluminum nitride thin films is presented in chapter 1. Piezoelectricity and electroacoustic devices are shown in order to establish the film characteristics desired for these applications, analyze the different possible materials and select the optimal, i.e. AlN. The general properties of AlN, its piezoelectricity and the specific needed properties of AlN films for SAW and BAW applications are presented in order to define precisely the microstructure and additional properties searched. Then, the different techniques to obtain AlN films are reviewed, and consequently the general principles of plasma assisted techniques are presented. The advantages of choosing a microwave - PECVD technique are discussed. Afterward, the general mechanisms proposed in the past to explain AlN film growth, as well as microstructure and residual stress development is shown. Finally, based on all the previous information, the objectives of the work are established.

In chapter 2, the experimental procedure conducted in this work is described, related with the deposition process and the characterization techniques.

The development of polycrystalline oriented AlN films is shown in chapter 3 and the optimization of films properties for piezoelectric applications is shown in chapter 4. Different correlations are established between depositions conditions, plasma characteristics and properties of the obtained films.

The constructions of SAW and BAW devices with the obtained AlN films and the evaluation of their frequency response are shown in chapter 5.

Finally, a comparison of these films with those obtained with a PVD (Physical Vapor Deposition) reactive sputtering technique is presented in chapter 6, with a discussion of the possible growth mechanisms that take place in both cases.

Appendix A, B and C show a general view of the different techniques for a piezoelectric characterization of thin films, and different models used to analyze the frequency response of the electroacoustic devices constructed.

Chapter 1

PIEZOELECTRIC ALUMINUM NITRIDE THIN FILMS: FUNDAMENTALS AND STATE OF THE ART

1.1 Piezoelectricity

A solid is defined as piezoelectric if it becomes electrically polarized when subjected to a mechanical stress (direct effect), and becomes mechanically deformed when an electric field is applied to it (inverse effect). In order to understand this remarkable phenomenon, the crystal structure of this solid and the symmetry of the crystal lattice must be taken into account.

The atoms of the crystal lattice share a given electronic density through the bonds found between them. If the electronic density happens to be spatially non-uniform, a periodic arrangement of local electric dipoles can be present in the crystal, although the sum of all the individual dipoles at a given moment should be zero due to their instantaneous random orientation.

When a mechanical stress is applied to a solid, the elastic strain generated in the crystal creates changes in the length and/or direction of the bonds between the individual atoms. This leads to changes either in magnitude and/or in the direction of the dipoles present in the crystal, and therefore, a net polarization of the lattice may result. This is the origin of the direct piezoelectric effect, and its presence or absence in a given crystal is determined by the symmetry of the lattice.

The discovery of the direct piezoelectric effect, by Pierre and Jacques Curie (1880), followed directly from the established principle that a phenomenon can only exist in a system having a symmetry that is a sub-group of the characteristic symmetry of the observed response [1, 2]. Consequently, any asymmetries found in different phenomena must already exist in the system composed by the crystal structure plus the stimuli that are causing them to appear.

In the case of the direct piezoelectric effect, an elastic compressive stress applied to a crystal that gives rise to an electric polarization as a response can only be observed if the system including the crystal and the compressive stress has an equal or lower symmetry than the point-group symmetry of the resulting polarization. In particular, the system comprised of the crystal and the compressive stress cannot exhibit piezoelectric activity if it contains a center of symmetry. Since applied elastic stresses are invariably centrosymmetric, therefore, the latter requirement for a dielectric polarization to be observed as a response must be provided by the crystal system, thus, centrosymmetric crystals cannot be piezoelectric. This conclusion was reached by Curie [1], and later confirmed experimentally since 20 of the 21 non-centrosymmetric classes of crystals are piezoelectric. In particular, for the 432 class, although it lacks of a symmetry center, the presence of other symmetry elements in the crystal system precludes the appearance of piezoelectric behavior in this particular case [1].

Piezoelectricity implies linear coupling between the mechanical and electrical magnitudes, thus, a set of general equations of state can be derived from basic thermodynamics in order to describe this phenomenon:

$$\underline{S} = \underline{s}^{E}.\underline{T} + \underline{d}.\underline{E} \tag{1.1}$$

$$\underline{D} = \underline{d}.\underline{T} + \underline{\varepsilon}^{T}.\underline{E} \tag{1.2}$$

where $\underline{\boldsymbol{S}}$: strain (m/m), $\underline{\boldsymbol{D}}$: electric displacement (C/m^2), $\underline{\boldsymbol{T}}$: stress (N/m^2), $\underline{\boldsymbol{E}}$: electric field (V/m), $\underline{\boldsymbol{s}}^{\boldsymbol{E}}$: compliance tensor (m^2/N), $\underline{\boldsymbol{\varepsilon}}^{\boldsymbol{T}}$: permittivity tensor (F/m), $\underline{\boldsymbol{d}}$: piezoelectric tensor (m/V).

In order to describe the linear coupling relations between stimuli and responses in an anisotropic medium, i.e., a crystal [1], tensors must be used to account for all the different effects, and to express the fact that a certain stimulus applied along one direction could result in responses in other directions as well.

Vector quantities, as the electric displacement and the electric field, are properly described by using three components as a first rank tensor with 3^1 components. These two quantities must be equated by the dielectric permittivity, a second rank tensor (3^2 components) which is a nine component matrix. Since the strain is a second rank tensor, thus it is related with the electric field by the piezoelectric tensor, a third rank tensor with, in principle, 27 components. In a similar fashion, the electric displacement and the stress are equated by a third rank tensor. Furthermore, the strain and the stress, both second rank tensors are related by a four rank tensor (3^4 components), the elastic compliance.

Symmetry considerations related to the intrinsic nature of tensor quantities reduce the number of independent components found in each tensor ($S_{ij}=S_{ji}$, $T_{ij}=T_{ji}$, $s_{ijkl}=s_{jilk}$, $d_{ijk}=d_{ikj}$, $\epsilon_{ij}=\epsilon_{ji}$), and this also allows for a simplified matrix notation:

$$S_\alpha = s^E_{\alpha\beta}.T_\beta + d_{i\alpha}.E_i \tag{1.3}$$

$$D_i = d_{i\alpha}.T_\alpha + \varepsilon^T_{ij}.E_j \tag{1.4}$$

with i,j = 1, 2, 3 and α, β = 1, 2, …6.

Depending of the variables conveniently chosen to be independent, different types of fundamental relations can be written, where Eq. 1.1 and Eq. 1.2 are presented in the so called “d-form” in which the stress ***T*** and the electric field ***E*** have been chosen as the independent variables.

Other representation commonly used is the so called “e-form” where the strain ***S*** and the electric field ***E*** are selected as the independent variables, both of which are related by $\underline{c}^E$ the stiffness tensor, and by ***e*** the piezoelectric tensor. In the latter, the piezoelectric e-coefficients are related with the d-coefficients by [3]:

$$d_{i\beta} = e_{i\alpha}.s^E_{\alpha\beta} \tag{1.5}$$

with i = 1, 2, 3 and α, β = 1,2,…6 where $s^E_{\alpha\beta}$ are the compliance coefficients in m^2/N, $d_{i\beta}$ and $e_{i\alpha}$ are the piezoelectric coefficients in m/V and C/m^2 respectively.

When the symmetry of a particular crystalline structure is considered, the number of independent components in each particular case associated with the piezoelectric tensor is further reduced. Furthermore, it can be shown that in general all crystal properties represented by odd rank tensors must be absent in centrosymmetric crystals, i.e., piezoelectricity. In the case of a non piezoelectric material, all the piezoelectric coefficients are zero giving a null piezoelectric tensor, and consequently, both equations of state become uncoupled.

The parameter known as electromechanical coupling coefficient (K^2) is widely used as an indicator of the energy conversion efficiency of a piezoelectric transducer, since it expresses the ratio of the stored energy and the supplied energy in either form, i.e. electrical or mechanical. This coefficient is defined as follows:

$$K_d^{\,2} = \frac{d^2}{s^E \varepsilon^T} \qquad \text{d-form} \qquad (1.6)$$

$$K_e^{\,2} = \frac{e^2}{c^E \varepsilon^S} \qquad \text{e-form} \qquad (1.7)$$

where the appropriate values of the piezoelectric, elastic, and dielectric coefficients corresponding to each tensor are selected depending on the propagation direction of the phenomenon in the crystal [3-5].

1.1.1 Applications of the piezoelectric effect

The technology world is fairly dominated by the use of mechanical and electrical energies. Since piezoelectricity is the link through which both systems are coupled, piezoelectric materials have lead to the development of many devices, and it has great potential in future applications [6].

Piezoelectric materials have been used in traditional applications as electromechanical transducers and actuators. Just to mention a few, the direct piezoelectric effect is employed in microphones to convert longitudinal sound vibrations in air, i.e., the mechanical driving force, to an electrical signal. Similarly, it has been used in turn table pick-ups to convert wobbles grooved in vinyl records into electrical signals, as well as passive sonar array sensors, lighters, etc. make use of the direct effect.

On the other hand, the reverse piezoelectric effect is used in earphones, as well as in transducers to launch sound waves into liquid media - like echo-sounders, active sonar devices, ultrasonic cleaning systems, etc., while agile piezoelectric actuators are used in variable focus camera lenses, electronic watches, etc. Traditionally, quartz, PZT (lead zirconate titanate), barium and lead titanate have been used in most of these cases.

The need to have stabilized oscillators to keep radio stations fine tuned to the allotted broadcast frequency derived in the development of one important application of piezoelectric materials. Electric resonant circuits formerly used become unstable for this demanding task, thus they have been substituted by piezoelectric technology. A piezoelectric crystal cuboid, inserted between two electrodes forming a capacitor, is connected into a resonant electric circuit, where the circuit electric resonance frequency will be locked in by the frequency of the mechanical oscillations of the piezoelectric crystal. The latter, in turn, is determined by the geometric dimensions of the crystal and the velocity at which acoustic waves travel through the solid. By putting the crystal in a constant temperature environment, it is possible to maintain a strict control of its geometric dimensions, and thus precisely controlling the broadcasting frequency.

Acoustic wave devices based on piezoelectric materials have been used in a wide variety of applications such as delay lines, oscillators, resonators, sensors, actuators, acoustic microscopy as well as in specialized military equipment. Research carried out in the field of microelectromechanical systems (MEMs) devices that integrate electrical and mechanical systems on a semiconductor substrate, led to the development of microsensors, microactuators, electronic control circuits, and other devices [7].

At the moment by far the largest market for acoustic wave devices is the telecommunication industry, primary for wireless communications in mobile cell phones, wireless telephones and base stations [8, 9]. These portable devices incorporate acoustic wave filters for precise frequency control that are chiefly based on surface acoustic wave (SAW) and bulk acoustic wave (BAW) resonator technology. The most commonly used materials in SAW devices have been bulk single crystal substrates of quartz, lithium tantalite, and lithium niobate. However, the enormous growth in communication systems has made frequency control in the low/medium GHz range, i.e. the microwave region, a key issue.

One of the main disadvantages of standard electroacoustic technology in the microwave region is that it makes use of single crystal piezoelectric materials. The materials that can be produced in these conditions are rather limited in number, and in all cases, they are incompatible with Integrated Circuits (IC) technology. Since the frequency is determined by the device dimensions and the crystal elastic properties, i.e. the acoustic velocity, for a given material the only available way to increase the operating frequency, is to reduce the device dimensions. The latter has inherently associated physical limits as well as a large increase in manufacturing costs.

In the recent years, thin piezoelectric films have been developed to extend the application range of electromechanical SAW and BAW devices to increasingly higher frequencies. The manufacturing of SAW devices employing materials with high acoustic wave velocities, as well as the development of BAW resonators as Thin Film Bulk Acoustic Resonators (FBAR) show the most promise to extend piezoelectric technology to the highest frequency bands. In order to obtain these devices, piezoelectric thin films with high uniformity and controlled properties must be grown over relatively large substrates. Additionally, the greatest potential of using thin films is that they open the door to the possibility of integrating the traditionally incompatible IC with electro-acoustic technologies.

1.1.2 Bulk acoustic wave devices

The core of a BAW device is a BAW resonator that consists of an acoustic cavity- i.e., a piezoelectric film- that is enclosed on both sides by metal electrodes in a sandwich configuration. This structure is acoustically insulated from the supporting substrate either by creating a gap between the bottom electrode and the substrate, a configuration known as a membrane resonator or Film Bulk Acoustic Resonators (FBAR), or by incorporating in this position a Bragg reflector known as a Solidly Mounted Resonator (SMR) (see Fig. 1.1) [10,11].

The aforementioned devices operate under the general principle by which a series of mechanical resonant frequencies of vibration in the piezoelectric film will be observed when the film characteristic dimension *d* is an odd number of half wavelengths. The fundamental mode will be found when *d* is equal to $\lambda_0/2$ (see Fig. 1.1). As the mechanical wave travels in the crystal at the speed of sound, the frequency of the mechanical oscillation will be given by:

$$f = \frac{V_{BAW}}{\lambda_0} = \frac{V_{BAW}}{2d} \tag{1.8}$$

where: *f*: resonant frequency (s^{-1}), V_{BAW}: velocity of sound as bulk acoustic waves (m/s), λ_0: acoustic wavelength (m), *d*: characteristic device dimension (m) related with the piezoelectric film thickness.

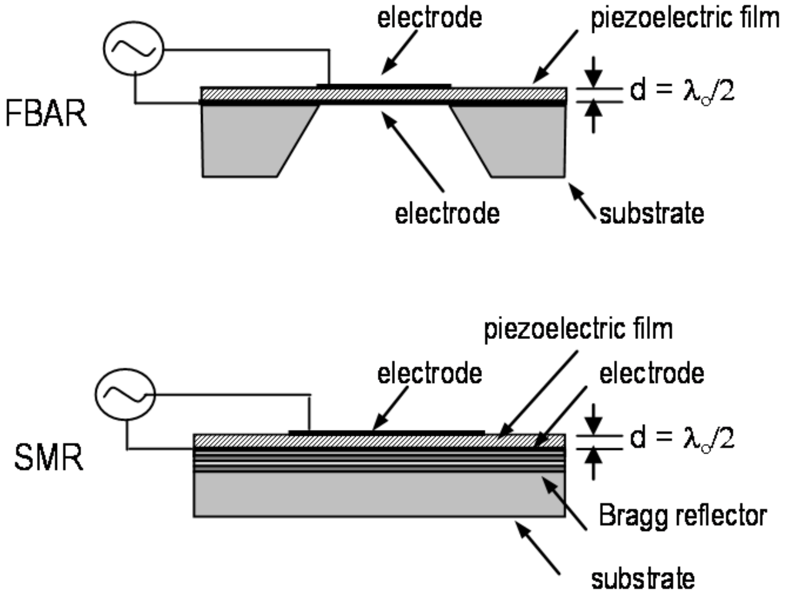

Figure 1.1: FBAR and SMR bulk acoustic wave devices.

As mentioned above, since the piezoelectric film is enclosed between metal electrodes, the capacitor derived from this configuration can be connected to an electric circuit having the same resonant frequency *f*. If thin piezoelectric films with thicknesses in the range of 0.1 – 1.0 µm can be manufactured with materials whose sound velocities are found on the order of 10^3 m/s to 10^4 m/s, a family of resonators that can operate in GHz frequency range can be developed, as the telecommunication market is demanding.

Appendix A shows a simplified model to predict the general frequency response of these BAW devices.

1.1.3 Surface acoustic wave devices

These devices are based on the generation of surface acoustic waves– i.e. Rayleigh waves - that propagate along the unclamped surface of a piezoelectric solid. A typical way to generate such acoustic waves in piezoelectric materials is by means of interdigital transducers (IDT) [6,12]. Fig. 1.2(a) shows the simplest device that can be constructed based on this principle. This device reproduces the same input waveform, at the output side after a given time delay. The electric signal is transformed by the input transducer into an acoustic signal. This signal travels at the speed of sound to the output transducer where it is in turn reconverted into an electric signal again.

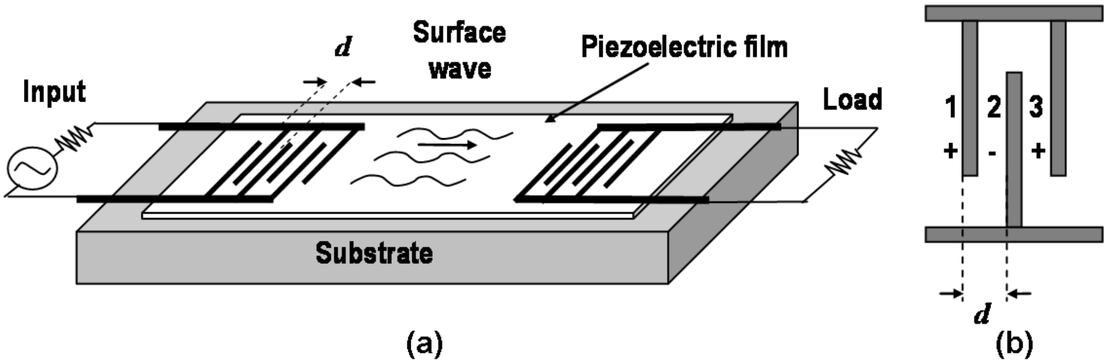

Figure 1.2: Surface acoustic wave device: (a) Sketch of a SAW device with two interdigital transducers. (b) Section of the interdigital transducer.

An electric signal simultaneously applied between fingers 1 and 2, then to fingers 2 and 3 (see Fig. 1.2 (b)), and so on, excites acoustic waves. These waves add up in a certain phase depending on the *d* distance between fingers. Considering that the adjacent electric signals are in opposite phases (+/- and -/+), when *d* is half wavelength of the generated acoustic waves, there is an addition effect in all finger pairs, and then maximum transmission is obtained. Once frequency is doubled, *d* becomes one wavelength, then the contribution of neighboring finger pairs is opposite and no net acoustic wave is produced by the transducer. Consequently, this device can work as a maximum transmission frequency filter, which frequency can be represented as:

$$f = \frac{V_{SAW}}{\lambda_0} = \frac{V_{SAW}}{2d} \tag{1.9}$$

where: f: maximum transmission frequency of the SAW filter (s^{-1}), V_{SAW}: velocity of sound of surface acoustic waves (m/s), λ_0: wavelength (m), d: distance between adjacent electrodes (see Fig. 1.10(b)) (m).

Many types of SAW devices for different applications have been developed, either with one or two ports, with or without interdigital reflectors and with different IDT shape. Among their interesting applications, the described devices have been used as sensors using the variation of acoustic wave velocity caused by the adsorption of specific species at the surface between both IDTs.

Since the frequency of SAW devices is determined by the size of IDT fingers, lately the increase of working frequencies in the microwave domain has led to a reduction of IDT finger size. By producing IDTs with fingers larger than one micrometer, traditional lithography processes of microtechnology allow for adequate productions costs. Smaller sizes need a technological change leading to significant increases in production costs [13]. Consequently, the acoustic velocity of the piezoelectric material becomes important in order to attain higher frequencies within a given finger size.

SAW devices constructed on thin films of piezoelectric materials are employed for the microwaves domain. And the performance of such devices can be optimized by a combination of different films with favorable piezoelectric and acoustic characteristics.

Appendix A shows a simple prediction model of frequency response for a typical SAW filter.

1.1.4 Characteristics of piezoelectric film for electro-acoustic devices

Piezoelectric films used in the construction of SAW and BAW devices for microwave frequencies should have the following characteristics.

a) Piezoelectric coupling

High piezoelectric coupling is required for SAW and BAW applications. Piezoelectric coupling is expressed by the effective electromechanical coupling coefficient K^2 which depends on both the type of material and the propagation direction in the crystal.

In order to determine the optimal configurations of a given piezoelectric material for BAW devices, the Christofel equation for the piezoelectric crystal is solved [14]. The results of such equation are represented by the "slowness surfaces" [1, 14], which show the acoustic wave velocities as function of the propagation directions for the different wave modes. By comparing scenarios with and without piezoelectric effect, the directions for which the different modes are piezoelectrically active, i.e. longitudinal and transverse, are possible to be found out. Thus, the optimal orientations of the crystal can be chosen by considering the directions of the applied field. Maximizing the electromechanical coupling coefficient, and avoiding the development of parasitic modes that could perturb the resonator response can be reached by this procedure [1, 15].

In the case of SAW devices, the Rayleigh mode guided wave equations and the corresponding boundary conditions are used for the same purpose as above. These equations are numerically solved and the evolution of the electromechanical coupling coefficient and acoustic wave velocity are obtained by progressive rotation of both the crystal cut and propagation direction [1, 15, 16].

b) High acoustic velocity

Small size devices or high-acoustic velocities are desired in order to allow higher operation frequencies of devices. Reduction of sizes can imply higher production costs or lower control of device geometries. Thus, materials with higher acoustic velocities are desired in order to work at higher frequencies. In a first approach, acoustic velocity depends on two properties of the material: its mechanical stiffness constant and its density, according to [1]:

$$V = \sqrt{\frac{c}{\rho}} \tag{1.10}$$

where: *V*: acoustic velocity of the excited mode (m/s), *c*: stiffness constant in the excited mode (N/m^2) when piezoelectrically stiffened (see Appendix 1), ρ : density of material (kg/m^3).

c) Thermal stability of material

The performance of these devices is determined by their ability to remain on the desired frequency, even under difficult environmental situations [14]. For a BAW resonator, this frequency depends on the crystal thickness (d) and sound velocity (V) based on equations 1.8 and 1.10, as follows:

$$f_r = \frac{V}{2d} = \sqrt{\frac{c}{\rho}}\frac{1}{2d} \tag{1.11}$$

which is valid for the fundamental resonance (first harmonic) of thickness excitation modes.

All factors in equation 1.11 are temperature-dependent. Therefore, all mutual dependencies must be taken into account in order determine the optimum crystal cut and orientation to minimize the effects and reach temperature stability. A derivative from equation 1.11, is the following:

$$\frac{1}{f_r}\frac{df_r}{dT} = \frac{1}{2}\left[\frac{1}{c}\frac{dc}{dT} - \frac{1}{\rho}\frac{d\rho}{dT}\right] - \frac{1}{d}\frac{dd}{dT} \tag{1.12}$$

The last term, representing the temperature variation of resonator thickness, is determined by the material’s linear coefficient of thermal expansion. The middle term, representing the material’s density temperature variation, generally tends to offset against the last one. And the first term, represents the variation of stiffness constants with temperature, which is almost always the largest. Usually, with temperature rise, stiffness components become softer. Device designers are interested in the exceptions to this rule, which allow temperature-stable orientations. This is the reason why quartz is particularly suited for resonators.

d) Low surface roughness

In the case of surface acoustic waves, all energy is concentrated almost within a wavelength from the surface to the inside (see Appendix 1). Consequently, when surface roughness is higher than one wavelength, the surface acoustic wave appears to be unable to pass through. With a rough surface, part of the surface acoustic wave is converted into a bulk acoustic wave, resulting in large loss for the SAW device [17, 18]. Consequently, surface roughness becomes more critical when the frequency of the SAW device is higher. Apart from acoustic losses emerging from surface roughness, there is also the complexity of producing IDTs with appropriate resolution.

e) Mechanical stresses

There should be no excessive internal stress in thin films so as to allow an adequate geometry and mechanical integrity of the devices.

Other desired characteristics of thin films for piezoelectric devices are: their adequacy for a deposition process to be feasible, their compatibility with other microtechnology processes, and chemical stability for their exposure to an operational environment.

1.1.5 Piezoelectric materials

In general, piezoelectric materials can be classified in two types as follows: *polar* piezoelectric materials, with a net dipole moment, and *nonpolar* piezoelectric materials, where added dipole moments with different directions result in a null total moment. Among the 20 non-centrosymmetric piezoelectric classes of crystalline structures [1, 19] 10 have a permanent net electrical polarization, i.e. they are polar piezoelectric crystals. Such polar crystals are further classified as *ferroelectric* and *nonferroelectric*.

Many materials have been studied after the discovery of piezoelectric effects in order to characterize the phenomenon and find applications. Ferroelectric piezoelectric materials as barium titanate, litium niobiate and litium tantalate, have shown strong piezoelectric properties. Non ferroelectric piezoelectric materials, such as quartz have several bulk applications. Quartz is rather popular thanks to its good temperature stability although its piezoelectric coefficients are not large [20].

Among the ferroelectric piezoelectric thin films, some types have strong piezoelectric properties. Consequently, they can be applied to microelectromechanical systems, acoustic wave transducers, sensors and resonators. The most important are lead titanate zirconate ($Pb(Zr_xTi_{1-x})O_3$), known as PZT, lead titanate ($PbTiO_3$), usually referred to as PT, and lithium niobate ($LiNbO_3$) referred to as LN, all of them with a perovskite related structure [19].

In the last decades, the most studied and used non-ferroelectric piezoelectric thin films have been zinc oxide and aluminum nitride. They are widely used in BAW and SAW devices, resonators and filters, in spite of their piezoelectric properties weaker than ferroelectrics [19]. These films have the advantage of low complexity of their deposition techniques and compatibility with other production processes which results in their extensive use.

Table 1.1 shows the general properties of AlN, ZnO and PZT, which are the most widely used materials for SAW and BAW applications.

AlN and ZnO show the lowest piezoelectric coefficients, but enough for these applications. AlN has the lowest piezoelectric constants, but it shows the highest propagation velocity of bulk acoustic waves. Also, AlN exhibits the highest surface acoustic wave velocity, which is enough for manufacturing higher frequency SAW devices at low cost microtechnology processes. Moreover, AlN shows higher electrical resistivity, high breakdown voltage, low dielectric loss, high thermal conductivity and low thermal expansion coefficients. These coefficients imply low thermal drifts for the devices.

With its higher chemical stability, AlN can be used in humid environments, which is not possible for the other two materials. At the same time, it can be etched under standard conditions to allow the production of multiple devices. Finally, AlN does not introduce contaminants into the CMOS micro-technology process [15], then becoming completely compatible with CMOS. The last is an additional important feature of AlN, completely different from the ZnO and PZT.

As a consequence, AlN seems to be the most adequate material for the applications analyzed here. The following section discusses the general properties of AlN, its origins and the specific characteristics of AlN films to optimize performance of piezoelectric devices.

Table 1.1: Properties of more used thin film piezoelectric materials for BAW and SAW applications [1, 19, 21-24].

	AlN	ZnO	PZT
Structure: System	Hexagonal	Hexagonal	Hexagonal
Class	6mm	6mm	6mm
Lattice constants (nm)	a = 0.311	a = 0.328	a = 0.578
	c = 0.498	c = 0.523	c = 0.710
Density (kg/m^3)	3,230	5,610	7,570
Young's modulus (GPa)	308	201	68
Acoustic velocity (BAW)	10,400	5,700	3,900
(m/s) (SAW)	5,100	2,600	
Thermal conductivity (W/m.ºC)	285	60	1.8
Thermal expansion coefficient	α_a = 4.2	α_a = 6.5	2
(10^{-6}/ºC)	α_c = 5.3	α_c =3.0	
Band Gap (eV)	6.2	3.4	2.7
Relative permittivity	8.9	10.8	650
Resistivity (Ohm.m)	10^9	10^5	10^7
Piezoelectric constants (pm/V)	d_{33} = 4.9	6.2	180
	d_{31} = -1.9	-2.7	-90
Ferroelectricity	No	No	Yes

1.2 Aluminum Nitride

At proper conditions nitrogen combines with most elements of the periodic chart to form compounds, and in particular with metals to form nitrides. These compounds can be grouped according to their properties in *saltlike*, *metallic* and *diamondlike* nitrides [25]. While the first two groups are characterized by sodium chloride type crystalline structures, the third group of nitrides shows a diamond type structure, with metallic and nitrogen atoms in tetrahedral distribution. Saltlike nitrides are a distinct group since ionic bonds are present. These solids are electric insulators or ionic conductors. Diamondlike nitrides show predominantly covalent bonds and correspond to nonconductive or intrinsic semiconductor materials.

The electronic configurations of Al, $[Ne]3s^23p^1$, and N, $1s^22s^22p^3$, allow the development of sp^3 hybridation of the electronic orbitals to obtain the typical tetrahedral distribution of the AlN diamondlike structure. The AlN chemical stability and hardness can be explained by the high energy covalent bonds, in spite of a certain level of ionic character – i.e. 43% -. Hardness is the reason why AlN is used for high performance mechanical applications [26].

AlN high acoustic wave velocity is directly related to the high “mechanical stiffness / density” rate, which is in turn increased by the high bond energy and low packing rate of its diamondlike structure - i.e. hexagonal, wurtzite type - (see Figure 1.3 (left) and Equation 1.10).

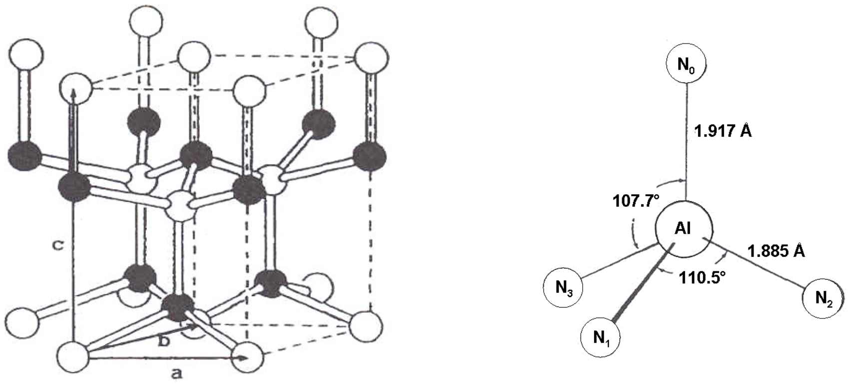

Figure 1.3: Wurtzite type structure of AlN: unit cell (left) and section of the unit cell showing its distorted coordination tetrahedral shape (right) [27].

In the AlN crystal structure (see Fig. 1.3) each Al atom is surrounded by four N atoms in a distorted tetrahedron with three side Al-N bonds (B_1), 1.885 Å long, and one Al-N bond (B_2) in the c-axis direction with a length of 1.917 Å. It has been considered that the sp^3 hybridation character of Al and N are the reasons for these distortions. Three orbitals of the tetrahedron are semifilled in both cases, but the remaining one is full for N and empty for Al. If It is assumed that the B_2 bonds are formed by the coupling of the empty Al and the filled N orbitals, an accumulation of ionic character in these B_2 bonds is produced. Lower bond energies along the c-axis direction are therefore expected [26, 27].

Since AlN shows a wide band gap of 6,2 eV, it is a semiconductor which, for some applications, can be considered as an insulator material. This fact has led to its use in several photonic applications, for instance deep ultraviolet light-emitting diodes.

In the insolent materials thermal conductivity is controlled by phonon transport. The high “mechanical stiffness / density” rate discussed above contributes to high thermal conductivity, which is one of the most interesting properties of AlN, which has led to its use for the support of electronic devices in order to conduct dissipated heat.

With its noncentrosymmetric crystalline structure, wurzite type, AlN is a piezoelectric material. Apart from being used in BAW and SAW devices associated with good piezoelectric coupling, high acoustic velocity and thermal stability, other interesting piezoelectric applications have been developed too. Such is the case of pressure sensors for combustion engines, where AlN combines the possibility of maintaining piezoelectric performance at high temperatures (non-ferroelectric), with chemical and thermal stability [28].

The equations of state corresponding to wurzite-type-structure aluminum nitride can be expressed in the following full matrix form, based on equations 1.3 and 1.4:

$$\begin{bmatrix} S_1 \\ S_2 \\ S_3 \\ S_4 \\ S_5 \\ S_6 \end{bmatrix} = \begin{bmatrix} s_{11} & s_{12} & s_{13} & 0 & 0 & 0 \\ s_{12} & s_{11} & s_{13} & 0 & 0 & 0 \\ s_{13} & s_{13} & s_{33} & 0 & 0 & 0 \\ 0 & 0 & 0 & s_{44} & 0 & 0 \\ 0 & 0 & 0 & 0 & s_{44} & 0 \\ 0 & 0 & 0 & 0 & 0 & 2(s_{11}-s_{12}) \end{bmatrix} . \begin{bmatrix} T_1 \\ T_2 \\ T_3 \\ T_4 \\ T_5 \\ T_6 \end{bmatrix} + \begin{bmatrix} 0 & 0 & d_{31} \\ 0 & 0 & d_{31} \\ 0 & 0 & d_{33} \\ 0 & d_{15} & 0 \\ d_{15} & 0 & 0 \\ 0 & 0 & 0 \end{bmatrix} . \begin{bmatrix} E_1 \\ E_2 \\ E_3 \end{bmatrix} \tag{1.13}$$

$$\begin{bmatrix} D_1 \\ D_2 \\ D_3 \end{bmatrix} = \begin{bmatrix} 0 & 0 & 0 & 0 & d_{15} & 0 \\ 0 & 0 & 0 & d_{15} & 0 & 0 \\ d_{31} & d_{31} & d_{33} & 0 & 0 & 0 \end{bmatrix} . \begin{bmatrix} T_1 \\ T_2 \\ T_3 \\ T_4 \\ T_5 \\ T_6 \end{bmatrix} + \begin{bmatrix} \varepsilon_{11} & 0 & 0 \\ 0 & \varepsilon_{11} & 0 \\ 0 & 0 & \varepsilon_{33} \end{bmatrix} . \begin{bmatrix} E_1 \\ E_2 \\ E_3 \end{bmatrix} \tag{1.14}$$

where there are only three independent piezoelectric coefficients, d_{33}, d_{31} and d_{15}, for the piezoelectric tensor.

A simple one-dimensional model, developed to understand the origin of piezoelectricity and the piezoelectric coefficient in asymmetric ionic crystals, can be applied to aluminum nitride [1].

AlN crystal lattice can be envisioned as consisting of successive layers of nitrogen and aluminum ions (see Fig. 1.4(a)), where ions are repeated along identical rows (see Fig 1.4(b)) perpendicularly to the layers. When an external agent, such as a mechanical stress or electric field is applied perpendicularly to these layers, considering only one row is sufficient because displacement of all ions in one layer is the same. Based on the assumption that –q and +q are the effective charges of nitrogen and aluminum ions linked to each other by springs, and that the closest neighboring ions are not symmetrically distributed, the springs on either side have different force constants k_1 and k_2. The chain is divided into cells, which length is *a*, each containing two dipoles with moments *q(a-b)/2* and *–qb/2*, where *b* is one of the interatomic distances. The dipole moment of one molecule is then

$$p_0 = \frac{q.(a-2b)}{2} \tag{1.15}$$

Therefore, the crystal is polar in this case. When at rest, and taking *n* as the number of AlN molecules per unit volume, the polarization P_o per unit volume is

$$P_0 = n\frac{q.(a-2b)}{2} \tag{1.16}$$

Under the action of stress, the chain is stretched or compressed, *a* and *b* length changes lead to a polarization change given by

$$P = \Delta P_0 = n\frac{q.(\Delta a-2\Delta b)}{2} \tag{1.17}$$

This is the direct piezoelectric effect.

In turn, an applied electric field causes the positive and negative ions to be displaced in opposite directions, so that if *(a-b)* is increased, then *b* is reduced (see Fig 1.4(c)). The different stiffness of each spring results in a deformation. This is the inverse piezoelectric effect.

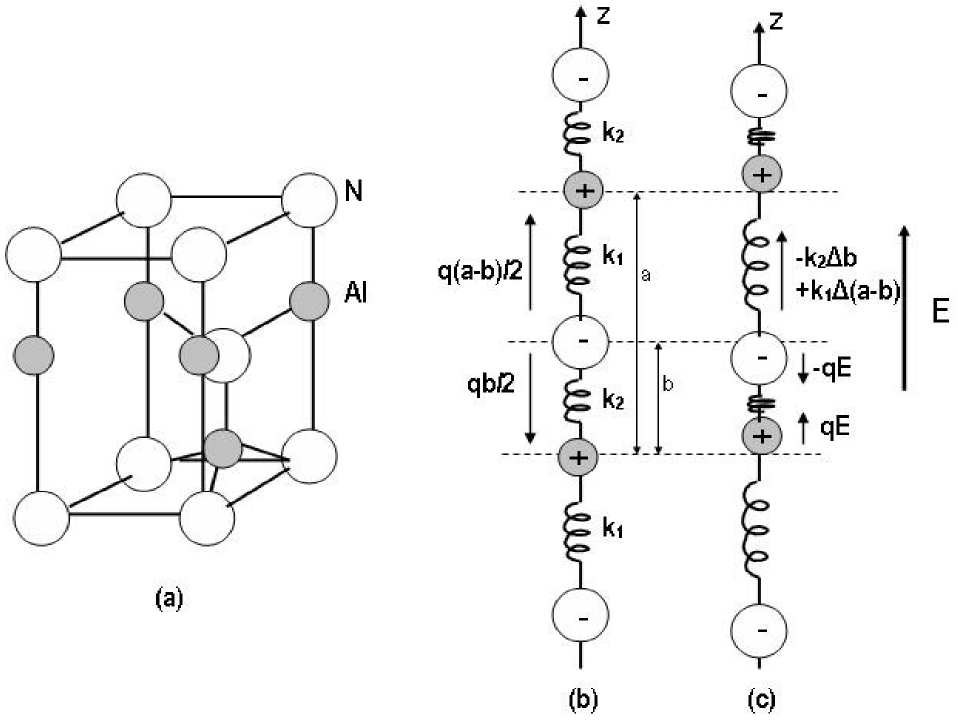

Figure 1.4: Piezoelectricity in an aluminum nitride crystal. (a) AlN wurtzite structure. (b) Model distribution of nitrogen and aluminum ions along a row parallel to the main axis. (c) Row deformation under the action of an electric field: Al and N ions are displaced in opposite directions and the cell length changes by Δa.

On the basis of the e-form scheme of equations of state, general expressions for the corresponding coefficients can be deducted, as follows:

$$T = cS - eE \tag{1.18}$$

$$D = \varepsilon_0 E + P = \varepsilon E + eS \tag{1.19}$$

with

$$\varepsilon = \varepsilon_0 + \chi_{ion} + \chi_e \tag{1.20}$$

$$c = na^2 (\frac{k_2 k_1}{k_2 + k_1}) \tag{1.21}$$

$$e = \frac{nq}{2} (\frac{k_2 - k_1}{k_1 + k_2}) a \tag{1.22}$$

being: ε: dielectric constant (F/m), χ_e electronic susceptibility (F/m), $\chi_{ion} = nq^2/(k_1+k_2)$ ionic susceptibility (F/m), *c*: stiffness constant (N/m^2), *e*: piezoelectric constant (C/m^2).

Equation 1.22 shows that the existence of piezoelectric effect is exclusively associated with the asymmetry in the spring constants, since $e = 0$ when $k_1 = k_2$. Thus, this model explains the origin of piezoelectricity in asymmetric ionic crystals, and can be applied to aluminum nitride. But in general the piezoelectricity mechanism is more complex since the piezoelectric effect can also occur in monoatomic crystals, as tellurium and selenium. In the cases of these crystals, the electronic polarization is attributed to changes in the electronic distribution.

1.2.1 AlN films for BAW and SAW electro-acoustic devices

The performance of AlN films for piezoelectric application in SAW and BAW electro-acoustic devices is closely related to the microstructure and compositions of the films. Although single crystal AlN films would be the ideal option for this application, it has been demonstrated that preferentially-oriented-polycrystalline films can also reach adequate performances.

In the case of BAW applications, the electric field is applied perpendicularly to the substrate in order to produce longitudinal acoustic waves in this direction. As the piezoelectric effect is maximum in the c-axis direction of the AlN crystal lattice (d_{33} piezoelectric coefficient), for this application <0001> oriented films are desired (see Fig. 1.5 and Appendix A) [19, 29].

On the other hand, the optimal orientation for SAW applications is not so evident. In general terms, the components of the applied electric field between the fingers of the interdigital electrodes are parallel and perpendicular to the substrate surface. Furthermore, there are displacement components of the generated surface acoustic waves in both directions (see Appendix A).

Normally <0001> oriented AlN films have been used for SAW applications with adequate performance [30]. And their effective electromechanical coupling coefficient has been directly associated to the d_{31} piezoelectric coefficient of films, based on the assumption that an electric field is perpendicular to the substrate and that generated surface acoustic waves are longitudinal [31].

Several authors have informed their interest in developing <10$\underline{1}$0> oriented AlN films for SAW applications [19, 32, 33], based on numerical resolutions of the fundamental equations for Raileigh waves [16] (see Fig. 1.5). Performance evaluations of SAW devices developed on single-crystal bulk aluminum nitride have confirmed the advantage of the <10$\underline{1}$0> orientation [4].

When using the <10$\underline{1}$0> orientation, the c-axis is parallel to the substrate surface, then the piezoelectric effect is maximized by the action of the d_{33} coefficient. In this simplified consideration these facts have been taken into account: the electric field component is parallel to the substrate surface and the surface acoustic waves are longitudinal.

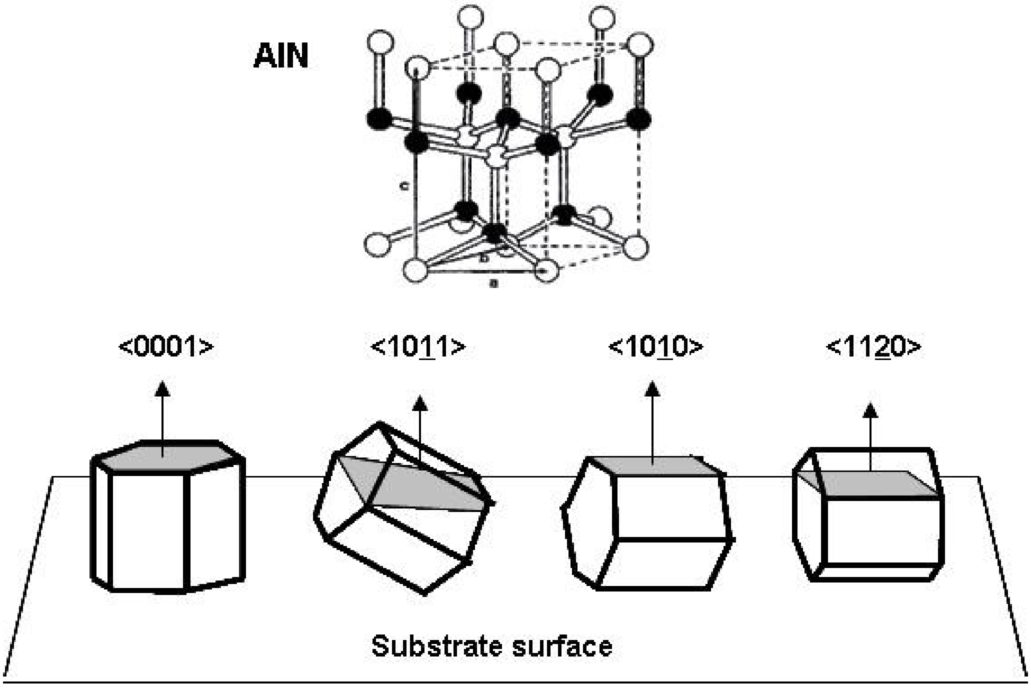

Figure 1.5: Different possible orientations of the AlN film with respect to substrate surface.

The development of this <10$\underline{1}$0> orientation has been optimized [32, 34] in some works, mainly by PVD techniques. However, no evaluation of their performance in SAW devices has been shown.

Consequently, the orientation grade, or texture, of a polycrystalline AlN film, is an important parameter associated with the piezoelectric film performance. The traditional XRD (x-ray diffraction) analysis in the configuration Bragg-Brentano $\theta/2\theta$ shows the diffraction response of plans parallel to the substrate surface. Then, the existence of reflection peaks and their relative intensity are primarily indicative of the film orientation. For a complete texture evaluation and to quantify the frequency distribution of orientation within a desired direction range, the “rocking curve” technique has been developed. The FWHM (full width at half maximum) of the distribution peak obtained is a direct measurement of dispersion. Many authors have established a link between the FWHM of the rocking curve and the piezoelectric performance of <0001> oriented AlN films. They suggest maximal FWHM values for an acceptable piezoelectric performance, e. g. : 4 - 8º [9, 21, 29, 31].

Moreover, this correlation has been modeled by Lughi [21] by using the AlN piezoelectric tensor, the transformation of coordinates, and a Gaussian-distributed analysis. The model results were in accordance with the measurements, mainly for low FWHM values.

In contrast, recent studies have suggested that it is not possible to exclusively link the FWHM of the rocking curve with the piezoelectric performance. It has been speculated that this absence of correlation is caused by inversion domains or other unknown microstructure defects [27, 31]. Inversion domains are grains with opposite crystallographic polarities ([0001] and [000$\underline{1}$]), with a resulting negligible net piezoelectric field (see Figure 1.6). These inversion domains are difficult to identified but their presence has been shown by some authors [35, 36].

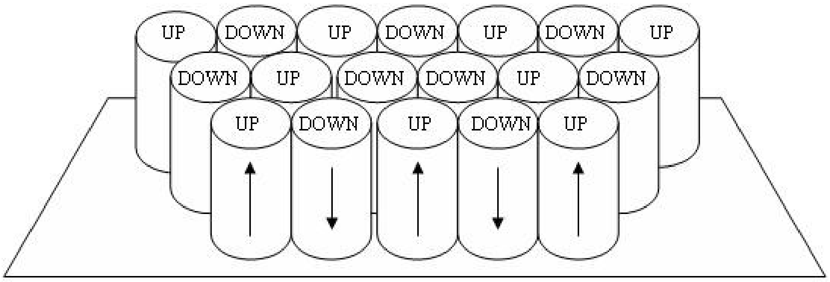

Figure 1.6: Representation of Inversion domains in the film.

Aluminum has high affinity of reaction with oxygen, and this oxygen is usually present in the deposition process as a consequence of the limited residual vacuum in the reactor chamber, among other possible reasons. Many works about films obtained by a Physical Vapor Deposition (PVD) sputtering deposition technique have been published, in many of them the value of AlN film oxygen impurity is linked to the FWHM of rocking curves and piezoelectric performance [19, 37, 38]. All of them have arrived to the conclusion that the increase of oxygen concentration in the film reduces piezoelectric performance.

The increase of piezoelectric performance has been related to the increase of film thickness prepared under the same process conditions [39]. However, a favorable evolution of the crystalline structure going up in the film profile has been observed for PVD techniques [40].

Acoustic velocities in the range of 10,400 m/s have been determined in BAW applications. AlN films deposited on Si(100) substrates have shown acoustic velocities of 5,100 m/s in SAW applications [8, 9, 41-43]. By deposition of AlN on diamond films [9, 18, 42], it has been possible to attain SAW velocities of approximately 9,500 m/s, due to the high acoustic velocities of diamond [9, 42].

Surface roughness of the AlN films is particularly critical, as previously discussed, to reduce the acoustic losses in SAW devices. Values lower than 30 nm have been informed as adequate for these applications [44].

In summary, in order to optimize the performance of the AlN films for the piezoelectric applications under study, it is necessary to maximize their crystalline development and crystallographic texture, in the <0001> or the <10$\underline{1}$0> directions, and simultaneously to minimize their roughness, impurity contents and mechanical residual stress.

The following section analyzes the different possible techniques in order to attain these objectives. As a result, the most promising option is selected for the research of this work.

1.3 Thin Film Manufacturing Techniques

Many techniques have been used to obtain AlN films in the past, ranging from MBE (Molecular Beam Epitaxy) or MOCVD (Metal-organic Chemical Vapor Deposition), to PVD (Physical Vapor Deposition). Different microstructures have been developed using these techniques, from single crystal type, to polycrystalline, or eventually amorphous [19].

Deposition techniques for single crystal films are typically associated with extremely controlled growth conditions and epitaxy effects on single crystal substrates. They generally imply very low growth velocities and/or very high deposition temperatures [45]. Consequently, time consuming operations and compatibility of other device components with the process temperature are the reasons why these processes are not practicable for industrial massive applications in the microelectronic industry.

Then, this research is focused on polycrystalline AlN film techniques, and particularly in "plasma assisted" techniques, which can be used at lower temperatures. In the following paragraphs the basis and types of such techniques are discussed.

1.3.1 Plasma assisted techniques for thin films deposition

A plasma is defined as a quasineutral gas composed of free electrons, ions and neutral particles exhibiting a collective behavior [46]. In general terms, plasmas can classified as thermal or cold. In thermal plasmas, all the species are in thermal equilibrium, being all of them at a common temperature. Conversely, in cold or low pressure plasmas, free electrons, ions and neutral particles are in independent thermal equilibriums, with different temperatures for electrons and heavy species. This particular behavior showed by cold plasmas is explained by the low collision frequency of species at low pressures and the low energy transfer associated with the elastic collisions of electrons with heavy species [47, 48].

Cold plasmas are used in film deposition processes with the object of providing the necessary activation energy for chemical reactions through the inelastic collisions of free electrons with heavy species. This is possible at a relatively low substrate temperature, which is related to the heavy species temperature, as a result of the non-equilibrium condition between electrons and heavy species. An additional effect of deposition process plasmas is the positive ion bombardment of the treated surface, before and during the film growth. Such ion bombardment can be used both for cleaning the substrate surface and controlling the film microstructure.

Appreciable radiations are emitted by this type of plasmas in a wide wavelength band, including the visible spectrum, by bound-bound, bound-free and free-free processes of electron energy transitions, as a consequence of the high electronic temperature. Bound-bound processes correspond to the transition of an electron in an atom or molecule, from an excited level to another lower energy level, and the corresponding emission of a photon of well defined *hv* energy. Since there is a line-spectrum resulting from these phenomena [49, 50], the species in the reaction medium taking part in the radiation processes can be identified by analyzing this plasma spectrum.

In case of disturbance of plasma neutrality for any reason, then large restoring forces are developed, striving to re-established charge neutrality. Because of the large mass difference between electrons and ions, electrons are the first to respond to the restoring forces. Restoring forces are proportional to displacement, then oscillations are generated [46, 51].

Electron oscillation occurs at plasma frequency f_{pe} according to:

$$f_{pe} = \frac{1}{2\pi}\sqrt{\left(\frac{n_e e^2}{m_e.\varepsilon_0}\right)} \quad (1.23)$$

where: n_e: electronic density per m^3, e: electron charge (C), m_e: electron mass (kg), ϵ_0: permittivity of vacuum (F/m).

This frequency is usually near a gigahertz. Higher ion mass ensures lower ion plasma frequency (f_{pi}) in a range from zero to ten megahertz.

Plasmas for material processing are produced by electrical energy transfer to the gas medium. The process is started by increasing gas conductivity, and maintained through the ionization of the species. Simultaneously, this species recombines quickly in the medium and on the walls [52]. These plasma generation techniques are known as electric discharges and can be based on the application of DC or AC potentials. In a DC glow discharge, an electric potential difference is applied between two conductor electrodes in a gas chamber. Once a certain voltage is exceeded, a complex setting with different glow and non-glow regions is created between both electrodes. Since, during the deposition process, the substrate is reached by a flow of charged species, this DC plasma discharge can be used only for processing electrically conductive substrates. AC discharges are used in order to work with insolent substrates. These AC discharges are classified according to their excitation frequencies, taking in account the typical plasma frequencies of ions (f_{pi}) and electrons (f_{pe}), as follows [52]:

a) low frequency ($f < f_{pi} < f_{pe}$), where the free electrons and ions follow the oscillations of the electromagnetic field;

b) radiofrequency ($f_{pi} < f < f_{pe}$), typically 13,56 MHz, where electrons follow the electromagnetic field oscillations, while ions are sensible to the average temporary local values of this field;

c) microwave ($f_{pi} < f_{pe} \approx f$), where behavior is similar to b), though enhanced.

Radiofrequency discharges are often used in the microelectronic industry. Their electronic density range is usually 10^{10} cm^{-3} and their ions are “frozen” in comparison with the radiofrequency field. In an oscillation the numbers of lost electrons on the cathode (substrate holder) and on the anode (chamber walls) are the same, then if their surfaces are different an auto-polarization voltage (bias) can be generated. This effect is caused by the different electric impedance of the system for each oscillation sense and the use of a serie capacitor in the circuit [47]. Thus, the acceleration of positive ions displacing from plasma to substrate have a specific impact on the film microstructure.

In the case of microwave discharges, excitation frequency is higher than plasma frequencies f_{pi} and f_{pe}. As a consequence, electrons and ions are “frozen” in relation to discharge electromagnetic field. Species distribution in microwave discharges is not defined by the electronic impact creation processes or by wall recombination lost processes. Compared with radiofrequency discharges, at equal power density, average microwave electronic energy is lower, however electronic density is higher ($n_e > 10^{11}$ cm^{-3}), resulting in dissociation rates above 10%. Consequently, with microwave discharges, higher thin film deposition rates can be attained using the higher densities of active species, i.e., electrons and ions [53-55].

Most microwave plasmas for deposition processes are based on “surface wave technology” [50]. One of the main features of these plasmas is that the maximum level of electric field is near the dielectric wall of the plasma chamber, and this field’s minimum level is at the plasma center. The structure known as “surfaguide” is composed of a dielectric tube (quartz) that keeps the environment and the plasma chamber apart, and a waveguide around such tube is used to conduct the incident power from the microwave generator to the plasma. Stable and reproducible plasmas in large diameter cavities can be generated with this structure. Good generator/plasma energy transfers and large pressure ranges are possible with this structure [50, 53, 54, 56, 57]. Simultaneously, with the absence of electrodes in the chamber, pollution risks of the processed materials are reduced. This fact is an important advantage of microwave discharge.

In order to increase microwave coupling and electronic density, a supplementary device known as ECR (Electron Cyclotron Resonance) can be used in microwave discharges. This is based on the generation of a magnetic field which, added to the microwave field, confines the plasma at resonant conditions [50, 55, 58].

1.3.2 Plasma assisted techniques for polycrystalline AlN films

Among the plasma assisted techniques for AlN deposition, two important groups can be distinguished: PAPVD (Plasma Assisted Physical Vapor Deposition) and PECVD (Plasma Enhanced Chemical Vapor Deposition) techniques.

PVD (Physical Vapor Deposition) techniques are based on matter transfer from condensed-phase evaporated or sputtered target sources. In particular, PAPVD "reactive sputtering" has been a widely used technique for AlN thin film deposition (see Fig. 1.7(a)) [19, 59]. Ionic bombardment by energetic Ar^+ ions of an Al target is produced in the presence of an Ar/N_2 plasma, and Al species are sputtered from this target by momentum transfer. Then, Al, N and Al-N species are deposited on the substrate producing the AlN film. DC or RF discharges are commonly used in this technique, with the "magnetron" supplement which allows improving the sputtering effect and consequently the deposition rate. It consist in a magnetic field near the target surface which changes the electron motion allowing higher ionization and consequently a higher sputtering effect [48, 51, 58].

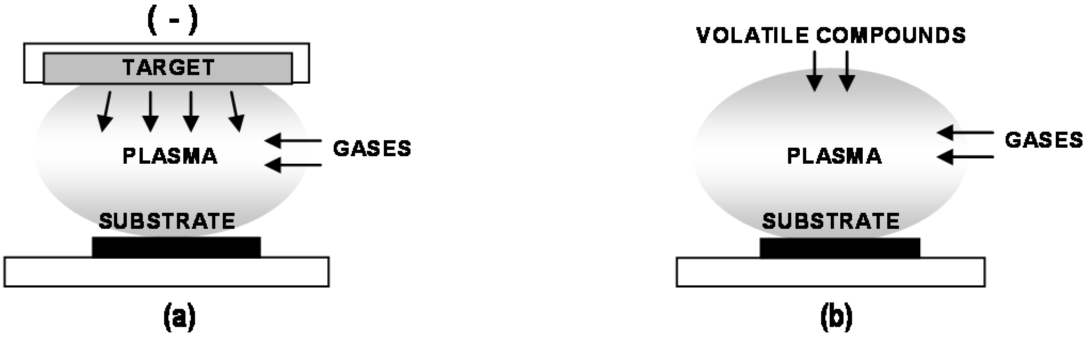

Figure 1.7: General sketches of the PAPVD (a) and PECVD (b) processes.

CVD (Chemical Vapor Deposition) techniques are processes where a chemical reaction takes place. Such reaction is between a volatile compound of material to be deposited– i.e. the Al precursor– and other gases– i.e. N_2 –, thus a nonvolatile solid is produced which is deposited on a suitably placed substrate [58]. CVD processes were used commercially prior to PVD processes because there is no requirement of vacuum or unusual levels of electric power to obtain several materials. Nowadays, high-temperature CVD processes for thin films and coatings production are increasingly applied by several technologies, such solid-state electronic devices manufacturing. Among the reasons for such adoption are the ability to produce a large variety of metal and insulating films and coatings, either by way of inorganic or organic compounds, in crystalline or vitreous form. And there are other reasons such as the ability to control films stoichiometry, the affordability of equipment, operation expenses and the compatibility with other processing steps. Many variants of CVD processing have been developed to optimize different applications, including hybridization with PVD techniques. By developing the Plasma Enhanced CVD techniques (PECVD), a temperature reduction has been possible and a substantial improvement of the process compatibility with other microtechnologies has been attained (see Fig. 1.7(b)) [48, 58]. Thus PECVD techniques have become an interesting option for the deposition of AlN films for electronic devices.

In general, a CVD process is composed by the fundamental sequential steps illustrated in Fig. 1.8 as follows [58]:

a) convective and diffusive transport of reactants from gas inlets to the reaction zone,

b) chemical reactions in the gas phase to produce new reactive species and by-products,

c) transport of the initial reactants and their products to the substrate surface,

d) adsorption and diffusion of these species on the substrate surface,

e) heterogeneous reactions catalyzed by the surface leading to film formation,

f) desorption of the volatile by-products of surface reactions,

g) convective and diffusive transport of the reaction by-products away from the reaction zone.

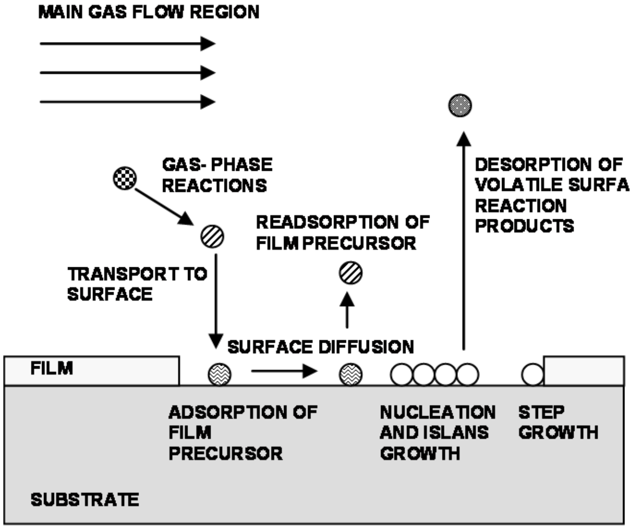

Figure 1.8: Sequence of processes contributing to Chemical Vapor Deposition film growth [58].

In CVD processes, it is important to point out that mass distribution on substrate surface is determined mainly by gas flow. Thus, it is possible to easily deal with special substrate geometries by using a flow distribution adequate design in the reactor chamber. Conversely, PVD sputtering techniques are highly directional in this sense, according to the trajectory of the high energy species sputtered from the target.

In the case of Plasma Enhanced CVD processes, the complex chemistry associated with the reactive species in the plasma is an additional fact to take into account. At the same time, the ion bombardment of film surface during the deposition is an additional parameter that can be controlled in certain configurations, with important effects on film microstructure. Although some works on the use of PECVD techniques for AlN films deposition have been published [60-67], very few deal with the development of piezoelectric characteristics [68].

This concise review of the different possible techniques to obtain AlN films focused our interest on the growth of piezoelectric AlN films by a Plasma Enhanced Chemical Vapor Deposition technique; more specifically by using single microwave excitation to generate the plasma. The reasons for this selection are the following:

- in order to obtain the desired film properties, several parameters can be optimized;

- low directional processes make the deposition on substrates with intricated geometries possible, such is the case of complex Micro-electromechanical Systems (MEMs);
- the absence of electrodes in the reactor chamber may reduce film contamination;
- scarce information associated with the characteristics of the AlN films obtained by this specific technique, and lack of necessary information related to their piezoelectric performance in electro-acoustic devices;
- comparing films obtained by these techniques with the traditional PVD sputtering techniques may result in new knowledge on film growth control mechanisms.

The following section contains a review on the general growth mechanisms for thin films. It is particularly focused on the different theories proposed to explain the development of preferential crystallographic orientation in AlN films. Finally, some general theories for the development of residual stresses in thin films are presented. Such information is taken into account in the following chapters both for the experimental design and also for the discussion of experimental results obtained.

1.4 Thin Film Growth Mechanisms

Film microstructures are essentially defined by their growth mechanisms. The growth process consists of a progression of events beginning with condensation of isolated atomic clusters on a bare substrate, continuing with film thickening due to additional deposition and resulting in fully developed films. With this process, single-crystal, polycrystalline or amorphous film microstructures can be developed. Three basic growth modes have been observed in film developments: island (Volmer - Weber), layer (Frank - Van der Maerwe), and layer plus island (Stranski - Krastanov), which are illustrated in Fig. 1.9 [58].

The growth mode for each case is defined by the free surface energies involved: those associated with film atom bonds or molecule bonds, and those associated with film species bonds to the substrate. While metal and semiconductor films deposited on oxide substrates initially form islands, single-crystal epitaxial semiconductor films form layers. Finally, the layer plus island mode is fairly common in metal-metal and metal-semiconductor systems.

The influence of deposition variables on the structural features developed in physical deposited films has been universally depicted in terms of structure-zone diagrams (SZDs), as shown in Fig. 1.10. These diagrams have been recently improved by introducing additional zones for a complete description of the structures [69]. Several models have been developed to simulate film growth and explain the effect of variables on film microstructures. Monte Carlo simulations have been used to explain the origin of columnar grain formation and the role played by the shadowing effect. Similarly, these simulations have been used to observe film densification at increasing temperatures, and to explain the associated diffusion effects [58, 59]. Additionally, molecular dynamics simulations have been used to explain the effect of ion bombardment on film densification [58, 59].

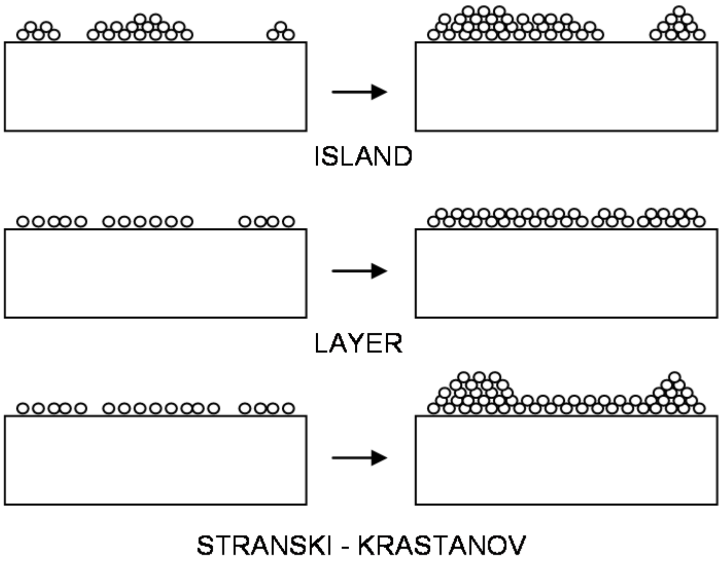

Figure 1.9: Basic modes of thin film growth.

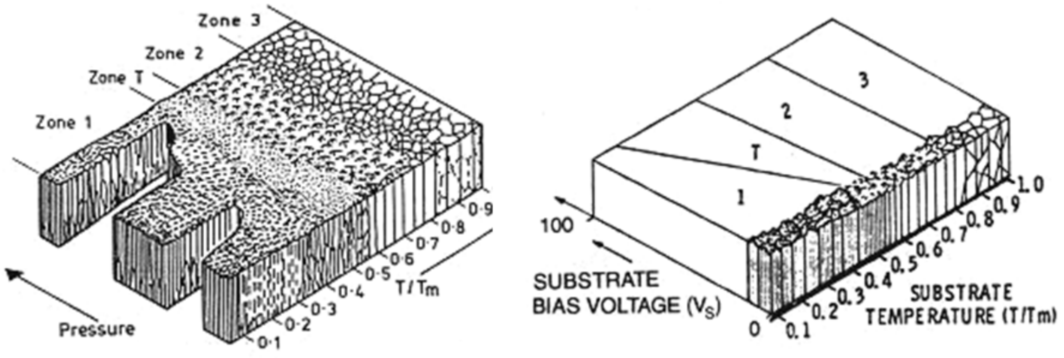

(a) (b)

Figure 1.10: Examples of structure-zone diagrams (SZDs): (a) effect of substrate temperature and total pressure, (b) effect of temperature and substrate bias voltage, in both cases for a PAPVD sputtering process [58, 70].

1.4.1 Development of preferential orientation in AlN thin films

In general, preferential orientation of thin films can be induced by two different effects [27]:

a) substrate epitaxially induced two-dimensional nucleation,

b) geometrical selection in the development of initially randomly deposited tiny crystals.

When there is epitaxial effect, film crystalline orientation corresponding to minimal mismatch between the basal planes of the substrate and the growing film is favored. This effect usually takes place in the deposition techniques leading to single-crystal AlN films on single-crystal substrates [71]. In addition, in many cases different techniques have shown significant epitaxial effect for the deposition of polycrystalline AlN films on single-crystal or polycrystalline oriented substrates [62, 72].

The geometrical selection effect is mainly controlled by the deposition process conditions. Oxygen residual pressure [19, 37] and bias potential values of the substrate holder [73, 74], have been connected to the development of well crystallized and highly <0001> oriented AlN films for PVD sputtering techniques among other parameters. Simultaneously, a progressive change of the preferential <0001> to <10$\underline{1}$0> oriented films has been observed by increasing the chamber pressure during the process or by increasing the target - substrate holder distance

[32, 34]. In the following paragraphs several models proposed to explain these facts are discussed. However, the orientation mechanisms of AlN films are still obscure.

1.4.1.1 Minimization of surface energy

The growth of <0001> oriented AlN films have been linked to the minimization of surface energy because planes parallel to the substrate correspond to the closely packed basal plane, with either aluminum or nitrogen atoms [40, 69, 75, 76]. The tendency to this orientation at higher temperatures, in some PVD processes, has been associated with the need of extra energy for the rearrangement of atoms and the formation of these closely packed structures with lower resulting surface energy [76].

1.4.1.2 Nucleation density model

The influence of chamber pressure on the development of different preferential orientations has been associated with the energy of species reaching the AlN film during PVD sputtering deposition processes [34, 77]. Any increase of the chamber total pressure corresponds to a decrease in the mean free path of the species in the reactor chamber [51]. Consequently, a lower mean free path of the sputtered species, from the target to the substrate holder, results in a higher reduction of the species kinetic energy. Thus, lower nucleation densities on the substrate surface are produced. Taking into account the (0001) plane of AlN crystal is the densest, leading to lower system energy, a faster nuclei growth in c-axis direction has been proposed. Under the assumption of random oriented original nuclei at low nucleation densities, <10$\underline{1}$0> and <10$\underline{1}$1> oriented nuclei can grow parallel to the surface (see Fig. 1.11 (a)), predominantly producing <10$\underline{1}$0> and <10$\underline{1}$1> oriented films. At low chamber pressures, and consequently high nucleation densities, <10$\underline{1}$0> and <10$\underline{1}$1> oriented nuclei stop growing soon as they immediately meet other grains. In turn, at low chamber pressures, <0001> oriented nuclei can grow perpendicularly to the substrate surface (Fig. 1.11 (b)) with the consequent development of <0001> oriented films.

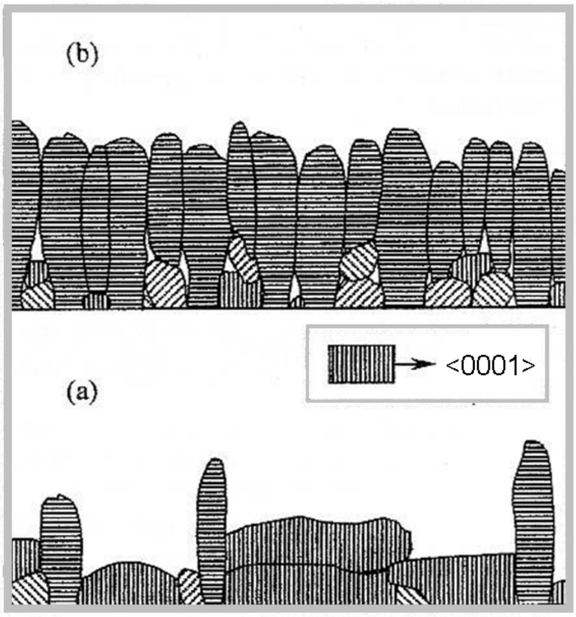

Figure 1.11: Nucleation density model. Sketch of AlN film orientation mechanism: (a) growth at low nucleation rate, (b) growth at high nucleation rate [77].

1.4.1.3 Dimmer model

Ishihara et al. [32] have reported that when the molecule mean free path is longer than substrate-target distance, Al and N atoms are directly deposited on the substrate and AlN films growth is usually <0001> oriented. However, when molecular mean free path is shorter than the substrate-target distance, Al-N dimmers are formed in the plasma and deposited on the substrate as well. In this case the preferred thin films growth is <10$\underline{1}$0> oriented.

These authors have used the extended periodic bond chain (PBC) theory to explain these facts. Nucleations grow randomly on a substrate, however, the surviving nucleations are predominantly those growing faster perpendicularly to the substrate surface, i.e., there is geometric selection. In the case of wurtzite type structures, these authors consider the hypothetical primitive prism units associated to the (0001) and (10$\underline{1}$0) planes respectively (see Fig. 1.12 (a)). The growth rate is defined in each case by the formation rate of these prism units. This formation rate is determined by the deposition rate of the growth units, i.e., Al and N atoms, or Al-N dimmers, on the sites of these prism units. In the case of individual atoms the necessary number of sites in a <10$\underline{1}$0> unit prism, is twice the number of sites in a

<0001> unit prism (see Fig. 1.12 (b)), then the growth rate of (0001) planes is higher and <0001> oriented films are developed. With Al-N dimmers, the number of sites is the same in both unit prisms, then the dissociation of the Al-N bond from the unit prism must be considered. In the case of the <0001> prism the dissociation is easier (see Fig. 1.12 (c)), the growth rate of the (10$\underline{1}$0) planes is higher, then the <10$\underline{1}$0> oriented films are favored.

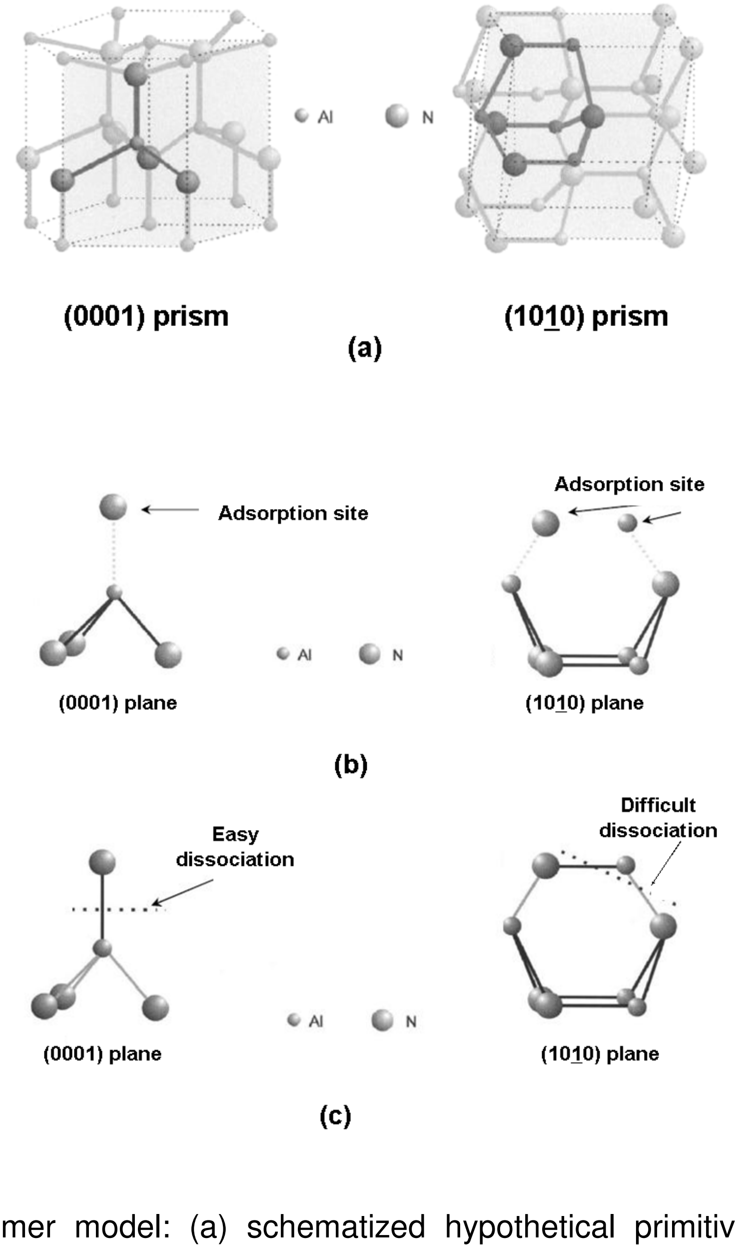

Figure 1.12: Dimmer model: (a) schematized hypothetical primitive prism units: (0001) prism and (10$\underline{1}$0) prism, (b) Schematic deposition of growth units of atoms (N, Al) on (0001) and (10$\underline{1}$0) prisms, (c) schematic deposition of a growth unit of dimmer (Al-N) on (0001) and (10$\underline{1}$0) prisms [32].

Other theories have explained the effect of the mean free path, and established a connection between the different ionic character of Al-N bonds in the c-axis direction and the energy of sputtered species reaching the substrate [44].

1.4.2 Residual stress in thin films

When a thin film firmly bonded to a substrate is prepared, any change in length along the film plane, not exactly matched by an equal change in substrate length, results in residual stress for such film. Film properties can be affected by the presence of high stress. Moreover, deformations or catastrophe phenomena, such as fractures or delaminations, can be produced by excessive residual stresses. As a consequence, the residual stresses of AlN thin films should be controlled in order to ensure device integrity and performance.

In overall residual stresses developed in thin films, currently three components can be distinguished, as follows.

a) Thermal stress, derived from different thermal expansion coefficients of films and substrates and the difference between deposition temperature and room temperature.

b) Intrinsic stress, related to the deposition conditions, which may be caused by incomplete structural-ordering processes during film growth.

c) Extrinsic stress, induced by external factors and resulting from interactions between deposited material and the environment, e.g. adsorption of water vapor in porous films.

Many theories have been proposed to explain intrinsic stress development in thin films, this stress can be either tensile or compressive according to the situation.

The development of tensile stresses in the early stages of polycrystalline film growth has been explained by Hoffman through the “grain boundary relaxation” model [58, 78, 79]. This model is based on the idea that crystallites tend to join together because their individual surface free energies are greater than free energies when grain boundaries are created by coalescence. As a result, the induced stress is tensile because the film tries to achieve higher packing. The evolution of stress after crystallite coalescence during film growth would depend on the availability of kinetically controlled strain relaxation processes. For high adatom mobility, diffusively controlled strain relaxation processes are available to relax the tensile strains in the film during subsequent film growth [79].

Conversely, a connection has been established between the development of compressive intrinsic stresses and ion bombardment of the surface during film growth. A simple model proposed by Davis [78, 80] assumes that compressive stress is produced by film atoms implanted below the film surface. This implantation known as “knock-on process”, is a consequence of energetic ions reaching such surface and transferring enough energy for film atoms to become implanted below the film surface. A progressive energy increase of the arriving ions commonly leads to the observation of an evolution to maximum compressive stress followed by a drop of such stress. This drop has been explained by the movement of the implanted atoms to the film surface. Such movement is caused by the local heating produced by the high energy ion impacts, effect known as “thermal spike”.

Film mechanical damage and particularly film fracture with excessive tensile stresses can be analyzed by using the Griffith fracture theory [78]. Film fracture is produced when the elastic energy per surface area *U* stored in the film is higher than the total surface energy increase 2γ caused by film fracture. Then, if biaxial and isotropic residual stress in the plane of the film is assumed, the critical point is defined as follows:

$$U_c = \frac{\sigma_c^2 t_{fc}}{E_f} \approx 2\gamma \qquad (1.24)$$

where: U_c: critical elastic energy stored in the film (J/m^2), σ_c: critical stress (Pa), t_{fc}: critical film thickness (m), E_f: Young’s modulus of a film (Pa), 2γ: increase of total free energy caused by fracture (J/m^2).

Taking into account that elastic energy depends on film thickness and on film stress ($\sigma^2 .\ t_f$), under a constant residual stress assumption, a film critical thickness t_{fc} above which the film will fracture can be determined as follows:

$$t_{fc} = \frac{2E_f\gamma}{\sigma^2} \qquad (1.25)$$

Then, this fact should be considered to avoid fractures when increasing film thickness.

1.5 Objectives

As consequence of the information presented in the previous general review, the objectives of this work are established in the following.

The aim of this work is to produce piezoelectric AlN films with suitable properties for BAW and SAW electro-acoustic devices using a MWPECVD technique.

Consequently, the object of this work is not only the production of <0001> oriented AlN films, which are traditionally used for these applications, but also the research of <10$\underline{1}$0> oriented films for SAW applications.

The piezoelectric performances of the prepared films are measured by several techniques, including the construction of electro-acoustic devices.

Film microstructure and compositions are also determined in this work in order to establish their effect on piezoelectric performance.

Characterizing the process plasma results in additional information for critical discussion of mechanisms and possibilities provided by the PECVD technique.

Finally, a comparison of the technique discussed in this work with the traditional PVD sputtering deposition technique for thin films is included.

There is scarce information about the use of this MWPECVD technique for the development of polycrystalline oriented AlN films and there is no research about controlling <0001> or <10$\underline{1}$0> oriented development. Simultaneously, only isolated information has been published on performance evaluations of electro-acoustic devices based on <0001> oriented films obtained by this technique.

Last but not least, although interest in developing the <10$\underline{1}$0> orientation for SAW devices has been shown in the past, there is no information published about measuring AlN film device performance for this orientation, regardless of the deposition technique.

Chapter 2

EXPERIMENTAL PROCEDURE

Once the objectives of the work were defined in the previous chapter, based on an overview of the fundamentals and the state of the art, the experimental procedure used to conduct the work is presented in the following. The MWPECVD deposition technique, a general description of the chosen experimental design and the different methods used to characterize the resulting AlN films are described.

2.1 The MWPECVD technique

2.1.1 The reactor

The reactor consists in a cylindrical chamber- 255 mm diameter and 200 mm height- constructed in stainless steel, with a quartz glass of the same diameter on top (see Fig. 2.1). This quartz tube is surrounded by a microwave applicator (280 mm diameter) opened to the air, which was optimized to obtain the coupling between microwaves and the plasma through the quartz tube. As the diameter of the quartz is twice the wavelength of the exciting microwaves- frequency 2,45 GHz, wavelength 127,5 mm-, this arrangement is known as a microwave system with large size plasma. The microwave energy is produced by a SAIREM 2,000 W generator, and is propagated through a standard rectangular guide- WR 34, TE_{10} mode-, to the cylindrical applicator. Homogeneous plasma is created due to the production of several modes in the quartz chamber [50]. According stubs placed in the wave guide are used in order to minimize the reflected power.

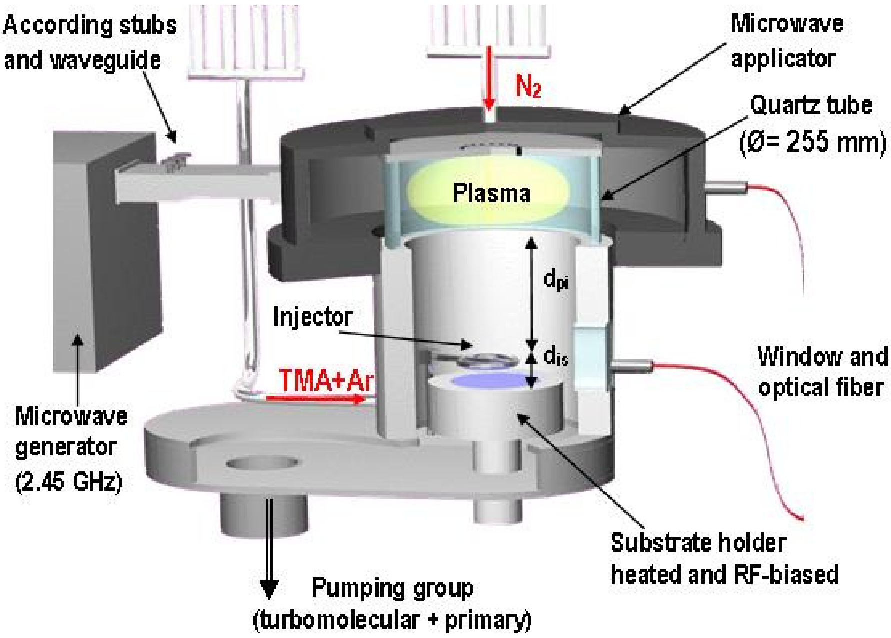

Figure 2.1: The MWPECVD reactor.

The substrate holder temperature can be set to a controlled value by using a thermoaxial resistance heater under the substrate plate associated with a thermocouple. However, a radiofrequency generator- ENI OEM-12A, 1,200W, 1,000V, can be used in order to biased the substrate holder. A matching box allows minimizing the reflected power.

The reactor chamber is connected to a Varian vacuum system, composed of a turbomolecular pump with variable speed - Turbo-V 700 ICE MacroTorr - coupled with a dual stage rotary vane pump – Varian SD-700. The residual pressure is measured by a cold cathode gauge – Penning - for the 10^{-1}-10^{-6} Pa range, and a capacitive gauge – Baratron - for the 10^{3}-10^{-1} Pa range.

The N_2 plasma generating gas is introduced on the top of the reactor, being its flow controlled by a mass flowmeter. The Ar carried trimethylaluminum (TMA, $Al(CH_3)_3$) precursor is introduced though an annular injector, 60 mm in diameters, with 14 orifices oriented down to the substrate holder. As the TMA is liquid at room temperature, it is introduced in the reactor using a special device. A defined flow of Ar bubbles through a TMA container, which is maintained at controlled pressure using an electromagnetic microvalve. It is possible to control the vapor pressure of TMA in the gas flux, by setting the total pressure with the microvalve and the temperature of the container fixed by a temperature-controlled water bath. Then, with the value of the TMA vapor pressure at the selected temperature obtained from the bibliography, the TMA flow can be calculated as follows [54, 81]:

$$F_{TMA} = \frac{P_v}{P - P_v} . F_{Ar} \tag{2.1}$$

where: F_{TMA}: TMA flow rate (sccm), F_{Ar}: Ar flow rate (sccm), P: total pressure (Pa), P_v: TMA vapor pressure (Pa).

The distance between the injector and the substrate holder (d_{is}) can be changed. A modification to the original design of the reactor was introduced in this work in order to have the possibility of changing the distance between the plasma and the injector (d_{pi}).

The microwave generator and several reactor parts are cooled by a water circuit in order to dissipate the produced heat. On the other side the TMA line must be heated to avoid its condensation before arriving to the reactor chamber.

2.1.2 The process

Substrate wafers of 30 mm x 10 mm were employed as substrates for film deposition. The wafers were ultrasonically cleaned in ethanol and acetone before placing them in the reactor chamber. Once closed, the vacuum system of the reactor was switched on in order to obtain a residual pressure lower than 5 x 10^{-3} Pa in the chamber. Before the deposition took place, the substrate surface was cleaned in situ using argon plasma, as will be specified. After pre-heating the substrate holder to the set temperature at 50℃/min and stabilizing during 15min, AlN films were deposited using nitrogen plasma in which the trimethylaluminum (TMA) was injected with argon as carrier gas. Once finished the deposition time, the substrate holder was cooled at 10°/min under vacuum. Finally the chamber was opened to extract the sample once the temperature of the substrate holder was less than 50℃. Table 2.1 shows the significant variables of substrate pre-treatment, and AlN film deposition. Variables selected for optimizing film properties in the experimental design are shown.

The substrate temperatures indicated in the following correspond to the set temperatures for the substrate holder. As the thermocouple is placed under the holder plate, certain difference must be expected between the set temperature and the real substrate temperature. So as to know this difference, an experiment was conducted by putting another thermocouple directly in contact with a substrate sample simultaneously. The observed results indicated that the real substrate temperature during the process was approximately 100ºC under the set temperature in all the used range. Nevertheless, the set temperature is informed in the following, which corresponds to that effectively measure in the experimental runs. When theoretical calculations are made, the estimated real temperature is employed.

Table 2.1: Variables of the PECVD deposition process indicating which were chosen for optimization (*).

Variable	Pre-treatment *	AlN film growth
Microwave power (kW)	1.0	1.6
Argon flow rate (sccm$^{(\#)}$)	100	50
Nitrogen flow rate (sccm)	0	125
RF bias potential (V)	- 100	- 200 – 0 *
Chamber pressure (Pa)	0.8	0.5 – 8 *
Processing time (min)	15	0 – 45 *
TMA flow rate (sccm)		1
Plasma-injector distance d_{pi}(cm)		3 – 11 *
Substrate temperature (°C)		400 – 800 *
Injector-substrate distance d_{is} (cm)		4 – 10 *
Substrate		Si(100), Pt(111), Si (111)*

2.1.3 Experimental design

The experimental work can be divided in three principal stages as follows:

a) Growth of polycrystalline oriented AlN films

Seven different variables were taken into account to produce and optimize the film properties, i.e. RF bias, the plasma-injector distance, the substrate temperature, the chamber total pressure, the injector-substrate distance, the process time, and three different substrates were used. A full fledged experimental design to map out all the variables and their interactions was excessive to be practical, thus, preliminary work was carried out to scout the influence of the plasma-injector distance and the RF bias. After proper values for these two variables were chosen, the rest of the variables were explored using several levels in each case.

b) Optimization of films properties

Additional experimental runs were conducted in order to optimize the performance of the films in electro-acoustic applications, taking the previous results as reference. A full fledged experimental design for substrate temperature and total pressure was done in order to optimize the development of <10$\underline{1}$0> oriented films. Film thickness and bias potential were explored separately using several levels in each case in order to optimize the properties of <0001> oriented films. Finer characterizations of the microstructure of the films, as well as the measurement of their piezoelectric performance were introduced at this stage. This was complemented by the process plasma characterization at different deposition conditions by Optical Emission Spectroscopy (OES).

c) Application to electro-acoustic devices

SAW electro-acoustic devices with <0001> and <10$\underline{1}$0> oriented AlN films were prepared at optimal conditions, as well as BAW electro-acoustic devices for <0001> oriented films. The frequency response of these devices was measured and models were used to explain the results obtained in each case.

2.2 Film characterization

The obtained films were characterized in their chemical compositions, microstructure, mechanical and piezoelectric properties using the following techniques.

Three simple tests were realized immediately after each run in order to have a first overview of the results:

- Deposited weight: in order to control the deposition rate and its homogeneity on different positions of the substrate holder.
- Film thickness: part of the sample surface was masked with a resin (“Apiezon”), and a complete chemical etching of the film using 1 M NaOH solution was made [82]. After eliminating the resin with an adequate solvent the thickness was obtained through the levels difference measurement with a profilometer.
- Chemical etching: part of the film was etched during 30 seconds at ambient temperature employing the previous procedure, which allowed obtaining the etch rate in nm/s.

2.2.1 Chemical composition

2.2.1.1 Fourier transform infrared spectroscopy (FTIR)

FTIR spectra were obtained, with a “Perking Elmer Spectrum One” equipment, at the normal incident angle in transmission mode between 4000 cm^{-1} and 400 cm^{-1}, with step 1 cm^{-1}, at 300 K. The substrate spectrum (Si) was used as background. In addition, spectra were obtained in reflection mode at 30º incident angle. Interference fringes patterns of FTIR spectra were used to determine the thickness or the refractive index of the thicker films (> 1 µm) in transmission mode [60].

Because of the transverse character of electromagnetic radiation in conventional transmission spectroscopy at normal incidence, only AlN transverse optical (TO) mode vibrations, parallel to the surface, interact with the radiation. In reflection spectroscopy at 30º, the oblique incidence radiation has components parallel and perpendicular to the film surface, which can excite both longitudinal optical (LO) and transverse optical (TO) modes [83].

2.2.1.2 X-ray photoelectron spectroscopy (XPS)

The XPS technique allows obtaining the proportion of elements at a surface, within a depth of some atoms– i.e. 10 nm. Then, only “the surface” of the films can be directly analyzed. The XPS measurements of this work were carried out with a Leybold LHS12 spectrometer (University of Nantes) with MgK radiation (1253.6 eV) as excitation source. Survey spectra, covering a wide range of energies, have been taken from -5 to 1,150 eV in binding energy in a constants pass energy mode of 126 eV. Multiregional spectra, for studying narrow energy regions of interest, have been taken of the predominant photoelectrons peaks at higher resolution using a constant pass energy mode of 31,5 eV. Multiregional spectra were recorded at 90º take off angle, i.e. the sample surface was at 90º with respect to the directions of emission of electrons, detected with a concentric hemispherical energy analyzer. Under these conditions the Ag 3d5/2 was recorded with 0.93 eV FWHM. The spectrometer was calibrated using Cu 2p3/2, Au 4f7/2 photoelectrons lines at 832.66 and 84.0 eV, respectively. The pressure in the analysis chamber was maintained lower than 10^{-7} Pa. The atomic concentrations were calculated from the photoelectron peak areas using Shirley background subtraction, sensitivity factors provided by the spectrometer manufacturer and transmission function of this instrument. Recorded spectra were calibrated in binding energy according to C 1s at 284.7 eV.

2.2.1.3 Rutherford backscattering spectrometry (RBS)

The principle of this technique rests on the study of the elastic scattering between the cores of an ion incident flux of high energy and the target atoms at rest. Samples were placed in the analysis chamber under a $2x10^{-6}$ torr vacuum with the zone of interest aligned with the beam of incident particles. This beam consisted in a 2,0 MeV He^+ ion flux delivered by a Van de Graff electrostatic accelerator, forming an incident current of 10nA on the target for an analysis surface of some mm^2. The incident particles retrodiffused by the cores of the target atoms were detected at 155° from the initial direction. Thus, a spectrum was obtained, where the particle energy detected after retro-diffusion was shown in X-coordinate and the number of these particles seen by the detector was shown in Y-coordinate. This number represented the detected element concentration at a given depth. Thus, the responses of the principal components of the sample are normally shown by this type of spectrum, as steps for massive materials, and as peaks for thin films. While the quantification of aluminum was possible on these spectra, C, N and O were more delicate to determine. The superposition of their signals, already weak, with that of the silicon caused by the substrate was the reason of this fact. Thus, RBS was used to determine the average proportion of aluminum present in the whole film (ARCANE, Gradignan, France), and the quantification of C, N, and O was done by the following technique.

2.2.1.4 Nuclear reaction analysis (NRA)

The principle of the NRA technique consists in creating nuclear reactions between cores of the atoms in a target and cores of an incident flux of ions with high energy. A flux of deutons (particles made up of a neutron and a proton) was used (ARCANE, Gradignan, France), which interacted with the cores of the analyzed atoms (C, N, O) creating made up cores. Those new cores were disintegrated giving rise to lighter particles which were detected, allowing the quantification of the species initially present by comparison with reference samples. As these detected light particles had high energies, they were in a zone of the spectrum where their signal was clearly distinguished from the background noise. Moreover, a mylar absorbent placed in front of the detector allowed to stop the incident particles retrodiffused by the heaviest atoms of the target.

The experimental conditions used for the detection of each element were as follows:

For nitrogen: reaction $^{14}N(d, p)^{15}N$ with a deutons flow of energy 1.8 MeV, a current of 50 nA and an integrated charge of 10 µC. A mylar with thickness 20µm was used as screen. A film of SiN deposited on silicon containing 721×10^{15} at/cm² of nitrogen was used as standard.

For oxygen: reaction $^{16}O(d, p)^{17}O$ with a deutons flow of energy 930KeV, a current of 50 nA and an integrated charge of 20 µC. A mylar with thickness 10µm was used as screen. A deposit of Al_2O_3 formed on aluminum containing 912×10^{15} at/cm² of oxygen was used as standard.

For carbon: reaction $^{12}C(d, p)^{13}C$ with a deutons flow of energy 1.020 MeV, a current of 100 nA and an integrated charge of 200 µC. A mylar with thickness 10µm was used as screen. A silicon substrate implanted with carbon with an amount of 6151×10^{15} at/cm² was used as standard.

2.2.2 Microstructure

2.2.2.1 X-ray diffraction (XRD)

X-ray diffraction (XRD) θ/2θ patterns– i.e. Bragg-Brentano configuration- were recorded between 15° and 80° (2θ), with a scanning step of 0.05°(2θ), using a D-5000 diffractometer (Siemens Kristalloflex) equipped with Cu anode and a graphite back-monochromator. With this arrangement, the incidence and detection angles relative to the substrate plane were equal during all the measurement (see Fig. 2.2 (a)). Then only information related with the planes parallel to the sample holder was obtained. Consequently, the crystalline development and a first indication of the preferential orientation relative to the substrate plane are obtained with this measurement. The incident angle was offset by 0.5° aiming to reduce the reflections of the Si (100) substrate between 30° and 40°(2θ). An indication of the average grain sizes in some of the films was estimated from the AlN reflection peaks taking the full width at half maximum (FWHM) with the Sherrer formula [84].

Rocking curves- i. e. intensity vs. incidence angle ω- of the pertinent AlN reflections- i.e. θ_{Bragg} - were conduct and their FWHM were estimated using gaussian/lorentzian fitting in order to quantified the film texture, i.e. preferential orientation grade (see Fig. 2.2 (b) and (c)).

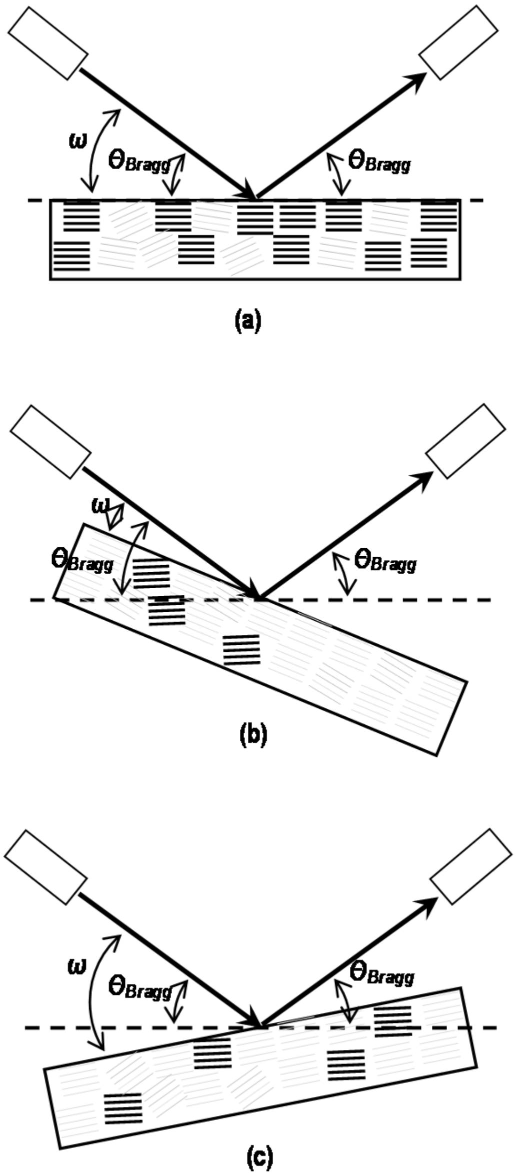

Figure 2.2: X-ray diffraction in Bragg - Brentano configuration: (a) θ/2θ - with the incidence angle $\omega = \theta_{Bragg}$, (b) and (c): change of the incidence angle ω for a fix θ_{Bragg} in order to obtain the rocking curve.

The textures of some relevant samples were confirmed using a diffractometer with Debye-Sherrer configuration and automated five - axis substrate holder.

2.2.2.2 Scanning electron microscopy (SEM)

As produced samples and fracture surfaces were observed by scanning electron microscopy (SEM) using a JEOL JSM-S900LV at 30 kV.

2.2.2.3 Transmission electron microscopy (TEM) – High resolution TEM (HR TEM) – Selected area electron diffraction (SAED)

Thin specimens for transmission electron microscopy (TEM) were prepared by cutting, mechanically grinding to ~30-50 µm, dimping (Gatan dimper), and ion-milling (Gatan PIP) to electron transparency. The observations were made using JEOL TEM JEM 2010 operating at 200 kV.

The fine structural study of the films was carried out by high resolution transmission electron microscopy (HRTEM) using a Hitachi HF 2000, and selected area electron diffraction (SAED) patterns were obtained with an acceleration voltage of 200 kV (Basam Abdallah, Eric Gautron, University of Nantes).

In the SAED technique, electrons are accelerated by an electrostatic potential in order to gain the desired energy and wavelength before they interact with the sample to be studied. The periodic structure of a crystalline solid acts as a diffraction grating, scattering the electrons in a predictable manner. Working back from the observed diffraction pattern, the structure of the crystal producing the diffraction pattern can be deduced [85].

2.2.2.4 Atomic force microscopy (AFM)

Surface morphology of the films was analyzed by atomic force microscopy (AFM) with a microscope “Molecular Imaging Scanner” operating in tapping mode near 75 kHz under ambient conditions (Valérie Coudert, SPCTS). Silicon tips with a force constant of 2,8 N/m and a nominal radius of curvature of 20 nm were employed. The

S_a roughness coefficient, i.e. the arithmetic mean of the absolute value of the surface rugosity, was determined by AFM.

2.2.3 Mechanical properties

2.2.3.1 Residual stress

Film residual stresses were estimated by measuring the radius of curvature of 5 mm x 20 mm x 200 µm Si substrates, after the growth of the AlN films, with a profilometer and using the Stoney equation [78].

$$\sigma_{res} = \frac{1}{6}\left(\frac{E_{subs}}{1-\upsilon_{subs}}\right)\cdot\left(\frac{t_{subs}^2}{t_{film}}\right)\cdot\left(\frac{1}{R_2}-\frac{1}{R_1}\right) \tag{2.2}$$

where: σ_{res}: residual stress (Pa), E_{subs}: substrate elastic modulus (Pa), v_{subs}: substrate Poisson's ratio, t_{subs}, t_{film}: substrate and film thicknesses (m), R_1, R_2: initial and final radius of curvature of the substrate, before and after the deposition (m) (University of Limoges, Bassam Abdallah- University of Nantes).

2.2.3.2 Nanoindentation: Young's modulus

Nanoindentation was performed on the films using a Nano Indenter XP™ (MTS Nano Instruments) with a Berkovich tip in order to determine the Young's modulus (ENSIL - SPCTS). The instrument was operated in the continuous stiffness mode allowing Young's modulus to be calculated at every data point acquired during the indentation experiment. This property was evaluated using the Oliver and Pharr's analysis technique [86, 87]. The indentations were made using a constant nominal strain rate of 0.05 s^{-1}, a frequency of 45 Hz and harmonic displacement of 2 nm. A Poisson's ratio of 0.25 was used to calculate the elastic modulus. The average of twenty indents was taken for each case. The tip correction coefficients were deduced from indents in fused silica.

2.2.3.3 Intrinsic stress

Thermal stresses of the films were calculated according to [78]:

$$\sigma_{the} = \frac{E_f}{(1-\nu_f)}(\alpha_f - \alpha_s)(T_d - T_a) \tag{2.3}$$

where: σ_{the}: thermal stress (Pa), E_f *:* Young´s modulus of the film obtained by nanoindentation (Pa), ν_f : Poisson´s ratio of the film, α_f = 4.1 x 10^{-6} K^{-1} and α_s = 2.6 x 10^{-6} K^{-1} [88]: thermal expansion coefficients of the film and the substrate, T_d and T_a : deposition and ambient temperatures (K).

By using the previous results (equations 2.2 and 2.3), the intrinsic stresses of the films (σ_{int}) were obtain from:

$$\sigma_{\text{int}} = \sigma_{res} - \sigma_{the} \tag{2.4}$$

2.2.4 Piezoelectric Characterization

Film piezoelectric performance was evaluated using three different techniques. Appendix B shows a general review of commonly applied techniques and fundamentals of AlN film piezoelectric response.

2.2.4.1 Piezoresponse force microscopy (PFM)

The piezoelectric response of the AlN films was evaluated using an atomic force microscope adapted to evaluate the piezoelectric coefficient d_{33} with the inverse piezoelectric effect (Florent Tetard, University of Paris XIII). Voltage values between 1 and 10 V were applied between the tip and the substrate (see Fig. 2.3), and the consequent dimensional variations of the piezoelectric film in the vertical directions were obtained. The equipment was operated in contact mode at 10 kHz, with scan size of 5 µm, scan rate 1 Hz, and acquisition time of 3 s. The photodiode potential (mV) was calibrated to nm displacement.

The effective piezoelectric coefficient in the z direction, d_{zz}, was obtained from the slope of the displacement vs. applied voltage plot. Since the film is clamped to the substrate, this substrate constrains the in-plane contraction and expansion of the film. Then, the following equation was applied in order to obtain the piezoelectric coefficient of the free sample, d_{33} [29, 89-91]:

$$d_{zz} = \frac{S_3}{E_3} = d_{33} - 2d_{31}\frac{s_{13}^E}{s_{11}^E + s_{12}^E} \tag{2.5}$$

where: d_{zz}: measured effective piezoelectric coefficient (m/V), d_{33}: piezoelectric coefficient of the free sample (m/V), d_{31}: transverse piezoelectric coefficient (m/V), s_{11}, s_{12}, s_{13}: mechanical compliances of the piezoelectric film (m^2/N). Compliance values were taken as $s_{11} = 3x10^{-12}$ m^2/N, $s_{12} = - 0.9 \times 10^{-12}$ m^2/N, $s_{13} =- 0.6 \times 10^{-12}$ m^2/N, and d_{31} was assumed to be $–d_{zz}/2$.

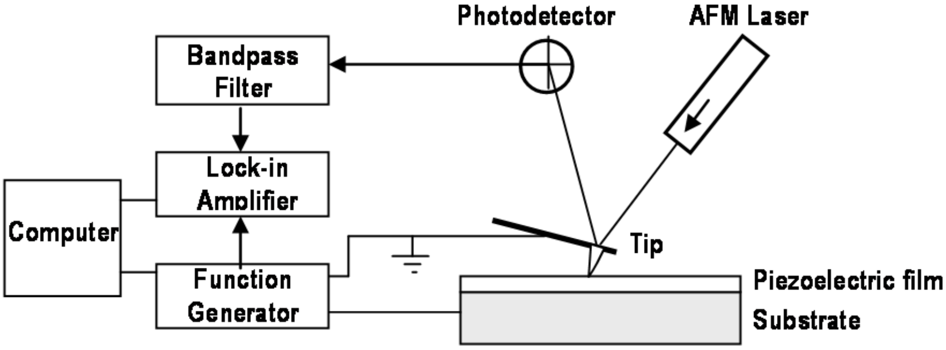

Figure 2.3: PFM setup to evaluate the d_{33} piezoelectric coefficient.

2.2.4.2 SAW devices

Surface acoustic wave devices were manufactured at the “Instituto de Microelelectrónica de Barcelona” cleanroom following a conventional lithographic process. Two interdigital electrodes (IDTs) were defined on a 200 nm thick metallic film deposited on the PECVD AlN films. Si(100) substrate wafers, 100 mm diameter, 525 µm thick, with resistivity 5 ohm.cm, were used in all the cases. Each IDT consisted of 100 pairs of fingers formed by 3.3 µm-wide metal strips separated by 6.7 µm, producing a SAW filter with an acoustic wavelength (λ) of 20 µm. The distance between the IDT centers was 2.00 mm and the electrode overlap was 2.00 mm too.

The IDTs development process had the following stages (see Fig. 2.4):

a) deposition of an Al-0.5%Cu metal film, 200 nm thick, on top of the AlN film, by PVD sputtering at 0.4 Pa, 600W and 10 cm distance substrate-target, using a “Leybold-Heraeus” equipment ;

b) deposition of a positive photoresist, 2 µm thick, onto the metallic film at 1500 rpm;

c) exposure of the photoresist to ultraviolet radiations using an appropriate mask during 30 s;

d) development of the photoresist, using OPD 4262 developer and ulterior annealing till 175°C;

e) patterning of the metal electrodes by chemical etching using DAE solution composed of phosphoric, acetic, fluoboric and nitric acid at 55°C during 30 s, ulterior rinse and dry;

f) resist removal with oxygen plasma using“Tepla” equipment.

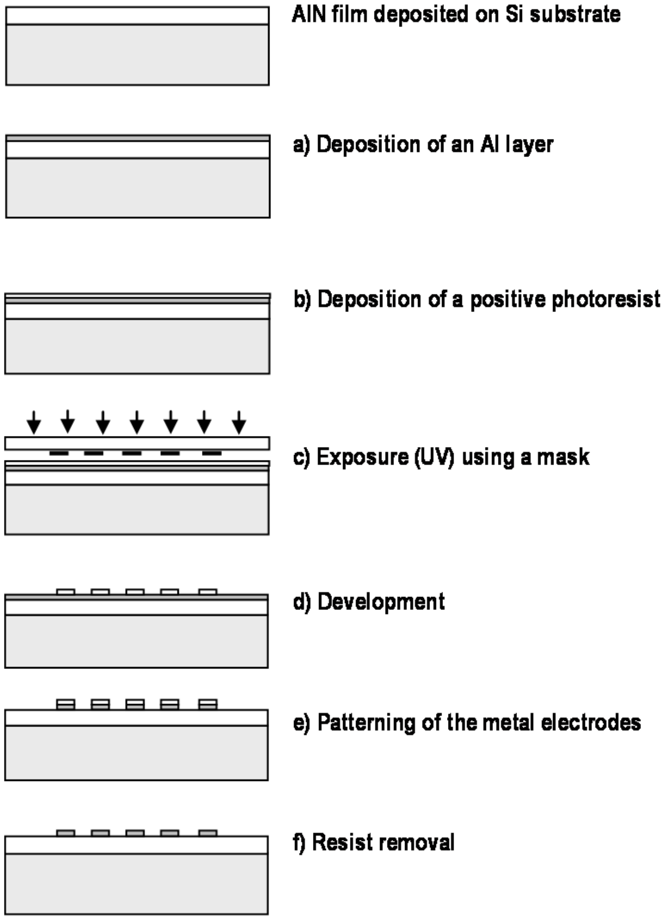

Figure 2.4: Scheme of the process to obtain the SAW devices.

The “frequency response” characteristics of the SAW devices were obtained by measuring the scattering parameter (S_{21}) between 100 and 400 MHz, with a vector network analyzer HP8722ES.

2.2.4.3 BAW devices

FBAR devices were manufacture at the “XLim - Université de Limoges” cleanroom (collaboration with Aurelian Crunteanu), following the general process given in Fig. 2.5. It should be noted that each point of the showed general scheme imply several stages, including different lithography steps, among others.

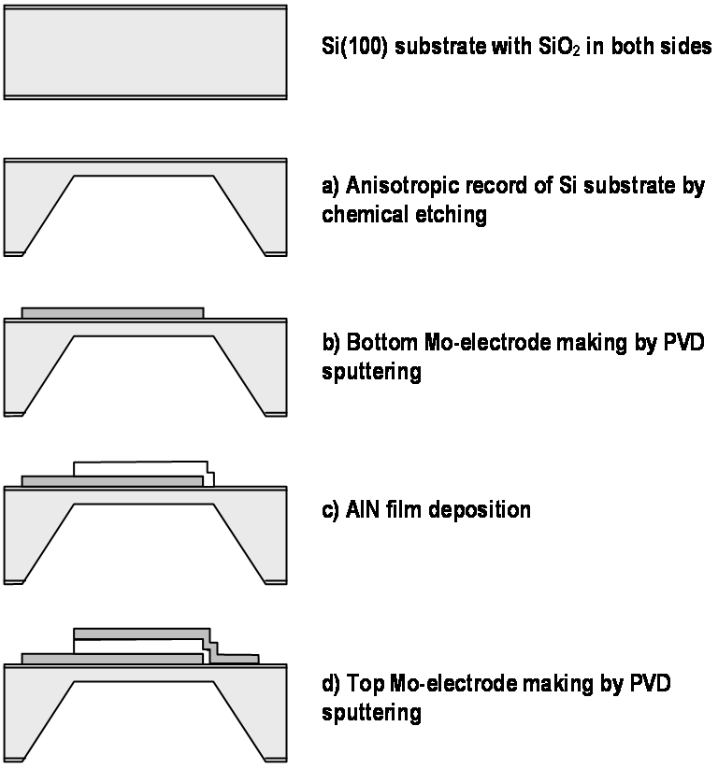

Figure 2.5: General scheme of the process to obtain BAW devices.

The “frequency response” characteristics of the FBAR devices were obtained by measuring the scattering parameter (S_{21}) between 0.5 and 14 GHz, with a vector network analyzer HP8722ES.

Although the design and the manufacture process of this device were not completely optimized, the obtained results allowed having a first approximation to AlN film performance under BAW configuration.

2.3 Plasma characterization by Optical Emission Spectroscopy (OES)

An experimental arrangement composed of the following elements was used:

- A Jobin Yvon THR 1000 monochromator, with 1 m focal distance, equipped with an holographic lattice with 1200 lines / mm, and resolution power λ / Δλ = 100 000 at 500 nm,
- A Charge Coupled Device (CCD) detector cooled with liquid nitrogen (-140ºC), composed of a 1024 x 250 photodiodes matrix to analyzed spectral fractions at each time,
- An UV - visible optical fiber (190-900 nm) with 0,4 mm opening.

The optical fiber was placed in the holes of the excitation guide at the top of the reactor chamber to analyze the plasma discharge, or in the window near the bottom of the reactor to analyze the species present near the substrate holder.

Spectra between 350 and 850 nm were obtained, with 0,36 s acquisition time, 10 repetitions, and opening from 2 to 5. Acquisition time of 10 s was used in order to evaluate the presence of small peaks for specific intervals.

Chapter 3

GROWTH OF POLYCRYSTALLINE ORIENTED AlN FILMS

A preliminary work had been conducted with the employed MWPECVD reactor with its standard configuration in order to explore the viability of AlN film deposition and the incidence of different variables on film characteristics [92]. This work had arrived to visualize, using FTIR characterization, the reduction impurities concentration in the film with the increase of substrate temperature. But, neither important crystalline development nor clear preferential orientation had been detected, with XRD patterns showing very low AlN pick intensities. However, an important development of pulverulent deposits had been observed, which made necessary frequently reactor cleaning in order to avoid excessive film contamination.

Consequently, those facts allowed speculating that the absence of significant crystalline development was related with the presence of impurities in the film, being associated to the presence of Al precursor by-products. Since the position of the substrate holder in the reactor standard configuration was far from the plasma, with almost a post-discharge conception, a modification in the reactor design was introduced, allowing working with the substrate nearer the plasma. This would place the injector and the substrate in a more energetic region, allowing a better activation and reaction of the species [50, 63]. Since the position of the precursor injector was fixed, a modification in the reactor design was necessary. Then, the injector could be placed nearer the plasma, reducing the injector-plasma distance, (d_{ip}, see Fig. 2.1), and the plasma - substrate distance (d_{pi} + $d_{is,}$ see Fig. 2.1).

Precursor flow was fixed at the minimal value of the allowed range (1-3 sccm) in order to have low deposition rates and consequently to favor the crystallization process during film growth. Gas flow was maintained at the standard process conditions. The microwave power was fixed at the higher standard value in order to increase the energy transfer to the plasma, and then, the generation of active species.

Consequently, there were seven different variables to take into account in order to optimize film properties, i.e. RF bias, the plasma-injector distance, the substrate temperature, the chamber total pressure, the injector-substrate distance, the process time, and the type of substrate. As was previously indicated (see section 2.1.3), a preliminary work was carried out to scout the influence of the plasma-injector distance and the RF bias, and the rest of the variables were explored using several levels in each case. In the following, the results obtained with this experimental design are discussed.

3.1 Plasma-injector distance

The initial steps of the work were conducted using the normal setup found in the reactor chamber fitted with a plasma-injector distance of 11 cm (see Fig. 2.1). This setup produced predominantly amorphous films with typical thicknesses of about 2 µm for the entire conditions tested (see Fig. 3.1). At the same time, pulverulent deposits on the walls of the reactor chamber and on the substrate holder were observed, confirming the observations of the preliminary work and suggesting that a lower plasma-injector distance could be tested in order to increase the concentration of more reactive species in the chamber.

A plasma-injector distance of 3 cm was set and films of about 2 µm were produced as well, employing the same deposition time used in the previous runs, i.e. 30 minutes. However under these conditions, polycrystalline films were obtained with a predominant <0001> orientation - (0002) reflection in Fig. 3.1-, in which the presence of this orientation was also confirmed by the observation of a sizable (0004) AlN reflection peak (see Fig. 3.1 (right)).

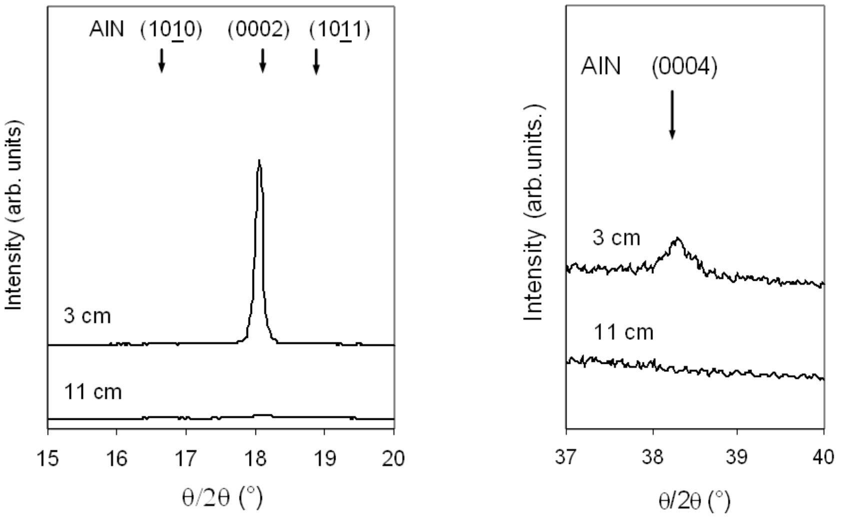

Figure 3.1: XRD patterns for AlN films obtained at 3 cm and 11 cm plasma-injector distances on Si (100) at 600ºC, 1 Pa, no RF bias, injector – substrate distance of 4 cm, and 30 min deposition time (reference : JCPDS 25-1133).

FTIR spectra exhibited a strong 672 cm^{-1} Al-N band (see Fig. 3.2(a)), as well as a multiple impurity band centered at around 2150 cm^{-1} was also observed. This band is typically present in PECVD AlN films only [60, 61, 81, 93, 94], where the 2150 cm^{-1} has been attributed in the past to the stretching of the Al-N$_2$ [81] or to the Al-H or Al-C≡N [60, 61, 94]. By comparing this impurity band, after absorbance normalization by thickness and background, a decrease of the area could be observed in films with larger average grain size (see Figs. 3.2 (b), 3.3) suggesting that a lower impurity concentration resulted in films with larger crystals. At the same time, an increase in the size of the columns present in the films was observed in the AFM images (see Fig. 3.3). As expected, this trend was also accompanied by an increase of the film surface roughness, from S$_a$ of 6.7 nm for an 11 cm plasma-injector distance to 18.5 nm for a 3 cm distance.

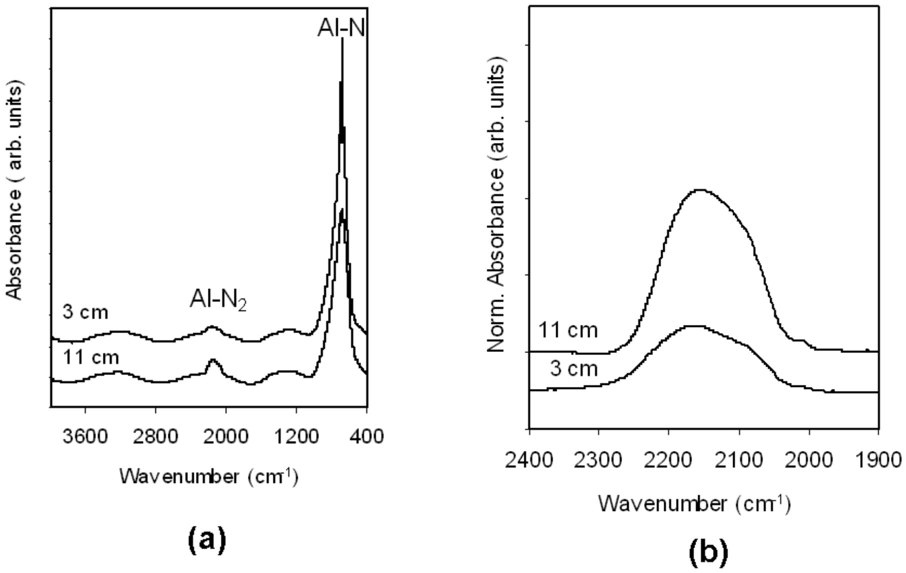

Figure 3.2: FTIR spectra for AlN films obtained at 3 cm and 11 cm plasma-injector distances on Si (100) at 600ºC, 1 Pa, no RF bias, injector – substrate distance of 4 cm, and 30 min deposition time: (a) complete spectra (b) partial normalized spectra.

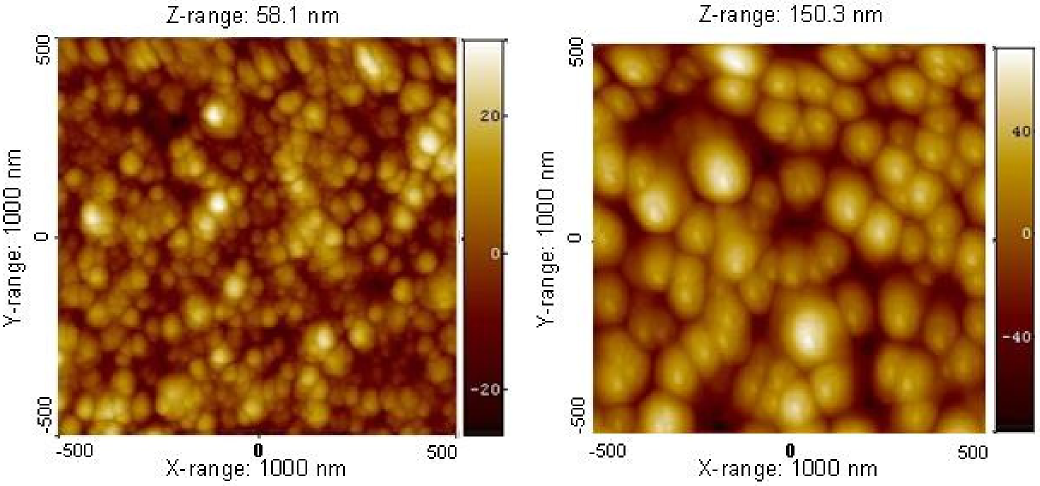

(a) (b)

Figure 3.3: AFM images for AlN films obtained at 3 cm and 11 cm plasma-injector distances on Si (100) at 600ºC, 1 Pa, no RF bias, injector –substrate distance of 4 cm, and 30 min deposition time. Plasma-injector distance: (a) 11 cm, S_a=6.7 nm, (b) 3 cm, S_a= 18.6 nm.

3.2 RF-bias

After the plasma-injector distance was set to 3 cm, RF bias of – 200 V and - 50 V as well as no RF bias were tested employing typical values for the substrate temperature and the chamber total pressure of 600℃ and 1 Pa respectively. It must be noted that when no RF bias potential was applied, a floating potential of +16 to +20 V was observed for the substrate holder.

Films obtained with – 200 V were mainly amorphous (see Fig. 3.4 (a)), and a fairly large 2150 cm^{-1} impurity band could be observed as well in the FTIR spectra when compared to films produced employing less negative bias values (see Fig. 3.4 (b)). Overall smoother surfaces (see Fig. 3.5 (b)) were observed in films obtained with more negative bias, where S_a increased from 5.9 nm to 18.5 nm from -200 V to floating bias respectively. The more negative bias value films also exhibited the absence of a clear columnar domed structure in the film and in fracture surfaces (see Fig. 3.5). These facts suggest that more negative bias values favored the deposition of increasingly amorphous films.

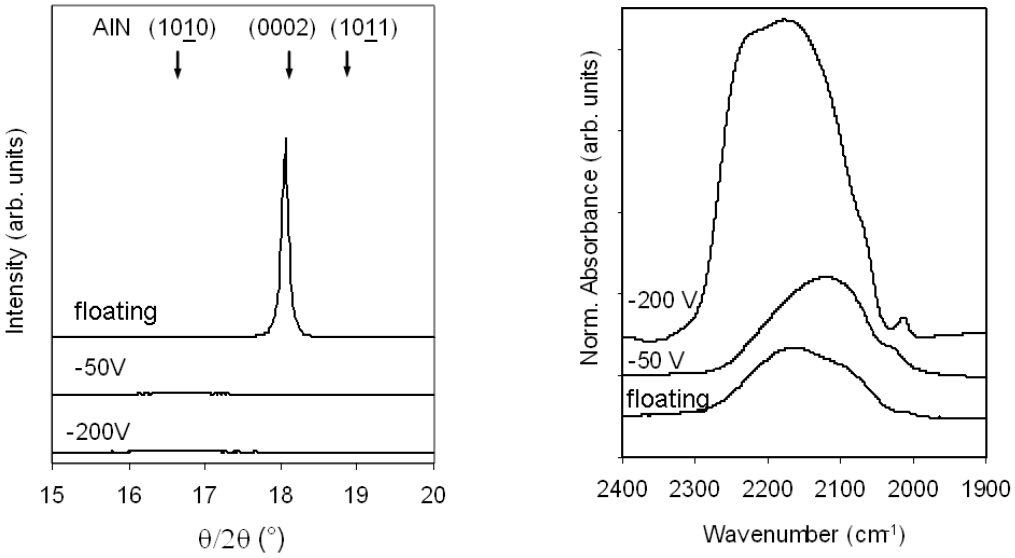

(a) **(b)**

Figure 3.4: XRD patterns (a) and FTIR partial spectra (b) of AlN films obtained with different bias potentials on Si(100) at 600ºC, 1 Pa, plasma-injector distance of 3 cm, injector-substrate distance of 4 cm, and 30 min deposition time. The RF bias potential is indicated.

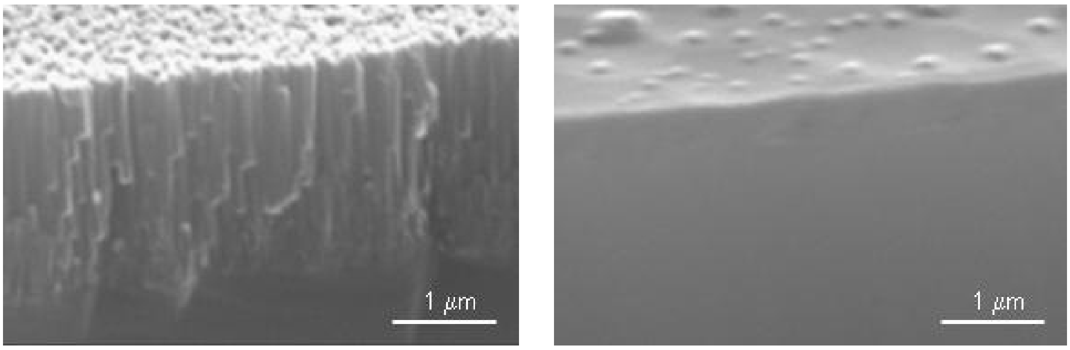

(a) (b)

Figure 3.5: SEM (secondary electrons) micrographs of AlN films obtained on Si (100) at 600ºC, 1 Pa, plasma-injector distance of 3 cm, injector-substrate distance of 4 cm, and 30 min deposition time: (a) fracture surface 25,000X with RF bias 0 V, idem (b) with RF bias -200V.

In contrast to this, films obtained with no RF bias were found to be polycrystalline (see Fig. 3.4 (a)) and strongly oriented in the <0001> direction. An intermediate RF bias level of –50 V produced films that still remained mainly amorphous.

Compressive residual stresses ranging up to 2 GPa were observed for all the films obtained with negative RF bias values, while tensile stresses resulted for films obtained under no bias. The development of compressive stresses with more negative bias voltage values has been attributed in the past to the higher kinetic energy of charged particles that impinge on the film surface during the growth process (see section 1.4.2). The development of amorphous films can be assigned to these charged impinging particles too.

The chemical attack of the films with NaOH solution have shown higher etching rate values for films obtained at more negative RF bias, in accordance with their amorphous characteristics.

3.3 Substrate temperature

Once the plasma injector distance and RF bias conditions were reasonably well established, the remaining 4 variables were investigated at various levels each for the different substrates.

Substrate temperatures of 400℃, 500℃, 600℃, 700℃, and 800℃ were tested. In general, the film deposition rate remained reasonably constant under the different conditions resulting in films of about 2 µm after 30 minutes of deposition time. The XRD patterns obtained for the different films exhibited a progressive increase in the AlN (0002) reflection peak height with higher deposition temperatures, suggesting an increasingly predominant orientation (see Fig. 3.6 (a)). The diffusion effects associated with greater substrate temperatures tend to favor crystal growth. The <0001> orientation observed in the films corresponded to the (0001) basal plane parallel to the substrate surface, where this plane exhibits a comparatively lower surface energy due to its high packing fraction (see section 1.4.1.1).

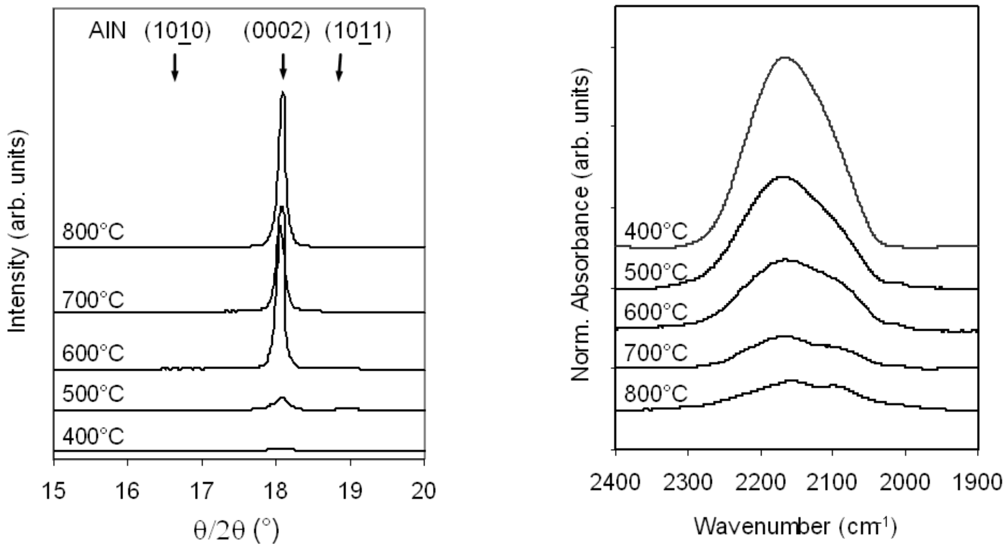

(a) **(b)**

Figure 3.6: XRD patterns (a) and FTIR partial spectra (b) of AlN films obtained on Si(100) at 1 Pa, no RF bias, plasma-injector distance of 3 cm, injector-substrate distance of 4 cm, and 30 min deposition time. The substrate temperature is indicated.

Once again, the 2150 cm^{-1} FTIR impurity band decreased with increasing deposition temperatures (see Fig. 3.6 (b)), while a more defined crystalline structure was also observed by AFM in the films deposited at higher temperatures (see Fig. 3.7) with increasingly marked column domed surfaces. Average grain sizes of around 40 nm could be estimated, from the peak FWHM in the XRD patterns, for films deposited at the higher temperatures, suggesting that the film columns correspond to one or perhaps just a few grains. Thus, the increase of the substrate temperature led to films increasingly oriented in the <0001> direction with fewer impurities.

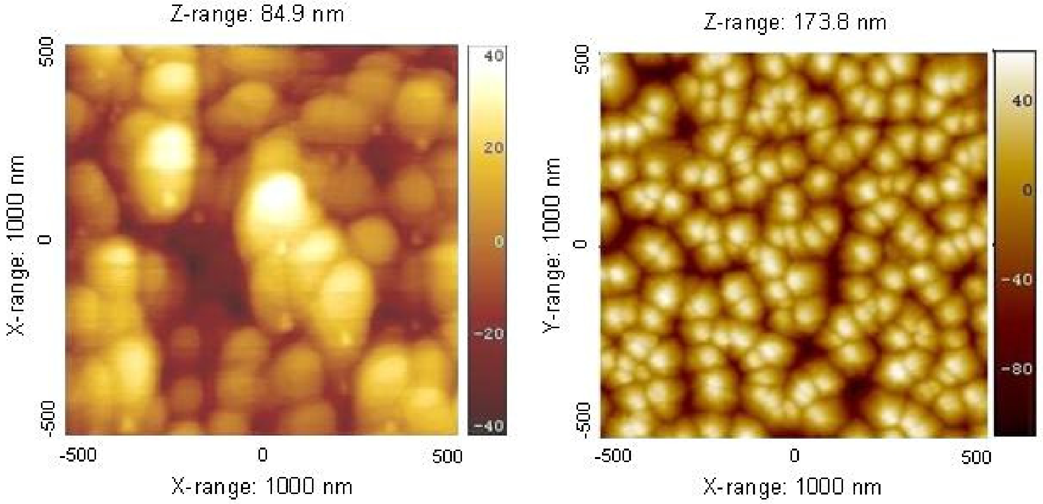

(a) **(b)**

Figure 3.7: AFM images of the AlN film surfaces obtained on Si(100) at 1 Pa, no RF bias, plasma-injector distance of 3 cm, injector-substrate distance of 4 cm, and 30 min deposition time. Substrate temperatures: (a) 400ºC, (b) 800ºC.

The chemical attack of the films with NaOH solution have shown higher etching rate values for films obtained at lower temperatures, in accordance with their amorphous characteristics.

3.4 Chamber total pressure

As it is desirable to work at the lowest possible substrate temperature to minimize thermal stresses and substrate deterioration, chamber pressures of 0.5, 1, 2, 4 and 8 Pa were tested by working at 600℃, since this value represented the lower temperature limit that yielded acceptable polycrystalline films.

While at low chamber pressures <0001> oriented films were observed, a <10$\underline{1}$0> orientation began to develop at pressures over 4 Pa (see Fig. 3.8 (a)). The formation within the plasma of Al-N species, favored by the reduction of the gas mean free path found in the chamber at higher pressures, has been speculated in the past to be responsible for the observed change in film orientation in PVD sputtering (see section 1.4.1.3). The estimated gaseous mean free paths [51] under the prevailing conditions for 1 Pa and 8 Pa were found to be around 10 cm and around 1 cm respectively. Keeping in mind that the injector-substrate distance employed was 4 cm, it appears that the above statement could be consistent to explain the change in orientation observed.

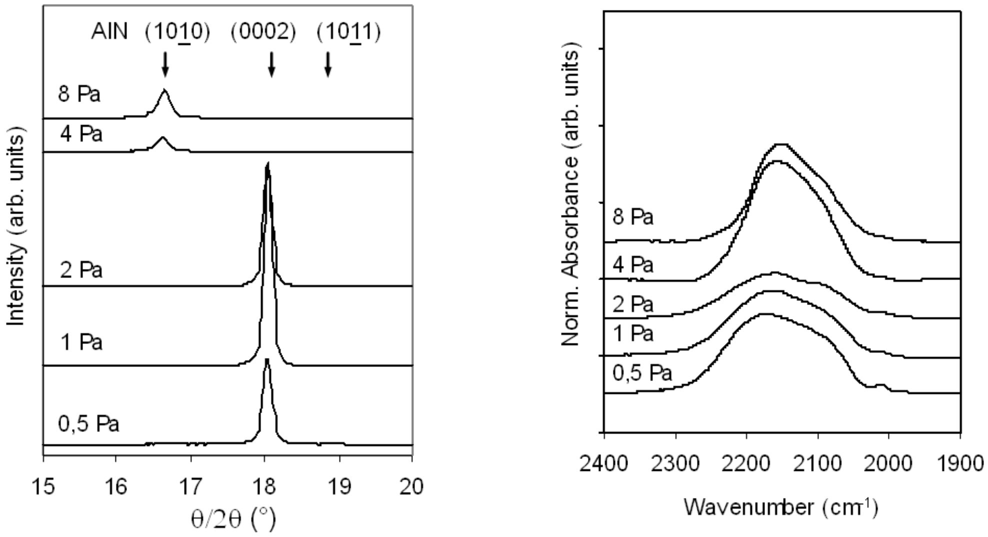

(a) **(b)**

Figure 3.8: XRD patterns (a) and FTIR partial spectra (b) of AlN films obtained on Si(100) at 600ºC, no RF bias, plasma-injector distance of 3 cm, injector-substrate distance of 4 cm, and 30 min deposition time. The chamber pressure employed is indicated.

A change in the widths of the corresponding peaks for the (0002) and (10$\underline{1}$0) reflection in the XRD patterns of the films was also observed suggesting that a reduction in grain size, from 37 nm at 2 Pa for the <0001> oriented film to about 23 nm at 8 Pa for <10$\underline{1}$0> oriented films, also took place. As pointed out before, the reduction in average grain size can be expected to result in higher impurity content and in a decrease in the film surface roughness. The FTIR 2150 cm^{-1} impurity band showed a change in shape (see Fig. 3.8 (b)) for the films deposited over 4 Pa, as well as the film surface roughness decreased, i.e. S_a from 15.3 nm for 0.5 Pa to 5.6 nm for 8 Pa (see Fig. 3.9).

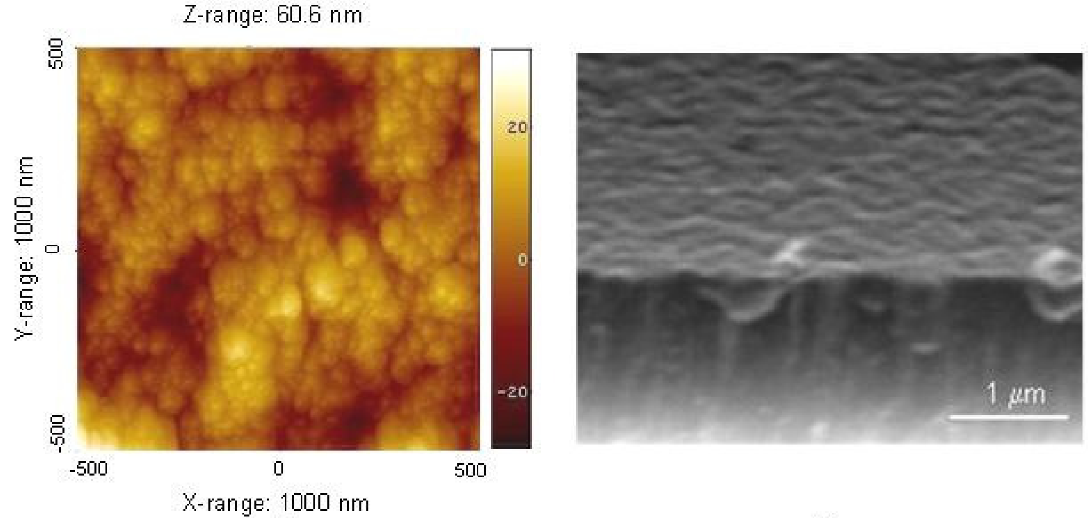

(a) (b)

Figure 3.9: AFM image of the film surface (a) and SEM (secondary electrons) micrograph of the fracture surface 25,000X (b) of AlN films obtained on Si (100) at 600ºC, plasma-injector distance of 3 cm, injector-substrate distance of 4 cm, 30 min deposition time, no RF bias, and chamber pressure 8 Pa.

3.5 Injector-substrate distance

Distances of 4, 6, 8, and 10 cm were tested at zero RF bias, 600°C substrate temperature, and 1 Pa total chamber pressure. An important reduction in the deposition rate was observed with increasing injector-substrate distances (see Fig. 3.10), although the characteristics of the films produced in most cases were not altered significantly. Although this, an incipient development of the (10$\underline{1}$0) direction could be observed for the 10 cm distance (see Fig. 3.11), suggesting that the change in preferred orientation found in the films at higher chamber pressures could be due to the formation of Al-N species in the plasma (see section 1.4.1.3).

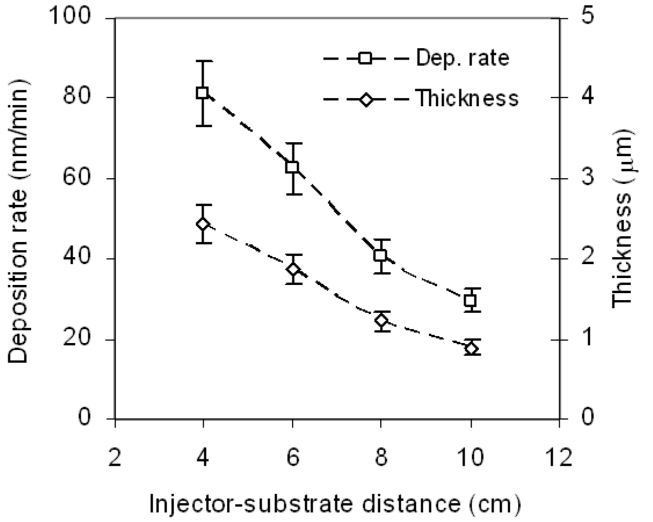

Figure 3.10: Evolution of film thickness and deposition rate for different injector-substrate distances at 600ºC, 1 Pa, no RF bias, plasma-injector distance of 3 cm, and 30 min depositions rate.

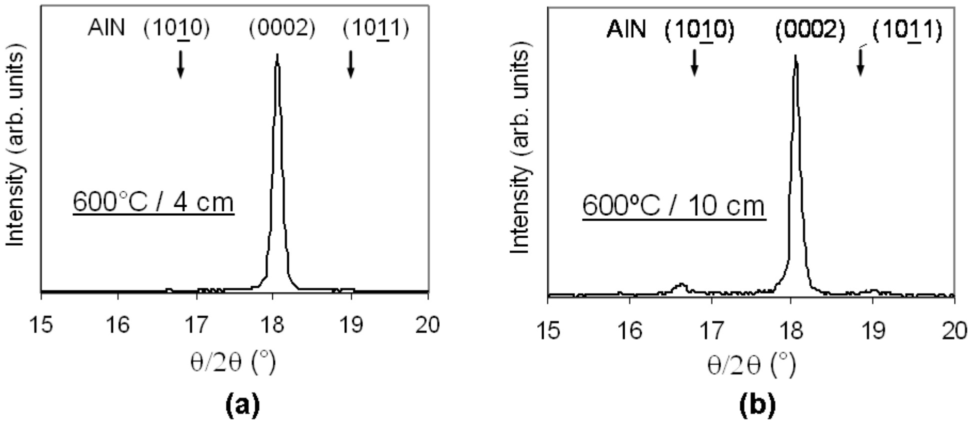

(a) **(b)**

Figure 3.11: XRD patterns for AlN films obtained on Si(100) at 1 Pa, no RF bias, plasma-injector distance of 3 cm, injector-substrate distance of 4 cm, and 30 min deposition time. The temperature and injector–substrate distance are specified. Intensity axes were set in each case in order to have the same relative AlN (0002) peak height.

3.6 Process time

Process times of 7.5, 15 and 30 minutes were tested at 700℃, 1 Pa, without RF bias, a plasma-injector distance of 3 cm, and a 4 cm distance injector-substrate. Progressive variations of the intensities of the XRD patterns as well as of the sizes of the FTIR bands were observed, in accordance with the expected variation of film thicknesses. Aside from that, no significant differences were observed in the XRD patterns or in FTIR spectra of the <0001> orientated films obtained with different times, suggesting, in a first approach, that there are no substantial changes in the growth process as the deposition of the film moves onward.

All films prepared under these conditions were found to be under tension, and an upper residual stress value of 0.7 GPa was estimated. The films deposited in 30 min were cracked, due to the thermal stresses derived from the difference in the thermal expansion coefficients of the substrate and that of the film, since it can be expected that the films can fail mechanically under tensile stress when a critical thickness value is exceeded (see section 1.4.2). Thus, <0001> oriented films with thickness up to about 2 µm could be obtained at 700℃ without the film failing mechanically.

It must be noted that deposition rates around 80 nm/min were produced, where the latter rate is significantly higher than the values observed in some PVD techniques [95].

3.7 Film Substrates

The characteristics of the films prepared on Si(100), Si(111) or Pt(111)/SiO_2/Si(100) substrates were fairly similar in all cases in spite of the different conditions employed. Fig. 3.12 shows the diffraction patterns for the films obtained on Pt(111)/SiO_2/Si(100) substrates at different process conditions – i.e. temperatures and pressures. The comparison of these patterns with that obtained on Si(100) substrate discussed in the previous sections, showed no significant differences. Similar results were obtained on Si(111) substrate. In order to show a finer comparison, XRD patterns and rocking curves were obtained for <0001> oriented AlN films deposited on Si(100) and Si(111) substrates (see Fig. 3.13). No significant differences are observed in the intensities of XRD (0002) AlN peaks as well as in the FWHM values of rocking curves, which correspond to the quantification of the orientation grades (see section 2.2.2.1). This suggests that no major epitaxial effects between the substrates used and the films took place under the conditions tested. Pt(111) and Si(111) should induce the <0001> orientations, in accordance with the lower mismatch between the corresponding crystallographic plans [96]. The Si (100) surface, that could induce the growth of a <10$\underline{1}$0> oriented AlN film, exhibited a thin interface material layer, between the film and the substrate (see Fig. 3.14). Although the markedly low thickness of the interface material, i.e. about 5 nm, its mere presence may upset the epitaxial effect discussed.

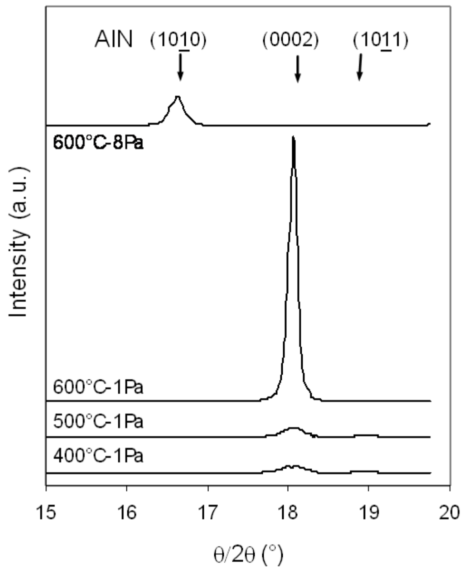

Figure 3.12: XRD patterns for films deposited on Pt(111)/SiO2/Si(100) substrate with no RF bias, plasma-injector distance of 3 cm, injector-substrate distance of 4 cm, and 30 min deposition time. The substrate temperature and chamber pressure employed are indicated.

In order to investigate the origin of observed interface, XPS analyses were conducted through the different stages previous to AlN film depositions (see Fig. 3.15). The original silicon surface shows the presence of silicon oxide (SiO_2), normally associated with the spontaneous oxidations of the surface. The analysis of the substrate surface after Ar-plasma pretreatment, have evidenced the contamination of the surface with substrate holder matter (Fe, Cr, Ni). The etching effect produced by this treatment could act on the holder surface as well as on the substrate, causing the ulterior deposition on the sample. Finally, the exposure of the sample to nitrogen plasma, previous to the deposition process, has made appeared the presence of nitrogen on the surface. The high resolution analysis of this peak indicates the nitrogen is present as silicon nitride (Si_3N_4).

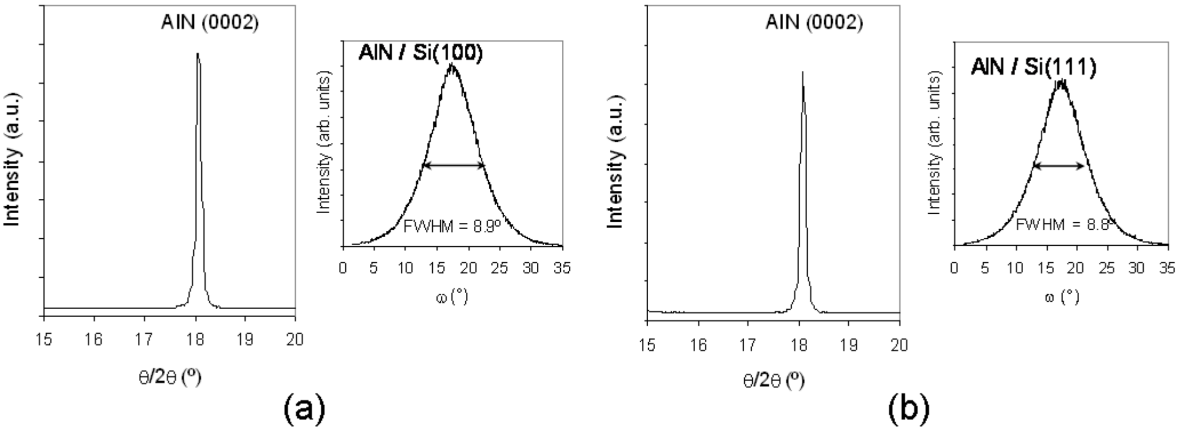

Figure 3.13: Comparison of the XRD Bragg-Brentano patterns and rocking curves for AlN films deposited on Si(100) (a) and Si(111) (b) at 800ºC, 1 Pa, no RF bias, plasma-injector distance of 3 cm, injector-substrate distance of 4 cm, and 15 min deposition time.

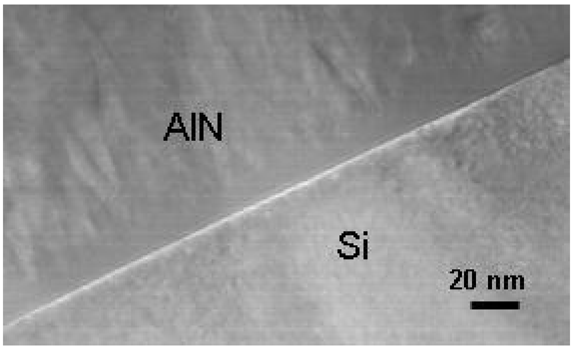

Figure 3.14: TEM micrograph of AlN film cross section obtained on Si (100) at 700ºC, 1Pa, injector-substrate distance of 4 cm, plasma-injector distance of 3 cm, 15 min deposition time.

Consequently, this observation allows speculating that the thin interface observed between the substrate and the film was composed of silicon oxide and nitride, derived from the original condition of the substrate and the initial stages previous to the deposition process.

At the same time it was proved that the Ar pretreatment could generate the contaminations of the original surface with the substrate holder matter. Then, in order to avoid this contamination it was decided to conduct the deposition runs without Ar pretreatment, maintaining the cleaning with solvents, previous to the introduction in the reactor chamber. Since no significant differences were observed in films properties with this simplification, the Ar pretreatment was eliminated from the procedure in the following experimental stage.

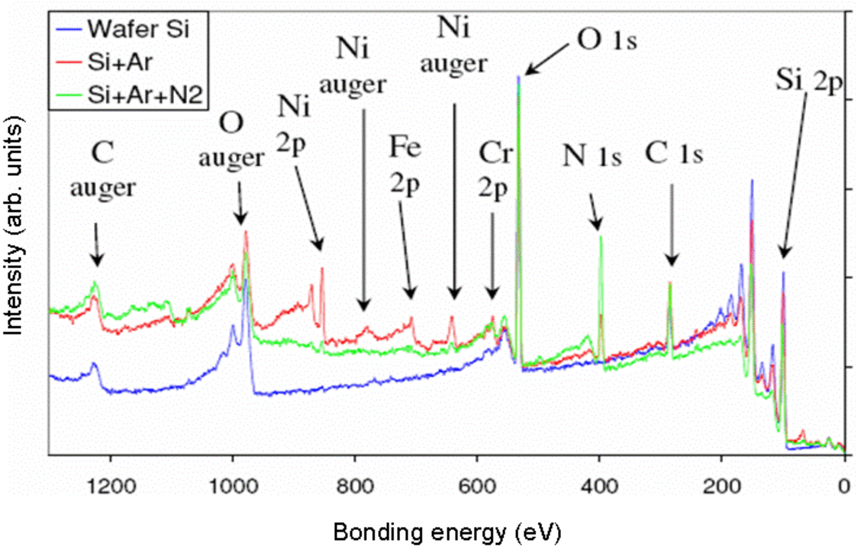

Figure 3.15: XPS analysis of the surfaces at the different stages previous to the deposition process.

3.8 Discussion

The first stage of this work showed the possibility of producing polycrystalline AlN films with a MWPECVD technique. A modification in the reactor configuration was introduced in order to favor this result through the reduction of the distance between the injector and the plasma. The effect of different process variables was scouted. The increase of substrate temperature favored crystalline development and exclusive <0001> orientation at low pressures, while the development of <10$\underline{1}$0> orientation was observed at high pressures, with lower crystalline development. On the other side, the use of RF bias conducted to amorphous films, accompanied with a significant change from tensile to compressive mechanical residual stresses.

Additionally, no important effects were observed with the change of substrate type, and the used Ar pretreatment has been shown as adverse or irrelevant for film crystalline development and orientation.

Therefore, by using all this information, it was necessary to optimize polycrystalline AlN films properties in order to maximize their piezoelectric performance. These objectives were attained with additional experimental designs as well as finer study of films characteristics, all of which are shown in the following chapter.

Chapter 4

OPTMIZATION OF FILM PROPERTIES

In the first part of this work it was demonstrated that polycrystalline AlN films are possible to be produced by MWPECVD technique and the film preferential orientation is possible to be controlled as <0001> or <10$\underline{1}$0> by adequate selection of the deposition conditions. In order to optimize the properties of the AlN films for electro-acoustic applications, additional experiences were conducted. A full fledged experimental design for substrate temperature and total pressure in three levels was done in order to optimize the development of <10$\underline{1}$0> oriented films. Film thickness and bias potential were explored separately using several new levels in each case in order to optimize the properties of <0001> oriented films. A finer characterization of the microstructure, as well as the measurement of the piezoelectric performance of the films was introduced in this stage. Plasma diagnostic by OES in optimal process conditions complete this chapter.

As a consequence of the results obtained in the previous chapter, the runs at this stage were conducted without Ar pretreatment. Moreover, films were prepared mainly with thicknesses lower than 1 µm in order to avoid cracking and at the same time to make a finer analysis of the FTIR transmission spectra.

4.1 Pressure-temperature combined effect

According to previous observations, temperature and pressure are important variables in order to reach crystalline development and change the preferential orientation. Then a complete study of the effect of both variables was considered important to optimize the properties of <10$\underline{1}$0> oriented films and to well understand the orientation mechanism.

AlN films were deposited at different pressures- i.e. 1 and 8 Pa-, and temperatures- i.e. 400ºC, 600ºC and 800ºC-, at the floating potential, with a deposition time around 7 min, to obtain films with thicknesses of 0.5 µm.

Fig. 4.1 shows the obtained XRD patterns for films deposited at different pressures and temperatures. A progressive increase of the reflection peak sizes with temperature is observed for films obtained both at 1 Pa and 8 Pa, which can be associated with crystalline development. While films obtained at 8 Pa were exclusively <10$\underline{1}$0> oriented for all the temperatures, films obtained at 1 Pa showed contribution of all the AlN crystalline orientations at low temperature and exclusive <0001> orientation at high temperatures.

It is possible to speculate about the reasons of these observations. For high pressures Al-N dimmers would be produced as a consequence of the low mean free path of the species in the reactor chamber and these dimmers would control the mechanism of orientation development at all temperatures (see section 1.4.1.3). Consequently, <10$\underline{1}$0> oriented films would be produced for all temperatures. On the other hand, at low pressures, films would only growth in the thermodynamically more favorable condition, that is with <0001> orientation (see section 1.4.1.1), when temperature is enough to make significant the diffusion effects during the process, giving the necessary activation energy.

Experimental results obtained at low pressure suggest that high temperatures are needed to favor AlN crystal growth in <0001> direction. Then, if the nucleation density model is supposed (see section 1.4.1.2), a random orientation at low temperatures would be expected, both for high pressures and low pressures. This is not the case, and orientation control at high pressures is not linked with diffusion effects in the substrate. Consequently, a factor not linked with substrate conditions should be the determinant. As Al-N dimmers production would depend of mean free path in the reactor chamber, independent of substrate conditions, the dimmers theory (see section 1.4.1.3) seems to be appropriated to explain the observed <10$\underline{1}$0> orientation of AlN films at high pressures.

When the XRD reflection peaks obtained at the higher temperatures are compared, in the case of the <0001> oriented films- i.e. 1 Pa- their intensities are significantly higher than in the case of the <10$\underline{1}$0> oriented- i.e. 8 Pa. This fact can be related with the existence of a better crystalline development in the case of <0001> oriented films.

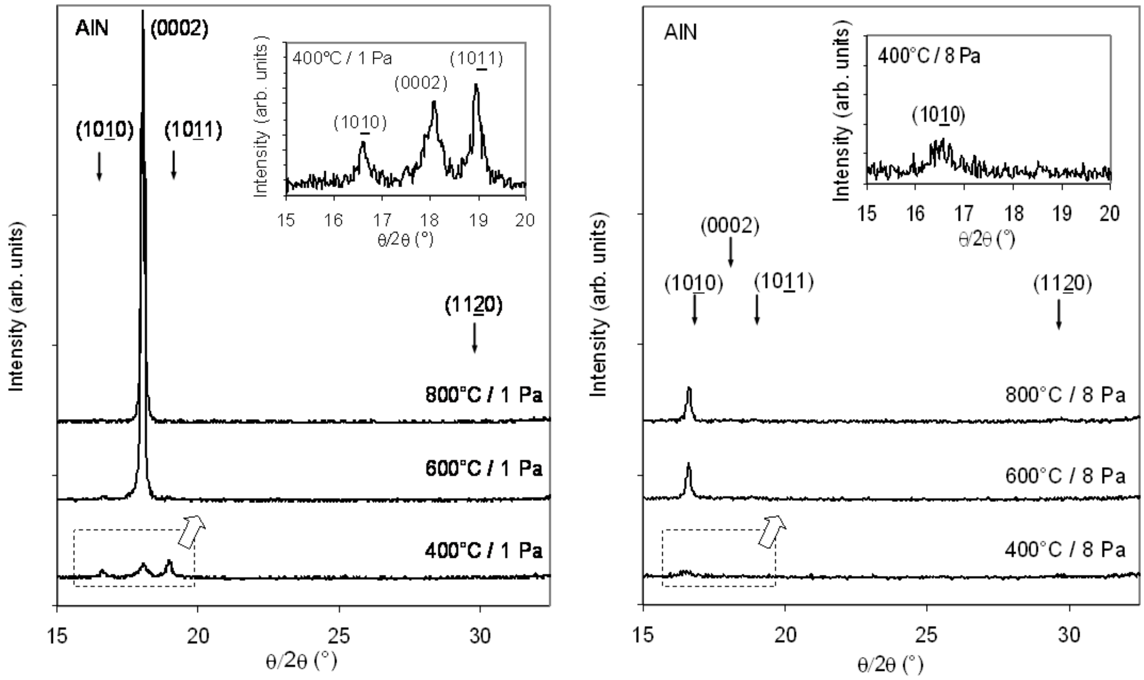

Figure 4.1: XRD patterns for AlN films obtained on Si (100) with no RF bias, plasma-injector distance 3 cm, injector–substrate distance of 4 cm, and 7 min deposition time. Substrate temperature and chamber pressure are indicated. Intensity axes were set with the same scale for comparison.

Figure 4.2 shows the obtained FTIR spectra for the different cases. It is possible to observe that around the positions of the AlN band there are two contributions, normally assigned to the E1(TO) and A1(TO) vibration modes, at 672 cm^{-1} and 613 cm^{-1} respectively (see section 2.2.1.1) [93, 94, 97]. A deconvolution of the bands using gaussien-loretzien fitting, could show the increase of the E1(TO) band relative contribution with the increase of process temperature at low pressure as well as with the reduction of pressure. The relative increase of the E1(TO) mode has been previously related with de development on <0001> oriented films [93], in line with our results. This is consistent with the fact that the vibration modes E1(TO) and A1(TO) correspond respectively to modes excited by a perpendicular and parallel electric field to the c-axis of the crystallite [98].

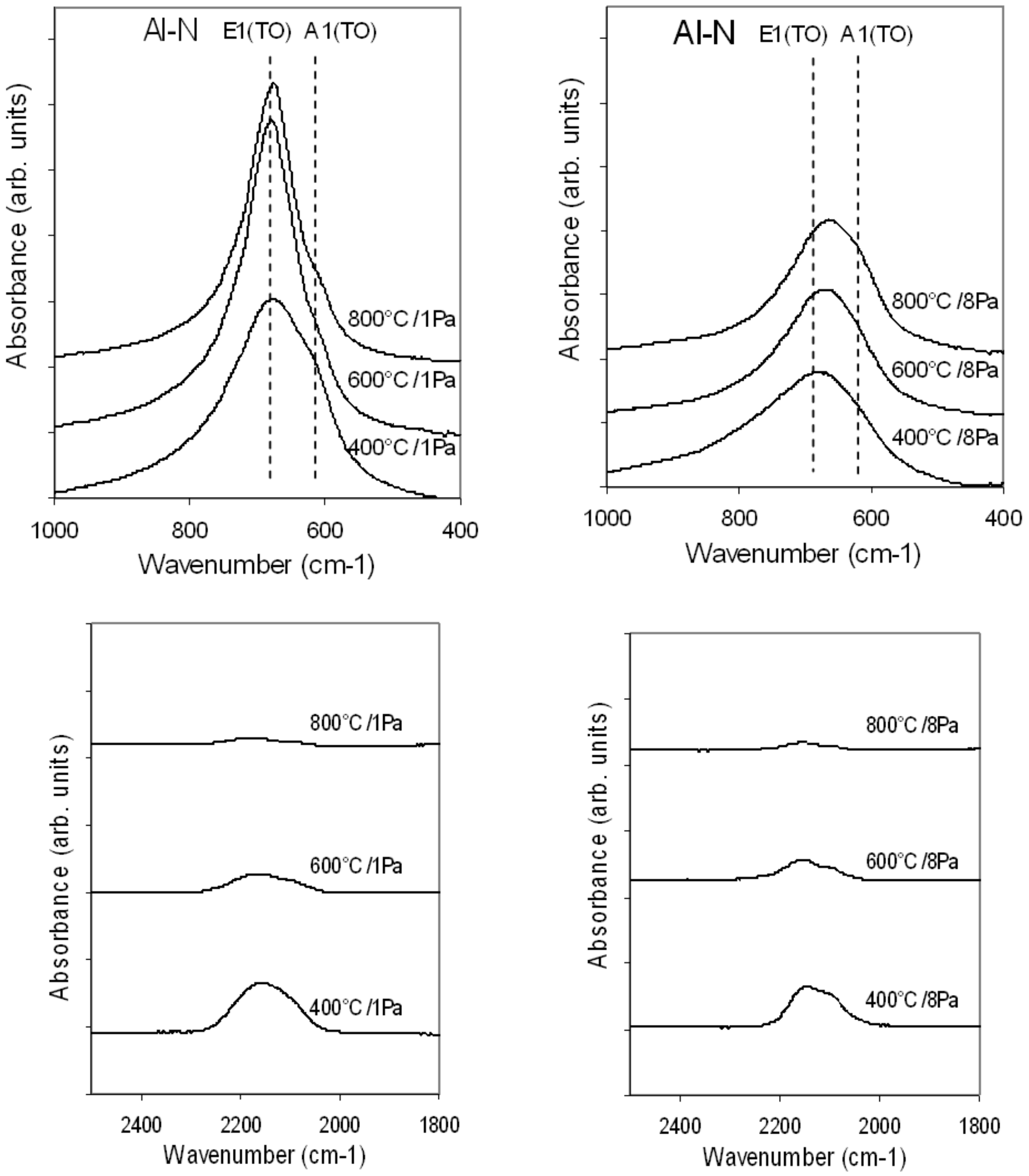

Figure 4.2: Partial FTIR transmission spectra for AlN films obtained on Si (100) with no RF bias, plasma-injector distance of 3 cm, injector–substrate distance of 4 cm, and thicknesses of 0.5 µm. Substrate temperature and chamber pressure are indicated. Absorbance axes of different wavenumber ranges were set with the same scale for comparison.

In addition, a significant decrease of the 2150 cm^{-1} impurity band with temperature increase has been observed for both pressures (see Fig. 4.2). This 2150 cm^{-1} band, has been traditionally assigned to different impurities- e.g. CN, Al-H- as was previously discussed (section 3.1). Simultaneously, the analysis of the plasma during the deposition process by Optical Emission Spectroscopy (OES) (see section 4.6) evidenced the presence of CN species in the reactor chamber. This species could result from the reaction between nitrogen and the Al-precursor (TMA) and could be incorporated as impurities in the film structure during its growth [61].

It can be speculated that at low process temperatures the impurities associated to the decomposition of TMA are incorporated in the film because they arrived to the surface, but probably they can not diffuse and desorbed from it [27]. Together, the low surface diffusion of AlN species does not allow a good crystal growth. However, at higher temperatures, the surface diffusion during the film growth allowed for a crystalline development.

Therefore, higher temperatures have allowed to improve the film crystalline development both for <0001> and <10$\underline{1}$0> oriented films. At the same time, <0001> oriented films reached a better crystalline development than the <10$\underline{1}$0> oriented films.

4.1.1 Annealing effect

In order to better understand temperature effect on the microstructure, AlN films obtained at 400℃ and 1 Pa were post-treated by annealing at 800℃ for 2 hours under vacuum. The comparison between XRD pattern of the samples before and after annealing (see Fig. 4.3) showed no improvement of film crystallization and preferential orientation since there were not significant changes in size and relative contribution of the (0002) reflection peaks. Conversely, XRD pattern of films obtained at 800ºC had shown marked crystalline development and preferential orientation (see Fig. 4.3). These differences suggest that thermal effect was determinant during film growth but had minor contribution after it. According to that previously discussed, high temperatures during film growth (800ºC) allowed surface diffusion of the arriving species and desorption of impurities associated with the precursor decomposition, all favorable for a better crystalline development. Simultaneously, <0001> orientation was favored by the minimization of surface energy. On the other hand, once the film has been grown at low temperature (400ºC), it is not possible to obtain the same crystallization by annealing at higher temperature (800ºC), probably because the impurities are incorporated in all the film thickness and the recrystallization needs a higher temperature to take place.

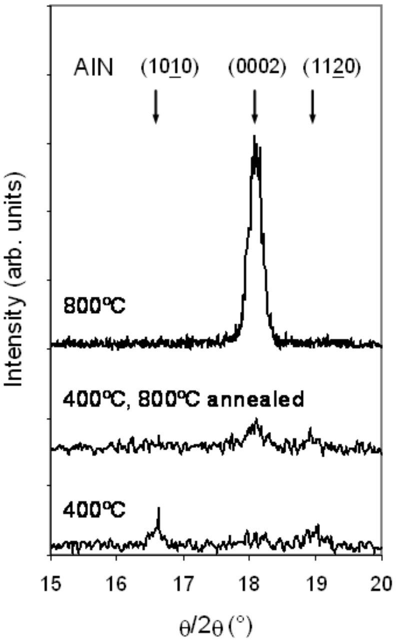

Figure 4.3: XRD patterns for AlN films obtained on Si (100) substrate at 1Pa, plasma-injector distance of 3 cm, injector-substrate distance of 4 cm, no RF bias, with 0.25 µm thickness: substrate deposition temperature and annealing post-treatment temperature are indicated.

4.1.2 Intrinsic stresses vs. temperature for <0001> oriented films

Residual stresses were determined for films obtained at 1 Pa and temperatures of 200, 400, 600 and 800ºC. Derived from the difference between the thermal expansion coefficients of the substrate and the film, a different thermal stress was generated for each deposition temperature. These thermal stresses were estimated using measured Young's modulus, obtaining +0.04, +0.10, +0.20, +0.29 GPa for films deposited at 200, 400, 600 and 800ºC respectively (see section 2.2.3). By subtracting these values from the measured total residual stresses, the intrinsic stresses for the different deposition temperatures were obtained (see Fig. 4.4). An increase of the estimated intrinsic stress with deposition temperature is shown, with tensile stresses for all the cases.

The grain boundary relaxation model (see section 1.4.2) has been used to correlate the development of tensile intrinsic stresses with grain size and grain boundary formation in films with columnar or fibrous microstructures. The obtained AlN films showed an evolution from amorphous and porous structures at low process temperatures to columnar and well crystallized structures at high process temperatures, with increase in grain size, and evolution of grain boundaries. Then, the observed increase in the tensile intrinsic stresses may be in accordance with the prediction of the model, though the amorphous films had not got a clear fibrous structure.

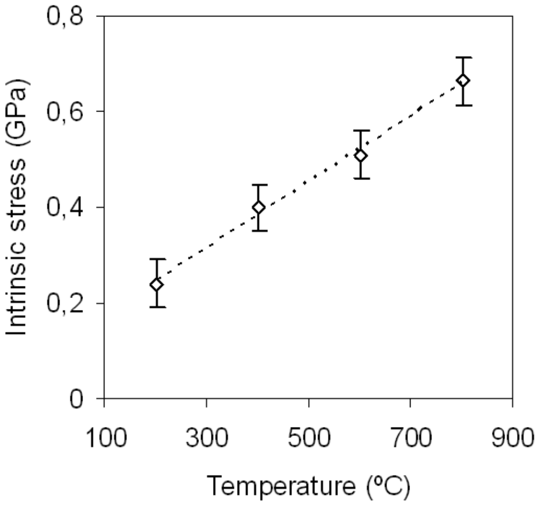

Figure 4.4: Intrinsic stresses vs. deposition temperature for AlN films obtained on Si (100) substrate at 1 Pa, plasma-injector distance of 3 cm, injector-substrate distance of 4 cm and no RF bias. Thicknesses: 0.25 µm.

Another aspect to take into account to explain the observed intrinsic stress evolution with process temperature would be the change of AlN film thermal expansion coefficient for different microstructures. An average reference value of this coefficient was considered for thermal stress estimation. But, in the case of AlN crystals, different linear thermal expansion coefficients for parallel (α_{par}) and perpendicular (α_{perp}) direction to the c-axis of the wurtzite type structure, are expected. Some authors [88] have quantified this anisotropy for AlN crystals, obtaining values of (α_{perp} / α_{par}) = 1.17 ± 0.05 over a wide temperatures range. Thus, the linear expansion coefficient in the direction perpendicular to the c-axis is higher than parallel to the c-axis. In the discussed case, films obtained at higher process temperatures are well crystallized and <0001> oriented, i.e., with the c-axis perpendicular to the surface. In this situation, film thermal stresses, which are mainly parallel to the substrate surface, and then perpendicular to the c-axis, should be higher than in the case of non textured films. This is the reason why thermal stresses in the well oriented films obtained at higher temperatures have been probably sub-evaluated; resulting in higher calculated intrinsic stresses.

4.1.3 Piezoelectric coefficient vs. temperature and pressure

The piezoelectric performance of films obtained at 400°C, 600°C and 800°C, at 1 Pa, with 0.5 µm thickness, was evaluated using the PFM technique. The d_{zz} coefficients were obtained, being z perpendicular to the substrate. As this case corresponds to films obtained at 1 Pa, - i.e. <0001> oriented -, the d_{33} piezoelectric coefficient can be calculated. An increase of piezoelectric performance with temperature was observed (see Table 4.1), in accordance with the observed improvement of microstructure and particularly orientation grade. The obtained piezoelectric coefficient for the film obtained at 800ºC is in the rank of theoretical and best experimental values informed in bibliography [22, 29].

Table 4.1: Piezoelectric coefficients for AlN films obtained at different substrate temperatures and pressures measured by PFM.

Pressure(Pa)	Temperature(ºC)	Oriented	d_{zz} (pm/V)	d_{33} (pm/V)
1	400	<0001>	2.7 ± 0.5	3.5 ± 0.7
1	600	<0001>	1.7 ± 0.3	2.2 ± 0.4
1	800	<0001>	6.3 ± 1.3	8.1 ± 1.6
8	800	<10$\underline{1}$0>	1.5 ± 0.3	-

The same technique was used to evaluate the <10$\underline{1}$0> oriented films obtained at 8 Pa. Low d_{zz} values were obtained, as expected for this film orientation. The reasons of this behavior are discussed in Appendix B.

4.2 Evolution of film properties with thickness

AlN films were deposited on Si (100) substrates at 800ºC and 1 Pa with different process times in order to obtain several thicknesses. A fine characterization of the obtained microstructures was conducted. This deposition condition corresponds to the optimal for <0001> oriented film development according to the previous experimental design.

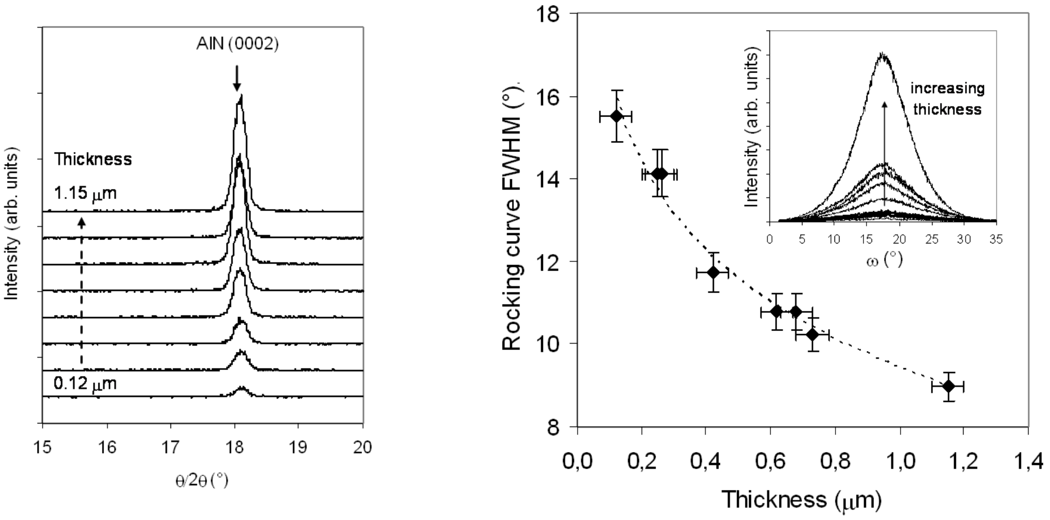

(a) (b)

Figure 4.5: Evolution of XRD patterns (a) and rocking curve FWHMs (b) with thickness for AlN films obtained on Si (100) substrate at 800ºC, 1Pa, plasma-injector distance of 3 cm, injector-substrate distance of 4 cm and no RF bias.

XRD patterns showed an exclusive <0001> orientation from the beginning of film growth, with a progressive increase in size of the (0002) reflection peak with film thickness, as expected (see Fig. 4.5 (a)). FWHM estimations of the (0002) reflection peak did not evidence important differences in grain sizes, being around 35 nm for all the cases. In order to evaluate the <0001> orientation grade of the different films- i.e. the texture-, rocking curves were obtained for the (0002) reflection in all the cases.

Fig. 4.5 (b) shows the evolution of the FWHM of the rocking curve for different film thicknesses. The significant reduction of FWHM value from 15º to 9º with film thickness increase was an evidence of film orientation grade improvement.

The FTIR transmittance spectra of films showed the typical pattern previously obtained for these process conditions (see Fig. 4.2), with the corresponding variation of band size expected for different thicknesses. No significant difference was detected in E1(TO) to A1(TO) AlN vibration modes size rate.

AFM images showed no important differences in surface topography shape (see Fig. 4.6), which evidenced the presence of column tops associated with the columnar microstructure of the films. However, an increase in sizes of the tops with thickness, as well as in the roughness was obtained (see Fig. 4.7). This fact suggests that for higher thicknesses, a better crystalline development is obtained, with columns that could be formed by one or a few grains on the top. The coincidence in the rank of grain size estimated from the XRD pattern and columns tops observed by AFM for higher thickness is consistent with these considerations (see Fig 4.6 (b)).

Consequently, several facts have shown the improvement of crystalline development and preferential orientation grade for higher thicknesses.

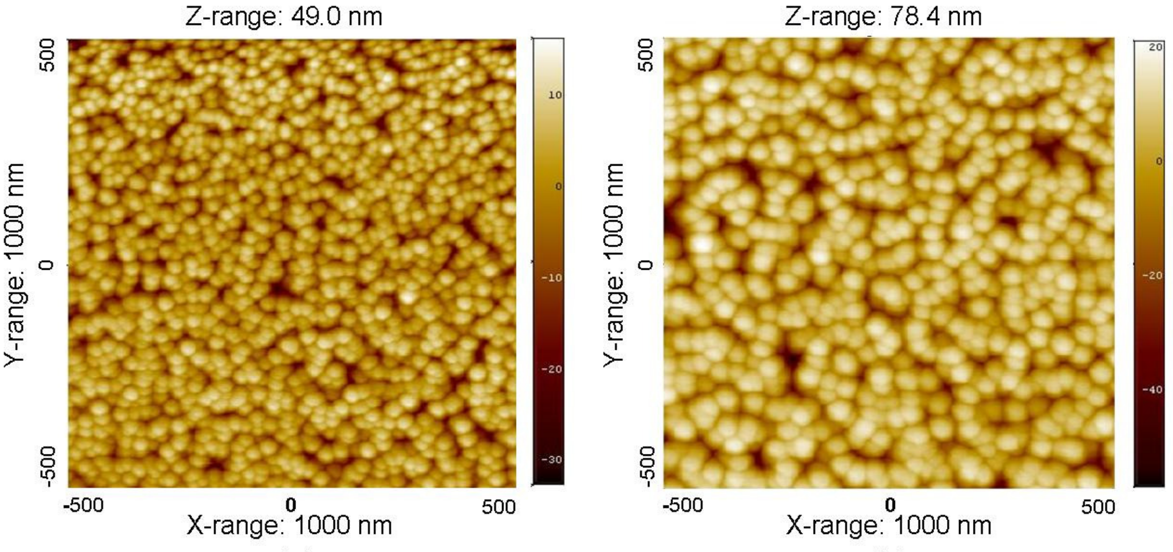

(a) **(b)**

Figure 4.6: AFM images of the AlN film surfaces obtained on Si (100) substrate at 800℃, 1 Pa, plasma-injector distance of 3 cm, injector-substrate distance of 4 cm and no RF bias. Process time and measured roughness: (a) 4.5 min, S_a= 4.8 nm, (b) 9 min, S_a =7.8 nm.

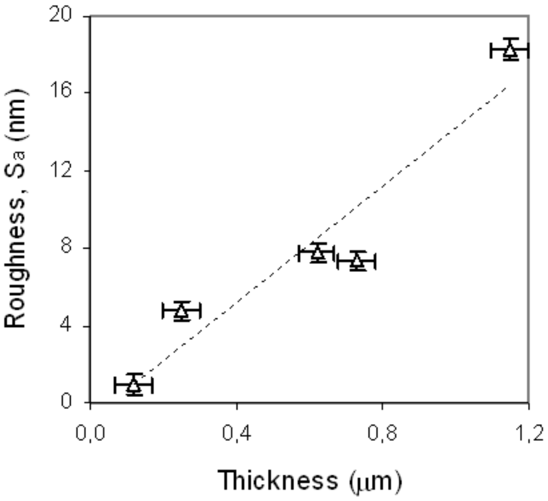

Figure 4.7: Roughness coefficient (S_a) vs. thickness for the surfaces of AlN films obtained on Si (100) substrate at 800℃, 1 Pa, plasma-injector distance of 3 cm, injector-substrate distance of 4 cm and no RF bias.

In order to understand the growing process of the film, the evolution of their mechanical stresses with thickness was followed. Residual stresses were measured for thicknesses between 0.12 and 1.25 µm. As films were obtained at 800ºC substrate temperature, a significant component of thermal stresses was estimated (+ 0.29 GPa). By subtracting this values to the measured film stresses, the intrinsic stresses were estimated for the different film thicknesses (see Fig. 4.8). The obtained intrinsic stresses were all tensile, showing an evolution to a maximum at about 0.25 µm and a further gradual reduction with thickness increase. The initial evolution to a maximum tensile intrinsic stresses can be explained by the film densification associated with coalescence of isolated clusters (see section 1.4.2). Grain boundaries are eliminated by grain growth while channels and holes are filled and closed. The ulterior columns growth after coalescence can generate spaces due to shadowing effects, and consequently, a reduction in tensile intrinsic stresses. Other possible reasons are the diffusively controlled relaxation processes (see section 1.4.2). The observed roughness increase with thickness by AFM (see Fig. 4.6) would be in line with the first explanation.

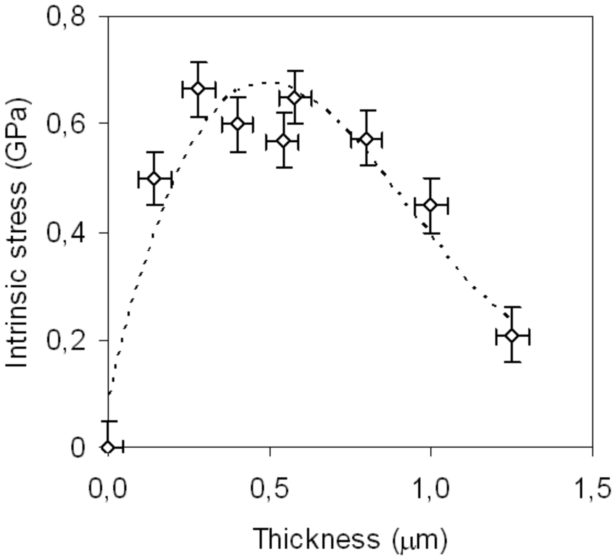

Figure 4.8: Intrinsic stress vs. thickness of AlN films obtained on Si (100) substrate at 800°C, 1 Pa, plasma-injector distance of 3 cm, injector-substrate distance of 4 cm and no RF bias.

4.2.1 Microstructure evolution in film profile

The profile of a <0001> oriented AlN film deposited on Si (100) substrate, at 800°C, 1 Pa, with 1 μm thickness, was analyzed using TEM and SAED.

The TEM cross section image of the film (Fig. 4.9 (a)) exhibits clearly the columnar structure. SAED patterns were taken over 400 nm diameter circular areas along the film profile, as indicated. The first pattern (Fig. 4.9 (b)) was located at the silicon substrate. The second pattern (Fig. 4.9 (c)) corresponds to the bottom of the AlN film profile and showed two intense arcs of (0002) reflections associated with (0001) plans with a misalignment angle of 15º. The third pattern (Fig. 4.9 (d)) corresponds to the center of the film profile and showed a highly <0001> textured columnar film with a misalignment angle of 6º. Finally, the top of film profile (Fig. 4.9 (e)) showed the complete development of a diffraction pattern, which approaches to the case of a <0001> oriented AlN single crystal for the observed area [45, 99]. These observations indicate that an exclusive <0001> orientation is present from the beginning of the film profile, near the interface with the substrate, and a gradual improvement of the texture as well as the crystalline quality is observed through the profile going to the film surface.

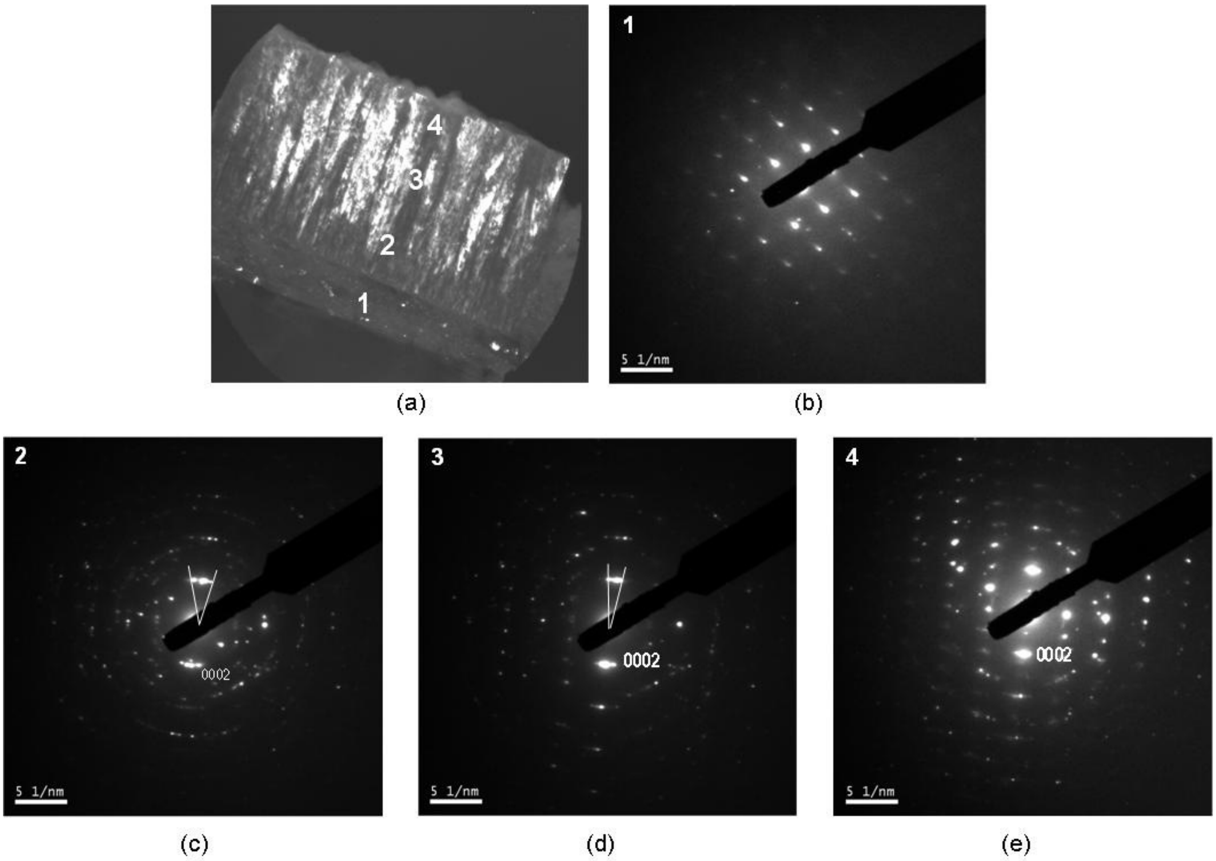

(a) (b)

(c) (d) (e)

Figure 4.9: TEM image and evolution of selected area electron diffraction patterns for the profile of an AlN film obtained on Si (100) substrate at 800℃, 1 Pa, plasma-injector distance of 3 cm, injector-substrate distance of 4 cm and no RF bias; thickness: 1 μm: (a) film profile, (b) electron diffraction pattern of Si(100) substrate, (c,d,e): electron diffraction patterns of AlN film at the bottom, middle and top of film profile, as indicated positions, with zone axis [01$\underline{1}$0].

In order to understand the observed evolution, HR TEM images of the film profile were obtained. The AlN/Si interface showed a 4 nm thick amorphous layer (Figure 4.10 (a)), followed by a polycrystalline AlN layer exhibiting crystallites mostly <0001> oriented and few <10$\underline{1}$1> oriented. The images of the profile at the middle and the top of film profile (Figure 4.10 (b)) showed a columnar structure with <0001> oriented crystallites, with inter-reticular distances between 0.251-0.254 nm. The observed average grain size was larger than 45 nm, corresponding to column size.

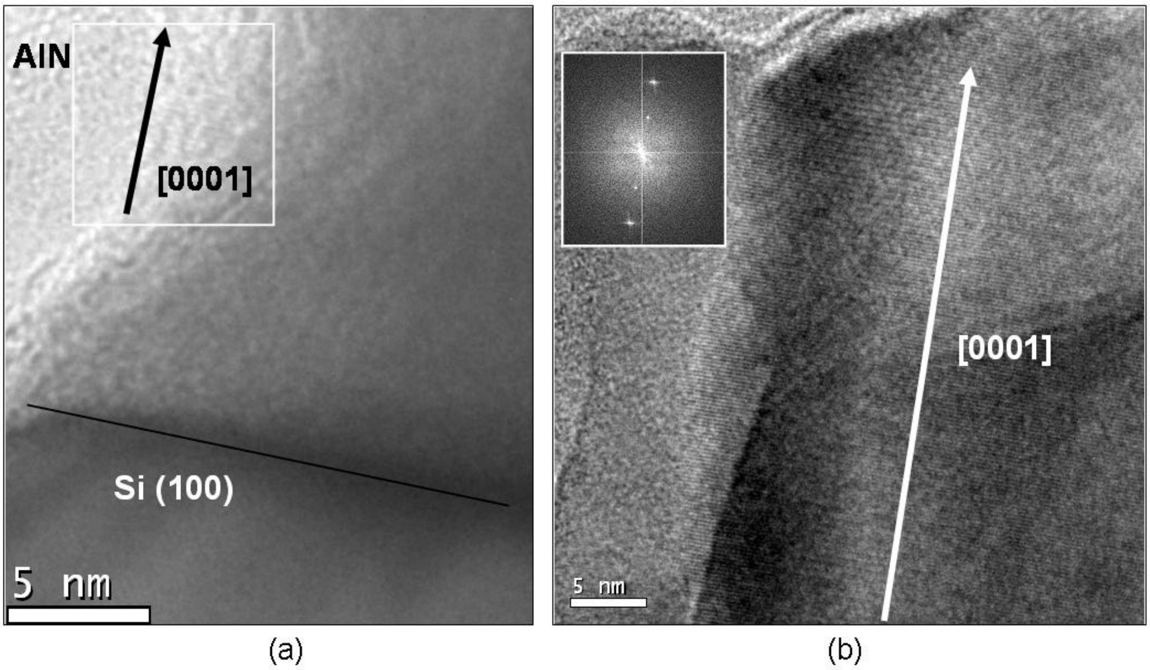

Figure 4.10: HRTEM images for the profile of an AlN film obtained on Si (100) substrate at 800℃, 1 Pa, plasma-injector distance of 3 cm, injector-substrate distance of 4 cm and no RF bias; thickness 1 µm: (a) adjacent to the substrate (b) near the top of the column, with the corresponding FFT pattern.

All the previous observations are consistent with the fact that an improvement of the crystalline quality and orientation grade takes place through the increase of film thickness. As was evidenced in the HRTEM images (Figure 4.10 (a)) and in our previous experimental design (see section 3.7), at the beginning of film growth there were no effects of epitaxy that could favor a particular texture development. Thus, the dominant variable to control the crystallization and orientation at 1 Pa was the temperature, which allowed the growth of <0001> oriented film, as this orientation minimizes the surface energy (see section 1.4.1.1). No ordered growth is obtained at the beginning of the deposition process due to the presence of an amorphous interlayer with the substrate. But a preferential orientation is quickly adopted, and progressive increase of texture to minimize surface energy is observed. Similar tendencies have been observed in AlN films obtained by PVD techniques [39, 40].

4.2.2 Piezoelectric coefficient vs. thickness

The piezoelectric performance of different films, 0.5 µm and 1.0 µm thick, obtained at 800℃ and 1 Pa was evaluated using the PFM techniques (see Table 4.2). No significant differences were observed in d_{33} coefficients with thickness increase at 800ºC, these coefficients being in the rank of the maximum informed bibliographic values [22, 29]. However, the high relative dispersion of the obtained values could prevent to appreciate minor differences of piezoelectric performance. In order to visualize the thickness effect, two films obtained at a less favorable process conditions- i.e. 600ºC and 1 Pa- were essayed. In this case (see Table 4.2) the 0.5 µm film showed a significantly lower d_{33} coefficient, and the increase of the thickness to 1.0 µm conducted to a typical maximum value. Thus, as expected, since the increase of the thickness favored crystalline and texture development, a piezoelectric performance improvement was obtained. Moreover, as temperature was another determinant factor in the same sense, films obtained at higher temperatures, i.e. 800ºC, can show optimal piezoelectric value, from lower thickness values.

Table 4.2: Piezoelectric coefficients for AlN films obtained at different thicknesses and substrate temperatures, measured by PFM.

Thickness (µm)	Temperature (ºC)	d_{33} (pm/V)
0.5	800	8.1 ± 1.6
1.0	800	5.8 ± 1.2
0.5	600	2.2 ± 0.4
1.0	600	8.0 ± 1.6

4.3 Effect of low RF bias potentials

The first part of this work (see section 3.2) has shown that change of deposition conditions from no biased substrate holder- i.e. +16 V floating potential- to – 50 V biased, had caused the loss of the polycrystalline microstructure as well as a significant change of film residual stresses from tensile to compressive. As a consequence of these facts it seemed interesting to research what would happen at intermediate bias values in order to optimize process conditions in the following direction:

- maximizing crystalline development, whose condition could be obtained at low bias potential values;
- minimizing film residual stresses by maintaining adequate crystalline development, as desired for electroacoustic devices;
- maximizing film thickness- without cracks- in order to improve microstructure and piezoelectric performance. The improvement of films microstructure with thickness was previously shown working with no bias potentials, but there was a maximum thickness for which films were possible to be produced without cracks. If residual tensile stresses are possible to be reduced with low bias potentials probably higher thickness could be attained without cracks. Then, if the observed tendency in microstructure evolution with thickness is maintained at low bias potentials, the microstructure and piezoelectric performance could be improved.

AlN films were deposited at different bias potentials, from the floating potential (+16V) to -40V, at 800ºC and 1 Pa, with a deposition time of 7 min, which allowed obtaining film thickness of 0.5 µm.

Figure 4.11 shows the XRD patterns obtained in different cases. An exclusive <0001> orientation was observed in the case of no biased substrate holder, i.e. at floating potential, as would be expected according to the previous work. Once the substrate holder began to be biased, the intensity of the (0002) reflection peak began to decrease progressively in the direction of negative bias potentials. At the same time, the FWHM of the reflection peak increased, associated with a grain size decrease. These facts can be linked with a progressive decrease in film crystalline development, in accordance with our previous results showing amorphous films for higher bias potentials (see section 3.2). Simultaneously, a significant displacement in the position of the (0002) reflection peak from +16V to -20V bias potentials can be observed. This effect can be assigned to the increase in spacing between (0001) plans of the lattice due to the change in film residual stresses. If a polycrystalline film, containing an isotropic biaxial tensile stress distribution in the xy plane (parallel to the substrate) and no stresses in the z direction ($\sigma_z = 0$), is assumed, the film contracts in the z direction (perpendicular to the substrate) by an amount given by [58]:

$$\varepsilon_z = -\nu_f(\varepsilon_x + \varepsilon_y) = -(\frac{\nu_f}{E_f})(\sigma_x + \sigma_y) \qquad (4.1)$$

where: ϵ_x, ϵ_y: strains (m/m), σ_x, σ_y: stresses (Pa), ν_f : Poisson's rate of the film, E_f : the Young's modulus of the film (Pa).

Then, the lattice spacing in stressed films (d) relative to unstressed bulk lattice (d_0) in the z direction can be linked with the strain (ϵ_z) according to:

$$\varepsilon_z = \frac{d - d_0}{d_0} \qquad (4.2)$$

Then:

$$\sigma_f = \sigma_x = \sigma_y = -(\frac{E_f}{2\nu_f})(\frac{d - d_0}{d_0}) \qquad (4.3)$$

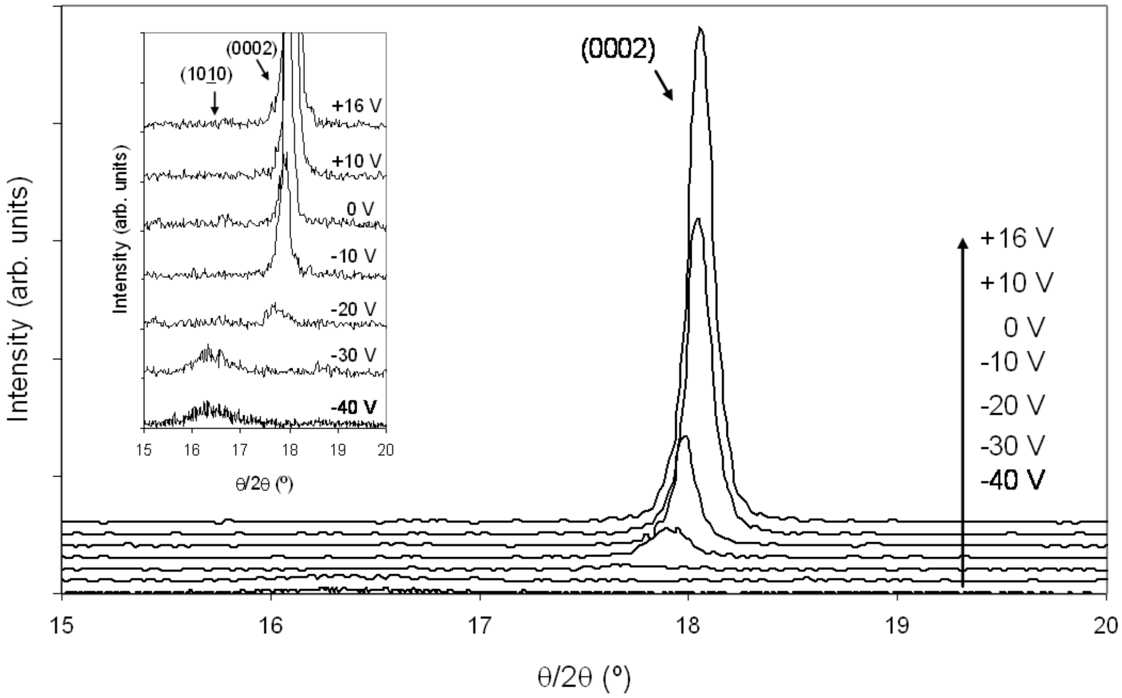

Figure 4.11: Evolution of XRD patterns with RF bias potential for AlN films obtained on Si (100) substrate at 800ºC, 1 Pa, plasma-injector distance of 3 cm and injector-substrate distance of 4 cm; thickness: 0.5 µm.

Consequently, the displacement of the (0002) reflection peak in the direction of lower θ values is probably connected to an increase of the distance between planes derived from tensile to compressive stresses evolution (Figure 4.12).

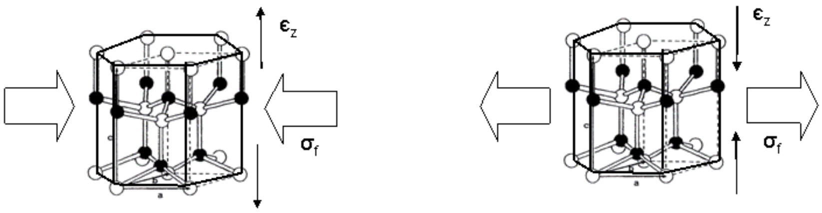

(a) COMPRESSIVE STRESS **(b) TENSILE STRESS**

Figure 4.12: Schematic representations of the effect of compressive (a) and tensile (b) stresses on the distance between (0001) panes for <0001> oriented AlN films.

The reflection peak corresponding to <0001> orientation was observed until bias potential of -20 V, being in this last case small, associated with low crystalline development. At -30V, a change to <10$\underline{1}$0> orientation was observed, which persisted at -40V. In these cases, according to the small sizes and high FWHMs of the diffraction peaks, no important crystalline development was obtained. Since the position of the small (10$\underline{1}$0) reflection peak is near the position of a Si(100) substrate parasitic peak normally observed when no tilt of the substrate is imposed, doubt about the change of orientation could be present. Thus, to confirm these observations, AlN films were deposited on Si (111) substrate at the same process conditions. In view of the facts that the parasitic peak was not present for this substrate and the same change in orientation was observed, the confirmation of the observed results was obtained.

Films residual stresses were measured through the substrate deflection method. The thermal stress developed in the deposition process was estimated as +0,29 GPa and subtracted to obtain the intrinsic stresses (see Fig. 4.13). Films produced at the floating potential showed tensile residual stresses as well as tensile intrinsic stress. An evolution to compressive stresses in the direction of negative bias potentials was observed, in accordance with the observed XRD patterns. At 0 V there was a low absolute value of residual stress, since the compressive intrinsic stress is compensated by the thermal stress derived from the process. From -10V to -20V there was an increase in the compressive stress, resulting in intrinsic stresses near -3 GPa. From -20V to -30V there was an abrupt diminution of compressive stress value, in coincidence with the observed change to <10$\underline{1}$0> preferential orientation (see Fig. 4.11 and 4.13). It can be speculated that the high compressive stresses developed, favored the change in the film microstructure in order to allow the stress relaxation associated to accumulation of elastic energy. At higher bias values- i.e. -40 V- the compressive stress continued its increasing tendency, maintaining the <10$\underline{1}$0> preferential orientation with no significant changes in crystalline development.

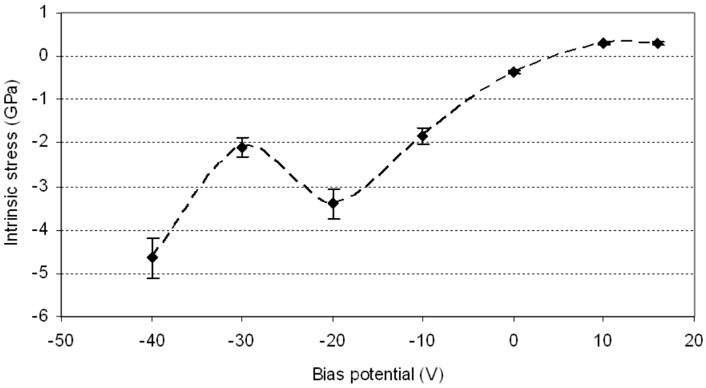

Figure 4.13: Intrinsic stress vs. RF bias potential of AlN films obtained on Si (100) substrate at 800°C, 1 Pa, plasma-injector distance of 3 cm and injector-substrate distance of 4 cm; thickness: 0.5 µm.

Consequently, a general tendency to compressive intrinsic stresses was observed with the evolution to more negative bias potential, showing a defined step at the point where a change from <0001> to <10$\underline{1}$0> preferential orientation took place.

Tensile stresses observed for films deposited at floating potential have been explained by the grain boundary relaxation model proposed in the literature (see sections 1.4.2, 4.1.2). The progressive application of negative bias potentials increases ion bombardment of films during deposition and conducts to compressive stresses. A simple model has been previously presented (see section 1.4.2) to explain the effect of ion bombardment on compressive intrinsic stresses development. The balance between “knock-on process” and “thermal spike” predicts an increase of compressive intrinsic stress with ion energy until a maximum, and the subsequent decrease of the stress with higher ion energies. In this particular case, with low bias potentials, the region of compressive stress increase could be assumed as applicable. Additionally, the relaxation observed at -30V, could be caused by changes in microstructure, a fact not considered by the simple model.

The observed change in film microstructure has been evidenced with AFM images of their surfaces (see Fig. 4.14). A surface with clear domed structure corresponding to the top of the columns was obtained at the floating potential. The progressive applications of RF bias conducted to the progressive degradation of this structure, with a decrease in the size of the domes and simultaneous generation of discontinuities between them. At -10V, an important change is observed in microstructure, with the absence of domed tops and the presence of grains development in all directions, with small sizes, in accordance with the change of preferential orientation and lost of crystalline development observed later. Subsequent increases in the bias conducted to a definitive lost of a grains appearance of the surface. This was associated with a defined decrease of films roughness (see Fig. 4.14).

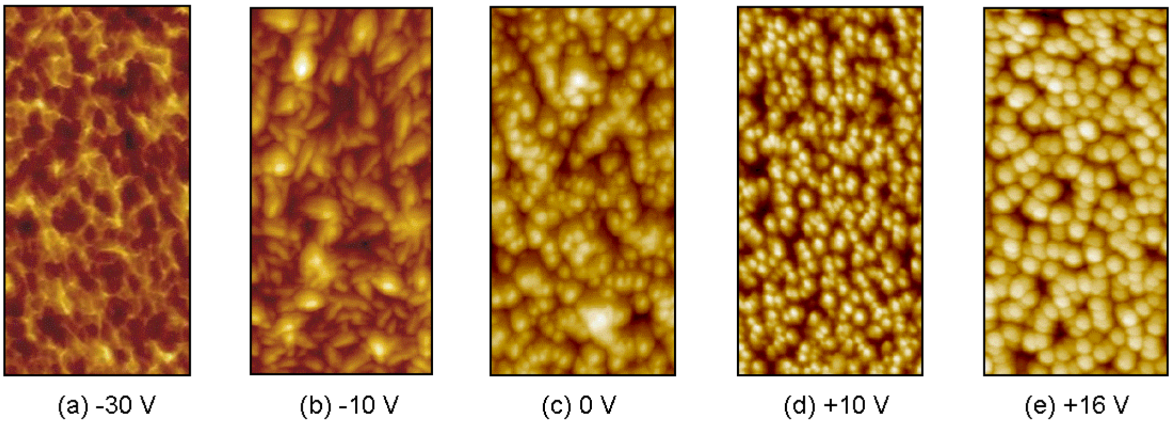
(a) -30 V (b) -10 V (c) 0 V (d) +10 V (e) +16 V

Figure 4.14: AFM images 0.5 µm x 1 µm of the AlN film surfaces obtained on Si (100) substrate at 800℃, 1 Pa, plasma-injector distance of 3 cm, injector-substrate distance of 4 cm with thicknesses of 0.5 µm. RF bias potential and obtained roughness as specified: (a) -30V, S_a= 4.0 nm, (b) -10V, S_a = 4.7 nm, (c) 0V, S_a = 4.7 nm, (d) +10V, S_a = 9.8 nm, (e) +16 V (floating potential), S_a = 7.4 nm.

FTIR transmission spectra (see Fig. 4.15) have shown both Al-N vibration modes, E1(TO) and A1(TO) in all the cases, but with a progressive decrease in the relative contribution of the E1(TO) mode band in the negative bias direction, in accordance with the lost crystalline development and <0001> preferential orientation [93,98].

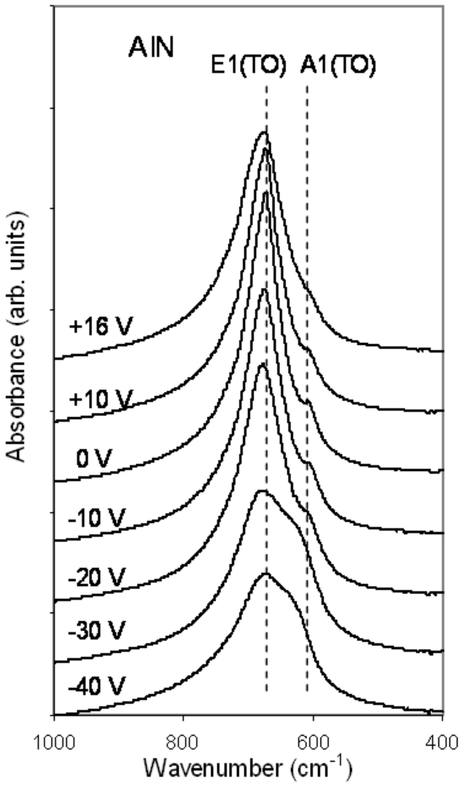

Figure 4.15: Partial FTIR spectra of the AlN films obtained on Si (100) substrate at 800℃, 1 Pa, plasma-injector distance of 3 cm, injector-substrate distance of 4 cm, with thickness of 0.5 µm. Bias potentials are indicated.

Finally, the piezoelectric performances of <0001> oriented films obtained at floating potential and at 0 V bias potential, were evaluated by PFM technique, in order to know the effect of the observed degradation of crystalline structure. The significant reduction of the piezoelectric coefficient d_{33} obtained at 0 V (see Table 4.3), confirmed the degradation of the piezoelectric performance in the same direction.

Table 4.3: Piezoelectric coefficient of AlN films obtained at different RF bias potentials measured by PFM.

Bias potential (V)	**d_{33} (pm/V)**
+16 (floating)	8.1 ± 1.6
0	3.2 ± 0.6

4.3.1 Development of thicker films

The previous observation have shown the progressive degradation of crystalline structure with bias potential, but at the same time the fact that minimal residual stresses can be attained applying very low bias potentials. Then, residual stresses can be significantly reduced maintaining adequate crystalline development. However, one of the main original objectives of this experimental design was to find the possibility to allowed higher films thicknesses without cracks, and eventually to obtain a better crystalline development in this way.

Since films obtained at 0 V or more negatives bias, showed important decrease in crystalline development, the +10V condition was chosen, as it has shown certain reduction in stresses and no great lose of crystalline development. Probably the low energetic ion bombardment favored the decrease of the stresses, but did not destroy considerably the crystalline structure. Films from 1 to 3 µm were then deposited at 800ºC, 1 Pa and +10V bias potential. Figure 4.16 shows the XRD Bragg-Brentano pattern and rocking curve obtained for a film of 2.7 µm in these conditions, which showed no cracks. The exclusive <0001> orientation was maintained, with an sensible reductions in the FWHM of the rocking curve to 7,9º, compared with the films of 1 µm obtained in the standard conditions for which it was in the rank of 9,0º (see section 4.2).

Table 4.4 shows the piezoelectric coefficient d_{33} measured using the PFM technique for films obtained at +10V for different thicknesses. Acceptable values with no significant differences were observed in all the cases essayed. For 1 µm thickness, films obtained at the floating potential and at +10V showed similar piezoelectric performance, an indicative of the fact that there was no significant microstructure degradation with the applied bias. Similar consideration can be made for the increase of film thickness working at +10V bias potential. Then, by applying a low RF bias, it was possible to obtain thicker films- with no cracks- maintaining, at least, the piezoelectric performance. A finer evaluation of piezoelectric performance would be required to demonstrate if a significant improvement was obtained.

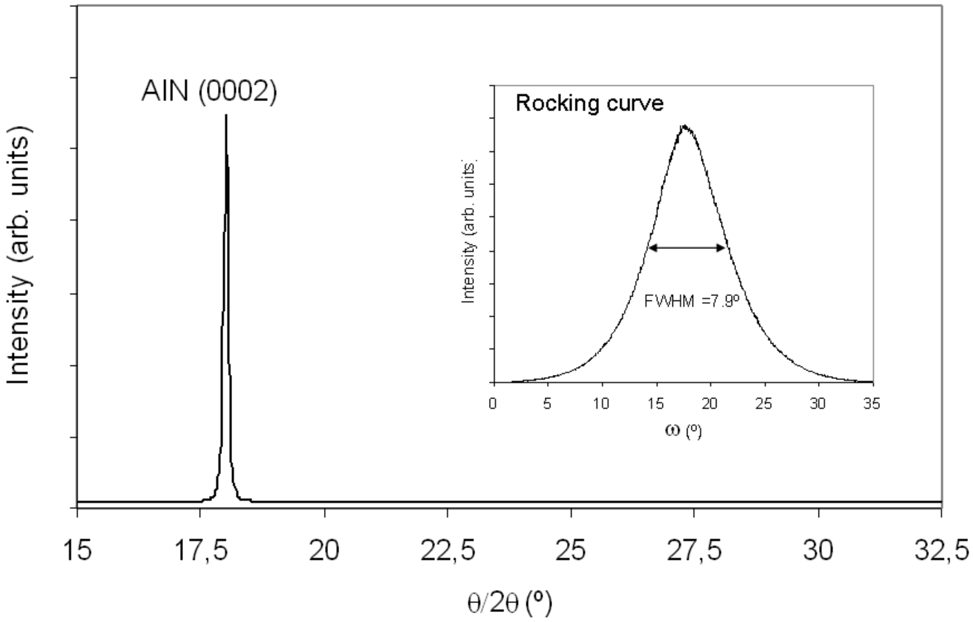

Figure 4.16: XRD pattern and rocking curve of an AlN film obtained at +10V RF bias, 800ºC, 1 Pa, plasma-injector distance of 3 cm and injector-substrate distance of 4 cm, with thickness 2.7 µm.

Table 4.4: Piezoelectric coefficients for AlN films obtained at different RF bias potentials and thicknesses, measured by PFM.

Bias potential (V)	Thickness (µm)	d_{33} (pm/V)
+16 (floating)	1	5.8 ± 1.2
+10	1	5.6 ± 1.1
+10	2	5.7 ± 1.1

4.4 Effect of the H_2 addition to the reaction chamber

The addition of certain proportion of H_2 to N_2 plasmas has been used in the past to increase the concentration of energetic species in reactor chambers [100]. Moreover, it has been speculated about the favorable effect for AlN chemical vapor deposition processes, because hydrogen can avoid the deposition of impurities with the film [61, 63]. In particular, the deposition of CN species with film would be avoided by the generation of HCN species [61].

AlN films with thicknesses of 0.5 µm were prepared under the standard process conditions- i.e. with N_2 flow - and working with a N_2/H_2 flow in order to verify if effects are observed in this sense. Figure 4.17 shows the XRD patterns obtained in both cases. No improvement was observed with hydrogen addition, neither in diffraction peak intensities nor in rocking curve FWHMs. These results were in accordance with the OES plasma characterization discussed later (see section 4.6.2).

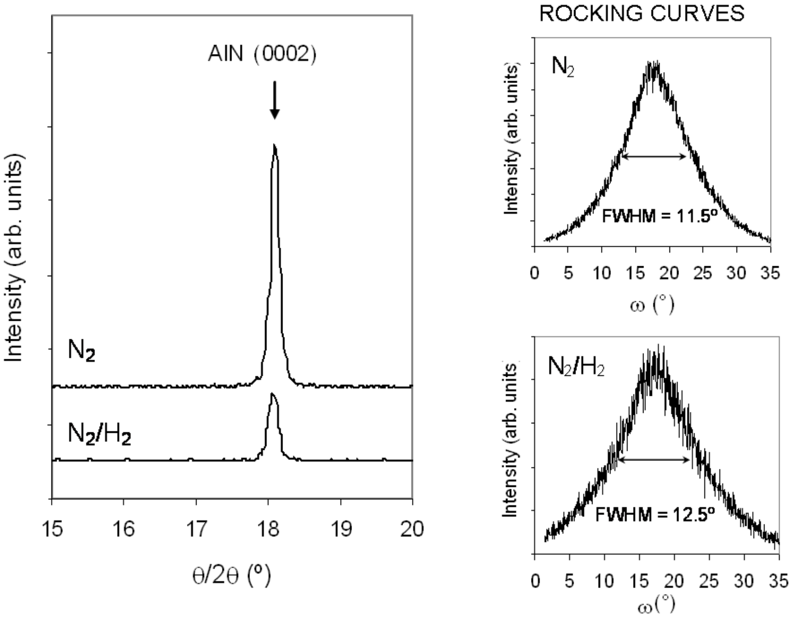

Figure 4.17: XRD patterns and rocking curves of the AlN films obtained at 800ºC, 1 Pa, no RF bias, plasma-injector distance of 3 cm and injector-substrate distance of 4 cm and depositions time 7 min. The plasma generating gas flows are indicated for each case: N_2 (125 sccm) or N_2/H_2 (112 sccm / 13 sccm).

4.5 Optimal process conditions

The optimal process conditions to obtain <0001> and <10$\underline{1}$0> oriented films were defined in accordance with the previous results (see Table 4.5). Low plasma injector distance (3 cm), and high temperature (800ºC) were selected to obtain <0001> oriented films at low pressures (1 Pa) and <10$\underline{1}$0> oriented films at high pressures (8 Pa). In order to reduce tensile residual stresses in films and/or to obtain thicknesses higher than 1.5 µm, a low RF bias potential must be applied, changing the typical values of +16 -+20 V (floating potential), to +10V.

Table 4.5: Optimal process conditions for AlN films deposition

Variable	AlN film growth
Microwave power (kW)	1.6
Nitrogen flow rate (sccm)	125
Argon flow rate (sccm)	50
TMA flow rate (sccm)	1
Plasma-injector distance d_{pi}(cm)	3
Injector-substrate distance d_{is} (cm)	4
RF bias potential (V)	Floating*
Substrate temperature (°C)	800
Chamber pressure (Pa)	1 (for <0001>oriented) 8 (for <10$\underline{1}$0> oriented)

*Until thickness of 1.5 µm, and +10V for thicker films until thickness of 2.5 µm

AlN films were deposited on whole Si(100) wafers under these process conditions with the purpose of constructing SAW devices. Two thicknesses were obtained, 0.5 µm and 1 µm, in order to evaluate the effect of thickness on devices performance. Films were finely characterized in microstructure and composition. Attention was focused on certain characteristics that have been related in the past with the piezoelectric performance: FWHM of the XRD rocking curve, E1(LO) and A1(LO) vibration modes of Al-N observed by FTIR in reflection configuration and the concentration of oxygen impurity in the film.

Fig. 4.18 shows the XRD pattern and rocking curve of the obtained films with thickness 1 µm. While <0001> AlN films showed well crystalline development with intense reflections peaks, and rocking curves with FWHM of 9.0º, <10$\underline{1}$0> AlN films showed small reflection peaks, indicative of lower crystalline development, and rocking curve with FWHM of 11.4º. It is interesting to note that in the second case it was observed a contribution of (112̲0) reflection, which corresponds to the other crystalline orientation with the c-axis parallel to the substrate surface (see Fig. 1.5).

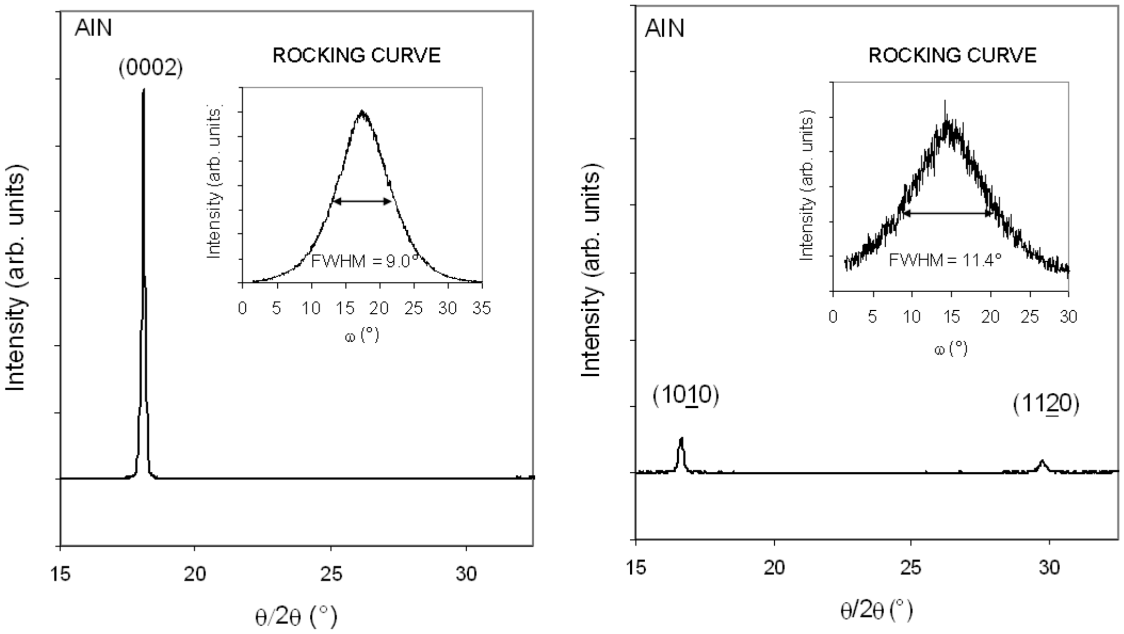

(a) (b)

Figure 4.18: XRD patterns and rocking curves of the <0001> oriented (a) and <101̲0> oriented (b) AlN films, with thicknesses of 1 μm obtained at the optimal process conditions.

The SEM images of the <0001> oriented films, showed a marked columnar structure, in accordance with AFM images of the surface, while the <101̲0> oriented films showed important difference in the morphology of film profile and in surface topography, as expected (see Fig. 4.19).

FTIR spectra were obtained in transmission configuration to confirm the previous observations and in reflection configuration to investigate the presence of longitudinal optical (LO) Al-N vibration modes (see Fig.4.20). In this case, a marked band corresponding to the A1(LO) mode was observed at 883 cm^{-1} for the <0001> oriented film, while a band around 926 cm^{-1} was observed for the <101̲0> oriented films. The existence of an exclusive band of A1(LO) mode has been recently related in the literature [101] with the performance of SAW electro-acoustic devices based on AlN <0001> oriented films.

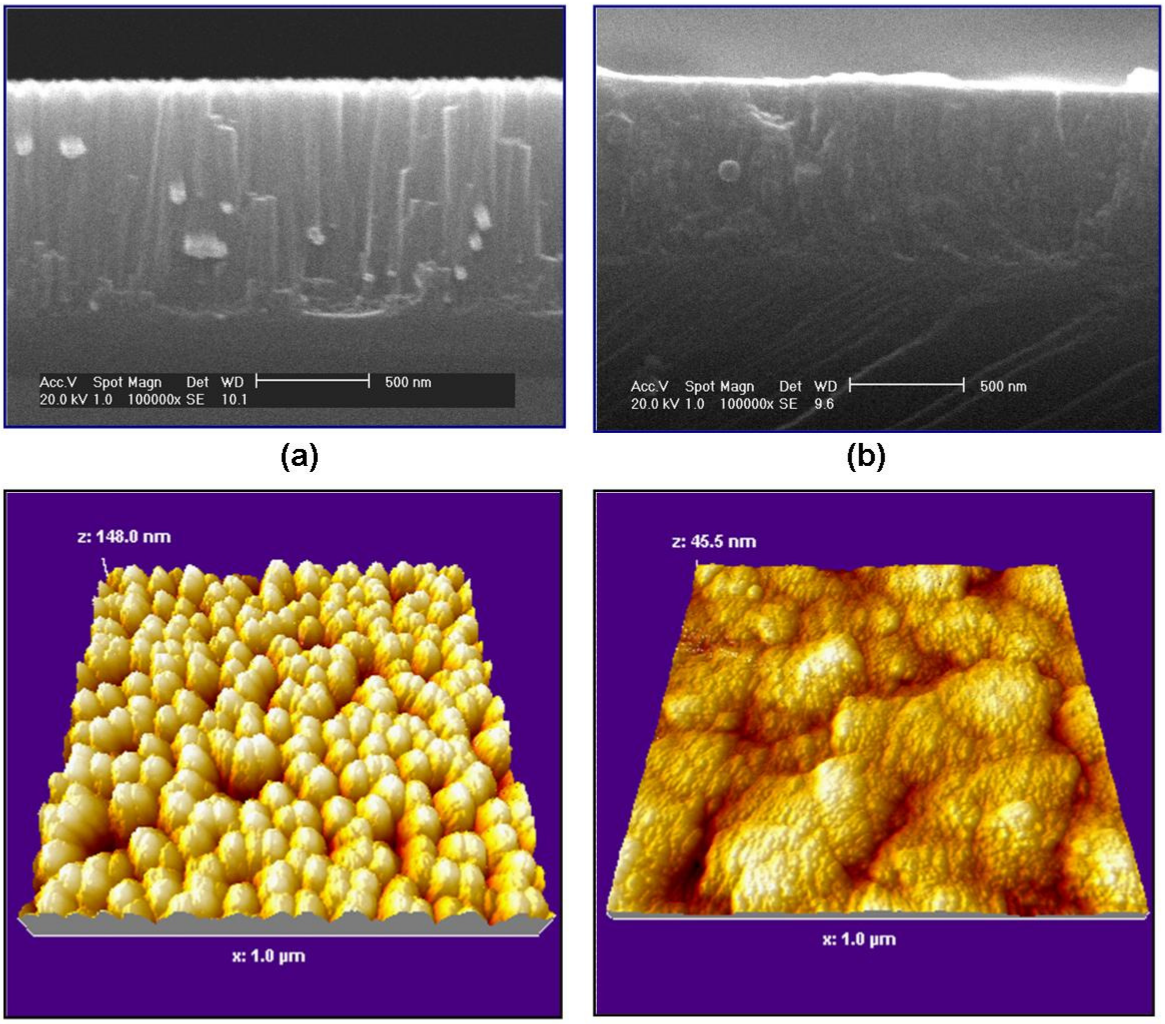

(a) (b)

(c) (d)

Figure 4.19: SEM (secondary electrons) micrographs of the fracture surfaces (50,000X) and AFM images of the surfaces (1µmx1µm) of AlN films obtained on Si (100) at the optimal process conditions: (a, c) <0001> oriented film, (b, d) <10$\underline{1}$0> oriented film, with thicknesses of 1 µm in both cases.

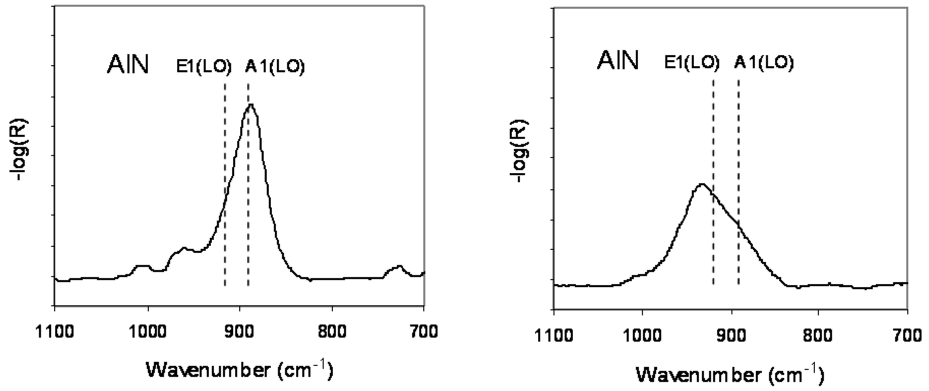

(a) (b)

Figure 4.20: FTIR partial spectra in reflection mode for : (a) <0001> oriented AlN film and (b) <10$\underline{1}$0> oriented AlN film, with 1 µm thickness obtained on Si(100) at the optimal process conditions.

The chemical composition of films obtained in both reference conditions was determined by RBS and NRA techniques. These techniques allow obtaining the mean concentration of the species in all the film profile. Then, films with thickness 0.05 µm were analyzed in addition to the 0.5 µm and 1.0 µm prepared films, in order to evidence differences of compositions near film surfaces. Table 4.6 shows the obtained results for both orientations.

Table 4.6: RBS / NRA analysis of AlN films with different thicknesses obtained on Si (100) at the optimal process conditions.

Film orientation	Thickness (µm)	Al (at.%)	N (at.%)	O (at.%)	C (at.%)
<0001>	0.05	43.0 ± 2	46.2 ± 2	6.5 ± 0.3	4.3 ± 0.2
	0.5	48.6 ± 2	45.9 ± 2	4.2 ± 0.2	1.3 ± 0.1
	1.0	46.8 ± 2	48.2 ± 2	4.4 ± 0.2	0.6 ± 0.03
<10$\underline{1}$0>	0.05	36.5 ± 2	38.8 ± 2	21.4 ± 1	3.3 ± 0.2
	0.5	46.8 ± 2	42.0 ± 2	9.5 ± 0.5	1.7 ± 0.1
	1.0	46.2 ± 2	44.6 ± 2	7.8 ± 0.5	1.4 ± 0.1

A significant decrease of impurity concentrations, i.e. oxygen and carbon, with thickness increase was observed, mainly from 50 to 500 nm. Taking in account that these values correspond to mean concentrations in film profiles, the observed evolutions can be associated with a region near film surfaces with higher impurity values. In the case of oxygen this fact can be related with the spontaneous oxidation of the AlN film surface after the deposition process under atmospheric conditions [102, 60]. However, in the case of carbon, it is possible to speculate about two possible reasons: first the adsorption of carbonated gases on the film surface in contact with the environment and second the injection of residual quantities of TMA (precursor) during the lines cleaning after the deposition process. XPS analysis conducted on film surfaces, which corresponded approximately to 10 nm depths, confirmed the elevated levels of aluminum oxide and carbon present in these cases.

Furthermore, the <10$\underline{1}$0> oriented films have shown oxygen concentration values significantly higher than the <0001> oriented films (see Table 4.6). These differences are consistent with the lower crystalline development evidenced by the XRD patterns for <10$\underline{1}$0> oriented films. It can be speculated that higher process pressures allowed higher concentrations of residual oxygen in the reactor chamber, which reacted with aluminum instead of nitrogen and was incorporated to the film structure as aluminum oxide.

Piezoelectric performance of the prepared films with 0.5 and 1 µm was evaluated by PFM for both orientations. Optimal piezoelectric d_{33} values were obtained for <0001> oriented films, as previously discussed (see section 4.2) and low or absence of piezoelectric response was obtained for <10$\underline{1}$0> oriented films, as expected for this configuration (see Appendix B).

4.5.1 Reproducibility of the MWPECVD technique

Three independent runs were conducted at both optimal process conditions in order to know the reproducibility of the technique for development of film microstructures. The obtained films for each process conditions have shown the same exclusive orientation as well as similar levels of crystalline development in all the runs (see Fig. 4.21(a)). Furthermore, the quantifications of the orientation grade for the different cases through the rocking curves have shown low dispersion (see Fig. 4.21(b)).

This high reproducibility of the technique had been observed in general for the different process conditions tested.

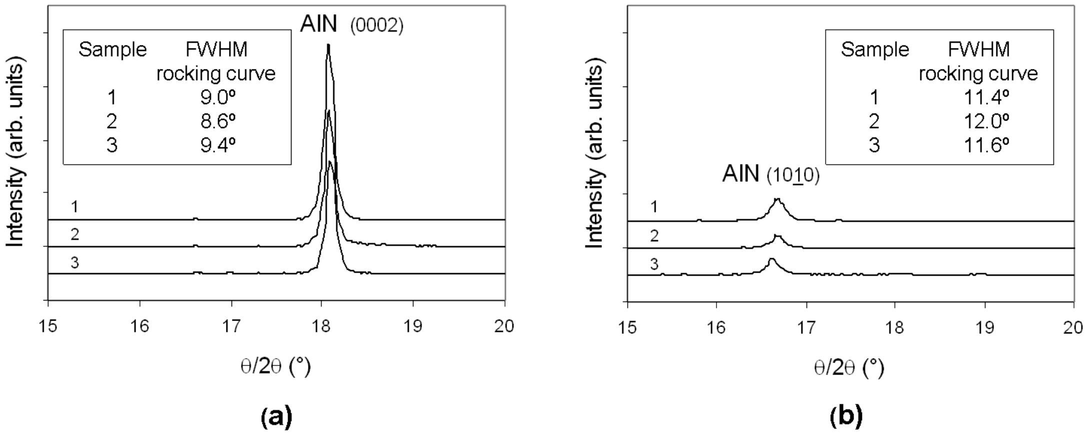

Figure 4.21: XRD Bragg-Brentano patterns and FWHM of the rocking curves of AlN films with thicknesses of 1 μm obtained at optimal process conditions in three independent runs: (a) <0001> oriented films, (b) <10$\underline{1}$0> oriented films.

An interesting case was observed for the films obtained at 600ºC and 1 Pa, which can be considered a boundary condition since this is the temperature from which the exclusive <0001> orientations was observed. In some cases, for the runs made after remounting the reactor previously cleaned, it was observed an incipient development of the other orientations accompanying the <0001>. This fact was easily corrected by a slight increase of the imposed temperature. Consequently, by applying the obtained knowledge of the effect of process parameters on film microstructures it was possible to adjust small deviations of the characteristics of the obtained films for this particular boundary condition. Furthermore, the importance of recomposing the adequate positions of all the elements in the reactor chamber after each cleaning practice in order to reproduce the process conditions was shown.

4.6 Effect of process parameters on plasma characteristics

Process plasmas were analyzed by OES with the purpose of correlating their characteristics with process parameters and the obtained film microstructures.

OES spectra were carried out in the plasma region - plasma zone - and next to the substrate holder- injector zone- (see Fig. 2.1) between 300 and 850 nm, in order to detect transitions, identify the corresponding species present in the plasma, and quantify this species in relative terms [50].

4.6.1 Identification of species present in the plasma

A preliminary study was conducted to facilitate the identification of the different peaks of the complex OES spectra: different plasmas were generated in the reactor chamber, with the progressive addition of different gas flows, i.e.: N_2, N_2+Ar, N_2+Ar+H_2 and N_2+Ar+TMA.

In the first case, where a N_2 plasma was produced, a complex spectrum was obtained, and it was possible to identify numerous peaks corresponding to different transitions: the first negative system $N_2^+(B^2\Sigma)\rightarrow N_2^+(X^2\Sigma)$, the second positive system $N_2(C^3\pi)\rightarrow N_2(B^3\pi)$, the first positive system $N_2(B^3\pi)\rightarrow N_2(A^3\Sigma)$, as well as that corresponding to atomic nitrogen [103,104]. With the addition of Ar flow, several peaks corresponding to Ar and Ar^+ transitions were identified. In the case of N_2+Ar+H_2 plasma, peaks corresponding to transitions of atomic hydrogen and NH species were detected [104,105].

Finally, plasmas with N_2+Ar+TMA flows, corresponding to the deposition process at optimal conditions, were characterized. In these cases, the species obtained for N_2+Ar plasma were detected, with the addition of Al^+ and Al, as would be expected, and the species CN, NH and H, probably derived from the precursor by-products (TMA) (see Fig. 4.22). No evidence of the presence of AlN species was observed in the spectra, in attention to the spectral lines informed in literature for AlN transitions [106,107].

4.6.2 Effect of H_2 addition

The addition of limited proportions of H_2 to N_2 plasmas has been considered favorable to improve the concentrations of reactive species [100]. Particularly, under certain conditions, the increase of atomic N concentration has been observed and assigned to the increase of density of high-energy electrons. These electrons contribute to the generation of atomic nitrogen by direct excitation by electronic impact ,i.e. : $N_2 + e^- \rightarrow N + N + e^-$ [108]. Conversely, for excessive H_2 concentrations only dilution effect is expected, since mechanisms favorable for reactive species generation are not induced [108].

Different H_2/N_2 rates were essayed, beginning from the lowest possible rate allowed by the flow control system of the reactor. A progressive reduction of relative intensities of atomic N peaks was obtained as result (see Fig. 4.23 (a)).

Consequently, a dilution effect was observed and there was not a favorable effect of H_2 addition under our particular process conditions. This behavior can be explained by the observed fact that H species are already present in the standard process plasma derived from the precursor decomposition. Consequently, the optimal concentration of hydrogen can have been exceeded without the addition of an H_2 flow to the reaction medium.

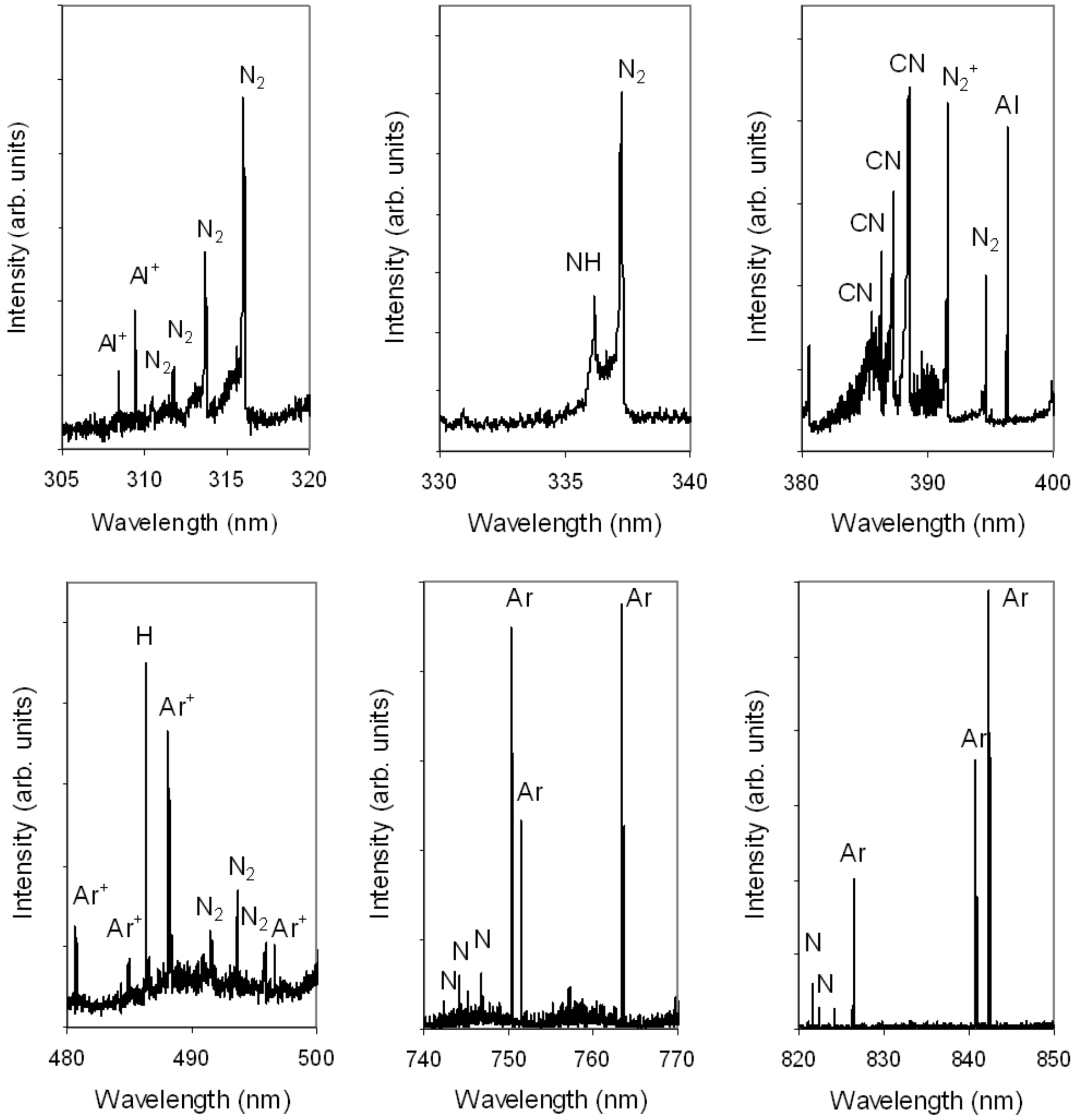

Figure 4.22: OES partial spectra of the process plasma showing some relevant emission peaks.

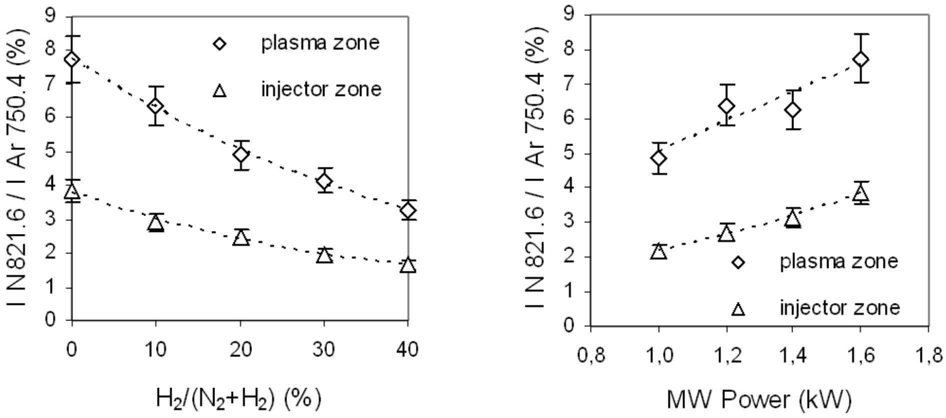

(a) **(b)**

Figure 4.23: Relative peak intensities of N 821.6 nm spectral line as function of: (a) hydrogen addition to gases inlet, (b) microwave power.

In order to demonstrate the favorable effect of high-energy electrons on the generation of atomic nitrogen species, the effect of microwave power employed to generate the plasma was evaluated. An improvement of the relative intensities of atomic N peaks was observed with the increase of microwave power (see Fig. 4.23 (b)). It should be noted that the microwave power used in the deposition processes was the more favorable, because 1.6 kW is the highest power considered sure for a continuous operation of our microwave generator.

4.6.3 Characterization of process plasmas in optimal conditions

OES spectra of plasma were obtained for the deposition of <0001> and <10$\underline{1}$0> AlN films at optimal conditions, i.e. at 1 Pa and 8 Pa. Figure 4.24 shows the relative peak intensities of selected spectral lines for different species detected in the plasma (plasma zone) and under the injector (injector zone). Ar (750.4 nm) line was chosen as reference for intensities comparison.

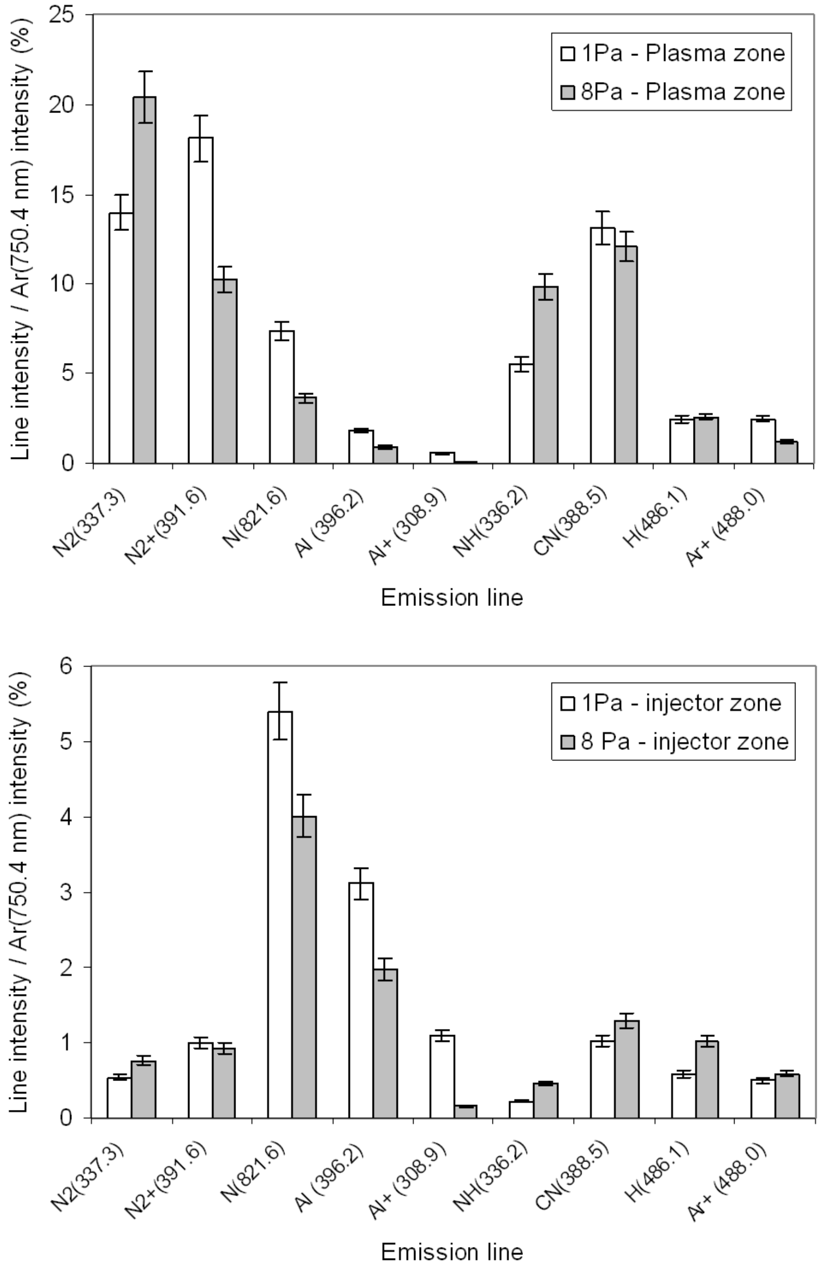

Figure 4.24: Relative peak intensities of selected lines of the OES spectra: process pressures and reactor zones are specified.

While at the plasma zone, N_2, N_2^+, NH and CN species showed higher relative intensities, at the injector zone, Al, Al^+ and N species showed higher relative intensities. Higher Al values would be expected under the injector due to the Al precursor injection (TMA) in this place. However, the presence of higher relative intensities of N_2 species in the plasma zone could be associated to the injection of the N_2 flow on the top of the chamber. The case of charged species, as N_2^+, is complex to analyze, because additional factors are present. A more important reduction in concentrations of charged species, compared with neutral species, should be expected with the increase of distance to the plasma zone, due to the electrostatic attractions ion-electron.

If the relative peak intensities of species for both pressures are compared, in the plasma zone there is an increase of N_2 and NH species (neutral diatomic) with the increase of pressure, while a decrease in N_2^+, N Al, Al^+ and Ar^+ is observed. Then, a decrease of all the referenced charged and monatomic species was observed with the increase of pressure. Probably this could be related with differences in energy of electrons and energy transfer to the species at each pressure condition. When the effect of pressure under the injector is observed, similar tendencies are shown for N_2, NH (increase), N, Al, Al^+ (decrease).

In general terms, it is important to observe that at high pressure there are lower relative intensities for the monatomic species Al and N, while similar or higher relative intensities for the species associated to impurities as CN, NH or H.

The absence of significant AlN peaks in the spectra, as previously discussed, in both cases, have made impossible to demonstrate the presence of Al-N dimmers at higher pressures, in accordance with the dimmers theory that explains the change of preferential orientation (see section 1.4.1.3). Since it has not been easy to detect this species by OES, other techniques as mass spectroscopy have been employed by some authors in this sense [32]. Although the lower relative intensities of monatomic Al and N species for higher pressure seem to be an evidence of Al-N dimmers presence in this case, other factors as the electrons energy should be taken in account to analyze these results.

The rate between N_2^+(391.6 nm) and N_2(380.5 nm) peak intensities has been linked in the literature with the electronic temperature for nitrogen plasmas [109]. This rate was calculated for both pressures in order to estimate the relative electronic temperature of the plasmas under the different process conditions (see Fig. 4.25). A reduction of this rate with the increase of pressure was observed in both cases, indicating lower electronic temperatures at higher pressures. At the same time, it is interesting to observe that only in the case of low pressures there was a significant difference between the plasma zone and the injector zone. Thus, lower electronic temperatures for higher pressures could be associated to lower generation of atomic species as N. This is in accordance with the lower peak intensities of atomic N and Al species observed in this plasma at higher pressure. Consequently, the difference in electronic temperatures could be related with the differences in the concentrations of atomic Al and N species in the plasmas. Thus, it was not possible to evidence the presence of Al-N dimmers at higher pressures, based on the lower concentrations of the atomic species in the plasma.

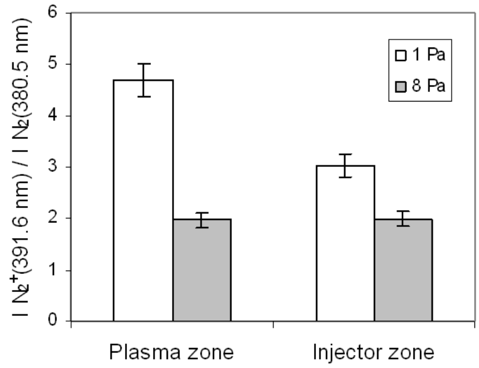

Figure 4.25: Intensities rate between N_2^+(391.6nm) and N_2(380.5nm) lines for the OES spectra obtained at different process pressures and reactor zones.

The chemical analysis of the films (section 4.5) showed the presence of oxygen impurity in their composition, with significant differences between both pressure conditions. Therefore, it seemed relevant to look for evidences of oxygen species, optically active, in the reaction media. No significant peaks were observed for the typical spectral lines normally observed in oxygen plasmas, as atomic oxygen - e.g.: 777.2 nm - and O_2^+ first negative system - e.g.: 563.2 nm -, as well as oxygenated species - AlO at 484 nm, OH at 310 nm - [53, 54]. Then, there was no evidence about the presence of significant concentrations of oxygen in the reactor chamber that could favor the contamination of the AlN film with oxygen during the deposition process, at both pressures.

Chapter 5

APPLICATION TO ELECTROACOUSTIC DEVICES

The optimization of properties of AlN films obtained by a microwave PECVD technique in order to developed piezoelectric characteristics has been described in the previous chapter. The construction of devices with AlN films obtained at optimal conditions is shown in this chapter in order to determinate film performance in SAW and BAW applications.

5.1 SAW devices

AlN films, with 0.5 µm and 1 µm thickness, were deposited on Si (100) wafers,- 100 mm diameters, 525 µm thickness, 5 Ohm.cm resistivity -, at optimal process conditions (see section 4.5). After deposition, aluminum interdigital electrodes were constructed on AlN films by a typical lithography process, in order to obtain SAW devices with defined geometrical characteristics (see section 2.2.4.2). Figure 5.1 shows the obtained devices with typical wavelength of 20 µm. Therefore, the devices were cut, mounted, and adequately connected to measure the frequency response with a vector network analyzer HP8722ES.

5.1.1 Frequency response

The obtained whole frequency response of a SAW device based on a <0001> oriented AlN film is shown in Fig. 5.2. The responses for S_{21} and S_{11} parameters are specified, and the peaks associated to the piezoelectric response are clearly identified.

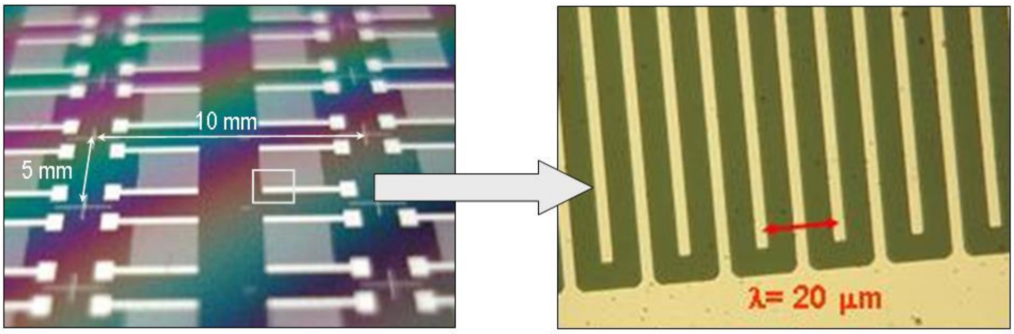

(a) (b)

Figure 5.1: Interdigital electrodes of the prepared SAW devices.

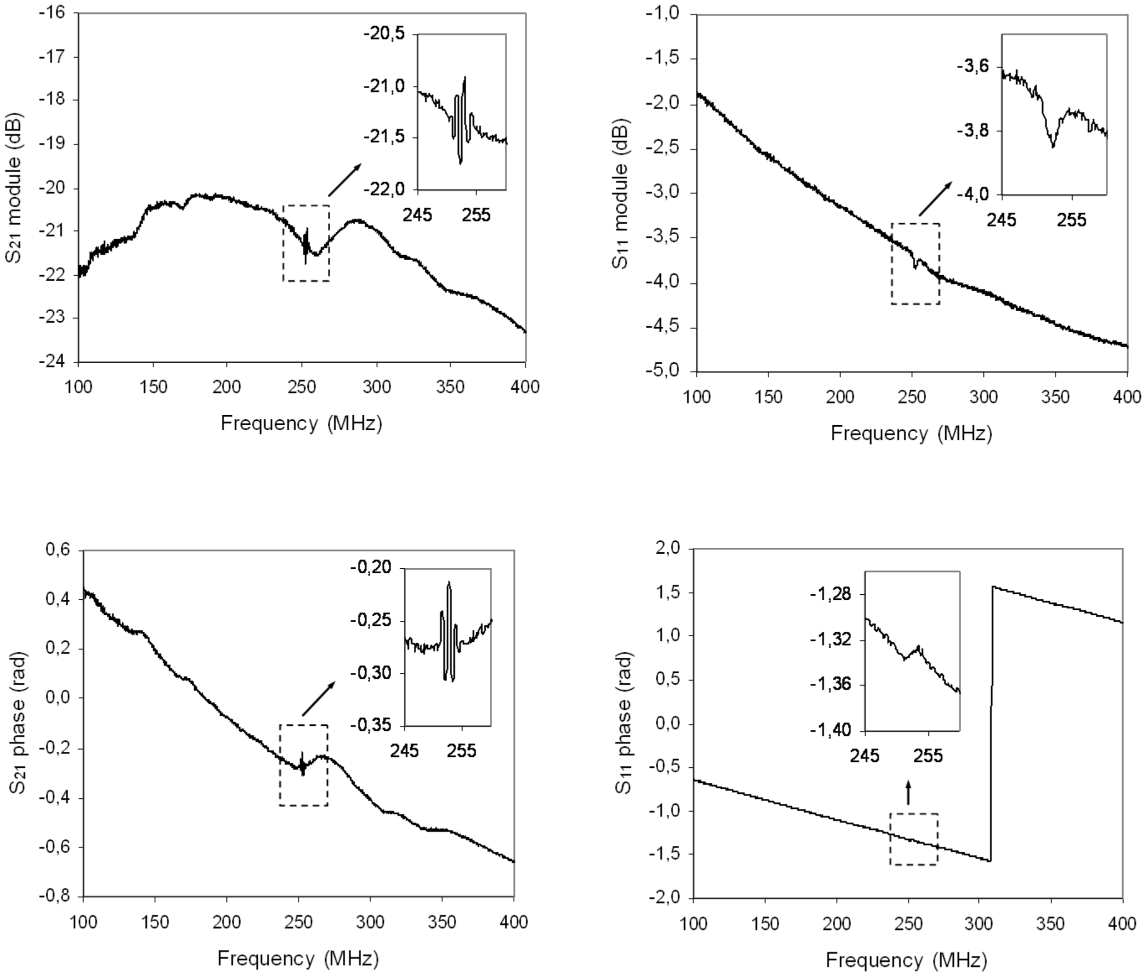

Figure 5.2: The complete frequency response S_{21} and S_{11}, between 100 and 400 MHz , for a SAW device prepared with a <0001> oriented AlN film.

Three different devices were essayed in each case in order to verify the variability of the procedure, taking in account the different stages involved not only in IDTs preparation, but also in cutting and mounting the devices. The results obtained for the scattering parameter S_{21} as function of frequency in the rank of interest are shown in Fig. 5.3 and 5.4.

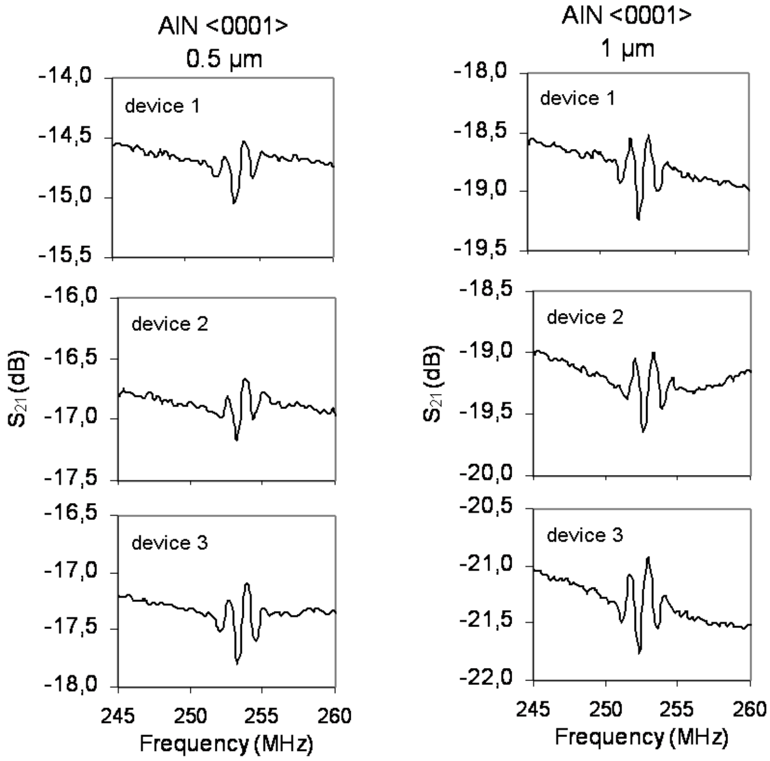

Figure 5.3: Frequency response S_{21} (module) around the characteristic frequency for the SAW devices based on <0001> oriented AlN films with thicknesses of 0.5 µm and 1 µm deposited at the optimal process conditions.

While the devices prepared with <0001> oriented films showed a clear piezoelectric response (Figure 5.3), around 252.5 MHz, both for 0.5 µm and 1 µm thicknesses, the devices prepared with $<10\underline{1}0>$ oriented films showed no significant response in the whole rank- i.e. between 100 and 400 MHz - (Figure 5.4).

AlN films with <0001> orientation had shown d_{33} piezoelectric coefficients in the rank of the maximum theoretical value for 0.5 µm and 1 µm thickness (see section 4.2.2), using the PFM technique. However, the characterization of films had shown an improvement of microstructure from 0.5 µm to 1 µm, which could generate differences in piezoelectric performance. The observed responses of SAW devices prepared with both film thicknesses did not show important differences, but a finer comparison can be made with the assistance of a SAW frequency response model. This is analyzed in the following section.

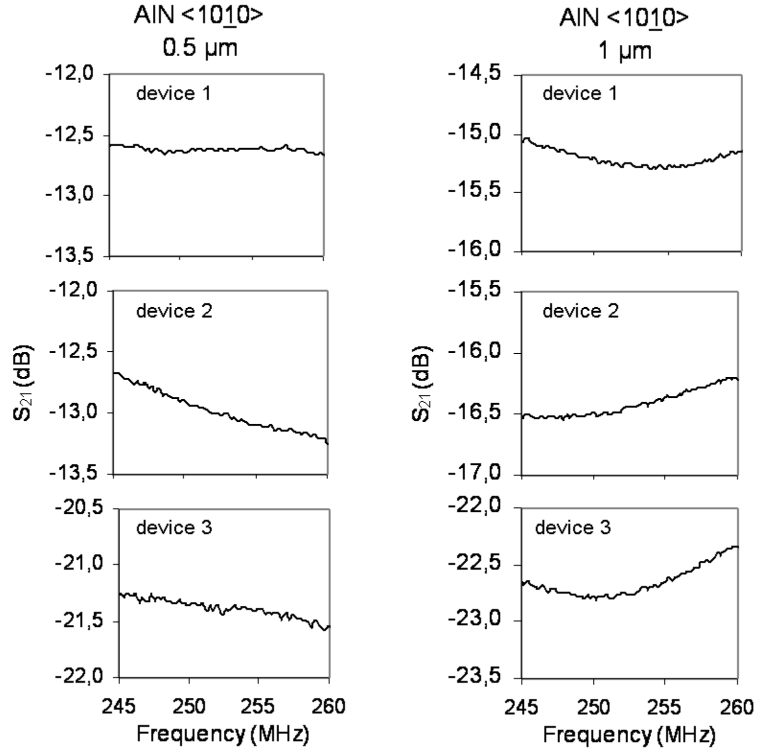

Figure 5.4: Frequency response S_{21} (module) around the expected characteristic frequency for the SAW devices based on <10$\underline{1}$0> oriented AlN films with thicknesses of 0.5 µm and 1 µm deposited at the optimal process conditions.

AlN films with <10$\underline{1}$0> orientation had not shown significant responses by PFM- d_{zz} value of 1.5 ± 0.3 pm/V for 0.5 µm and 0.0 ± 0.2 pm/V for 1 µm- in accordance with the expected absence of response in the PFM essayed configuration (see Appendix B). The strictly null coefficient for the <10$\underline{1}$0> oriented film with 1 µm thickness, could be a consequence of a better crystallized and well texture film for higher thickness in this particular orientation. Independently, the observed absence of response in the essayed SAW configuration could be attributed to several reasons, related with the film microstructure or the geometry of the essayed configuration, and is discussed later in this chapter.

5.1.2 Modeled response

A simple model has been proposed in the past to describe the frequency response of SAW devices (see Appendix A), in which the effect of low resistivity substrates is taken in account. Since our AlN films were deposited on low resistivity silicon substrates, this model has seemed adequate to be applied. The position and general form of the frequency response S_{21} can be predicted, for a given coupling coefficient and acoustic velocity. Parameters of the model to be selected are IDTs geometry, IDTs capacitance [110] and an admittance that takes in account the electromagnetic feed-through effect caused by the low resistivity silicon substrate and other parasitic effects.

The model was fitted to the experimental results obtained for <0001> oriented films, following this procedure:

1- The device geometrical parameters were introduce (M,N,λ) and the capacitance C_t was estimated according to the procedure suggested by the model.

2- The acoustic velocity V was selected in order to fit the position of the piezoelectric response in the frequency domain.

3- An admittance Y_p in parallel with Y_{21} was introduced in order to fit S_{21} module and phase background values next to the typical frequency.

4- The k^2 coefficient was selected in order to fit size and shape of the S_{21} module response.

5- The necessary interactions were done from 1 to 4, to improve the fitting.

Figure 5.5 illustrates the effect of acoustic velocity and electromechanical coupling coefficient on the position, shape and size of the frequency response.

Consequently, it was possible to estimate the acoustic velocity for the different cases, and obtain approximated values of electromechanical coupling coefficients. Since a simplified model was used, approximated fitting of theoretical response to observed response was obtained. Table 5.1 shows the obtained values of V and k^2 for SAW devices constructed with 0.5 µm and 1.0 µm thickness <0001> oriented AlN films.

Using this k^2, some authors [31] have directly estimated d_{31} piezoelectric coefficient for <0001> oriented films from:

$$k_{31}^2 = \frac{d_{31}^2 c_{11}}{\varepsilon_{33}} \tag{5.1}$$

where c_{11} (3.45×10^{11}Pa) is the elastic stiffness constant and ϵ_{33} is the dielectric constant (9.5×10^{-11} F/m). This simplified estimation assumes the electric field perpendicular to the substrate surface, as in the model of the response ("cross field" approach) and the excitation of longitudinal acoustic waves parallel to the surface-the surface acoustic waves-. Table 5.1, shows the obtained estimations for d_{31} coefficients.

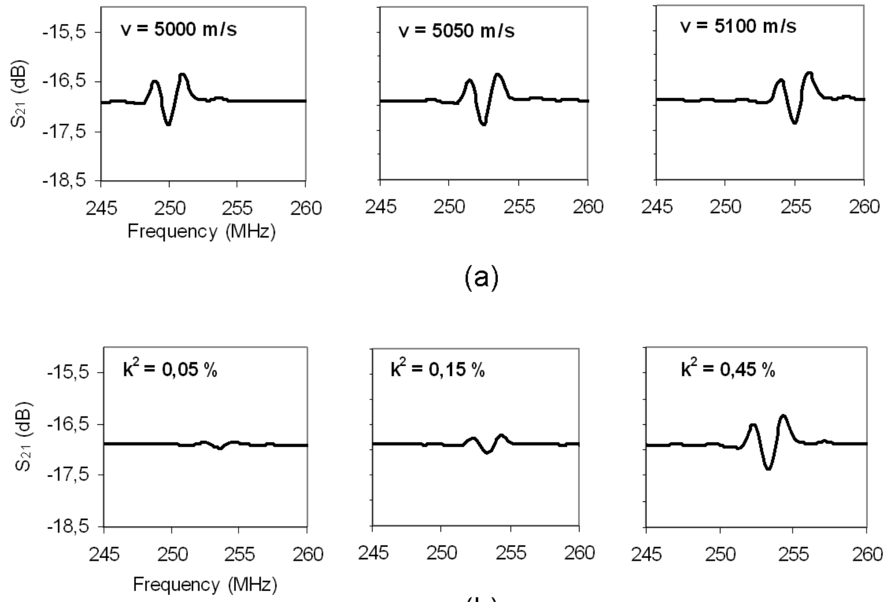

(a)

(b)

Figure 5.5: Prediction of the effect of the acoustic velocity (a) and electromechanical coupling coefficient (b) on the frequency response for the prepared SAW devices around the typical frequency. Parameters: $\lambda = 20$ µm, $C_t = 6.5$ pF, M = 100, N = 100, $Y_p = (0.072 + j\omega\, 4.5 \times 10^{-11})\ \mathrm{Ohm}^{-1}$, $k^2 = 0.45\%$ (a), V = 5,067 m/s (b).

Table 5.1: Estimation of AlN film characteristics based on SAW device frequency responses.

Orientation	Thickness (µm)	SAW velocity (km/s)	k^2 (%)	d_{31} (pm/V)
<0001>	0.5	5.07±0.01	0.2 ± 0.1	0.7 ± 0.2
<0001>	1.0	5.05±0.01	0.4 ± 0.1	1.0 ± 0.2

Values of SAW velocities between 4900 and 5100 m/s have been informed for AlN films on Si substrate [30, 43], and values of d_{31} between 0 and 2.2 pm/V are showed in the bibliography [31].

If S_{21} responses obtained at 0.5 and 1 µm thickness are compared, an increase of losses (reduction of S_{21}) with the increase of thickness can be in general observed (see Fig. 5.3). This fact could be related with the increase of paths and consequent reduction of feed-through effect at higher thicknesses, taking in account the high electrical resistivity of AlN film compared with that of the substrate.

Simultaneously, it is important to note that there is a sensible increase in the estimated electromechanical coupling constant and d_{31} coefficients between 0.5 and 1 µm. This improvement in piezoelectric performance at higher thickness would be in line with the observed improvement of film microstructure (see section 4.2).

5.2 BAW devices

FBAR devices were constructed with <0001> oriented AlN films, 0.5 µm thickness, obtained at the optimal process conditions by the microwave PECVD technique in order to evaluate the piezoelectric performance in this configuration (see section 2.2.4.3).

Since in this case the piezoelectric film had to be placed between two metallic electrodes in “sandwich” configuration, the AlN film was deposited on a <110> oriented Mo film, in accordance with standard X-LIM’s cleanroom procedures. In order to verify the orientation grade of the AlN film on this particular substrate its microstructure was evaluated by XRD. No significant differences were observed between films microstructures developed on <110> oriented Mo and on Si (100) substrate, since rocking curve FWHM value of 12.6º was obtained on Mo. This is an additional fact that confirms the absence of significant epitaxial effects in our PECVD deposition process.

Since FBAR construction process of X-LIM cleanroom had not been completely optimized, a Si layer with thickness of 20 µm rested under the AlN film “sandwich”, with the projected 1 µm SiO_2 layer. Therefore, a frequency response with multiple peaks was expected in the rank of the typical frequency of the projected device [14], in place of the single response obtained in standard FBAR resonators (see Appendix A). Figure 5.6 shows a general view and dimensions of the prepared devices.

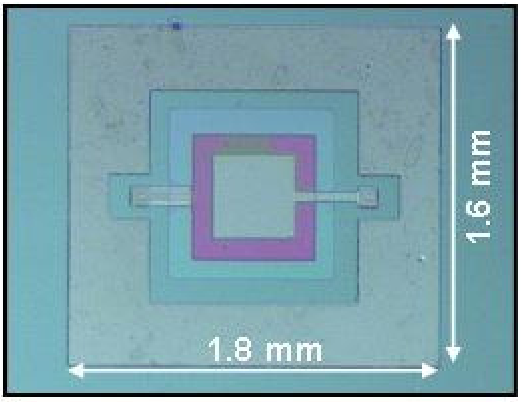

Figure 5.6: General view of a prepared FBAR device.

5.2.1 Frequency response

Figure 5.7 (a) shows the frequency response of the device between 0.5 and 8.5 GHz, where several peaks in the rank of 3 GHz are observed, corresponding to the resonance frequency of the first harmonic- i.e. $\lambda/2$-. A second resonance mode was observed around 9 GHz (see Fig. 5.7 (b)) which confirms the piezoelectric response of the film. As only the odd modes are excited in this type of devices, this second mode corresponds to $3\lambda/2$ [15].

5.2.2 Modeled response

The one-dimensional model developed for BAW free resonators in Appendix 1 shows only an approximated frequency response of FBAR configurations. FBAR devices for high frequencies must be strictly modeled considering not only the piezoelectric film but also the whole geometry of the device, including the electrodes and other layers, since their thicknesses are significant [11, 15]. Since the thickness of the metallic Mo electrodes were 400 nm, the AlN film 500nm, and the SiO_2 layer 300 nm, the half wavelength associated to the total thickness would correspond to approximately 1.6 µm, in a first approach. If the acoustic velocity of bulk acoustic waves in AlN from bibliography is supposed- i.e. 10,400 m/s-, the resonance frequency associated to the first harmonic should be in the rank of 3 GHz. This corresponds to the observed value in the measured device’s frequency response.

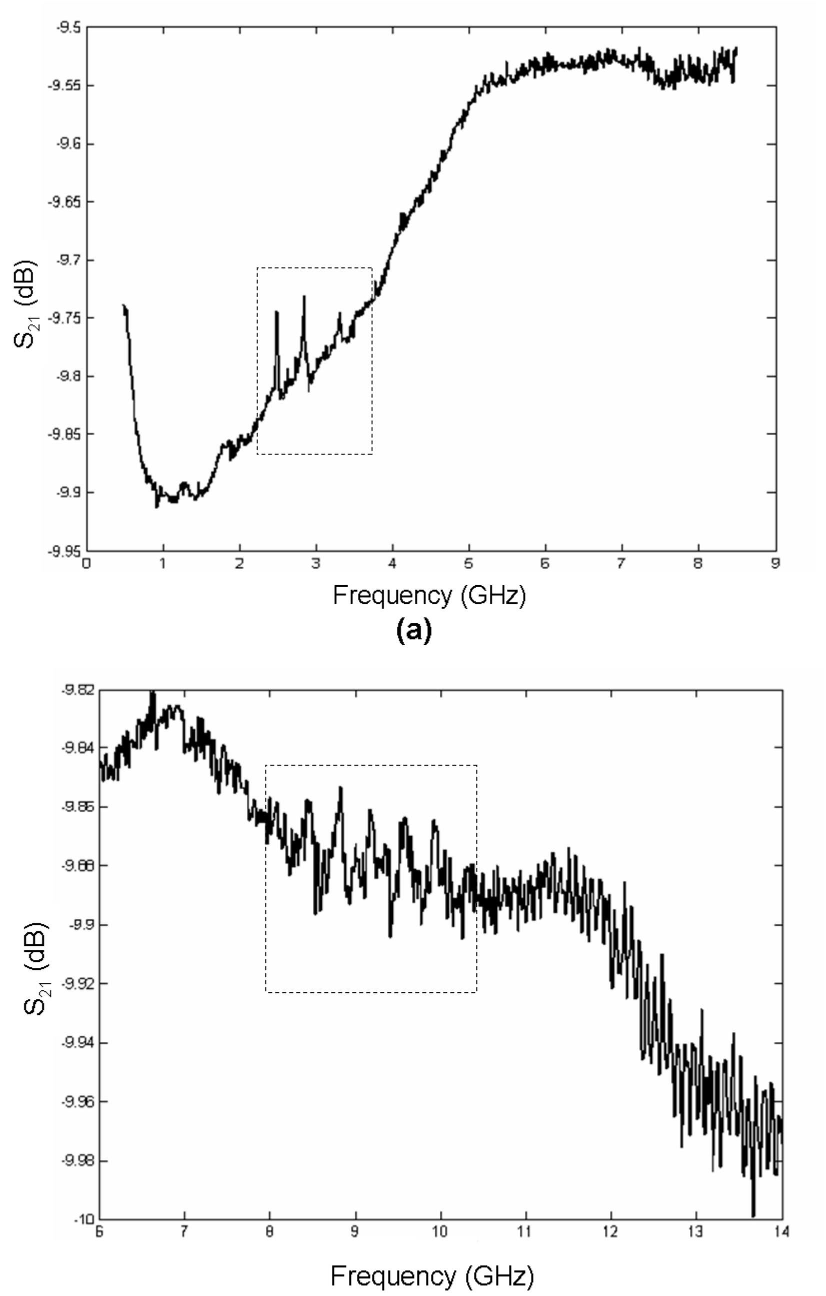

Figure 5.7: Frequency response of the essayed FBAR device based on a <0001> oriented AlN film, with thickness 0.5 µm, deposited by PECVD at the optimal process conditions: (a) between 0.5 and 8.5 GHz, (b) between 6 and 14 GHz.

But the particular case of the constructed FBAR is even more complex due to a Si remnant not etched layer, with thickness around 20µm. This Si layer, with a thickness equal to several times the acoustic wavelength generated, acts as an acoustic cavity.

Consequently, the response approaches to that of a high overtone bulk acoustic resonator (HBAR), at a very high harmonic of its fundamental [8, 14]. The typical response of this configuration consists of a series of resonances and anti-resonances with frequency separation inversely proportional to the cavity length d_c, as given by the Fabry-Perot formula [14] $\Delta f = V_a / (2(d+d_c))$, V_a being the acoustic velocity in the material and d the thickness of the piezoelectric film. The obtained response with multiple peaks is then in accordance with these considerations.

As a consequence of the complexities previously indicated, as well as the fact that the design and manufacture process of this device was not completely optimized, the electromechanical coupling coefficients were not estimated for this configuration.

5.3 Discussion

<0001> oriented AlN films obtained at optimal process conditions have shown piezoelectric response both in SAW configurations as well as in prototype BAW configurations. However, for the case of <10$\underline{1}$0> oriented AlN films no piezoelectric response was observed in SAW configurations. This fact seems inconsistent, in a first approach, with several references which establish that there should be a better performance for this orientation (see section 1.2.1). Instead of that, no results have been published referred to the measurements of performance of <10$\underline{1}$0> oriented films in SAW devices. Some authors have indicated that appropriated <10$\underline{1}$0> oriented films are difficult to be produced and that these films have been used for SAW devices with characteristic frequencies of some GHz [32]. Thus, it seems necessary to analyze the facts further, in order to understand the behavior observed.

First, several reasons associated to microstructure and composition of the obtained <10$\underline{1}$0> oriented films can be proposed in order to explain the absence of piezoelectric response in the SAW configurations. As it was previously shown, <10$\underline{1}$0> oriented films showed lower crystalline development as well as higher impurities concentration than <0001> oriented films. These facts should favor a lower piezoelectric performance of the obtained films. However, there is another possible reason associated with microstructure. In the same way that domain inversion has been observed for <0001> films and associated to reduction in piezoelectric performance (see section 1.2.1), this type of effect could happen in

<10$\underline{1}$0> oriented films. Moreover, while in the case of a perfectly <0001> oriented film there is only one direction where the domain inversion can take place – i.e. the direction perpendicular to the substrate-, in the case of <10$\underline{1}$0> oriented films, there could be domains with infinite possible directions parallel to the substrate surface. If the domains distribution were perfectly random in the plane, a net domain inversion could take place (see Fig. 5.8), which could reduce or eliminate the piezoelectric response.

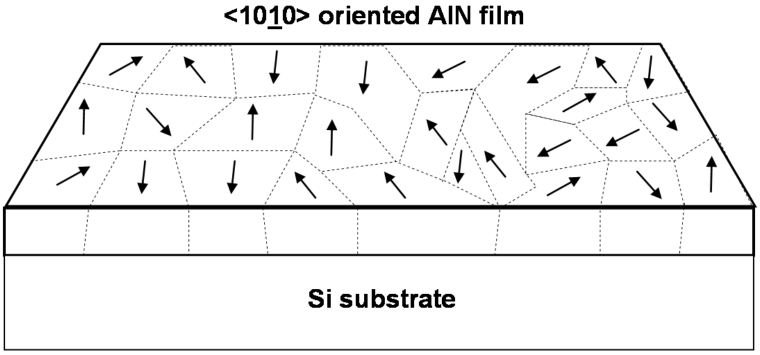

Figure 5.8: Hypothetical net domain inversion in the case of <10$\underline{1}$0> oriented AlN film.

Second, some reasons associated with the particular essayed SAW configurations could be indicated. If the geometry of these configurations is taken in account, the electric field distribution under the electrodes, in the AlN film, is possible to be predicted. Appendix B presents the model used to estimate this distribution for different geometries. In the case of the essayed configuration geometry, dominates the electric field E component perpendicular to film surface under the electrodes (see Fig. 5.9 (a)). This fact derives from the low resistivity of Si substrate and the distance between the electrodes to AlN film thickness rate. As a first approach, it is clear to visualize that if the distance between the electrodes is significantly higher than twice the film thickness, the lower electric impedance is through the low resistivity Si substrate. Consequently, the electric field in the AlN film is perpendicular to the surface. On the other side, if a device geometry with distance between electrodes to AlN film thickness rate significantly lower is supposed (see Fig. 5.9 (b)), the electric field distribution in the film is concentrated between the electrodes, near the surface.

Thus, there is a higher contribution of the electric field E component parallel to the surface. This hypothetical situation corresponds to thicker AlN films with the same IDTs geometry - and consequently the same typical frequency -, or to smaller IDTs- and consequently higher typical frequency-, if the film thickness is maintained. It should be also noted that, if the AlN film is deposited on a non conductive substrate or non conductive thick film, the second situation is applicable. Obviously, it is applicable as well, if AlN single crystal substrates instead of films are used.

When the piezoelectric response of an AlN crystal under the presence of an electric field is analyzed (see Appendix I) higher piezoelectric coupling is obtained once the E field is applied in the c-axis direction, corresponding to the d_{33} coefficient. Thus, in order to generate surface acoustic waves through the piezoelectric effect in a <10$\underline{1}$0> oriented AlN film, i.e. with the c-axis parallel to the surface, the presence of E field component parallel to the surface in the piezoelectric film is relevant to obtain an adequate response. Consequently, the essayed configuration, that corresponds to the case shows in Fig. 5.9 (a), does not favor the optimal piezoelectric coupling of the AlN <10$\underline{1}$0> oriented films.

Finally, as we have observed for the piezoelectric response of <0001> aluminum nitride SAW devices, the effect of working with a low resistivity Si substrate produced an important feedthrough effect, reducing the relative size of the response around the characteristic frequency (Appendix A). If the response in this case were low, associated with the previously indicated reasons, it would become probably undetectable due to this particular effect.

The construction of a SAW device that could eliminate the discussed effects and show the piezoelectric performance of the deposited <10$\underline{1}$0> films is out of the objectives of the present work. Nevertheless, it is interesting to discuss which would be the different options to conduct the work. First it is possible to think in smaller IDTs, that means higher frequencies. If film thickness of 1 µm is maintained, distances between fingers lower than 1 µm should be considered, that means fingers of around 0.5 µm wide. They are possible to be constructed, but require more sophisticated processes, being in the limit of the traditional microtechnology. In order not to reduce so much the electrodes size, the AlN film thickness could be increased. As was demonstrated for <0001> oriented films, it would be possible to arrive to appropriated thicker films, - i.e. 3 µm or more-, acting on the RF-bias potential during the deposition process if necessary. Last of all, other possibility to favor the piezoelectric evaluation of <10$\underline{1}$0> oriented films would be the deposition on a non conductive substrate.

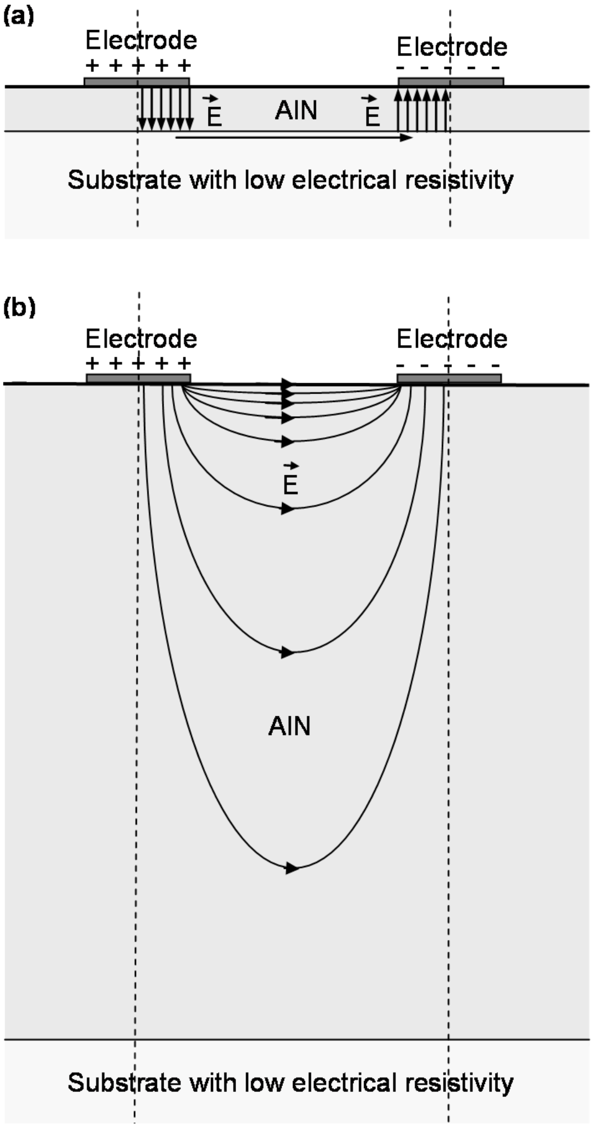

Figure 5.9: Schematic representation of the electric field under two adjacent fingers of interdigital electrode of a SAW device, supposing the AlN film deposited on a substrate with low resistivity: (a) AlN film thickness substantially lower than the distance between the electrodes, (b) AlN film thickness substantially higher than the distance between electrodes.

Chapter 6

COMPARISON WITH A PVD TECHNIQUE

The previous chapters have shown the optimal process conditions to obtain piezoelectric AlN films using a microwave PECVD technique. Also, the piezoelectric performance of the obtained films in electro-acoustic applications, as SAW and BAW, was verified. Since PVD sputtering has been the most investigated technique in the past, a comparison of the films obtained by this process and the PECVD process has seemed interesting to be conducted. In order to make this comparison, AlN thin films prepared at the “Institut des Materiaux de Nantes”, using a PVD reactive sputtering technique, were chosen.

6.1 PVD sputtering

<0001> oriented films were first obtained using a PVD sputtering reactor equipped with a magnetron cathode and a DC generator. The standard process conditions essayed where the following: $P_{N2} / (P_{Ar} + P_{N2}) = 0.3$, distance substrate-target = 3 cm, total pressure of 0.4 Pa, temperature < 200℃ and deposition rate = 35 nm/min. The obtained films showed orientation grades quantified by the rocking curve FWHM in the rank of 7°. The evaluation of microstructure of film profiles by HRTEM and SAED showed columnar shapes and the improvement of the crystalline quality with film thickness. After a 5 nm amorphous interface, the microstructure changed from misalignment angle of 23° to 6° in 1.5 µm thickness for the (0002) reflection. The measured oxygen concentration in the films was 5.2 % [111].

All these observations indicate that films obtained under these conditions by PVD sputtering have not shown important differences with PECVD films, in relation with their properties for piezoelectric applications. Moreover, a stricter comparison of the evolution of crystalline quality and orientation grade in film profiles by SAED, indicated a better quality of PECVD films (see section 4.2.1).

When the deposition conditions of both processes are compared, an important difference of substrate temperatures is observed. While for PECVD process, substrate temperatures over 600℃ - i.e. real temperature over 500℃ -, were employed in order to obtain <0001> oriented AlN films, in the case of PVD process the films were obtained at temperatures under 200℃. It is possible to speculate that different factors favor diffusion effects and consequently crystalline development in each deposition technique: high substrate temperature in the PECVD process and high kinetic energies of sputtered species reaching the film surface in PVD process [74, 112]. Consequently, adequate crystalline development would be possible to be obtained by PVD technique at lower substrate temperatures.

Simultaneously, the change of preferential orientation from <0001> to <10$\underline{1}$0>, by increasing the total pressure from 0.4 Pa to 0.8 Pa, was observed for the PVD depositions technique. This similitude between both techniques confirms the importance of the effect of the mean free path in the control of film orientations, independently of the deposition process (see section 3.4).

The use of increasing bias potentials of substrate holder in the PVD process, going from 0 to -200V have shown a reduction in the film crystalline development, and at a certain level (-150 V), the change in the preferential orientations to <10$\underline{1}$0> [74]. This is another important similitude in the observed behavior of both techniques. Nevertheless, the bias value for orientation change in the case of the PECVD technique was significantly lower (-20 V) (see section 4.3).

Since AlN films contamination with oxygen had been previously related with their microstructures and piezoelectric performances [19, 37], the PVD process previously described was improved in order to reduce this contamination. With the purpose of arriving to this objective, two important changes were made: a) the vacuum system was improved to arrive to lower residual pressures (10^{-4} Pa), and consequently lower oxygen concentration in the reactor chamber before the deposition process, b) the deposition rate was increased by rising the power applied to the target (70 nm/min),

c) the ion to neutral species rate in the reaction medium was increased significantly as a consequence of the increase of the magnetic field of the magnetron [111].

These changes introduced in the PVD technique allowed obtaining film orientation grades corresponding to rocking curve FWHM in the rank of 2°, and at the same time allowed to reduce the oxygen content to 0.4%. The evaluation of film microstructure by HRTEM showed a dense columnar structure. The SAED confirmed the significant improvement in the texture showing single crystal patterns in all the film profile [111]. These significant differences, which should be related with an increase in the piezoelectric performance, were associated to reduction of the oxygen content. Furthermore, these PVD films showed roughness values (S_a) lower than 1 nm and compressive residual stresses- e.g.: -1 GPa for 0.5 µm thickness.

6.2 Piezoelectric performance

In order to evaluate the piezoelectric performance of the films obtained by the PVD technique in electroacoustic devices, and at the same time to compare them with the films obtained by the PECVD technique, BAW devices were prepared as was previously described (see section 2.2.4.3). Figure 6.1 shows the XRD patterns of 0.5 µm AlN films deposited on <110> oriented Mo film for the construction of these BAW devices.

The XRD patterns of both films showed exclusive <0001> orientation, but a higher intensity of the (0002) reflection peak was observed for the PVD film. This fact could be related with a higher crystalline development of the PVD films. At the same time the evaluation of the orientation grade by rocking curve showed a FWHM significantly lower for the PVD film, in the rank of 4.5°, indicative of a better texture development.

The evaluations of the frequency response of BAW devices prepared with the PVD film showed a first resonance mode in the rank of 3 GHz, and the second resonance mode in the rank of 9 GHz (see Fig. 6.2). These were the expected frequencies as a function of the geometry and properties of the materials, and they were similar to the case of the PECVD films (see Fig. 5.7). Taking in account the consideration done for the construction of the BAW devices with PECVD films (see section 5.2), multiple peaks were expected.

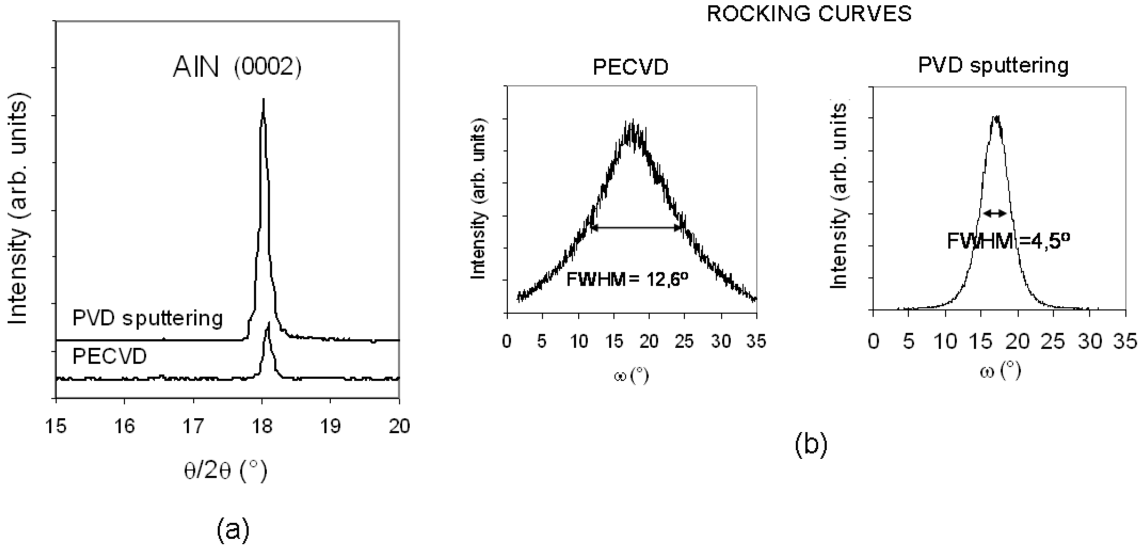

Figure 6.1: XRD patterns and rocking curves for 0.5 µm thickness films deposited on <110> oriented Mo films by PECVD at the optimal process conditions and PVD sputtering in order to construct the FBAR devices.

When the frequency responses for both types of films are compared the resonances are obtained at similar frequencies, and in accordance with the expected values. These facts suggest that bulk acoustic velocities are comparable for both film and in the rank of the expected bibliographic value- i.e. 10,400 m/s -.

Simultaneously, FBAR based on PVD films showed a marked and more intense response, being an indicative of a better performance. This fact could be assigned unless in part to piezoelectric coupling since significant differences of orientation grade, i.e. rocking curve FWHM-, were previously observed. Nevertheless, this PECVD film had shown optimal piezoelectric coefficient d_{33} using the PFM technique (see section 4.2.2). Then, additional variables could have distorted the overall performance of the prepared FBAR, related not only with the piezoelectric coefficient but also with the geometrical definition and acoustic losses of the prototype device. Film roughness, thickness homogeneity and chemical etching during the FBAR preparation are relevant variables which could be optimized for PECVD films. While PECVD film roughness was in the rank of 7 nm, PVD film roughness was lower than 1 nm.

Then, AlN films with 0.5 µm thickness prepared on Mo film by the PVD process allowed to obtain FBAR devices with better performance, compared with the PECVD process. If these differences are consequence of differences in piezoelectric coupling, the origin of the behavior could be in film microstructure and orientation grade, and particularly the oxygen content, as was evidenced in the optimizations of the PVD process.

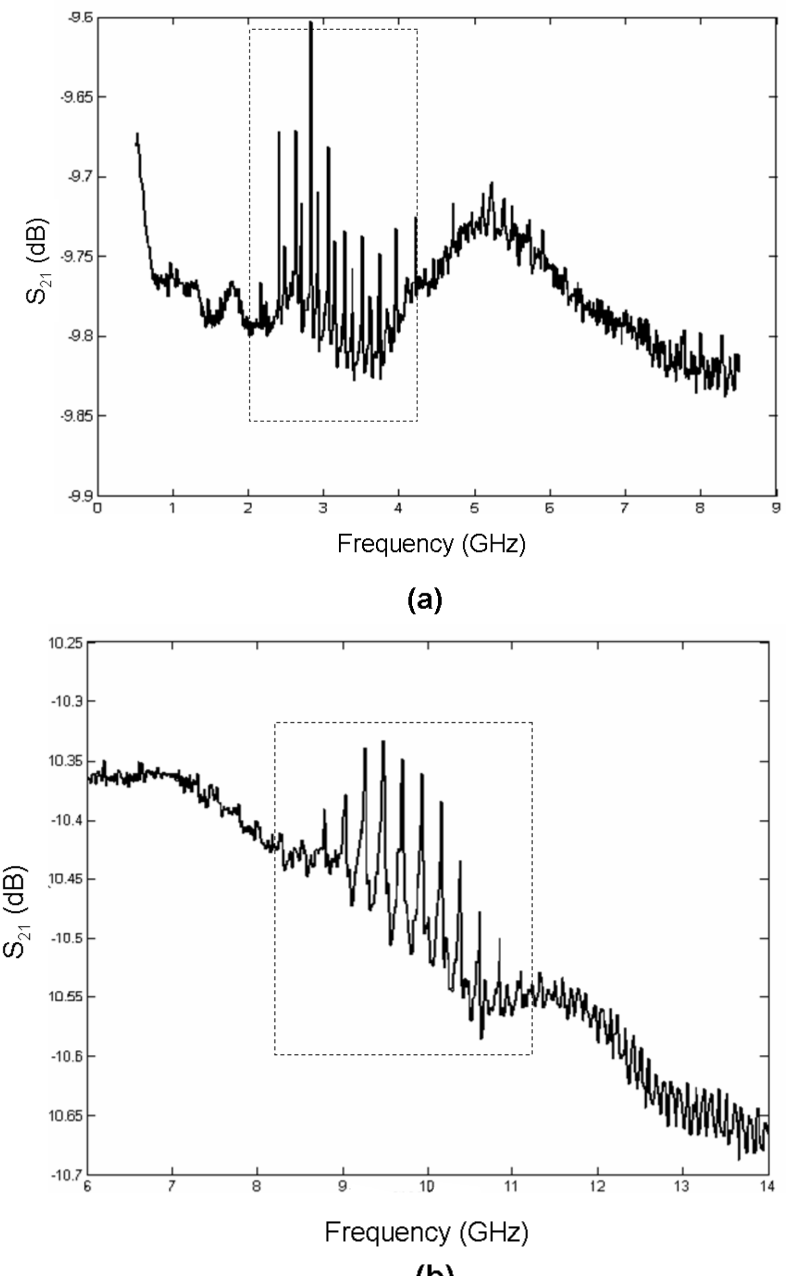

(a)

(b)

Figure 6.2: Frequency response of the essayed FBAR device based on <0001> oriented AlN films, with thickness of 0.5 µm, deposited by PVD sputtering at the optimal conditions.

6.3 Discussion

The PECVD technique has allowed to obtain polycrystalline AlN films, as well as to control their preferential orientation. The substrate temperature has been a relevant variable to improve the crystalline development of the films as well as to allow the development of texture and piezoelectric response, particularly for <0001> oriented AlN film at low pressures.

The PVD sputtering technique has allowed obtaining similar results in film microstructure at lower substrate temperatures, under standard conditions. The optimization of this process conducted to significant improvement of obtained films.

The evaluation of FBAR devices constructed with 0.5µm films obtained using both techniques have shown BAW velocities in the same rank and a more consistent piezoelectric response for PVD films. This difference can be related, among other reasons, with observed differences in the microstructure, evidenced by the XRD patterns and rocking curves as well as the oxygen content in both cases.

It has been speculated in this work that the high kinetic energy of the sputtered species in the PVD technique provided the necessary energy to allow the diffusion in the surface during deposition and the crystallization of the film. Simultaneously, this kinetic energy could explain the compressive stresses and low roughness observed in these films, if the effects proposed in Davis theory for ion bombardment (see section 1.4.2) are applied for neutral species bombardment in this case.

Conversely, in PECVD technique, the increase of substrate temperature was necessary to favor the diffusional effects, as a consequence of the low kinetic energy of the species reaching the substrate. Moreover, in the PECVD process an additional variable is present: the aluminum precursor, and its by-products. Although the high reactivity of this precursor is favorable, the elimination of the derived by-products is an additional step to consider. In this case the desorption of these by-products from the surface of the growing film is needed, and the temperature plays an important role in this sense, as was evidenced through the experimental work.

It is possible to speculate at this point about the reason why the application of RF bias potential was not favorable for crystalline development in the PECVD process, since species with high kinetic energy reach the surface in this condition, reproducing, in certain way, the dominant effect of the PVD process. The answer to this question would be not only in the different energies of species but also in the type of species considered for each case. While in the PVD process Al species sputtered from an Al target reach the substrate, in the case of the PECVD process with RF bias, the bombardment of the surface by all the ionic species present in the plasma is produced- e.g.: Ar^+, N_2^+, Al^+. This phenomenon favors the incorporation of impurities to the film (see section 3.2) at the time it prevents the adequate film crystallization- e.g.: possible presence of $Al\text{-}N_2$ in the film. The lost of crystalline development with the progressive polarization of the substrate holder in the PVD process is an additional evidence in this sense. The ionic species derived from the plasma associated to the polarization of the substrate holder had an adverse effect in this case process too.

Then, in the PVD process, where the contribution of precursor by-products is not present, rest as relevant the oxygen contamination. It is well known the fact that aluminum nitride oxidizes spontaneously in the presence of oxygen, causing the oxidation of films surface after deposition. Thus, the presence of low levels of oxygen in the reactor can contribute to the incorporation of this oxygen to the film during the deposition process, as aluminum oxide.

The optimization of the PVD films microstructure was accompanied by a substantial reduction of oxygen concentration in the films, with values significantly lower than that obtained for PECVD films. Then, taking in account the similarities and differences observed between both techniques, it could be proposed that one way to improve the microstructure and performance of the PECVD films would be to modify the process in order to reduce the oxygen contamination. Taking into account this idea, some observations are discussed in the following.

The concentration levels of oxygen species in the PECVD reactor chamber during the deposition process were as low as it was not possible to detect the corresponding emission peaks in the OES characterization of the plasma (see section 4.6.3). Thus, this fact confirms that a very low concentration of oxygen could conduct to a significant oxygen contamination of the film.

The increase of pressure in the PECVD reactor chamber, favored less crystallized films, with change in the preferential orientation and higher oxygen contamination (see section 4.5). This was attained maintaining the inlet flows, and reducing the velocity of the turbo-molecular vacuum pump. Thus, it would be possible to speculate that a higher residual concentration of oxygen or the reduction of the mean free path of the species are reasons for the obtained result. But the comparison is complex since additionally, a reduction of the electronic temperature of the plasma was observed. The electronic temperature of the plasma as well as the concentration of free electrons, ionized species, and activated species derived from the inelastic collisions, should be a relevant variable for the crystallization of the film. These effects were shown with the improvement of crystalline structure of the films at lower plasma-injector distance, at the beginning of the experimental work.

The increase of the substrate temperature in the PECVD process allowed reducing the concentration of impurities associated to precursor by-products in the film, but no evidence was shown for the evolution of oxygen contamination.

Consequently, a possible way to reduce the oxygen contamination in the PECVD process would be to decrease the residual pressure in the reactor chamber before the deposition and, in the same line, to make a stricter desorption of gases from the chamber walls. The experimental work in the PECVD reactor was conducted opening the reactor chamber before each run in order to introduce the sample. This operation can favor not only the absorption of oxygen in the walls chamber but also the oxidation of the deposited aluminum nitride or precursor by-products deposited on these walls. The residual total pressure was reduced to less than 5×10^{-3} Pa each time before each run, favoring the desorption of the adsorbed gases. However, the reactor configuration could be improved in order to reduce the oxygen contamination. The addition of a pre-chamber, in order to introduce the samples and avoid breaking the vacuum of the reactor chamber each run, could be an option in this sense.

In order to find other origins of oxygen contaminations in the reactor chamber it could be speculated with the presence of the quartz tube (SiO_2) at the top of the reactor, which allows obtaining the coupling between the microwaves and the plasma. This fact should not be discarded.

Nevertheless, all the modifications of the reactor configuration that could be considered to improve its performance should take in account its long term perspectives.

CONCLUSIONS

Polycrystalline and preferentially oriented AlN films have been obtained using a MW-PECVD technique. By appropriate selection of process parameters, it has been possible to produce <0001> or <10$\underline{1}$0> oriented films, both of interest for piezoelectric applications.

The reduction of the distance between plasma and precursor injector, by changing the reactor standard configuration, improved film crystalline development.

The increase of substrate temperature was determinant to improve film crystalline development and to reduce their impurity contents.

While no epitaxial effects were observed working with different substrates, film profile analysis has evidenced an improvement of crystalline development with thickness.

Controlling preferential orientations was possible by the selection of working pressure being <0001> at low pressures and <10$\underline{1}$0> at high pressures.

When high RF-bias potentials were applied amorphous films with high compressive residual stresses were produced. While all the films obtained with floating potential had shown tensile residual stresses, the use of low RF-bias potentials allowed a reduction of such tensile stresses and higher thickness film production, while maintaining the desired microstructure.

Then, strong evidence was obtained about the general mechanisms that control the crystalline development and preferential orientation in this MW-PECVD technique.

Crystalline development was favored by increasing the concentrations of more energetic and consequently active species present near the substrate. This increase was reached by the reduction of the plasma-injector distance.

Increasing the substrate temperature during film growth improved the diffusional effects of the species after reaching the surface. The desorption of impurities associated to the Al-precursor decomposition was also improved. Furthermore, <0001> orientation of film at low pressures was privileged by temperature increase because this orientation is thermodynamically more favorable to minimize surface energy.

At the beginning of film deposition there was no evidence of substrate epitaxial effects and growth occurred randomly, then preferential orientation improved progressively as film thickness also increased. This improvement was evidently favored at higher temperatures.

Increasing pressure allowed better development of <10$\underline{1}$0> orientation associated with the reduction of the mean free path of the reactor chamber species. Al-N dimmers formation has been considered as the most adequate mechanism to explain this phenomenon, in relation with kinetic effects of species deposition. Although Al-N dimmers were not detected by the analysis techniques used, their presence in the reaction media should not be neglected.

While <0001> exclusive orientation was developed only at low pressures and high temperatures, <10$\underline{1}$0> exclusive orientation was developed at high pressure at all temperatures. This is an evidence of the different types of mechanisms that control both phenomena. Moreover, the theory of Al-N dimmers formation is reinforced by the observation that <10$\underline{1}$0> orientation is reached at all temperatures for high pressures. This finding discards other earlier proposed mechanisms.

Film residual stresses have been explained by the contribution of thermal stresses associated with the deposition temperature and intrinsic stresses derived from the growing process. Some theories proposed in the past for the development of tensile and compressive stresses have been applied to explain film intrinsic stresses, giving additional elements about growth mechanism in each case.

The effect of the use of low RF-bias has meant a possibility to control film residual stresses, and such research has also evidenced another mechanism to control film preferential orientation. High compressive stress development has favored the change from <0001> to <10$\underline{1}$0> orientation, because this change allowed relaxing the structure. Although this phenomenon occurred in conditions of low crystalline development –which, in principle, does not apply to this research– it is an option to be studied further for this or other applications.

When the PECVD technique results were compared with those of a PVD sputtering technique, some coincidences were observed. Coincidences were related to the general effects of process parameters, such as pressure and bias potential. These facts showed that there may be some similarities between growth mechanisms in both techniques. But simultaneously there are some substantial differences that were evidenced by substrate temperatures needed in both cases. In PVD sputtering processes there is a substantial contribution of kinetic energy of species sputtered from the target that reach the substrate and favor the diffusional effects. This contribution may substitute the temperature needed in PECVD processes, and allow for lower temperatures in PVD processes. In the case of the PVD sputtering technique, plasma conditions must be adequately optimized in order to produce active species. However, in the PECVD process both the high reactivity of the Al precursor and the excitation from plasma contribute to create active species. In spite of these facts, a disadvantage of PECVD processes involves precursor by-products which can be included in the film and consequently need to be desorbed during film growth. Furthermore, oxygen is an important impurity present in both processes that must be minimized.

The <0001> oriented films obtained by MW-PECVD in optimal conditions showed marked columnar structure with grain sizes in the rank of 40 nm, minimal rocking curve FWHM of 8º, roughness lower than 20 nm and tensile residual stresses lower than 1 GPa. These films were characterized in their piezoelectric performance by a method based on the inverse effect – i.e. PFM-, as well as by the construction of SAW and BAW devices. The results showed significant piezoelectric responses in all cases, with optimal values of d_{33} piezoelectric coefficients, – e.g. 5.8 ± 1.2 pm/V -, evaluated by PFM, and acoustic wave velocities, – e.g. 5.05 ± 0.01 km/s -, for surface acoustic waves. These observed performances are indicative of the absence of significant concentrations of inversion domains in the microstructure of these films. The evaluation of the effect of different parameters on piezoelectric coefficient, as substrate temperature, film thickness and RF-bias potential confirmed the importance of crystalline development and orientation grade on film piezoelectric performance. Through the construction of SAW devices, it was also possible to determine a correlation between thickness and piezoelectric performance at the optimal process temperature. The minimization of residual stresses with the application of low RF bias showed the possibility of obtaining higher thicknesses with appropriate microstructure and optimal piezoelectric coefficients. Microstructure differences, orientation grade and oxygen impurity were directly related with piezoelectric performance when films obtained by PECVD and PVD sputtering technique were compared.

The <10$\underline{1}$0> oriented films obtained by MW-PECVD in optimal conditions did not show a marked columnar structure, but the following features: grain sizes in the rank of 20 nm, minimal rocking curve FWHM of 11º and roughness lower than 10 nm. These films did not show significant piezoelectric response under the essayed configurations either. This was the expected result for the PFM method, in accordance with the piezoelectric tensor of aluminum nitride wurtzite-type crystalline structure. The absence of response obtained in the essayed standard SAW configuration, does not discard an adequate performance with other dimensions of the device. An electric field under the electrodes of the SAW configurations was modeled in order to demonstrate that this films could show response with another geometries, more complex but possible to construct. If this were not the case and these films do not have an adequate piezoelectric performance, the reason should be found in the lower crystalline development or in the occurrence of inversion domains in the surface plane. All of these statements may be the reason why there has not been research works published with evaluations about the performance of <10$\underline{1}$0> oriented films on SAW. Nevertheless, this orientation is considered optimal for SAW by many authors.

Process plasma diagnosis by OES has identified several species present in the reaction media such as Al, Al+, N_2, N_2+, N, which are directly related to film growth. Simultaneously, other species corresponding to precursor by-products as CN, NH, H have also been identified. These results are consistent with the observed impurity band in PECVD AlN films by FTIR in the rank of 2150 cm^{-1}, which has been assigned to CN , Al-H or Al-N_2 species, among other possibilities. Additionally, an evaluation of the favorable effect of microwave power on the generation of active species has been possible, as well as an explanation of the negative effect of hydrogen addition in this sense. Furthermore, lower electronic temperature and lower concentrations of atomic active species were estimated at higher pressures, which could be related to the lower crystalline development observed in <10$\underline{1}$0> oriented films. At the same time, a reduction of electronic temperature with the increase of distance to the plasma was confirmed.

Future Work

As a result the present work, some open issues are left that concern mainly the process plasma, the AlN film properties and the PECVD reactor configuration.

Additional evidences of the mechanisms of film growth and preferential orientation can be obtained through process plasma diagnosis by other techniques, as mass spectroscopy.

A better knowledge of the <10$\underline{1}$0> film microstructure in order to evaluate the possible presence of inversion domains can be attained by other characterization techniques, as the determination of in-plane orientation by XRD.

A better evaluation of the PECVD AlN films for SAW devices can be done with the construction of other geometries and substrates, mainly for the case of <10$\underline{1}$0> oriented films. A finer evaluation of <0001> oriented films in BAW devices is possible with the construction of optimized configurations.

The evaluation of the piezoelectric performance of the films would be completed by the use of a technique based on the direct effect.

Several modifications can be proposed for the configuration of the reactor in order to improve the quality of the obtained films. The protection of the sample before and after the deposition process to avoid the surface contamination could be achieved by the construction of a metal box. Other modifications, associated with the reduction of the oxygen contamination, would go from the improvement of the vacuum system, to the construction of a pre-chamber in order to maintain the reactor under vacuum all the time. The possibility of oxygen contamination coming from the quartz tube could be evaluated through the effect of microwave power applied.

References

1. ROYER D., DIEULESAINT E., *Elastic waves in solids: I and II.* First ed. Berlin: Springer, 1996, p.69-303 (I), p.5-46 (II).

2. JAFFE B., COOK W. R., JAFFE H., *Piezoelectric ceramics.* First edition. London: Academic Press, 1971, p. 1-47, 271-301.

3. IKEDA T., *Fundamentals of piezoelectricity.* First ed. Oxford: Oxford University Press, 1996, 263 p., p. 56-82.

4. BU G., CIPLYS D., SHUR M., Electromechanical coupling coefficient for surface acoustic waves in single-crystal bulk aluminum nitride. *Appl. Phys. Lett.*, 2004, 84, p. 4611-4613.

5. CIPLYS D., RIMEIKA R., Measurements of electromechanical coupling coefficient for surface acoustic waves in proton-exchanged lithium niobiate. ISSN 1392-2114, Ultragarsas, 1999, 3(33), p. 14-20.

6. SOLYMAR L., WALSH D., *Lectures on the electrical properties of materials.* Fourth editions. New York: Oxford University Press, 1990, p. 262 - 291.

7. POLLA D.L., Integrated ferroelectric microelectromechanical systems, *Science and technology of electroceramic thin films /* ed. by O. Auciello, R. Waser, Kluwer. London: Academics Publishers, 1995, p. 413-426.

8. ENGELMARK F., *AlN and high-k thin films for IC and electroacoustic Appliccations*, Thesis: Solid State Electronics : Uppsala : 2002; 757 , 80 p.

9. FUENTES IRIARTE G.. *AlN thin film electroacoustic devices*. Thesis: Solid State Electronics : Uppsala : 2003; 817, 67 p.

10. DUBOIS M.-A., *Thin film bulk acoustic wave resonators: a technology overview*, MEMSWAVE-03, Toulouse, France, July, 2003.

11. SOUTHIN J. E. A., WHATMORE R. W., Finite element modeling of nanostructured piezoelectric resonators. *IEEE Transactions on Ultrasonics, Ferroelectrics, and Frequency Control*, 2004, 51, p. 654-662.

12. WHITE R.M., VOLTMER F.W., Direct piezoelectric coupling to surface elastic waves. *Appl. Phys. Lett.*, 1965, 7, p. 314-316.

13. PALACIOS T., CALLE F., MONROY E., GRAJAL J., EICKHOFF M., AMBACHER O., PRIETO C., Nanotechnology for SAW devices on AlN epilayers. *Mater. Sci. Eng., B*, 2002, 93, p. 154-158.

14. ROSENBAUM J. F., *Bulk acoustic wave theory and devices.* First ed. London : Artech House, 1988, 462 p., p. 435-447.

15. GABORIAUD E., *Etude des resonateurs piézoélectriques dans le domaine des microondes: applications au filtrage*, Thesis: Electronic of high frequencies and optoelectronic : 2004 : Limoges, 181 p. , p. 142-157.

16. TANAKA T., SHIBATA K., TAKEUCHI K., SAKATA M., OKANO H., KUROKI K., *Surface acoustic wave device*, U.S. Patent 5059847, 22 Oct. 1991.

17. MORTET V., NESLADEK M., D'HAEN J., VANHOYLAND G., ELMAZRIA O., ASSOUAR M., ALNOT P., D'OLIESLAEGER M., Deposition of aluminium nitride film by magnetron sputtering for diamond-based surface acoustic wave applications. *Phys. Status Solidi A*, 2002, 193, p. 482-488.

18. MORTET V., ELMAZRIA O., NESLÁDEK M., ELHAKIKI M., VANHOYLAND G., D'HAEN J., DÓLIESLAEGER M., ALNOT P., Structural characterizations of AlN/diamond structures used for surface acoustic wave device applications. *Phys. Status Solidi A,* 2003, 199, p. 145-150.

19. CRACIUN F., VERARDI P., DINESCU M., Piezoelectric thin films: processing and properties, *Handbook of thin film materials, Vol. 3: Ferroelectric and dielectric thin films /* edited by H. S. Nalwa. First ed. New York : Academic Press, 2002, p. 231-307.

20. FELDMANN M., HENAFF J., *Traitement du signal par ondes élastiques de surface.* First ed . Paris : Masson, 1986, 399 p., p.307.

21. BOESHORE S. E., *Aluminum nitride thin films on titanium: piezoelectric transductions on metal sustrate*, Thesis: Materials: Santa Barbara, California : 2006, 166 p., p. 7-32.

22. KAMIYA T., Calculation of crystal structures, dielectric constants and piezoelectric properties of wurtzite-type crystals using ab-initio periodic Hartree-Fock method*, Jpn. J. Appl. Phys.*, 1996, 35, p. 4421-4426.

23. AHN B.-Y., KIM N.- K., Perovskite phase developments and dielectric characteristics in barium-substituted lead zinc tantalate system. *Mater. Res. Bull.,* 2000, 35, p. 1677-1687.

24. DUBOIS M.A., MURALT P., Properties of aluminum nitride thin films for piezoelectric transducers and microwave filter applications. *Appl. Phys. Lett.*, 1999, 74, p. 3032-3034.

25. BENESOVSKY F., KIEFFER R., ETTMAYER P., Nitrides, *Kirk - Othmer Encyclopedia of chemical technology, Vol. 15. /* edited by M. Grayson, D. Eckroth. Third edition. New York: John Wiley & Sons, 1984, p. 871-887.

26. MARCHANT D.D., NEMECEK T. E., Aluminum nitride: preparation, processing and properties, *Advanced Ceramics: International Symp. on Ceramic Substrates, Packages, Electron. Applied*, American Ceramic Society,1989, 26, p. 19-54.

27. RODRÍGUEZ-CLEMENTE R., ASPAR B., AZEMA N., ARMAS B., COMBESCURE C., DURAND J., FIGUERAS A., Morphological properties of chemical vapour deposited AlN films. *J. Cryst. Growth,* 1993, 133, p. 59-71.

28. KISHI K., OOISHI Y., NOMA H., USHIJIMA E., UENO N., AKIYAMA M., TABARU T., Measurement of output voltage of aluminum nitride thin film as a pressure sensor at high temperature. *J. Eur. Ceram. Soc.*, 2006, 26, p. 3425-3430.

29. TONISCH K., CIMALLA V., FOERSTER CH., ROMANUS H., AMBACHER O., DONTSOV D., Piezoelectric properties of polycrystalline AlN thin films for MEMS applications. *Sens. Actuators, A,* 2006, 132, p. 658.

30. CLEMENT M., VERGARA L., SANGRADOR J., IBORRA E., SANZ-HERVÁS A., SAW characteristics of AlN films sputtered on silicon substrates. *Ultrasonics,* 2004, 42, p. 403-407.

31. SANZ-HERVÁS A., CLEMENT M., IBORRA E., VERGARA L., OLIVARES J., SANGRADOR J., Degradation of the piezoelectric response of sputtered c-axis AlN thin films with traces of non-(0002) x-ray diffraction peaks. *Appl. Phys. Lett.*, 2006, 88, p.161915.

32. ISHIHARA M., LI S. J., YUMOTO H., AKASHI K., IDE Y., Control of preferential orientation of AlN films prepared by the reactive sputtering method. *Thin Solid Films,* 1998, 316, p. 152-157.

33. XU X.-H., WU H.-S., ZHANG C.-J., ZHANG F.-Q., LI Z.-Y., The effect of experimental parameters on the orientation of AlN nano films. *Int. J. Nonlinear Sci. Numer. Sim.,* 2002, 3, p. 495-498.

34. CHEN Y., WANG R., WANG B., XING T., SONG X., ZHU M., YAN H., Effects of mean free path on the preferentially oriented growth of AlN thin films. *J. Cryst. Growth,* 2005, 283, p. 315-319.

35. JASINSKI J., LILIENTAL-WEBER Z. , Inversion domains in AlN grown on (0001) sapphire. *Appl. Phys. Lett.*, 2003, 83, p. 2811-2813.

36. RUFFNER J. A., CLEM P.G., TUTTLE B. A., DIMOS D., GONZALES D.M., Effect of substrate composition on the piezoelectric response of reactively sputtered AlN thin films, *Thin Solid Films,* 1999, 354, p. 256-261.

37. VERGARA L., CLEMENT M., IBORRA E., SANZ-HERVÁS A., GARCÍA LÓPEZ J., MORILLA Y., SANGRADOR J., RESPALDIZA M.A., Influence of oxygen and argon on the crystal quality and piezoelectric response of AlN sputtered thin films. *Diamond Relat. Mater.,* 2004, 13, p. 839-842.

38. NAIK R.S., REIF R., LUTSKY J.J., SODINI C.G., Low-temperature deposition of highly textured aluminum nitride by direct current magnetron sputtering for applications in thin-film resonators. *J. Electrochem. Soc.*, 1999, 146, p. 691-696.

39. MARTIN F., MURALT P., Thickness dependence of the properties of highly c-axis textured AlN thin films. *J. Vac. Sci. Technol. A* , 2004, 22, p. 361-365.

40. HWANG B. H., CHEN C. S., LU H. Y., HSU T. C., “Growth mechanism of reactively sputtered aluminium nitride thin films”, *Mater. Sci. Eng., A,* 2002, 325, p. 380-388.

41. HICKERNELL F. S., LIAW H. M., The structural and acoustic properties of sputtered aluminum nitride on silicon, *Proceedings of the Ninth IEEE International Symposium on Applications of Ferroelectrics,* 1994, p. 543-546.

42. BÉNÉDIC F., ASSOUAR M.B., MOHASSEB F., ELMAZRIA O., ALNOT P., GICQUEL A., Surface acoustic wave devices based on nanocrystalline diamond and aluminium nitride. *Diamond Relat. Mater.,* 2004, 13, p. 347-353.

43. ASSOUAR M.B., JIMÉNEZ RIOBÓO R.J., VILA M., ALNOT P., Effect of deposition temperature on surface acoustic wave velocity of aluminum nitride films determined by Brillouin spectroscopy. *J. Appl. Phys.*, 2005, 98, p. 096102.

44. XU X.-H., WU H.S., ZHANG C.-J., JIN Z.-H., Morphological properties of AlN piezoelectric thin films deposited by DC reactive magnetron sputtering, *Thin Solid Films,* 2001, 388, p. 62-67.

45. KAISER U., BROWN P.D., KHODOS I., HUMPHREYS C. J., SCHENK H.P.D., RICHTER W., The effect of growth condition on the structure of 2H-AlN films deposited on Si(111) by plasma-assisted molecular beam epitaxy. *J. Mater. Res.*, 1999, 14, p. 2036-2042.

46. CHEN F., *Introduction to plasma physics and controlled fusion, Volume 1: Plasma physics.* Second edition. New York : Plenum Press, 1984, 415 p. , p.3.

47. RODRIGO A., FARENGO R., ALVAREZ F., BRUHL S., CABO A., PASCUAL R., IPOHORSKI M., MÍNGOLO N., ORTIZ M., OVIEDO C., FORLERER E., *Cuarto curso latinoamericano de procesamiento de materiales por plasma*, Comisión Nacional de Energía Atómica - Agencia de Cooperación Internacional de Japón, Buenos Aires, 2001, 293 p., p.1-137.

48. ARNAL Y., SILVA F., *Traitements de surface par plasma - Introduction à l'interaction particules –surface*, Institut National Polytechnique de Grenoble, Formation continue, 2003, 31 p.

49. BOND J. W., K. WATSON M., WELCH J. A., *Atomic theory of gas dynamics.* First ed., Massachusetts: Addison-Wesley, 1965, . 507 p., p. 68-175.

50. LIEBERMAN M. A., LICHTENBERG A. J., *Principles of plasma discharges and materials processing.* First edition. New York: John Wiley & Sons, 1994, 571 p., p. 412-449, p. 217-264, p. 44-264.

51. CHAPMAN B., *Glow discharge processes: sputtering and plasma etching.* First edtion. New York: John Wiley & Sons, 1980, 406 p., p. 77.

52. BECHU S., *Production de plasmas froids*. CNRS – Université Joseph Fourier, Grenoble, France – 2003, p.1-30.

53. NAUDIN F., *Dépôt chimique en phase vapeur de silice dans une post-décharge micro-onde de grand diamètre – Paramètre de dépôt, propriétés des films, diagnostic et modélisation du milieu réactif,* Thesis : Ceramic materials and surface treatments : Limoges : 2000, 192 p.

54. HIDALGO H., *Dépôt chimique en phase vapeur de couches minces d'alumine dans une post-décharge micro-onde*, Thesis : Ceramic materials and surface treatments: Limoges : 2003, 267 p.

55. MUSIL J., Microwave plasma: its characteristics and applications in thin film technology. *Vacuum*, 1986, 36, p. 161-169.

56. CHAKER M., MOISAN M., ZAKRZEWSKI Z., Microwave and RF surface wave sustained discharges as plasma sources for plasma chemistry and plasma processing. *Plasma Chem. Plasma Process.*, 1986, 6, p. 79-96.

57. MOISAN M., PELLETIER J., *Microwave excited plasmas.* First edition. New York: Elsevier Science Publisher, 1992, p. 11-52.

58. OHRING M., *Materials science of thin films deposition and structure.* Second edition. New York: Academic Press, 2002, 794 p., p. 145.

59. RICKERBY D. S., MATTHEWS A., *Advanced surface coatings: a handbook of surface engineering.* First ed. New York : Blackie & Sons Ltd., 1991, 365 p., p. 14-40.

60. AZEMA N., DURAND J., BERJOAN R., DUPUY C., COT L., Oxidation of aluminium nitride thin films obtained by plasma-enhanced chemical vapour deposition (PECVD*). J. Eur. Ceram. Soc.,* 1991, 8, p. 291-298.

61. MEIKLE S., NOMURA H., NAKANISHI Y., HATANAKA Y., Reactions of atomic nitrogen and trimethyl aluminum downstream from a nitrogen microwave plasma. *J. Appl. Phys.,* 1990, 67, p. 483-485.

62. ZHANG W., VARGAS R., GOTO T., SOMENO Y., HIRAI T., Preparation of epitaxial AlN films by electron cyclotron resonance plasma-assisted chemical vapor deposition on Ir- and Pt-coated sapphire substrates. *Appl. Phys. Lett.,* 1994, 64, p. 1359-1361.

63. SOH J., JANG S., JEONG I., LEE W., C-axis orientation of AlN films prepared by ECR PECVD. *Thin Solid Films,* 1996, 279, p. 17-22.

64. MENG G., LIU X., XIE S., PENG D., <0001>- oriented growth of AlN films on Si(111) by microwave plasma CVD with $AlBr_3$-NH_3-N_2 system. *J. Cryst. Growth*, 1996, 163, p. 232-237.

65. STAUDEN T., EICHHORN G., CIMALLA V., PEZOLDT J., ECKE G., The deposition of aluminum nitride on silicon by plasma-enhanced metal-organic chemical vapour deposition. *Diamond Relat. Mater.,* 1996, 5, p. 1210-1213.

66. BUTCHER K., TANSLEY T., LI X., ZHOU B., Photolytic absorbate removal during the growth of aluminium nitride by remote microwave plasma chemical vapour deposition. *Solid-State Electron.,* 1997, 41, p. 305-314.

67. ECKE G., EICHHORN G., PEZOLDT J., REINHOLD C., STAUDEN T., SUPPLIETH F., Deposition of aluminium nitride films by electron cyclotron resonance plasma-enhanced chemical vapour deposition. *Surf. Coat. Technol.,* 1998, 98, p. 1503-1509.

68. SOH J-W., LEE W-J-, SAW Characteristics of AlN films deposited on various substrates using ECR plasma enhanced CVD and reactive RF sputtering, *IEEE Ultrasonics Symposium*, 1996, p. 299-302.

69. MAHIEU S., CHEKIERE P., DEPLA D., DE GRYSE R., Review: Biaxial alignment in sputter deposited thin films. *Thin Solid Films,* 2006, 515, p. 1229-1249.

70. THORNTON J. A., Coating deposition by sputtering, *Deposition technologies for films and coatings: development and applications /* ed. by R. F. Bunshah et al. New Jersey : Noyes Publications, 1982, p.170-243.

71. DOVIDENKO K. , OKTYABRSKY S. NARAYAN J., Aluminum nitride films on different orientations of sapphire and silicon. *J. Appl. Phys.*, 1996, 79, p. 2439-2444.

72. LEE J. – B., JUNG J.- P, LEE M.- H., PARK J.- S., Effects of bottom electrodes on the orientation of AlN films and the frequency responses of resonators in AlN-based FBARs.. *Thin Solid Films,* 2004, 447-448, p. 610-614.

73. WANG B., ZHAO Y., HE Z., The effects of deposition parameters on the crystallographic orientation of AlN films prepared by RF reactive sputtering, *Vacuum*, 1997, 48, p. 427-429.

74. ABDALLAH B., CHALA A., JOUAN P.-Y., BESLAND M.P., DJOUADI M. A., Deposition of AlN films by reactive sputtering: Effect of radio frequency substrate bias. *Thin Solid Films,* 2007, 515, p. 7105-7108.

75. FUJIMURA N., NISHIHARA T., GOTO S., XU J., ITO T., Control of preferred orientation for ZnO$_x$ films: control of self-texture. *J. Cryst. Growth*, 1993, 130, p. 269-279.

76. LEE J. W., CUOMO J. J., Aluminum nitride thin films on an LTCC substrate. *J. Am. Ceram. Soc.,* 2005, 88, p. 1977-1980.

77. BO W., MEI W., RUZHI W., ANPING H., HUA Z. , YUNJUAN Z., HUI Y., SEIPING W., The growth of AlN films composed of silkworm-shape grains and the orientation mechasnism. *Mater. Lett.,* 2002, 53, p. 367-370.

78. PAULEAU Y., Residual stresses in physically vapor-deposited thin films. *Handbook of thin film materials, Vol. 1: Deposition and processing of thin films /* ed. by H. S. Nalwa. New York : Academic Press, 2002, p. 455-522.

79. NIX W.D., CLEMENS B.M., Crystallite coalescence: a mechanism for intrinsic tensile stresses in thin films*, J. Mater. Res.,* 1999, 14, p. 3467-3473.

80. DAVIS C. A., A simple model for the formations of compressive stress in thin films by ion bombardment. *Thin Solid Films*, 1993, 226, p. 30-34.

81. ECKE G., EICHHORN G., PEZOLDT J., REINHOLD C., STAUDEN T., SUPPLIETH F., Deposition of aluminium nitride films by electron cyclotron resonance plasma-enhanced chemical vapour deposition. *Surf. Coat. Technol.,* 1998, 98, p. 1503-1509.

82. MILEHAM J.R., PEARTON S. J., ABERNATHY C.R., MACKENZIE J.D., Wet chemical etching of AlN. *Appl. Phys. Lett.*, 1995, 67, p. 1119-1121.

83. LORETZ J., DESPAX B., MARTI P., MAZE A., Hydrogenated aluminum nitride thin films prepared by r.f. reactive sputtering. Infrared and structural properties. *Thin Solid Films,* 1995, 265, p. 15-21.

84. DE KEIJSER T. H., MITTEMEIJER E. J., ROZENDAAL H. C., The determination of crystalline-size and lattice-strain parameters in conjunction with the profile-refinement method for the determination of crystal structures. *J. Appl. Crystallogr.,* 1983, 16, p. 309-316.

85. EBERHART J.-P., *Méthodes physiques d´étude des minéraux et des matériaux solides.* First edition Paris: Doin éditeurs, 1976, p. 307-376.

86. OLIVER W.C., PHARR G.M., An improved technique for determining hardness and elastic modulus using load and displacement sensing indentation experiments. *Mater. Res. Soc. Symp. Proc.*, 1992, 7, p. 1564-1583.

87. OLIVER W.C., PHARR G.M., Measurement of hardness and elastic modulus by instrumented indentation: advances in understanding and refinements to methodology. *Mater. Res. Soc. Symp. Proc.*, 2004, 19, p. 3-19.

88. SLACK G. A., BARTRAM S. F., Thermal expansion of some diamond like crystals. *J. Appl. Phys.*, 1975, 46, p. 89-98.

89. LEFKI K., DORMANS G., Measurement of piezolelectric coefficients of ferroelectric thin films. *J. Appl. Phys.,* 1994, 76, p. 1764-1767.

90. ZHAO M., WANG Z., MAO S., Piezolelectric characterization of individual zinc oxide nanaobelt probed by piezoresponse force microscope. *Nano Lett.*, 2004, 4, p. 587-590.

91. XU F., CHU F. TROLIER-MCKINSTRY S., Longitudinal piezoelectric coefficient measurement for bulk ceramics and thin films using pneumatic pressing rig. *J. Appl. Phys.*, 1999, 86, p. 588-594.

92. WU A., *AlN thin films deposition by RMWPECVD: design of experiment.* Faculté des Sciences et Techniques, Université de Limoges. 2004. Post-doc report , 26 p.

93. SANZ-HERVÁS A., IBORRA E., CLEMENT M., SANGRADOR J., AGUILAR M., Influence of crystal properties on the absorption IR spectra of polycrystalline AlN thin films. *Diamond Relat. Mater.,* 2003, 12, p. 1186-1189.

94. DAGDAG S., *Matériaux et revêtements céramiques multifunctionnels par PECVD et SPS pour l'intégration de puissance haute température - haute tension*, Thesis: Material science and engineering: Tarbes, France : 2005, 217 p., p. 75-86.

95. AKIYAMA M., XU C., NONAKA K., SHOBU K., WATANABE T., Statistical approach for optimizing sputtering conditions of highly oriented aluminum nitride thin films. *Thin Solid Films,* 1998, 315, p. 62-65.

96. ZHANG J. X., CHENG H., CHEN Y.Z., UDDIN A., YUAN S., GENG S.J., ZHANG S., Growth of AlN films on Si (100) and Si(111) substrates by reactive magnetron sputtering. *Surf. Coat. Technol.,* 2005, 198, p. 68-73.

97. CHENG H., SUN Y., ZHANG J., ZHANG Y., YUAN S., HING P., AlN films deposited under various nitrogen concentrations by RF reactive sputtering. *J. Cryst. Growth,* 2003, 254, p. 46-54.

98. PROKOFYEVA T., SEON M., VANBUSKIIRK, J., HOLTZ, M., Vibrational properties of AlN grown on (111)-oriented silicon. *Phys. Rev. B: Condens. Matter Mater. Phys.*, 2001, 63, 125313.

99. LEBEDEV V., JINSCHEK J., KRAÜßLICH J., KAISER U., SCHRÖTER B., RICHTER W., Hexagonal AlN films grown on nominal and off-axis Si (001) substrates. *J. Cryst. Growth*, 2001, 230, p. 426-431.

100. HIROHATA Y., TSUCHIYA N., HINO T., Effect of mixing hydrogen into nitrogen plasma. *Appl. Surf. Sci.,* 2001, 169-170, p. 612-616.

101. IBORRA E., CLEMENT M., VERGARA L., SANZ-HERVÁS A., OLIVARES J., SANGRADOR J., Dependence of the IR reflectance LO absorption bands on the crystalline texture of AlN films. *Appl. Phys. Lett.,* 2006, 88, p. 231901.

102. MAHMOOD A., RAKOV N., XIAO M., Influence of deposition conditions on optical properties of aluminum nitride (AlN) thin films prepared by DC-reactive magnetron sputtering, *Mater. Lett.*, 2003, 57, p. 1925-1933.

103. LOFTHUS A., KRUPENIE P., The spectrum of molecular nitrogen. *J. Phys. Chem. Ref. Data*, 1977, 6, p. 113-307.

104. TIMMERMANS E. A. H., *Atomic and molecular excitation processes in microwave induced plasmas: a spectroscopic study*. Thesis: Physics: Eindhoven University of Technology: 1999, 138 p., p. 42-80.

105. Atomic spectra database, National Institute of Standards and Technology, Physics Laboratory, U.S.A, Available on: http://www.nist.gov.

106. GOLOMB D., BROWN J.H., Chemiluminescence of trimethyl aluminum in active oxygen and nitrogen. *Combust. Flame,* 1976, 27, p. 383-389.

107. ISHIHARA M., YAMAMOTO K., KOKAI F., KOGA Y., Aluminum nitride films prepared by radical-assisted pulsed laser deposition. *Vacuum,* 2000, 59, p. 649-656.

108. BELMONTE T., Génie des procédés de traitement de surfaces, *Elaborations de materiaux et genie des procédés*, École d´été, Saint-Pierre d'Olécon, France, June 2005.

109. CROLLY G., OECHSNER H., Comparative determinations of the electron temperature in Ar - and N_2 - plasmas with electrostatic probes, optical emission spectroscopy OES and energy dispersive mass spectrometry EDMS. *Eur. Phys. J.* AP, 2001, 15, p. 49-56.

110. DEN OTTER M. W., Approximate expressions for the capacitance and electrostatic potential of interdigitated electrodes. *Sens. Actuators, A,* 2002, 96, p. 140-144.

111. ABDALLAH B., DUQUENE C., SÁNCHEZ G., DJOUADI A., JOUAN P., GAUTRON E., TRISTANT P., TIXIER C., BOLOGNA ALLES A., Structure investigation in AlN films deposited by DC reactive sputtering and microwave plasma enhanced chemical vapor deposition, Poster, *Innovations on Thin Films Processing and Characterization* - Nancy, France , 11/2007.

112. HULTMAN L., MÜNZ W.-D., MUSIL J:, KADLEC S., PETROV I. GREENE J.E., Low-energy (≈100 eV) ion irradiation during growth of TiN deposited by reactive magnetron sputtering: Effects of ion flux on film microstructure. *J. Vac. Sci. Technol., A*, 1991, 9, p. 434-438.

113. DATTA S., *Surface acoustic wave devices.* First ed. New Jersey: Prentice-Hall, 1986, 252 p., p. 41-69.

114. LÜTH H., *Solid surfaces, interfaces and thin films.* First edition. New York: Springer, 2001, p. 230 – 243.

115. CAMPBELL C. K., *Surface acoustic wave devices for mobile and wireless Communications.*. First edition. New York : Academic Press, Inc., 1998, 619 p., p. 67-135.

116. IBORRA E., VERGARA L., SANGRADOR J., CLEMENT M., SANZ-HERVÁS A., OLIVARES J., Circuital model for the analysis of the piezoelectric response of AlN films using SAW filters. *IEEE Transactions on Ultrasonics, Ferroelectrics and Frequency Control*, 2007, 54, p. 2367-2375.

117. PARK G., CHOI J., RYU J., FAN H., KIM H., Measurement of piezoelectric coefficients of lead zirconate titianate thin films by strain-monitoring pneumatic loading methods. *Appl. Phys. Lett.,* 2002, 80, p. 4606-4608.

118. HO C., SHING T, LI P., Prefered orientation control and characterization of AlN thin films using reactive sputtering. *Tamkang Journal of Science and Engineering*, 2004, 7, p. 1-4

119. KHOLKIN A. L., WÜTHRICH C., TAYLOR D.V., SETTER N., Interferometric measurements of electric field-induced displacements in piezoelectric thin films. *Rev. Sci. Instrum*., 1996, 67, p. 1935-1941.

120. MCKELVEY J. P., GROTCH H., *Física para ciencias e Ingeniería.* First edition. New York: Harper & Row Latinoamericana, 1981, 1239 p., p. 607-674.

121. CHAPRA S. C., CANALE R. P., *Métodos numéricos para ingenieros.* Third edition. New York: McGraw-Hill, 1999, 982 p., p. 84-109, 855-945.

Appendix A

BAW AND SAW DEVICES

The following section deals with some fundamentals that allow a better understanding about how the BAW and SAW devices work. Simplified models are developed to explain their frequency responses.

A.1 BAW devices

Uniform plane waves in solids can be longitudinal or transverse depending on the relative motion of the crystal planes with respect to the propagation direction in which the wave travels (see Fig. A.1). Longitudinal or compression waves are developed when the crystal plane motion is parallel to the direction of propagation, while transverse or shear waves are observed when the plane motions are perpendicular to the propagation direction [113].

The Christoffel equation [14] describes the propagation of mechanical waves in three dimensions based on the fundamental dynamic equations of motion such as Newton´s law, Hooke´s law, crystal strain, and particle velocity. For any crystalline material, the Christoffel tensor can be calculated which, in turn, indicates the three phase velocities of the possible propagating waves, i.e. one longitudinal and two transverse waves, as well as the corresponding particle velocity directions, i.e. the acoustic polarization. In general for a given material, the phase velocity of longitudinal waves is higher than the phase velocity of transverse waves.

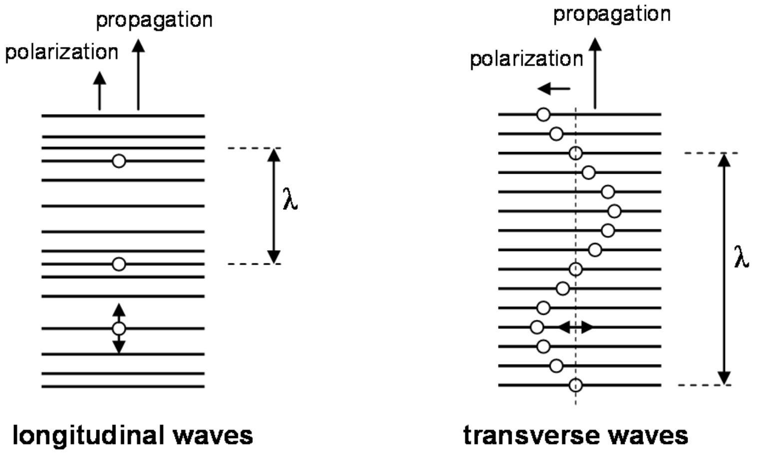

Figure A.1: Schematic representations of longitudinal and transverse elastic waves in solids.

A.1.1 One-dimensional model of the BAW resonator

A one-dimensional model is presented in Fig. A.2 where the proper conditions for the propagation of a longitudinal wave are met, by considering a piezoelectric film with thickness $d = z_2 - z_1$ and section *A*, under an electric tension *U*, where F_1 and F_2 are the restraining forces exerted from the neighboring materials [14, 1]. Assuming that the distortion derived from the elastic waves generated in the thickness *d* are negligible compared with the device dimensions *x-y*, and considering that the electric field *E* is parallel to *z* axis, the equations of state for the piezoelectric solid in the e-form are given by:

$$T = c^E \frac{\partial u}{\partial z} - eE \qquad \text{(A.1)}$$

$$D = \varepsilon^S E + e\frac{\partial u}{\partial z} \qquad \text{(A.2)}$$

$$\frac{\partial u}{\partial z} = S \qquad \text{(A.3)}$$

where $u = u_z$: particle displacement (m), $S = S_z$: strain (m/m), $D = D_z$: electric displacement (C/m^2), $T = T_z$: stress (N/m^2), $E = E_z$: electric field (V/m), $c^E = c_{zz}{}^E$: stiffness coefficient (m^2/N), $\epsilon^S = \epsilon_{zz}{}^S$: permittivity coefficient (F/m), $e = e_{zz}$: piezoelectric coefficient (C/m^2).

In the absence of mechanical energy source, Newton second's law states:

$$\frac{\partial T}{\partial z} = \rho \frac{\partial^2 u}{\partial t^2} \tag{A.4}$$

where ρ: density (kg/m^3), and t: time (s).

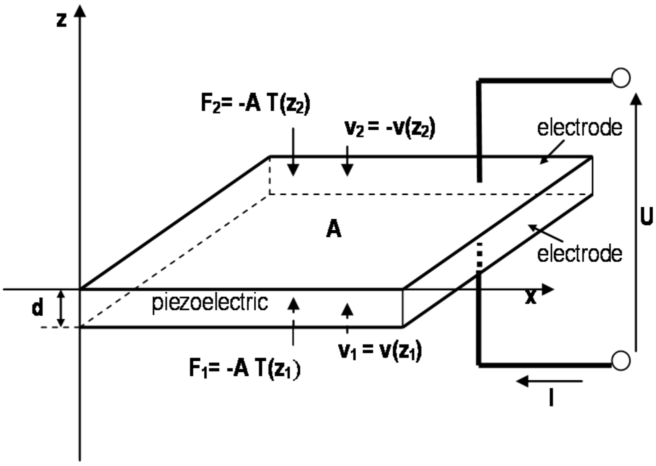

Figure A.2: One-dimension model of the bulk acoustic wave transducer.

Poisson's equation can be used to relate the bulk density of electric charge resulting from the polarization of an insulating material, i.e., the piezoelectric film, with an applied electric field, where also overall electric neutrality must be conserved as well with the appearance of a charging current density:

$$\frac{\partial D}{\partial z} = \rho_e \tag{A.5}$$

$$\frac{\partial D}{\partial t} = J(t) \tag{A.6}$$

where ρ_e: charge density (C/m^3), $J(t) = I(t)/A$: current density (A/m^2).

By combining the equations (A.1-A.6), the characteristic propagation equation of the longitudinal acoustic wave can be obtained:

$$\rho \frac{\partial^2 v}{\partial t^2} = c \frac{\partial^2 v}{\partial z^2} \tag{A.7}$$

$$v = \frac{\partial u}{\partial t} \tag{A.8}$$

where v is the particle velocity and $c = c^D = c^E + (e^2 / \epsilon^S)$ is the stiffness at constant electric displacement.

The general solution of the propagation equation is the sum of two waves that travel in opposite directions at a velocity *V* given by:

$$V = \sqrt{\frac{c}{\rho}} \tag{A.9}$$

In the harmonic regime the particle velocity is given by,

$$v = \left(\frac{v_1}{i.tg(kd)} \right) e^{i(\varpi t - kz)} + \left(\frac{v_2}{i.tg(kd)} \right) e^{i(\varpi t + kz)} \tag{A.10}$$

where: ω: angular frequency (radian.s^{-1}), $k = \omega/V$: wavenumber (m^{-1}), $v_1 = v(z_1)$, $v_2 = -v(z_2)$

By using the stress equations of state:

$$F_1 = ZA\left(\frac{v_1}{i.tgkd} + \frac{v_2}{i.\sin kd}\right) + \frac{hI}{i\varpi} \tag{A.11}$$

$$F_2 = ZA\left(\frac{v_1}{i.\sin kd} + \frac{v_2}{i.tgkd}\right) + \frac{hI}{i\varpi} \tag{A.12}$$

where

$Z = \rho V = ck/\omega$: characteristic elastic impedance of the propagation wave (kg.m $^{-2}$.s), $Z.A$: is the elastic impedance (kg/s), $h = e/\varepsilon^S$: rate between piezoelectric coefficient (e) and the permittivity (V/m).

The electric tension U applied between the metalized faces can be calculated from the electric field:

$$U = \int_{z_1}^{z_2} E dz \tag{A.13}$$

$$E = -h\frac{\partial u}{\partial z} + \frac{D}{\varepsilon^S} \tag{A.14}$$

The charging current that flows through the film with section A:

$$I = i\varpi DA \tag{A.15}$$

Introducing the particle velocities v_1 and v_2 and the geometric capacity C_o of the transducer:

$$v_1 = i\varpi .u(z_1) \tag{A.16}$$

$$v_2 = -i\varpi .u(z_2) \tag{A.17}$$

$$C_o = \frac{\varepsilon^S A}{d} \tag{A.18}$$

$$U = h\left[u(z_1) - u(z_2)\right] + \frac{Id}{i\varpi\varepsilon^S A} = \frac{h}{i\varpi}(v_1 + v_2) + \frac{I}{i\varpi C_o} \tag{A.19}$$

This behavior can be represent by a three-port circuit, with one electrical port – i.e., applied tension *U*, and charging injected current *I* – and two acoustic ports where the forces F_1 and F_2 applied on the surface of the film and the input velocities v_1 and v_2 mimic the role of tension and current respectively in the electric circuit (see Fig. A.3).

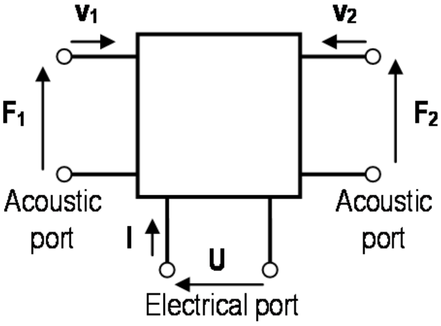

Figure A.3: The three-port circuit.

If the equations that describe the model are expressed in a matrix form, the electromechanical impedance matrix is:

$$\begin{bmatrix} F_1 \\ F_2 \\ U \end{bmatrix} = -i \begin{bmatrix} ZA/tgkd & ZA/\sin kd & h/\varpi \\ ZA/\sin kd & ZA/tgkd & h/\varpi \\ h/\varpi & h/\varpi & 1/\varpi C_o \end{bmatrix} \begin{bmatrix} v_1 \\ v_2 \\ I \end{bmatrix} \tag{A.20}$$

Based on the same fundamental considerations equivalent circuit models have been developed to explain the behavior of the piezoelectric transducer in different situations [1].

The analysis of the frequency response can be simplified, in a first approach, if the mechanical effect of the metallic electrodes is discarded because of their comparatively smaller thickness. However, when the main transducer frequencies are in the order of the GHz range, the thickness (λ/2) of the film is found to be in the micrometer range. Under these conditions, the effect of the electrodes must be taken into account.

The electrical impedance Z_e of the transducer in these conditions can be deduced from equation A.20:

$$Z_e = \frac{1}{iC_o\varpi}\left(1+\frac{K^2}{\varphi}Z_p\,\frac{2Z_p(1-\cos\varphi)-i(Z_1+Z_2)\sin\varphi}{-(Z_P^2+Z_1Z_2)\sin\varphi+iZ_P(Z_1+Z_2)\cos\varphi}\right) \tag{A.21}$$

where: Z_1, Z_2: elastic impedances of the mediums situated on top and bottom of the piezoelectric medium, Z_P: elastic impedance of the piezoelectric medium, $\varphi = k\,d = \omega\,d\,/\,V$, $K^2 = \frac{e^2}{\varepsilon^S c^D}$: electromechanical coupling coefficient.

The free resonator can be supposed as a simple piezoelectric blade, with electrodes on both sides, been then a transducer not charged, thus $Z_1 = Z_2 = 0$. In the hypothetical case of absence of dissipated power, the impedance is purely imaginary:

$$Z_e = \frac{1}{iC_o\varpi}\left(1-K^2\,\frac{tg(\varphi/2)}{\varphi/2}\right) \tag{A.22}$$

The corresponding admittance module $|Y| = 1/|Ze|$ is represented in Fig. A.4.

The electric impedance is infinite ($Z_e = \infty$) when

$$f_a^{(n)} = (2n+1)f_a \tag{A.23}$$

$$\text{with}\quad f_a = \frac{V}{2d} \tag{A.24}$$

been f_a the antiresonance frequency.

The electric impedance is annulled ($Z_e = 0$) when

$$K^2 tg\left(\frac{\pi}{2}\frac{f_r^{(n)}}{f_a}\right) = \frac{\pi}{2}\frac{f_r^{(n)}}{f_a} \tag{A.25}$$

where f_r is the resonant frequency.

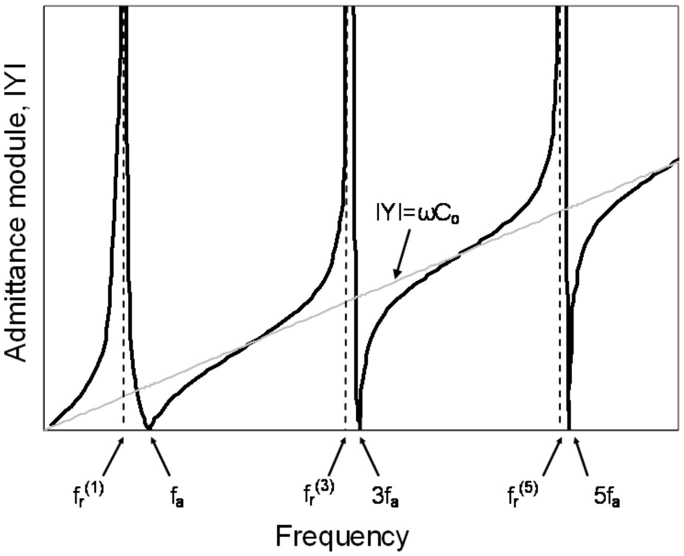

Figure A.4: Frequency response, as admittance module vs. frequency, of a free piezoelectric resonator under ideal conditions.

Then, measuring the antirresonant and resonant frequencies from the frequency response, the phase velocity and the electromechanical coupling coefficient can be obtained:

$$V = 2f_a d \tag{A.26}$$

$$K^2 = \frac{\pi}{2}\frac{f_r}{f_a}tg\left(\frac{\pi}{2}.\frac{f_a - f_r}{f_a}\right) \cong \frac{\pi^2}{4}.\frac{f_a - f_r}{f_a} \tag{A.27}$$

The free resonator can be represented by a equivalent electric scheme composed of a static capacity C_0 of the blade and a resonant circuit LC series in parallel with the former (see Fig. A.5).

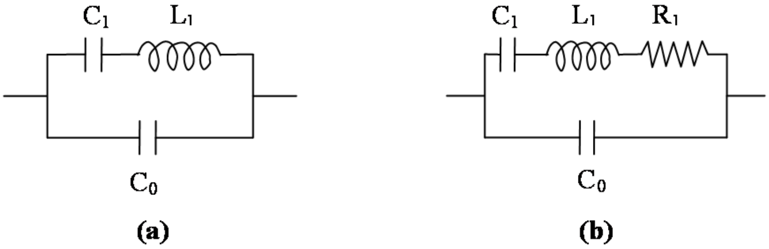

Figure A.5: Equivalent electric scheme of the free resonator: (a) ideal, (b) with losses.

The analysis of this electrical scheme conducts to:

$$Y = iC_o\varpi\left(1+\frac{C_1/C_o}{1-L_1C_1\varpi^2}\right) \tag{A.28}$$

Where it can be demonstrated that:

$$C_o = \frac{\varepsilon_o A}{d} \tag{A.29}$$

$$C_1 = \frac{8K^2}{\pi^2}C_o \tag{A.30}$$

$$L_1 \cong \frac{\rho.d^3}{8e^2A} \tag{A.31}$$

The resonance angular frequency ω_r:

$$\varpi_r^2 = \frac{1}{L_1C_1} \tag{A.32}$$

The antirresonance angular frequency ω_a:

$$\varpi_a^2 = \varpi_r^2(1+\frac{C_1}{C_o}) \tag{A.33}$$

In the real situation where there are losses associated to the intrinsic attenuation of the material or to it fixing, a resistance R_1 is introduced in the scheme (see Fig. 1.6(b)). The “quality factor” of the resonator is thus given by

$$Q = \frac{L_1\varpi_1}{R_1} \tag{A.34}$$

The typical frequency response observed in the real situation with looses is given in Fig. A.6.

By combining several resonators, in series-parallel configurations a filter can be developed, which has a frequency response as indicated in Fig. A.7 with a specific transmission band. This is the most important application of these devices in the telecommunications field [15].

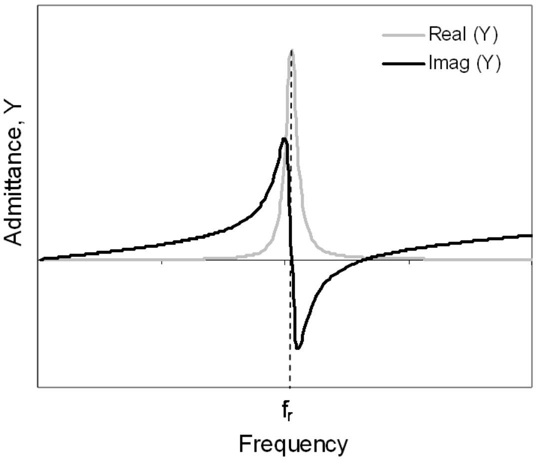

Figure A.6: Typical frequency response expressed as admittance vs. frequency of a free resonator with losses. The resonance frequency f_r in indicated.

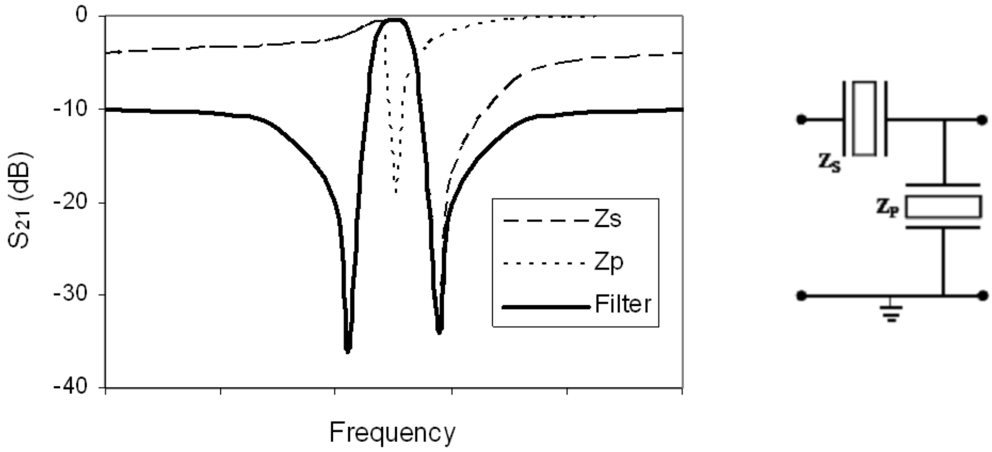

Figure A.7: Frequency response of a series-parallel configuration of BAW devices, i.e. a filter, expressed in terms of the transmission coefficient S_{21} in dB [14].

A.2 SAW devices

A surface acoustic wave, particularly known as Rayleigh wave for the type used in these devices, consists of a compression wave and a shear wave coupled together in a fixed ratio that propagates at the free surface of an elastic solid. Due to the absence of retraining force perpendicular to the surface, compressing the material in the *z* direction automatically produces motion in the *y* direction, thus compression and shear motion (u_z and u_y respectively) are coupled together (see Fig. A.8). This type of guided waves propagates along the surface and decay into depth within a distance on the order of a wavelength (see Fig. A.8 (d)). The Rayleigh-wave velocity is lower than the velocity of bulk transverse waves because the solid behaves less rigidly in the absence of material above the surface. In the particular case of piezoelectric solids there is also an accompanying electrostatic wave as a consequence of the piezoelectric effect [1,3, 113, 114].

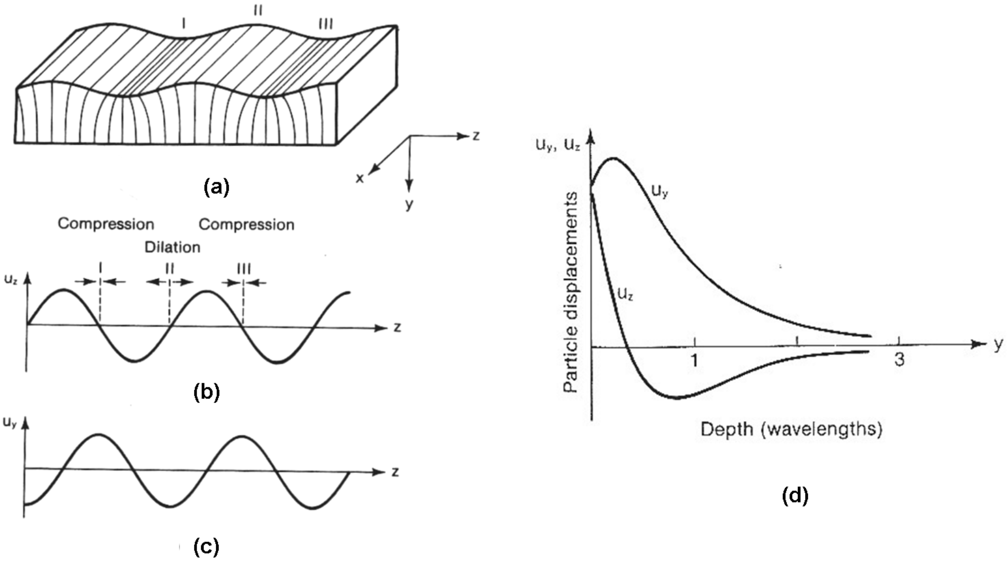

Figure A.8: (a) Surface wave in a semi-infinite solid; (b) particle displacement u_z versus z at the surface; (c) particle displacement u_y versus z at the surface, (d) particle displacements versus depth [113].

The velocity of bulk acoustic waves in a piezoelectric crystal, for a given propagation direction and polarization, is related with the electromechanical coupling coefficient according to [1, 5]:

$$V' = \sqrt{\frac{c(1+K^2)}{\rho}} \cong V(1+\frac{K^2}{2}) \tag{A.35}$$

where: V', V: bulk acoustic wave velocities with and without piezoelectric effect (m/s), c: stiffness mechanical coefficient (N/m^2), ρ: density (kg/m^3), K^2: electromechanical coupling coefficient, usually much less than unity.

As the crystal acts as it had a stiffness constant $c'=c.(1+K^2)$, it is said that the piezoelectricity "stiffens" the crystal lattice.

The electromechanical coupling coefficient for a surface acoustic wave propagating in a piezoelectric crystal is defined "by analogy" with bulk acoustic waves (see eq. A.35) as:

$$K^2 = 2\frac{V_f - V_m}{V_f} \tag{A.36}$$

where V_f is the SAW velocity on a free surface of the piezoelectric, and V_m is the SAW velocity on a electrically short-circuited surface of the crystal [3, 1, 4, 5]. The idea for such definition is that the tangential component of the electric field created by the wave due to the piezoelectric effect is shortened in the second case, reducing the contribution of this effect.

Several models have been proposed to analyze the SAW devices as function of the material properties [1, 113, 115, 20]. The following section will present a simple model developed for typical SAW filter based on the relevant properties of the piezoelectric material: the electromechanical coupling coefficient (K^2) and the acoustic velocity (V).

A.2.1 Simple circuital model for SAW filters

A correct analysis of the frequency response of a SAW filter must take into account not only the electromechanical behavior of the piezoelectric material but also the parasitic electromagnetic phenomena in the whole device. For this purpose a simple circuital model has been proposed, which describes the filter by its admittance matrix Y [30, 115, 116].

Based on the SAW crossed-field model, the electric field distribution under the electrodes of a IDT is approximated as being normal to the piezoelectric surface. Each IDT is represented by a three-port network (see Fig. A.9), where ports *1'* and *2'* are those for an acoustic, and passive, SAW transmission line, and port *3'* is where the actual signal voltages are applied or detected.

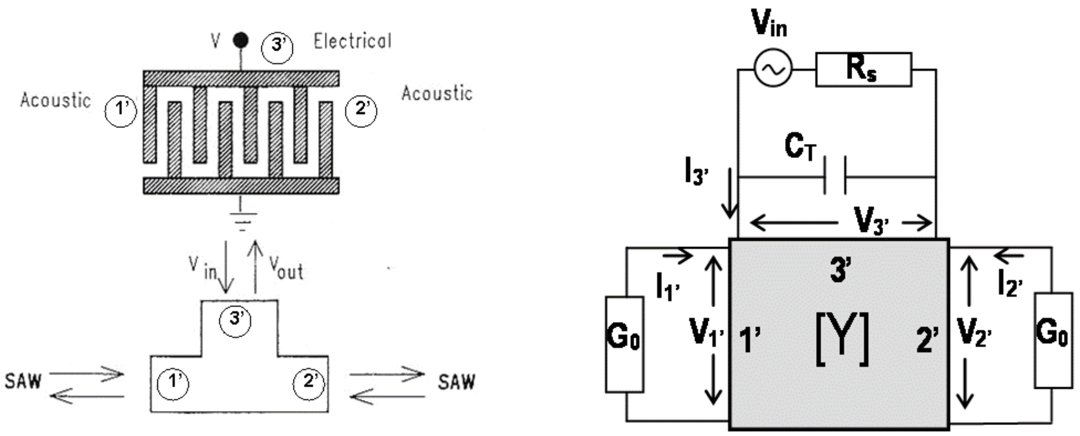

Figure A.9: Representation of the input IDT of a SAW filter as a three-port equivalent admittance network [115]

The input admittance $Y_{3'}$ at the centre frequency f_o may be expressed as

$$Y_{3'}(f_0) = \left.\frac{I_{3'}}{V_{3'}}\right|_{f_o} = G_a(f_0) + j2\pi f_0 C_T \tag{A.37}$$

with

$$G_a(f_0) = 8N^2 G_0 = 8N^2 K^2 C_s f_0 \tag{A.38}$$

where: $G_a(f_o)$: the radiation conductance (Ohm^{-1}) at the centre frequency f_o, C_T: total IDT capacitance (F), $G_0 = K^2 C_s f_o$: equivalent characteristic admittance (Ohm^{-1}) of the SAW transmission line, C_s: static capacitance of one periodic section (F), N: number of electrode pairs (periods), K^2: electromechanical coupling coefficient.

If the value ratio between metallization thickness and wavelength is low enough (<<1%) the acoustic reflections from IDT fingers discontinuities can be neglected. As a consequence, the radiation conductance parameter $G_a(f)$ can be approximated with a sinc-function amplitude response near the centre frequency [115]:

$$G_a(f) = G_a(f_0).\left|\frac{\sin x}{x}\right|^2 \tag{A.39}$$

with $x = N\pi(f-f_0)/f_0$.

Then the general expression for the input admittance $Y_{3'}$:

$$Y_{3'}(f) = G_a(f) + j2\pi f C_T \tag{A.40}$$

An expression for the radiation suceptance $B_a(f)$, normally omitted in calculations because of its magnitude, can be derived from the $G_a(f)$ expression [115]:

$$B_a(f) = G_a(f_0).\left(\frac{\sin(2x) - 2x}{2x^2}\right) \tag{A.41}$$

Based on the same principles, the model can be applied to the output IDT, which is considered to be excited by a high-impedance current source proportional to the surface acoustic wave amplitude, and obtain the overall equivalent circuit of the SAW filter.

In order to obtain the overall SAW filter response, the only concern is with the ratio of voltages at electrical ports in both input and output IDTs (*1* and *2*), considered as a two-port network, as depicted in the block diagram of Fig. A.10. With the aim of obtaining the admittance parameters, current-voltage relations from standard circuit theory are used at input and output:

$$I_1 = Y_{11}.V_1 + Y_{12}V_2 \tag{A.42}$$

$$I_2 = Y_{21}.V_1 + Y_{22}V_2 \tag{A.43}$$

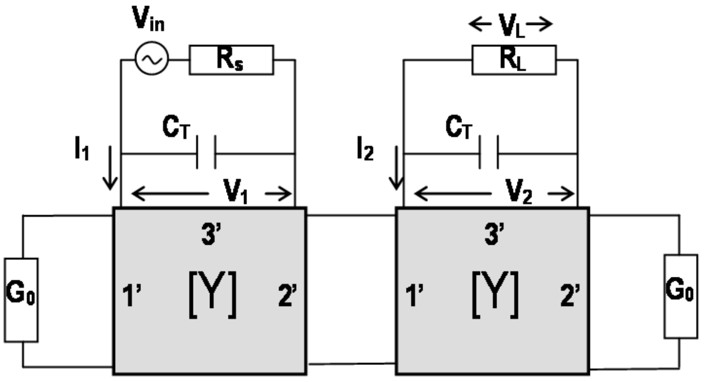

Figure A.10: Representations of the complete SAW device using three-port electrical admittances applied to the input and outpout IDTs.

By introducing the terms associated with the three ports IDT formalism and considering two identical input and output IDTs, the admittance parameters are obtained:

$$Y_{11} = Y_{22} = G_a + j(B_a + 2\pi.f.C_T) \tag{A.44}$$

$$Y_{12} = Y_{21} = G_a.\exp(-j.2\pi.f.\frac{M}{f_0}) \tag{A.45}$$

where: *M*: distance between the IDTs in wavelengths.

Then, the transmission coefficient S_{21}, the actually measured magnitude in the frequency response [115], is given by:

$$S_{21} = \frac{-2.Y_{21}.Y_0}{(Y_0 + Y_{11})^2 - Y_{21}^2} \tag{A.46}$$

where Y_0: characteristic admittance of the experimental arrangement (Ohm^{-1}).

Thus, by means of this model it is possible to estimate the frequency response of the filter around the centre frequency (see Fig. 1.13) as a function of the piezoelectric coupling coefficient, the surface acoustic velocity of the material, the geometrical characteristics and C_T. The last can be estimated according to [110] as a function of the geometry and electrical properties of the material.

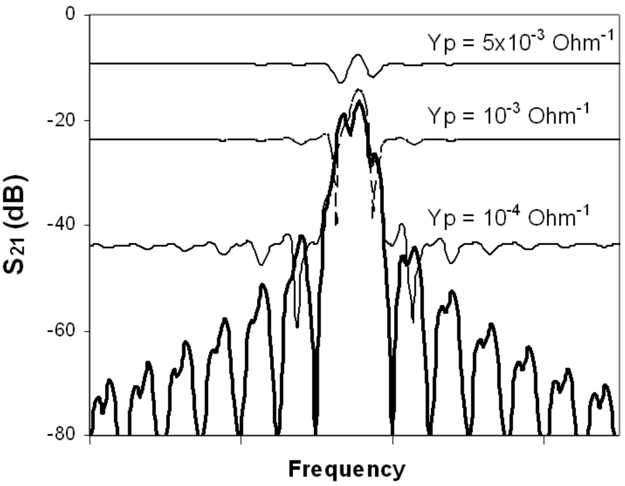

Figure A.11: Frequency response of a SAW filter around the characteristic frequency expressed as the transmission coefficient S_{21} vs. frequency. The effect of different electrical admittances associated to the substrate feedthrough (Y_P) is indicated.

The effects of the electromagnetic feedthrough can be important in the case of piezoelectric films over low resistivily substrates. In order to take in account this effect, the addition of a real term Y_P to the Y_{12} parameter has been proposed as a first approximation. This is equivalent to a purely resistive admittance in parallel and has had good accordance with measurements [115, 116]. Fig A.11 shows the effect of the electromagnetic feedthrough on the frequency response.

Appendix B

PIEZOELECTRIC CHARACTERIZATION OF THIN FILMS

Piezoelectric properties of thin films can be determined by two main types of techniques: static or quasi-static measurements and dynamic measurements [19]. While the first group of techniques is typically used for non-resonant applications, e.g. sensors and actuators, the second group is typical for those applications where the piezoelectric thin film is used for the generation or detection of high-frequency bulk acoustic waves (BAW) or surface acoustic waves (SAW).

B.1 Quasi-static measurements

Quasi-static measurements of piezoelectric properties of thin films are based on either the direct or the converse piezoelectric effect. While in direct measurements the voltage produced by an applied stress is measured; in the second case the displacement produced by an applied electric field is obtained through different methods.

B.1.1 Techniques based on direct piezoelectric effect

If a piezoelectric film of a material with wurtzite-type structure, as AlN, is supposed, the equation of state 1.14 describes the direct piezoelectric effect.

If stress is applied exclusively in the c-axis direction, without external electric field (see Fig. B.1(a)), the electric displacement is given by:

$$\begin{bmatrix} D_1 \\ D_2 \\ D_3 \end{bmatrix} = \begin{bmatrix} d_{15}.T_5 \\ d_{15}.T_4 \\ d_{31}.T_1 + d_{31}.T_2 + d_{33}.T_3 \end{bmatrix} = \begin{bmatrix} 0 \\ 0 \\ d_{33}.T_3 \end{bmatrix} \tag{B.1}$$

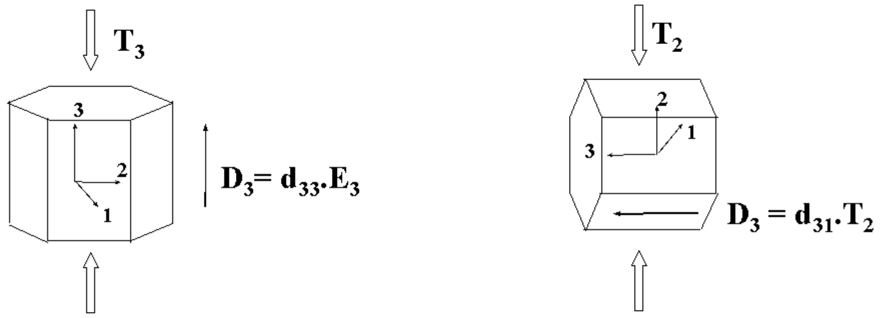

(a) (b)

Figure B.1: Electric displacement (D) associated with an applied stress (T) in a hexagonal wurtzite-type structure: (a) in the c-axis directions (T_3), (b) perpendicular to the c-axis direction (T_2).

Then the piezoelectric coefficient d_{33} can be estimated knowing the applied stress (T_3) and measuring the electric displacement (D_3). Various methods have been described for the measurement of the piezoelectric coefficients by this means.

However, when the stress is applied perpendicular to the c-axis direction (see eq. 1.14), the electric displacement is given by:

$$\begin{bmatrix} D_1 \\ D_2 \\ D_3 \end{bmatrix} = \begin{bmatrix} d_{15}.T_5 \\ d_{15}.T_4 \\ d_{31}.T_1 + d_{31}.T_2 + d_{33}.T_3 \end{bmatrix} = \begin{bmatrix} 0 \\ 0 \\ d_{31}.T_2 \end{bmatrix} \tag{B.2}$$

Then, no electric displacement should be obtained in directions perpendicular to the c-axis direction (D_1, D_2) (see Fig. B.1 (b)). This is the reason why <10$\underline{1}$0> oriented AlN films – i.e. with the c-axis parallel to film surface -, should not show electric displacement in the direction perpendicular to film surface when stress is applied in this last direction.

The followings are different techniques that have been proposed based on the direct piezoelectric effect.

a) Method of the pneumatic pressure rig

In order to measure the longitudinal piezoelectric coefficient d_{33} in <0001> oriented AlN films, a calibrated stress can be applied perpendicular to the film surface and the generated charge collected. This requires the film to be deposited on an electrode (on bottom) and the application of another electrode on top of the film surface.

It has been argued that in these methods the results does not represent the piezoelectric coefficient of the free sample, but an effective coefficient since the film is clamped to the substrate [91]. Moreover, the major obstacle which prevents this kind of measurements for thin films is believed to be the simultaneous bending of the sample when force is applied perpendicular to the film plane to produce a uniaxial stress. As a consequence even a small substrate bending can generate very large biaxial stresses in the piezoelectric thin film, which produces a large amount of electrical charge through the transverse piezoelectric effect. This makes the accurate measurement of the charge induced by the applied uniaxial stress very difficult. On the other hand, the small thickness of the sample makes stress alignment very difficult. In order to solve these problems, a method using a pneumatic pressure rig designed to apply a uniaxial stress to piezoelectric thin films has been proposed (see Fig. B.2). The sample is placed between two fixtures with cavities both above and beneath it. The two cavities are connected so that the pressure inside them is always equal. O-rings are used on both sides of the sample for sealing. By introducing high-pressure nitrogen gas into theses cavities simultaneously, force is imposed which acted uniformly and equally on both sides of the sample, thus a uniform uniaxial compressive stress is applied to it. Because the applied force was balanced everywhere across the faces of the sample, the application of pneumatic pressure would not bend the sample even if it had an initial curvature due to the thermal expansion coefficient mismatch between the piezoelectric film and the substrate.

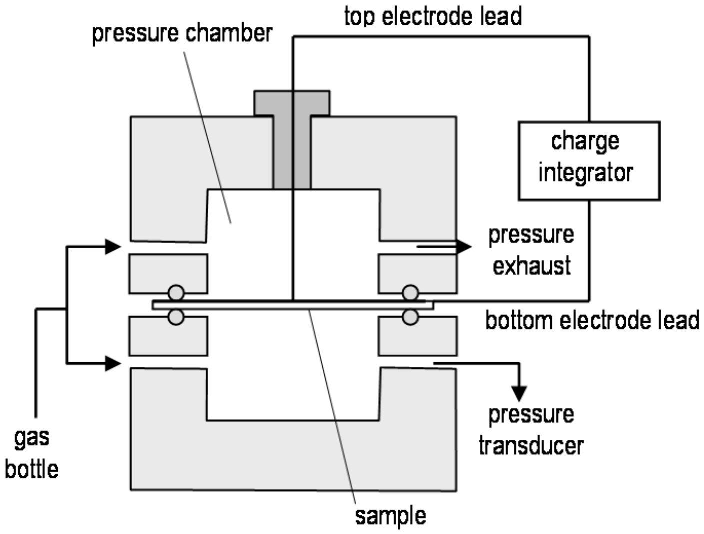

Figure B.2: Experimental setup for d_{33} measurement by the method of the pneumatic pressure rig [91].

The induced charge produced upon applying pressurized gas is collected using a charge integrator which converts the collected charge into a variation of voltage on a capacitor of known size placed in series with the stressed sample.

The effective piezoelectric coefficient of the film is calculated using the equation:

$$d_{33} = \frac{\partial D_3}{\partial T_3} = \frac{\Delta Q}{\Delta P.A} \tag{B.3}$$

where D_3 and T_3 are the electrical displacement and mechanical stress in thickness direction, ΔP is the change of the cavity pressure, ΔQ is the measured electric charge induced by that pressure change, and A is the area of the electrode.

Some authors have evaluated the radial strain associated to the radial stress produced by the o-rings, obtaining the transverse piezoelectric coefficient (d_{31}) in addition to the longitudinal (d_{33}) [117]. The piezoelectric equation is thus given by:

$$D_3 = d_{33}T_3 - 2d_{31}T_r = d_{33}T_3 - 2d_{31}Y\varepsilon_r \tag{B.4}$$

where T_3, T_r are the mechanical stress to the thickness and the radial direction, ε_r the radial strain, Y the Young's modulus of the sample (bulk).

Additionally, since the film is clamped to the substrate the obtained effective d_{33} coefficient can be related with the piezoelectric coefficient of the free sample using some reasonable assumptions [89]. Small relative differences are obtained for measurements based on direct piezoelectric effect.

b) Method of the metallic rod

This method [19, 118] does not required the application of an electrode on top of the film surface and has been designed to make a preliminary quantitative check of the piezoelectric films after the deposition and before the realization of the complete devices (see Fig. B.3). A low-frequency transducer (2 MHz), bonded on one end of a metallic rod, when driven with a short pulse (0.1-1ns) produces a longitudinal wave propagating in the rod. The other end of the rod, shaped as a truncated cone with a small flat tip, is put in contact with the film using a droplet of water. This ensures a good mechanical energy transfer from the rod to the film. The consequent voltage generated in the stressed region is picked up from the bottom metal layer and the rod that acts as ground electrode. In order to evaluate the d_{33} constant, the measured voltage is compared with that obtained from a known thin piezoelectric plate measure in the same conditions. These methods allow tracing a map of the d_{33} coefficient over the deposited area. The sensitivity of the system can be estimated to be 1 pC/N.

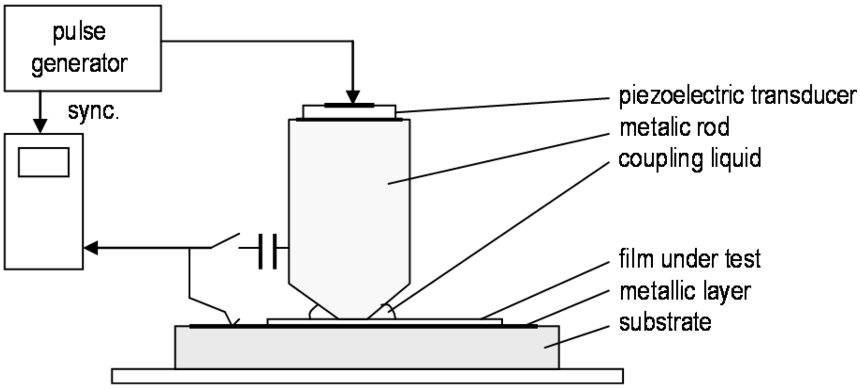

Figure B.3: Experimental setup for d_{33} measurement by the method of the metallic rod [19].

c) Method of the cantilever beam

This technique allows to evaluate the transverse piezoelectric coefficient (in this case the e_{31}) based on the direct piezoelectric effect [19]. The film is deposited on a cantilever beam between two electrodes. The free edge of the cantilever is first statically displaced, causing a bending of it, and then it is suddenly release. The consequent damped oscillation of the cantilever at its natural frequency can be revealed through the voltage appearing between the electrodes. There is a relation of proportionality between the first maximum of the damped oscillation and the e_{31}. A variation of this technique consists of measuring the electrode charge at a frequency imposed by an external exciter moving the free edge of the beam (see Fig B.4).

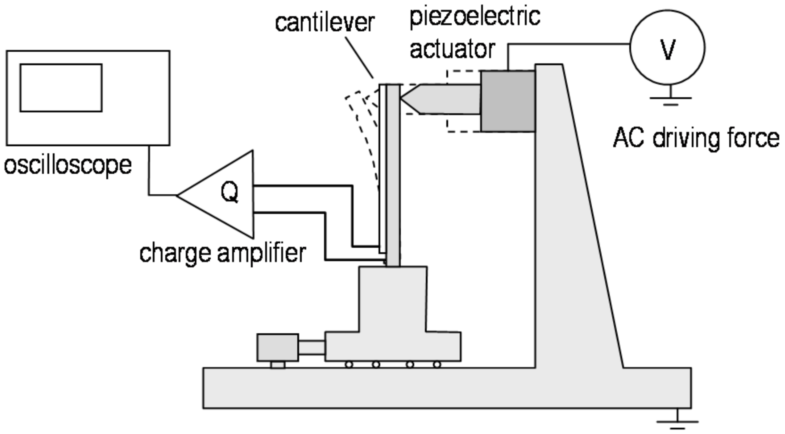

Figure B.4 Experimental setup for the measurement of the transverse piezoelectric coefficient by the method of the cantilever beam [19].

B.1.2 Techniques based on converse piezoelectric effect

The equation of state 1.13 describes the inverse piezoelectric effect for a wurtzite-type structure as AlN.

Then, if the applied electric field has component exclusively in the c-axis direction (E_3), with no external stresses (see Fig. B.5(a)), the strain is given by :

$$\begin{bmatrix} S_1 \\ S_2 \\ S_3 \\ S_4 \\ S_5 \\ S_6 \end{bmatrix} = \begin{bmatrix} d_{31}.E_3 \\ d_{31}.E_3 \\ d_{33}.E_3 \\ d_{15}.E_2 \\ d_{15}.E_1 \\ 0 \end{bmatrix} = \begin{bmatrix} d_{31}.E_3 \\ d_{31}.E_3 \\ d_{33}.E_3 \\ 0 \\ 0 \\ 0 \end{bmatrix} \qquad (\text{B.5})$$

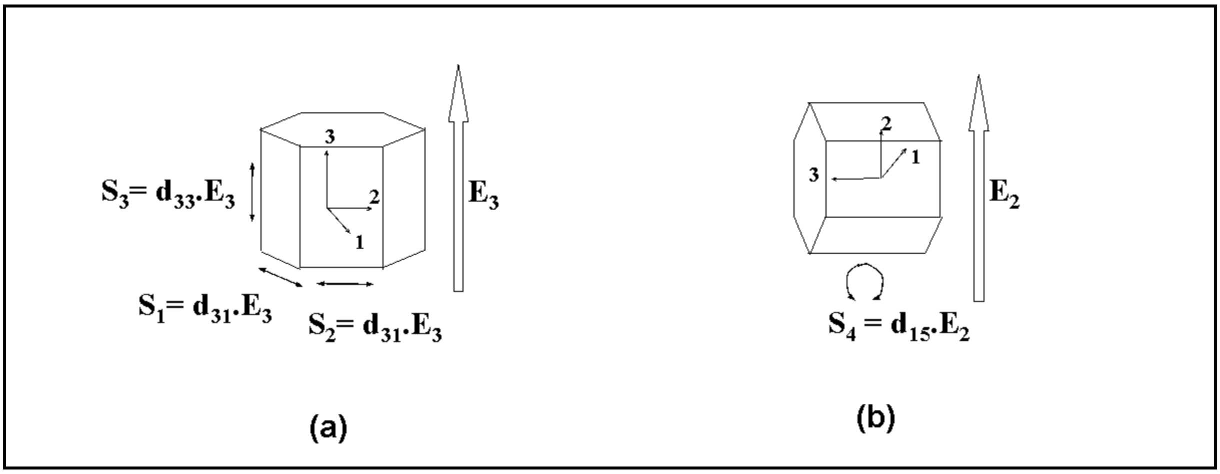

Figure B.5: Strains (S) associated with an applied electric field (E) in a hexagonal wurtzite-type structure: (a) in the c-axis directions (E_3), (b) perpendicular to the c-axis directions (E_2).

Consequently, the piezoelectric coefficient (d_{33}) can be estimated knowing the applied electric field (E_3) and measuring the strain in the same direction (S_3).

When the electric field is applied perpendicular to the c-axis directions (E_1, E_2), no relevant response is expected in the same direction (S_1, S_2) (see eq. 1.13, Fig. B.5 (b)) in accordance with the resulting strain equation:

$$\begin{bmatrix} S_1 \\ S_2 \\ S_3 \\ S_4 \\ S_5 \\ S_6 \end{bmatrix} = \begin{bmatrix} d_{31}.E_3 \\ d_{31}.E_3 \\ d_{33}.E_3 \\ d_{15}.E_2 \\ d_{15}.E_1 \\ 0 \end{bmatrix} = \begin{bmatrix} 0 \\ 0 \\ 0 \\ d_{15}E_2 \\ 0 \\ 0 \end{bmatrix} \tag{B.6}$$

This is the reason why <10$\underline{1}$0> oriented AlN films with wurtzite type structure- i.e. the c-axis parallel to film surface-, should not show stain in the direction perpendicular to the film surface when a voltage is applied en the last direction.

Consequently, in these techniques a defined voltage is applied through the film, and the strain is measured. As the magnitude of the displacements to be measured is in the range of angstroms, sensitive methods able to detect such small deformations must be used, e.g. interferometers or piezoresponse force microscopy (PFM).

a) Double-beam interferometry

Among the various categories of optical interferometers [19, 119], an interesting and reliable one is the double-beam Mach-Zender type in which the difference of the displacements of the two faces of the sample is measured, eliminating the contribution of substrate bending motion (see Fig. B.6). This method has been considered the more confident for the determination of piezoelectric constants, and its results have been employed as references in the development of the other techniques.

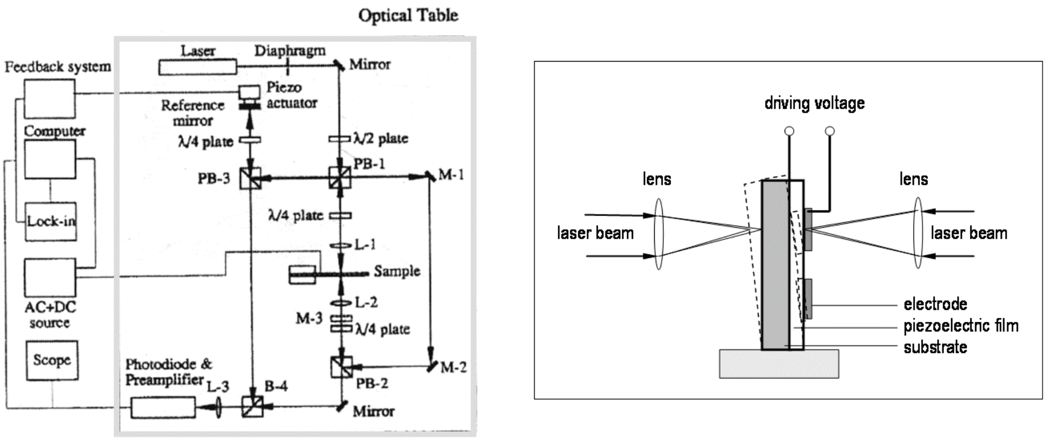

Figure B.6: Schematic of the double-beam interferometer (a) and principle of elimination of bending motion of the substrate (b) [19].

b) Piezoresponse force microscopy

In this promising technique the voltage is applied directly between the electrode under the film and the atomic force microscope tip. Various configurations have been presented, in order to minimize the effect of the applied electric field with the microscope tip. Fig. 5.3 shows a particular set up.

Since the film is clamped to the substrate the obtained effective d_{33} coefficient can be related with the piezoelectric coefficient of the free sample using some reasonable assumptions [89]. Significant relative differences are obtained for measurements based on inverse piezoelectric effect (see section 5.2.4.1).

B.2 Dynamic measurements

These methods are based on the evaluation of the performance of BAW or SAW devices constructed with the piezoelectric films. As these applications are of main interest, they are of great importance.

Typically, the frequency response of the device is measured using a Network Analyzer. Based on this, the electromechanical coupling coefficient, acoustic velocity and other parameters can be estimate using the appropriate model for the response (see Appendix A) [24, 8].

In the particular case of SAW devices, the determination of the characteristic frequency with the surface between the IDTs metalized and non-moralized, allows for the estimation of the electromechanical coupling coefficient in accordance with its definition (see Appendix A) [13, 8]. Additionally, models of the frequency response can be used to obtain the relevant parameters.

Appendix C

A MODEL OF THE ELECTRIC FIELD UNDER THE ELECTRODES

The electric field distribution under the IDTs of SAW devices was consider relevant in order to explain the frequency response obtained for devices based on different AlN films. Therefore, the finite differences method was used to solve the differential equations that describe this phenomenon, under different configurations of interest.

C.1 The problem

The basic configuration of interdigital electrodes that compose the SAW device are supposed as shown in Fig. A.18. The rate value electrode size to distance between electrodes is fixed in accordance with the used geometry. The electrodes are placed on the surface of a dielectric film with variable thickness, i.e. the AlN film, which is deposited over an electrical conductive substrate. Adjacent electrodes are considered with opposite electrical potential in a given moment. Then, the object of the problem is to find the electric potential distribution and consequent electric field distribution in the film profile. Since, the length of the electrodes is substantially higher than the other dimensions – i.e. electrode width, distance between electrodes or film thickness - , a two dimensional analysis in the x-z plane can be done to solve the problem. Additionally, the symmetry elements allow restricting the analysis to the indicated portion of the profile (see Fig. C.1).

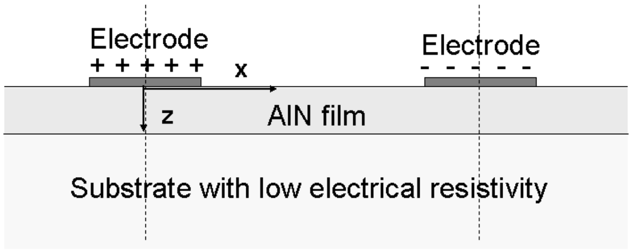

Figure C.1: Sketch for the profile of two adjacent electrodes of an IDT in the prepared SAW devices.

C.2 Fundamental Equations

In the case of the presented configuration the charge distribution can be assumed to be concentrated on the conductive surfaces of the electrodes. Thus, as a consequence of the conservation of charge in a medium with uniform value of electric conductivity, the Laplace's equation describes the electric potential distribution in the film profile, [120]:

$$\nabla^2 \Phi = 0 \tag{C.1}$$

where: Φ : electric potential (V).

The electric field in each point of the same region can be obtained from [113]:

$$\vec{E} = -\nabla \Phi \tag{C.2}$$

where: E : electric field (V/m).

C.3 Finite differences method

The finite differences method is used to solve the fundamental equation to our particular geometry. This method divides the region of interest by a regular grid, and approximates the Laplace´s equation at each grid-point [121]. Then, the resulting equations are solved by iteration.

The Laplace´s equation of electric potential for two dimensions x-z is given by:

$$\frac{\partial^2 \Phi}{\partial x^2} + \frac{\partial^2 \Phi}{\partial z^2} = 0 \tag{C.3}$$

Thus, it is possible to found an expression that relates the potential at the point (x,y) of the grid with its value at the adjacent points, using the Taylor series development [121]:

$$\Phi(x,z) = \frac{1}{4}\{\Phi(x+h,z) + \Phi(x-h,z) + \Phi(x,z+h) + \Phi(x,z-h)\} + O(h^4) \tag{C.4}$$

where $O(h^4)$ is a residual term with fourth order.

Then, the solution is estimated by fixing the values of the grid-points in accordance with the boundaries conditions and iterating the potentials until the results agree within the desired tolerance.

An over-relaxation parameter λ is introduced in order to speed the convergence of the iterations. Then,

$$\begin{aligned}&\Phi_{n+1}(x,z) = \Phi_n(x,z) + \\ &(\lambda+1)\left\{\frac{1}{4}[\Phi_n(x+h,z)+\Phi_n(x-h,z)+\Phi_n(x,z+h)+\Phi_n(x,z-h)] - \Phi_n(x,z)\right\}\end{aligned} \tag{C.5}$$

where: Φ_{n+1}: electric potential value for the n+1 iteration, Φ_n: electric potential values for the n iteration.

The electric field for two dimensions x-z:

$$\vec{E} = -\vec{i}_x \frac{\partial \Phi}{\partial x} - \vec{i}_z \frac{\partial \Phi}{\partial z} \tag{C.6}$$

Thus, for each point of the grid the electric field can be estimated in accordance with:

$$\overrightarrow{E_x}(x,z) = -\left\{\frac{\Phi(x+h,z) - \Phi(x-h,z)}{2h}\right\} \tag{C.7}$$

$$\overrightarrow{E_z}(x,z) = -\left\{ \frac{\Phi(x,z+h) - \Phi(x,z-h)}{2h} \right\} \tag{C.8}$$

C.4 Results

Results corresponding to two extreme situations are present in the following, in order to visualize the effect of the thickness of the dielectric film on electric potential and electric field distribution.

First, the distributions for the case of a rate value thickness to distance between electrodes of 0.15 are analyzed, which corresponds to the geometry of the essayed SAW devices with 1μm AlN films.

Second, the distributions for the case of a rate value thickness to distance between electrodes of 3 are analyzed, which corresponds to a thickness of dielectric film in the rank of 20 μm, if the electrodes size is maintain.

The comparison between the electric potential distributions around the electrodes (see Figs. C.2 and C.3 (up)) shows a higher concentration of gradient under the electrodes for the first case, in vertical sense. However, in the second case the gradient is more concentrated between the electrodes, with higher contribution of the horizontal direction (x).

Figures C.2 and C.3 (down) show the electric field distributions under the electrodes, in the dielectric material, in accordance with the previous observations.

Then, the model of the electric field have allowed to predict the electric field distribution previously discuss (see section 8.3) and consequently confirm the effect of the geometry of the device.

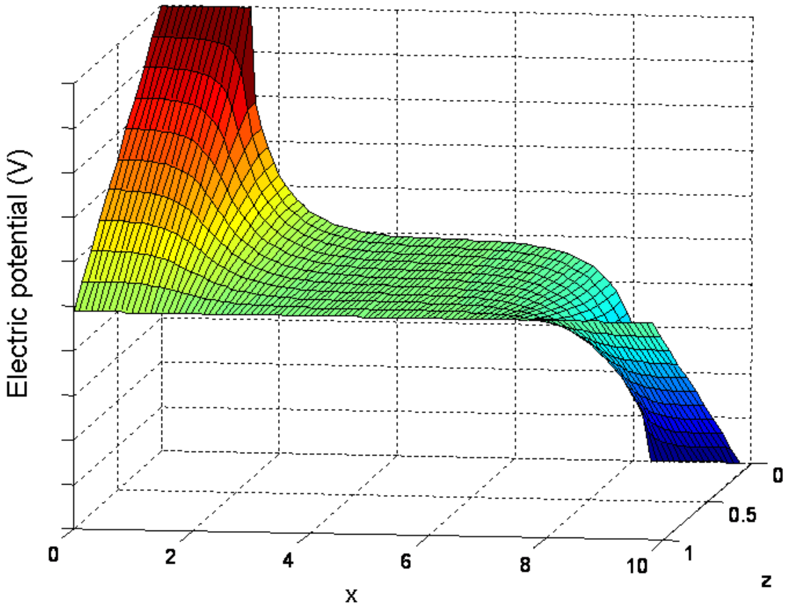

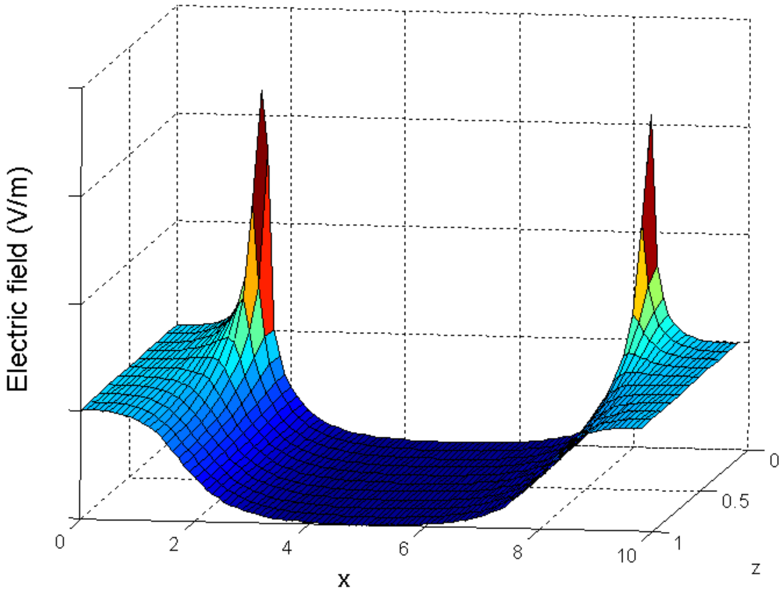

Figure C.2: Electric potential (up) and electric field distribution (down) under the electrodes in the film profile for a 1 µm film thickness.

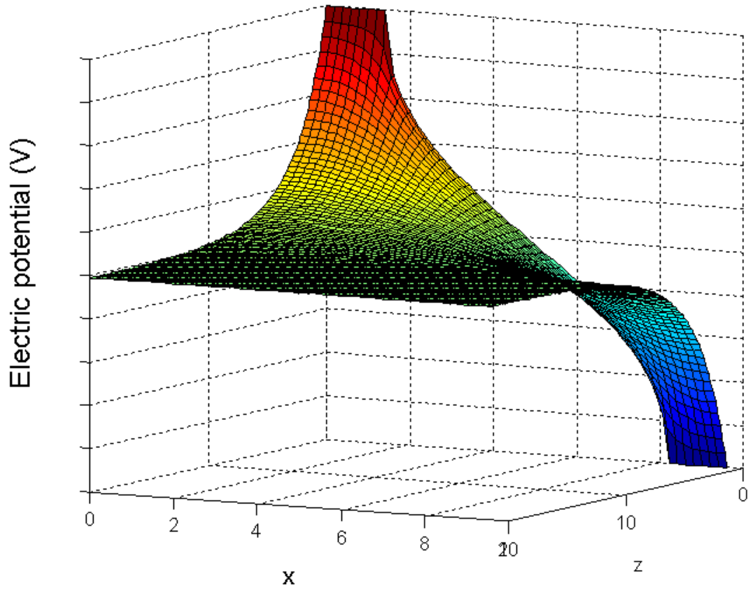

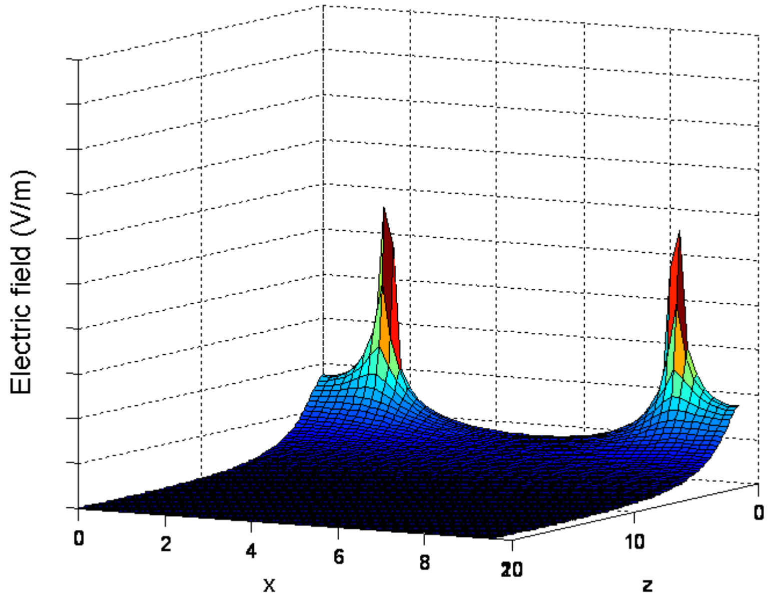

Figure C.3: Electric potential (up) and electric field distribution (down) under the electrodes in the film profile for a 20 µm film thickness.

Resumen ejecutivo

PELÍCULAS DELGADAS PIEZOELECTRICAS DE NITRURO DE ALUMINIO POR PECVD

Un sólido es piezoeléctrico si se polariza eléctricamente bajo la acción de una fuerza mecánica (efecto directo), y se deforma mecánicamente cuando se aplica un campo eléctrico sobre él (efecto inverso). El origen de este fenómeno está en la estructura cristalina del sólido, y particularmente en la simetría de la misma. La distribución de densidad electrónica no uniforme en los enlaces entre los átomos genera un arreglo periódico de dipolos en la red cristalina. Cuando se aplica una fuerza, la deformación generada en el cristal crea cambios en los largos y direcciones de los enlaces entre los átomos de la red. Como consecuencia, se producen cambios en las magnitudes y direcciones de los dipolos individuales. Este hecho puede conducir a una polarización neta de la red cristalina, dando lugar al efecto piezoeléctrico. Como consecuencia, este efecto está presente en 20 de las 21 estructuras cristalinas no-centro-simétricas. Dado que la piezoelectricidad implica un acoplamiento lineal entre los sistemas mecánico y eléctrico, las ecuaciones de estado que describen el fenómeno se pueden representar como:

$$S_{\alpha} = s^{E}_{\alpha\beta}.T_{\beta} + d_{i\alpha}.E_{i} \quad (1)$$

$$D_{i} = d_{i\alpha}.T_{\alpha} + \varepsilon^{T}_{ij}.E_{j} \quad (2)$$

con i, ,j = 1, 2, 3 y α, β = 1, 2, …6; siendo S : deformación (m/m), D : desplazamiento eléctrico (C/m^2), T : tensión (N/m^2), E : campo eléctrico (V/m), s^E : constante elástica (m^2/N), ϵ^T : constante dieléctrica (F/m) y d : constante piezoeléctrica (m/V).

Como consecuencia del empleo generalizado de las energías mecánica y eléctrica en la vida cotidiana, los materiales piezoeléctricos ofrecen un gran potencial en el desarrollo de dispositivos para numerosas aplicaciones. Los dispositivos electroacústicos basados en materiales piezoeléctricos -ampliamente empleados como osciladores, sensores, y resonadores- presentan actualmente su mayor demanda en la industria de las telecomunicaciones. En el sector de las comunicaciones inalámbricas, existe un importante consumo de filtros para el control de la frecuencia de operación del dispositivo en cuestión, normalmente componentes del tipo “surface acoustic wave” (SAW) y “bulk acoustic wave” (BAW). La frecuencia característica de operación de los mismos (f, en s^{-1}) es la dada por la expresión:

$$f = \frac{V}{\lambda_0} = \frac{V}{2d} \tag{3}$$

donde: V es la velocidad de onda acústica en el material (m/s), λ_0 la longitud de onda (m) y d la dimensión característica del dispositivo.

El marcado crecimiento de los sistemas de comunicación ha generado la necesidad de emplear frecuencias cada vez más elevadas hasta, actualmente, el rango de los GHz, v.g. microondas. El aumento de la frecuencia (f) de operación del dispositivo se consigue, para un dado material, reduciendo sus dimensiones (d).

Esto se ha logrado a costos razonables mediante el empleo de películas delgadas piezoeléctricas, para las cuales las técnicas de obtención adecuadas abren la posibilidad de unificar las tecnologías de circuitos integrados y de dispositivos electro-acústicos.

Las características buscadas en un material adecuado para la fabricación de películas delgadas piezoeléctricas para estas aplicaciones son: alto acoplamiento piezoeléctrico, alta velocidad de onda acústica, estabilidad térmica, y baja rugosidad superficial.

El nitruro de aluminio es un material piezoeléctrico debido a su estructura cristalina hexagonal tipo wurtzita, y al mismo tiempo presenta una velocidad de onda acústica particularmente elevada debido a sus excelente propiedades mecánicas. Además de poseer una excelente estabilidad térmica, se caracteriza por su alta conductividad térmica, y un elevado “band gap”, de 6,2 eV siendo un excelente aislante eléctrico cuando se encuentra puro y el compuesto es estequiométrico.

El desempeño de las películas delgadas de nitruro de aluminio para aplicaciones piezoeléctricas está directamente relacionado con la microestructura y composición de las mismas. Aunque en la situación ideal sería deseable emplear películas monocristalinas para estas aplicaciones, las películas policristalinas con orientación preferencial respecto al plano del sustrato tienen un desempeño excelente siendo su producción mucho más sencilla y económica.

Los dispositivos BAW se basan en la generación de ondas acústicas longitudinales perpendiculares a la película. Como consecuencia, filmes delgados orientados en la dirección <0001>, con el eje *c* perpendicular a la superficie del sustrato, son los preferidos de manera de optimizar el acoplamiento piezoeléctrico. Para los dispositivos SAW, basados en ondas acústicas de superficie, se emplean filmes con la misma orientación, aunque se ha sugerido la conveniencia de utilizar también la orientación <10$\underline{1}$0> con el eje *c* paralelo a la superficie del sustrato.

El grado de orientación de las películas delgadas policristalinas de AlN constituye un parámetro importante de la microestructura ya que está directamente relacionado con el desempeño piezoeléctrico del componente fabricado. La configuración Bragg-Brentano $\theta/2\theta$, tradicionalmente empleada en el análisis por difracción de rayos X (DRX), muestra en el difractograma las reflexiones correspondientes a los planos paralelos al sustrato, constituyendo así una primera indicación de la orientación preferencial del la película. Pueden emplearse también otras técnicas para obtener una medida más fina de la dispersión en la orientación de la película respecto a la dirección de referencia, para las cuales el ancho a la altura media (FWHM) de la curva obtenida es una medida directa del la dispersión en la orientación normalmente empleada como referencia. Aunque en general se ha relacionado este último parámetro con el desempeño piezoeléctrico, estudios recientes han sugerido que esa correlación no existe en todos los casos. La razón de esta ausencia de correlación es asignada a la presencia granos con polaridades cristalográficas opuestas, denominados dominios de inversión, indistinguibles mediante DRX, y difíciles de identificar por otros medios.

Varias técnicas han sido empleadas para obtener películas delgadas de AlN, como MBE (Molecular Beam Epitaxy), MOCVD (Metal-Organic Chemical Vapor Deposition), o PVD (Physical Vapor Deposition) obteniéndose en cada caso diferentes tipos de microestructuras, desde monocristalinas a policristalinas e incluso amorfas. La obtención de películas monocristalinas implica elevadas temperaturas o tiempos de deposición incompatibles con los objetivos económicos necesarios para la fabricación de dispositivos de uso masivo.

Entre las técnicas disponibles para la obtención de filmes policristalinos, las que emplean un plasma, v.g. las “asistidas por plasma”, son particularmente importantes ya que permiten reducir la temperatura de procesamiento. Teniendo en cuenta que un plasma es un gas quasi-neutro compuesto de electrones libres, iones y especies neutras que exhibe un comportamiento colectivo, los plasmas de baja densidad poseen la propiedad particular de presentar las diferentes especies en equilibrio térmico independiente. Como consecuencia, los electrones y las especies pesadas presetan temperaturas asociadas muy diferentes. Este tipo de plasma proporciona la energía de activación para las reacciones químicas a través de colisiones inelásticas de los electrones libres de alta energía con las especies reaccionantes, manteniendo simultáneamente una temperatura de sustrato relativamente baja. Adicionalmente se pueden generar efectos sobre la microestructura de las películas controlando el bombardeo de iones positivos sobre la película antes y durante la deposición.

Dentro de las técnicas asistidas por plasma se encuentran las PVD (Physical Vapor Deposition) asociadas con la transferencia de material desde un material blanco (target) por evaporación o “sputtering”, y las CVD (Chemical Vapor Deposition) que involucran el ingreso de compuestos volátiles químicamente reactivos a la cámara de reacción. Las técnicas PECVD (Plasma Enhanced Chemical Vapor Deposition), y en particular las que emplean excitación por microondas para generar el plasma, ofrecen numerosas ventajas: a) disponibilidad de diversos parámetros a ajustar para alcanzar la optimización de las propiedades de las películas, b) posibilidad de minimizar los efectos de contaminación debido a la ausencia de un electrodo en la cámara de reacción, c) posibilidad de deposición sobre sustratos con geometrías más complejas, al ser procesos de deposición menos direccionales que los de “sputtering”.

A pesar de las ventajas enumeradas, la técnica PECVD con excitación por microondas no ha sido muy empleada, y tampoco se ha informado la capacidad de controlar la orientación del film, como <0001> o <10$\underline{1}$0>, cuando esta técnica ha sido empleada. Como consecuencia, el objetivo del presente trabajo es la determinación del efecto de las diferentes variables del proceso con el fin de obtener películas delgadas de nitruro de aluminio piezoeléctricas orientadas en las dos orientaciones referidas.

Procedimiento experimental

Obleas de sustrato con dimensiones de 30 mm x 10 mm y espesor 525 µm fueron empleadas como sustrato para la deposición de las películas delgadas. Las obleas fueron lavadas con etanol y acetona previamente a su colocación en la cámara del reactor. Se empleó un reactor PECVD con excitación por microondas, con el portasustrato polarizable mediante radiofrecuencia, y calefacción para controlar la temperatura del sustrato. La superficie del sustrato fue limpiada in situ empleando un plasma de Ar, previo a la deposición. Las películas de AlN fueron depositadas empleando un plasma de nitrógeno, en el cual fue inyectado TMA (tri-metil-aluminio) usando Ar como gas de transporte. Las condiciones experimentales empleadas se muestran en la Tabla 1.

Tabla 1: Condiciones experimentales para la obtención de AlN.

Variable	Pre-tratamiento	Deposición de AlN
Potencia de microondas (kW)	1,0	1,6
Flujo de argón (sccm(#))	100	50
Flujo de nitrógeno (sccm)	0	125
Potencial de polarización RF (V)	- 100	-200V - flotante
Presión de la cámara (Pa)	0,8	0,5 – 8
Tiempo de procesamiento (min)	15	2 – 45
Flujo de TMA (sccm)		1
Distancia plasma-inyector (cm)		3 - 11
Temperatura de sustrato (°C)		400 – 800
Distancia inyector-sustrato (cm)		4 - 10
Sustrato		Si(100), Si(111), Pt(111)/Si(100)

(#) Standard cubic centimeters per minute

El trabajo experimental efectuado se puede dividir en tres etapas principales:

a) Crecimiento de películas delgadas de AlN policristalinas orientadas

Siete variables diferentes fueron tomadas inicialmente para producir y optimizar las propiedades del film, i.e. potencial de polarización RF, distancia plasma-inyector, temperatura de sustrato, presión total de la cámara, distancia inyector sustrato, tiempo de procesamiento y tipo de sustrato. Dado que un diseño experimental completo resultaba excesivo para verificar el efecto de todas las variables y sus interacciones, se efectuó un trabajo preliminar para conocer la influencia de la distancia plasma-inyector y potencial de polarización RF. Luego que los valores adecuados de estas dos variables fueron escogidos, el resto de las variables fueron exploradas usando varios niveles en cada caso.

b) Optimización de las propiedades de las películas

Se efectuaron corridas experimentales adicionales para optimizar el desempeño de las películas en aplicaciones electroacústicas, tomando los resultados anteriores como referencia. Se efectuó un diseño experimental completo para temperatura de sustrato y presión total con el fin de optimizar el desarrollo de las películas orientadas <10$\underline{1}$0>. El espesor de las películas y el potencial de polarización fueron explorados separadamente empleando varios niveles en cada caso con el fin de optimizar el desarrollo de películas orientadas <0001>. Una caracterización más fina de la microestructura de las películas, así como la medida de su desempeño piezoeléctrico, fueron efectuadas en esta etapa. Esto fue complementado por la caracterización del plasma de proceso en diferentes condiciones de deposición mediante epectroscopia óptica de emisión (OES).

c) Aplicación dispositivos electroacústicos

Dispositivos electroacústicos tipo SAW fueron preparados empleando películas delgadas de AlN orientadas <0001> y <10$\underline{1}$0> en condiciones óptimas, así como dispositivos electroacústicos tipo BAW con películas orientadas <0001>. La respuesta de frecuencia de estos dispositivos fue medida y se emplearon modelos para explicar los resultados obtenidos en cada caso.

Los diagramas $\Theta/2\Theta$ de difracción de rayos X (DRX) fueron obtenidos entre 15° y 80° (2Θ). Se obtuvieron medidas de la dispersión de las orientaciones para los filmes mono-orientados, v.g. “rocking curves”, y sus anchos a la altura media (FWHM) fueron estimados para evaluar el grado de orientación.

Se empleó espectroscopía infrarroja con transformada de Fourier (IRTF), en modo transmisión entre 4000 cm^{-1} y 400 cm^{-1}, usando el espectro del sustrato de Si como referencia y en modo de reflexión.

La morfología superficial de las películas fue analizada por microscopía de fuerza atómica (AFM). El coeficiente de rugosidad S_a, i.e. la media aritmética del valor absoluto de la rugosidad superficial, fue determinado por AFM.

Las muestras producidas y sus superficies de fractura fueron observadas por microscopía electrónicas de barrido (MEB). Se empleó microscopía electrónica de transmisión del alta resolución y SAED para un estudio fino de la microestructura del perfil de las películas.

Se analizó la composición de las películas emplenado la técnica RBS (Rutherford Backscattering Spectrometry) para determinar el contenido de aluminio, NRA (Nuclear Reaction Analysis) para determinar los contenidos de carbono, nitrógeno y oxigeno, así como la técnica XPS (X-ray Photoelectron Spectroscopy) para el análsis de las superficies.

La respuesta piezoeléctrica de las películas fue evaluada empleando la técnica PFM (Piezoresponse Force Microscopy), basada en el efecto piezoeléctrico inverso. En base a esta información se estimó el coeficiente d_{33} del material.

Se fabricaron dispositivos SAW con las películas obtenidas y longitud de onda acústica 20 µm, siguiendo un procedimiento de microlitografía convencional. Asimismo se fabricaron dispositivos BAW experimentales. Se determinó la repuesta en frecuencia de los mismos, midiendo el parámetro de transmisión S_{21}, con un analizador de redes vectorial.

El plasma de reacción fue caracterizado por espectroscopia óptica de emisión (OES) entre 350 nm y 850 nm.

Resultados y discusión

Películas delgadas de nitruro de aluminio policristalinas y con orientación preferencial fueron obtenidas empleando la técnica de deposición MW-PECVD. Mediante la adecuada selección de los parámetros de proceso, fue posible producir películas orientadas <0001> o $<10\underline{1}0>$, ambas de interés para aplicaciones piezoeléctricas.

La reducción de la distancia entre el plasma y el inyector de precursor, lograda mediante una modificación en la configuración estándar del reactor, permitió mejorar el desarrollo cristalino de las películas.

El incremento de la temperatura de sustrato fue determinante para mejorar el desarrollo cristalino de las películas y reducir su contenido de impurezas.

Mientras que no se observó evidencia de efectos epitaxiales trabajando con diferentes sustratos, el análisis de perfil de las películas mostró una progresiva mejora del desarrollo cristalino con el aumento de espesor.

La selección de la presión de trabajo permitió controlar la orientación preferencial, obteniéndose películas orientadas <0001> a bajas presiones y orientadas <10$\underline{1}$0> a altas presiones.

Cuando se aplicaron altos potenciales de polarización RF se obtuvieron películas amorfas con elevadas tensiones residuales compresivas. Mientras que todas las películas obtenidas con potencial flotante habían mostrado tensiones residuales de tracción, el empleo de bajos potenciales de polarización RF permitió la reducción de esa tensión de tracción y la producción de películas con mayores espesores, manteniendo simultáneamente la microestructura buscada.

Varias evidencias fueron obtenidas relacionadas con los mecanismos generales que controlan el desarrollo cristalino y la orientación preferencial en esta técnica de deposición MW-PECVD.

El incremento de las concentraciones de las especies más energéticas y consecuentemente activas cerca del sustrato, derivada de la reducción de la distancia plasma-inyector, favoreció el desarrollo cristalino.

El incremento de la temperatura de sustrato durante el crecimiento de film incrementó los efectos difusionales de las especies que alcanzan la superficie, al mismo tiempo que favoreció la desorción de impurezas asociadas a la descomposición del precursor (tri-metil-aluminio). De este modo, el desarrollo cristalino fue favorecido. Además, el incremento de la temperatura favoreció la orientación <0001> de las películas a bajas presiones ya que esta es la orientación termodinámicamente más favorable debido a que permite la minimización de la energía superficial.

Al comienzo de la deposición de la película no hubo evidencia de efectos epitaxiales, el crecimiento de la película comenzó en forma aleatoria y posteriormente la orientación mejoró en forma progresiva con el incremento de espesor. Esta mejora fue evidentemente favorecida a mayores temperaturas.

El incremento de la presión permitió la obtención de la orientación <10$\underline{1}$0> asociada a la reducción del paso libre medio de las especies en la cámara del reactor. La formación de dímeros Al-N ha sido encontrada como el mecanismo más adecuado para explicar este fenómeno, ligado a efectos cinéticos de la deposición de las especies. Aunque los dímeros no fueron posibles detectar con las técnicas de análisis empleadas, su presencia en el medio de reacción no pudo ser descartada.

Mientras que la orientación exclusiva <0001> se desarrolló con bajas presiones solamente altas temperaturas, la orientación exclusiva <10$\underline{1}$0> se desarrolló con elevada presiones pero a todas las temperaturas. Esto es una evidencia de los diferentes tipos de mecanismos que controlan ambos fenómenos. Más aún, la observación de orientación exclusiva <10$\underline{1}$0> a todas las temperaturas para altas presiones favorece la teoría de formación de dímeros Al-N respecto a otros posibles mecanismos que han sido propuestos para crecimiento de películas.

El efecto de empleo de potenciales de polarización RF ha mostrado la posibilidad de controlar la tensiones residuales de tracción, pero al mismo tiempo ha puesto en evidencia otro mecanismo para controlar la orientación preferencia de los filmes. El desarrollo de elevadas tensiones residuales compresivas ha favorecido el cambio desde orientación <0001> a <10$\underline{1}$0>, asociado a la relajación de esas tensiones compresivas de la estructura. Aunque este fenómeno ocurrió en condiciones de bajo desarrollo cristalino, no interesante para las aplicaciones en curso en primera aproximación, es una opción que debería ser estudiada más profundamente para estas u otras aplicaciones.

Cuando los resultados fueron comparados con los obtenidos con una técnica de deposición PVD sputtering (Physical Vapor Depsition), algunas coincidencias fueron observadas relacionadas con los efectos generales de los parámetros de proceso, como la presión y el potencial de polarización del portasustrato. Estos hechos muestran que debería haber algunas similitudes entre los mecanismos de crecimiento en ambas técnicas. Pero simultáneamente hay algunas diferencias sustanciales que fueron evidenciadas por las temperaturas de sustrato necesarias en ambos casos. En los procesos PVD hay una contribución sustancial de la energía cinética de las especies proyectadas desde el blanco que llegan al sustrato, lo cual favorece los efectos difusionales. Este efecto puede sustituir la contribución de la temperatura necesaria en los procesos PECVD, y permitir trabajar a menores temperaturas de sustrato en los procesos PVD.

En la técnica PVD sputtering las condiciones del proceso deben ser adecuadamente optimizadas para generar las especies activas en el plasma. En el caso de los procesos PECVD tanto la alta reactividad el precursor de Al como la excitación proporcionada por el plasma favorecen de generación de especies activas. Pero, en los procesos PECVD hay simultáneamente una desventaja: los productos secundarios del precursor pueden ser incorporados a la película y consecuentemente deben ser desorbidos de la misma durante el proceso de deposición. Por otra parte, del oxígeno es una impureza importante presente en ambos procesos que debe se minimizada.

La tabla 2 siguiente muestra las condiciones óptimas de procesamiento encontradas para la obtención de películas con microestructura favorable a un adecuado desempeño piezoeléctrico.

Tabla 2 : Condiciones óptimas de proceso para la deposición de AlN

Variable	Deposición de AlN
Potencia de microondas (kW)	1,6
Flujo de nitrógeno (sccm)	125
Flujo de argón (sccm)	50
Flujo de TMA (sccm)	1
Distancia plasma-inyector cm)	3
Distancia inyector-sustrato (cm)	4
Potencial de polarización RF (V)	flotante*
Temperatura de sustrato (℃)	800
Presión de la cámara (Pa)	1 (para orientados<0001>) 8 (para orientados<10$\underline{1}$0>)

*Hasta espesores de 1,5 µm, y +10V hasta espesores de 2,5 µm.

Las películas orientadas <0001> obtenidas por MW-PECVD en condiciones óptimas mostraron una marcada estructura columnar con tamaños de grano en el orden de 40 nm, valores mínimos de FWHM de “rocking curve” de 8º, rugosidades menores de 20 nm y tensiones residuales de tracción menores a 1 GPa. Estas películas fueron caracterizadas en su desempeño piezoeléctrico por un método basado en el efecto inverso- v.g. PFM-, así como mediante la construcción de dispositivos SAW y BAW. Los resultados mostraron respuestas piezoeléctricas significativas en todos los caso, con valores óptimos de coeficientes piezoeléctricos d_{33} – e.g. 5.8 ± 1.2 pm/V -, evaluados por PFM, y velocidades de onda acústica- e.g.

5.05 ± 0.01 km/s-, para ondas acústicas de superficie. Estos desempeños observados son indicativos de la ausencia de concentraciones significativas de dominios de inversión en la microestructura de estas películas.

La evaluación del efecto de diferente parámetros sobre el coeficiente piezoeléctrico, como la temperatura de sustrato, el espesor de película y el potencial de polarización del portasustrato RF permitieron confirmar la importancia del desarrollo cristalino y el grado de orientación en el desempeño piezoeléctrico de las películas. El efecto del espesor a la temperatura óptima de proceso fue posible de correlacionar con el desempeño piezoeléctrico a través de la construcción de dispositivos SAW. La minimización de las tensiones residuales compresivas con la aplicación de bajos potenciales de polarización RF mostró la posibilidad de obtener mayores espesores con apropiada micoestructura y coeficientes piezoeléctricos óptimos. Las diferencias en la microestructura, grado de orientación y tenor de impurezas de oxígeno fueron directamente relacionados con el desempeño piezoeléctrico obtenido cuando las técnicas PECVD y PVD sputtering fueron comparadas.

El diagnóstico de plasma de proceso por OES ha permitido identificar varias especies presentes en el medio de reacción como as Al, Al+, N_2, N_2+, N directamente relacionados con el crecimiento del film. Simultáneamente, otras especies correspondientes a productos secundarios del precursor como CN, NH, H fueron identificados. Estos resultados fueron consistentes con la banda de impurezas FTIR observada en los filmes de AlN obtenidos por PECVD en el entorno de 2150 cm^{-1}, la cual ha sido asignada a especies CN, Al-H o Al-N_2 en la bibliografía, entre otras posibilidades. Adicionalmente, fue posible evaluar el efecto favorable de la potencia de microondas en la generación de especies activas así como explicar el efecto negativo de adicionar hidrógeno en ese sentido. Además, menor temperatura electrónica y menores concentraciones de especies activas atómicas fueron estimadas a altas presiones, lo cual podría relacionarse con el menor desarrollo cristalino observado para los filmes orientados <10$\underline{1}$0>. Asimismo, la reducción de la temperatura electrónica con la distancia al plasma fue confirmada.

Las películas orientadas <10$\underline{1}$0> obtenidas por MW-PECVD en condiciones óptimas mostraron una estructura no columnar con tamaños de grano en el orden de los 20 nm, valores mínimos de FWHM de “rocking curve” de 11º y rugosidades menores a 10 nm. Estas películas no mostraron respuesta piezoeléctrica significativa para las configuraciones ensayadas. Este era el resultado esperado para el método PFM de acuerdo al tensor piezoeléctrico del nitruro de aluminio con estructura cristalina tipo wurtzita. Por otra parte, la ausencia de respuesta obtenida en la configuración SAW estándar ensayada no descarta el desempeño adecuado con otras dimensiones del dispositivo. El campo eléctrico bajo los electrodos de las configuraciones SAW fue modelado con el fin de mostrar que estas películas podrían mostrar respuesta con otras geometrías más difíciles, pero posibles de construir. Si este no fuera el caso y estas películas no tuvieran un adecuado desempeño piezoeléctrico, la razón debería buscarse en el menor desarrollo cristalino o la posible inversión de dominios en el plano de la superficie. Todas estas razones han contribuido posiblemente a la ausencia de trabajos publicados donde sea evaluada el desempeño de las películas orientadas <10$\underline{1}$0> en dispositivos SAW a pesar de ser considerados la orientación óptima por varios autores.

Résumé étendu

COUCHES MINCES PIEZOELECTRIQUES DE NITRURE D'ALUMINIUM PAR PECVD

Un solide est piézoélectrique quand il se polarise électriquement sous l'action d'une force mécanique (effet direct) et est déformé mécaniquement quand un champ électrique lui est appliqué (effet inverse).

L'origine de ce phénomène provient de la structure cristalline du solide et particulièrement de sa symétrie. La distribution de densité électronique non uniforme des liaisons entre les atomes produit un arrangement périodique des dipôles du réseau cristallin. Quand une force est appliquée, la déformation générée dans le cristal crée des changements dans les longueurs et directions des liaisons entre les atomes du réseau. En conséquence, des changements des normes et des directions des dipôles individuels sont induits. Ce phénomène peut conduire à une polarisation nette du réseau cristallin, et donner lieu à l'effet piézoélectrique. Cet effet est présent dans 20 des 21 structures cristallines non–centrosymétriques. Vu que la piézoélectricité implique un couplage linéaire entre les systèmes mécanique et électrique, les équations d'état qui décrivent le phénomène peuvent s'écrire comme suit :

$$S_\alpha = s^E_{\alpha\beta}.T_\beta + d_{i\alpha}.E_i \qquad (1)$$

$$D_i = d_{i\alpha}.T_\alpha + \varepsilon^T_{ij}.E_j \qquad (2)$$

avec i, j = 1, 2, 3 et α, β = 1, 2, …6, *S* : déformation (m/m), *D* : déplacement électrique (C/m^2), *T* : contrainte (N/m^2), *E* : champ électrique (V/m), s^E : constante élastique (m^2/N), ϵ^T : constante diélectrique (F/m) et *d* : constante piézoélectrique (m/V).

Etant donné l'emploi généralisé des énergies mécaniques et électriques dans la vie quotidienne, les matériaux piézoélectriques offrent un grand potentiel pour le développement de dispositifs dans de nombreuses applications électroniques. Les dispositifs électroacoustiques basés sur des matériaux piézoélectriques, largement employés comme oscillateurs, capteurs et résonateurs, sont très recherchés dans l'industrie des télécommunications. Dans le secteur des communications sans fils, il y a une importante utilisation de filtres, pour le contrôle des fréquences, sous forme de composants à ondes acoustiques de surface (ou «surface acoustic wave», SAW) et à ondes acoustique de volume (ou «bulk acoustic wave», BAW). La fréquence caractéristique de fonctionnement de ces dispositifs (f, en s^{-1}) est donnée par l'expression :

$$f = \frac{V}{\lambda_0} = \frac{V}{2d} \qquad (3)$$

où : V est la vitesse d'onde acoustique dans le matériau (m/s), λ_0 la longueur d'onde (m) et d la dimension caractéristique du dispositif.

Le développement important des systèmes de communication a rendu nécessaire l'utilisation de fréquences de plus en plus élevées, qui se situent actuellement dans le domaine des GHz, *i.e.* micro-ondes. L'augmentation de la fréquence (f) de fonctionnement du dispositif est obtenue, pour un matériau donné, par réduction de ses dimensions (d).

Ce but a été atteint avec des tailles raisonnables en utilisant des couches minces piézoélectriques. L'utilisation de techniques de dépôt adéquates ouvre la possibilité d'unifier les technologies de fabrication de circuits intégrés et de dispositifs électroacoustiques.

Les caractéristiques recherchées dans un matériau utilisé pour la fabrication de couches minces piézoélectriques dans ce secteur d'applications sont : un fort couplage piézoélectrique, une vitesse d'onde acoustique élevée, une bonne stabilité thermique et une faible rugosité de surface.

Le nitrure d'aluminium est piézoélectrique par sa structure cristalline hexagonale de type wurtzite, et il présente une vitesse d'onde acoustique particulièrement élevée grâce à ses excellentes caractéristiques mécaniques. En plus de posséder une excellente stabilité thermique, il est caractérisé par une conductivité thermique élevée et une énergie de bande interdite de 6,2 eV. C'est un excellent isolant électrique quand il est pur et de composition stœchiométrique.

La performance des couches minces de nitrure d'aluminium pour des applications piézoélectriques est directement liée à leur microstructure et leur composition.

Bien que, dans le cas idéal, il serait souhaitable d'employer des couches monocristallines, pour les applications visées, les couches polycristallines avec une orientation préférentielle par rapport au plan du substrat présentent d'excellentes performances pour une production beaucoup plus simple et économique.

Les dispositifs BAW sont basés sur la génération d'ondes acoustiques longitudinales perpendiculaires au film. Par conséquent, des couches minces orientées selon la direction <0001>, avec l'axe *c* perpendiculaire à la surface du substrat sont préférées pour optimiser le couplage piézoélectrique. Pour les dispositifs SAW basés sur la génération d'ondes acoustiques de surface, la même orientation est employée, bien qu'il ait été suggéré la possibilité d'utiliser l'orientation <10$\underline{1}$0> avec l'axe *c* parallèle à la surface du substrat.

La qualité d'orientation des couches minces polycristallines d'AlN constitue un paramètre important de la microstructure puisqu'elle est directement reliée aux performances piézoélectriques du composant fabriqué. La configuration Bragg-Brentano θ/2θ, traditionnellement employée pour l'analyse par diffraction des rayons X (DRX) et dont le diagramme met en évidence les réflexions correspondant aux plans parallèles au substrat, constitue une première indication de l'orientation préférentielle de la couche. Une autre technique, dite méthode des « rocking-curves » peut être employée pour obtenir une mesure plus fine de la dispersion dans l'orientation de la couche par rapport à la direction de référence : la largeur à mi-hauteur (FWHM) de la courbe obtenue est une mesure directe du degré de désorientation du film étudié. Bien que, en général, ce dernier paramètre ait été mis en rapport avec la performance piézoélectrique, des études récentes ont suggéré que cette corrélation n'est pas valable dans tous les cas. La raison de cette absence de corrélation est attribuée à la présence de grains d'orientations cristallographiques opposées, appelés domaines d'inversion, indiscernables par DRX et difficiles à identifier par d'autres méthodes.

Plusieurs techniques ont été employées pour obtenir des couches minces d'AlN comme la MBE (Molecular Beam Epitaxy), MOCVD (Metal-Organic Chemical Vapor Deposition), ou PVD (Physical Vapor Deposition) conduisant dans chaque cas à différents types de microstructures (monocristallines, polycristallines et même amorphes). L'obtention de couches monocristallines implique des températures élevées ou des temps de dépôt incompatibles avec les objectifs économiques imposés par la fabrication en masse de dispositifs.

Parmi les techniques disponibles pour l'obtention de films polycristallins, celles qui emploient un plasma, *i.e.* les procédés « assistés par plasma », sont particulièrement importants puisqu'elles permettent de réduire la température de traitement. En tenant compte qu'un plasma est un gaz quasi-neutre composé d'électrons libres, d'ions et d'espèces neutres, caractérisé par un comportement collectif des espèces chargées, les plasmas de faible densité possèdent la propriété particulière d'être hors équilibre thermodynamique, c'est-à-dire que les électrons et les espèces lourdes ont des températures associées très différentes. Cette classe de plasma fournit l'énergie d'activation nécessaire aux réactions chimiques grâce aux collisions inélastiques entre les électrons libres d'énergie élevée et les molécules gazeuses, permettant simultanément d'éviter un échauffement important du substrat. Par ailleurs, la microstructure des couches peut être modifiée en modulant le bombardement par les ions positifs de la couche en croissance.

Parmi les techniques assistées par plasma, on trouve les procédés PVD (Physical Vapor Deposition) qui utilisent un transfert de matière à partir d'un matériau solide par évaporation ou pulvérisation (« sputtering ») et les procédés CVD (Chemical Vapor Deposition) qui consistent en l'introduction de précurseurs volatiles dans l'enceinte de dépôt et qui, par réaction chimique, vont conduire à la formation d'un film. Les techniques PECVD (Plasma Enhanced Chemical Vapor Deposition), et en particulier celles qui emploient une excitation par micro-onde pour générer le plasma offrent plusieurs avantages : a) possibilité d'ajuster plusieurs paramètres de façon à atteindre l'optimisation des films b) possibilité de minimisation des effets de contamination du fait de l'absence d'électrodes dans la chambre de dépôt, c) possibilité de déposer sur substrats de géométries plus complexes, par comparaison avec des procédés de dépôt plus directionnels comme les procédés PVD de type pulvérisation cathodique.

Malgré les avantages énumérés, la technique PECVD avec excitation micro-ondes n'a pas été très employée pour l'élaboration de films piézoélectriques d'AlN, et, en aucun cas, la possibilité de contrôler l'orientation de la couche, comme <0001> ou <10$\underline{1}$0> n'a été rapportée. Par conséquent, l'objectif du présent travail est la détermination de l'effet des différentes variables du procédé dans le but d'obtenir des couches minces de nitrure d'aluminium piézoélectriques orientées selon les deux orientations indiquées.

Démarche expérimentale

Des substrats de silicium de dimensions de 30 mm x 10 mm et d'épaisseur 525 µm ont été utilisés pour le dépôt des couches minces. Ces substrats ont été nettoyés avec de l'éthanol et de l'acétone avant introduction dans le réacteur. Le plasma est entretenu par une excitation micro-onde, le porte-substrat est polarisable en radiofréquences et peut être chauffé jusqu'à 800℃. La surface des substrats a été nettoyée in situ par un plasma d'Ar avant la phase de dépôt. Les couches d'AlN ont été déposées à partir d'un plasma d'azote, dans lequel a été injecté du TMA (triméthylaluminium) acheminé jusqu'au réacteur par un gaz porteur qui était l'Ar. Les conditions expérimentales sont reportées dans le Tableau 1.

Tableau 1: Conditions expérimentales pour l'obtention d'AlN

Variable	Pré-traitement	Dépôt d'AlN
Puissance micro-onde (kW)	1,0	1,6
Débit d'argon (sccm[#])	100	50
Débit d'azote (sccm)	0	125
Tension de polarisation RF (V)	- 100	-200V - flottant
Pression (Pa)	0,8	0,5 – 8
Temps de process (min)	15	2 – 45
Débit de TMA (sccm)		1
Distance plasma-injecteur (mm)		30 - 110
Température de substrat (℃)		400 – 800
Distance injecteur-substrat (mm)		40 - 100
Substrat		Si(100), Si(111), Pt(111)/Si(100)

[#] Standard cubic centimeters per minute

Le travail effectué peut être divisé en trois étapes principales :

a) <u>Croissance de couches minces d'AlN polycristallines orientées</u>

L'influence de sept variables a été initialement étudiée pour optimiser les propriétés des couches : la tension de polarisation RF, la distance plasma-injecteur, la température du substrat, la pression totale, la distance injecteur-substrat, le temps de dépôt et la nature du substrat. Comme un plan d'expériences complet aurait été trop lourd pour vérifier l'effet de toutes les variables et leurs interactions, un travail préliminaire a été réalisé pour connaître l'influence de la distance plasma-injecteur et de la tension de polarisation RF appliquée au substrat. Après avoir déterminé les valeurs adéquates de ces deux variables, les autres ont alors été étudiées en utilisant plusieurs niveaux pour chacune.

b) <u>Optimisation des propriétés des couches</u>

Des expériences complémentaires ont été effectuées pour optimiser les couches en vue d'applications électroacoustiques, en prenant les résultats de l'étude préliminaire comme référence. Une étude paramétrique complète portant sur la température du substrat et la pression totale a été réalisée dans le but d'optimiser le développement de couches orientées <10$\underline{1}$0>. L'épaisseur des films et la tension de polarisation ont été étudiées séparément en employant plusieurs niveaux pour optimiser le développement des couches orientées <0001>. Une caractérisation plus fine de la microstructure des couches ainsi que la mesure de leurs performances piézoélectriques ont été réalisées à ce stade. Ceci a été complété par la caractérisation du plasma dans différentes conditions de dépôt par spectroscopie d'émission optique (OES).

c) <u>Applications aux dispositifs électroacoustiques</u>

Des dispositifs électroacoustiques de type SAW ont été préparés à partir de couches minces d'AlN orientées <0001> et <10$\underline{1}$0> réalisées dans les conditions optimales ainsi que des dispositifs électroacoustiques de type BAW avec des couches orientées <0001>. Les réponses en fréquence de ces dispositifs ont été mesurées et des modèles ont permis d'expliquer les résultats obtenus dans chaque cas.

Des diagrammes θ/2θ de diffraction de rayons X (DRX) ont été réalisés entre 15º et 80º (2θ). La détermination de leur largeur à mi-hauteur (FWHM) des « rocking curves » sur des couches mono-orientées a permis d'évaluer le degré d'orientation des films.

La spectroscopie infrarouge à transformée de Fourier (IRTF) a été employée en mode transmission entre 4000 cm^{-1} et 400 cm^{-1} et en mode réflexion.

La morphologie des couches a été analysée par microscopie à force atomique (AFM). Le coefficient de rugosité Sa, *i.e.* la moyenne arithmétique de la valeur absolue de la rugosité de surface, a été déduite de ces analyses.

L'observation des échantillons a été réalisée par microscopie électronique à balayage (MEB), en surface et en coupe à partir de fractures. La microscopie électronique en transmission haute résolution (HRTEM) et la diffraction électronique (SAED) ont permis une étude fine de la microstructure du profil des couches.

La composition des couches a été analysée par la technique RBS (Rutherford Backscattering Spectrometry) pour déterminer la teneur en aluminium, NRA (Nuclear Reaction Analysis) pour déterminer les teneurs en carbone, azote et oxygène et la technique XPS (X-ray photoelectron spectroscopy) pour analyser les surfaces.

La réponse piézoélectrique des couches a été évaluée par un dispositif AFM adapté à ce type de mesures (PFM ou Piezoresponse Force Microscopy), basé sur l'effet piézoélectrique inverse. A partir de ces mesures, le coefficient d_{33} du matériau a été estimé.

Des dispositifs SAW avec une longueur d'onde acoustique de 20 µm ont été fabriqués à partir des couches déposées en suivant un procédé de microlithographie conventionnel. De même, des dispositifs BAW prototypes ont été fabriqués. Les réponses en fréquences de ces dispositifs ont été déterminées en mesurant le paramètre de transmission S_{21}, à l'aide d'un analyseur de réseau vectoriel.

Le plasma utilisé lors de la phase de dépôt a été caractérisé par spectroscopie d'émission optique (OES) entre 350 et 850 nm.

Résultats et discussion

Des couches minces de nitrure d'aluminium polycristallines présentant une orientation préférentielle ont été obtenues par la technique MW-PECVD. Le choix des paramètres de dépôt a permis la réalisation de couches orientées <0001> ou <10$\underline{1}$0>, toutes deux intéressantes pour des applications piézoélectriques.

La réduction de la distance entre le plasma et l'injecteur de précurseur après modification de la configuration standard du réacteur, a permis d'améliorer le développement cristallin des films.

L’augmentation de la température de substrat a été déterminante pour améliorer la cristallinité des couches et réduire leur teneur en impuretés.

Alors qu’il n’a pas été mis en évidence d’effets d’épitaxie en travaillant avec différents substrats, l’analyse du profil des couches a montré une progressive amélioration du développement cristallin avec une augmentation de l’épaisseur du film.

La sélection de la pression de travail a permis de contrôler l’orientation préférentielle, en obtenant des couches orientées <0001> à basse pression (1 Pa) et des couches orientées <10$\underline{1}$0> à plus haute pression (8 Pa).

Pour de fortes valeurs de la polarisation RF, des couches amorphes présentant des contraintes résiduelles compressives ont été obtenues. Alors que toutes les couches obtenues au potentiel flottant présentaient des contraintes résiduelles en tension, l’utilisation de faibles tensions de polarisation RF a permis la réduction de cette contrainte de tension et par là même, la production de couches plus épaisses, tout en maintenant la microstructure recherchée.

Plusieurs informations ont été obtenues sur les mécanismes généraux qui contrôlent le développement cristallin et l’orientation préférentielle dans cette technique de dépôt MW-PECVD.

L’accroissement des concentrations des espèces plus énergétiques et en conséquence actives près du substrat, résultant de la réduction de la distance plasma-injecteur, a favorisé le développement cristallin.

L’accroissement de la température du substrat pendant la phase de dépôt a augmenté la mobilité des espèces arrivant à la surface et, en même temps, a favorisé la désorption des impuretés associées à la décomposition du précurseur (triméthylaluminium). En conséquence, le développement cristallin a été favorisé. En outre, l’accroissement de la température a favorisé l’orientation <0001> des couches réalisées à basse pression, qui correspond à l’orientation thermodynamiquement plus favorable permettant la minimisation de l’énergie de surface.

Aucun effet d’épitaxie correspondant aux premiers instants du dépôt n’a pu être mis en évidence. La croissance de la couche commençant de manière aléatoire, l’orientation s’est améliorée progressivement avec l’augmentation d’épaisseur. Cette amélioration a été fortement favorisée aux plus hautes températures.

L'augmentation de la pression a entraîné la réduction du libre parcours moyen des espèces dans l'enceinte du réacteur et permis l'obtention de l'orientation <10$\underline{1}$0>. La formation en phase gazeuse des dimères Al-N a été proposée comme le mécanisme le plus adéquat pour expliquer ce phénomène, en considérant la cinétique liée au dépôt des espèces. Bien qu'il n'ait pas été possible de détecter ces dimères avec les techniques d'analyse disponibles, leur présence dans le mécanisme réactionnel ne peut être écartée.

Tandis que l'orientation exclusive <0001> s'est développée à basse pression et seulement à haute température, l'orientation exclusive <10$\underline{1}$0> s'est développée pour les pressions élevées mais quelles que soient les températures. Il est donc possible de conclure que des mécanismes différents contrôlent les deux phénomènes. Plus encore, l'observation de l'orientation exclusive <10$\underline{1}$0> à toutes les températures aux hautes pressions tend à orienter vers la théorie de formation de dimères Al-N par rapport aux autres mécanismes qui ont été proposés pour la croissance des couches.

Il a été montré que l'application d'une tension de polarisation RF permet le contrôle des contraintes résiduelles en tension, mais, qu'en même temps, il existe un autre mécanisme de contrôle de l'orientation préférentielle des films. Le développement de contraintes résiduelles compressives élevées a favorisé le changement d'orientation de <0001> à <10$\underline{1}$0>, associé à une relaxation des contraintes compressives du film. Bien que ce phénomène se soit produit pour des films de faible développement cristallin, donc non intéressants pour les applications visées en première approximation, c'est une voie qui devrait être étudiée plus en détails pour ces applications ou d'autres.

La comparaison de ces résultats à ceux obtenus par la technique PVD (Physical Vapor Deposition) a conduit à la mise en évidence de similitudes concernant l'influence des paramètres des procédés comme la pression et la tension de polarisation du porte-substrat. Ceci montre donc qu'il devrait y avoir quelques similitudes entre les mécanismes de croissance des deux techniques. Cependant, quelques différences substantielles ont été démontrées en considérant les températures de substrat nécessaires dans chacun des cas. Dans les procédés PVD, il y a une contribution substantielle de l'énergie cinétique des espèces éjectées de la cible qui arrivent au substrat, laquelle favorise la diffusion des espèces adsorbées. Cet effet peut remplacer la contribution de la température nécessaire dans les procédés PECVD et permettre de travailler à plus basse température pour les procédés PVD.

Dans la technique PVD, les conditions expérimentales doivent être optimisées pour générer des espèces actives dans le plasma. Pour les procédés PECVD, tant la haute réactivité du précurseur d'Al que l'excitation fournie par le plasma favorisent la génération d'espèces actives. Mais, l'inconvénient du procédé PECVD réside dans le fait que les produits secondaires issus de la dissociation du précurseur peuvent être incorporés à la couche et, par voie de conséquence, doivent être désorbés pendant le processus de dépôt. D'autre part, l'oxygène est une impureté importante, présente dans les deux procédés, qui doit être minimisée.

Le tableau 2 ci-dessous résume les conditions optimales de dépôt pour l'obtention de couches avec une microstructure favorable aux performances piézoélectriques.

Tableau 2: Conditions optimales de dépôt d'AlN

Variable	Dépôt d'AlN
Puissance de micro-onde (kW)	1,6
Débit d'azote (sccm)	125
Débit d'argon (sccm)	50
Débit de TMA (sccm)	1
Distance plasma - injecteur mm)	30
Distance injecteur - substrat (mm)	40
Tension de polarisation RF (V)	flottant*
Température de substrat (℃)	800
Pression (Pa)	1 (pour orientation <0001>) 8 (pour orientation <10$\underline{1}$0>)

*Jusqu'à des épaisseurs de 1,5 μm, et +10V jusqu'à des épaisseurs de 2,5 μm.

Les couches orientées <0001> obtenues par MW-PECVD en conditions optimales ont montré une structure colonnaire marquée avec une taille de grains autour de 40 nm, des largeurs à mi-hauteur de 8º pour les « rocking-curves », des rugosités inférieures à 20 nm et des contraintes résiduelles de tension inférieures à 1 GPa. Les performances piézoélectriques de ces couches ont été caractérisées par PFM (Piezoresponse Force Microscopy), ainsi que par la construction de dispositifs SAW et BAW. Les résultats ont montré des réponses piézoélectriques significatives dans tous les cas, avec des valeurs optimales de coefficients piézoélectriques d_{33}, *i.e.* 5.8 ± 1.2 pm/V, évaluées par PFM et de vitesses d'onde acoustique, *i.e*. 5.05 ± 0.01 km/s, pour des ondes acoustiques de surface. Ces valeurs prouvent l'absence de concentrations significatives de domaines d'inversion dans la microstructure des couches.

L'évaluation de l'effet des différents paramètres sur le coefficient piézoélectrique, comme la température du substrat, l'épaisseur du film et la tension de polarisation RF appliquée au porte-substrat, a permis de confirmer l'importance du développement cristallin et du degré d'orientation sur les performances piézoélectriques des couches. L'effet de l'épaisseur pour une température optimale de dépôt a pu être relié aux propriétés piézoélectriques via la construction de dispositifs SAW. La minimisation des contraintes résiduelles compressives avec l'application de faibles tensions de polarisation RF a montré la possibilité d'obtenir de plus grandes épaisseurs avec une microstructure appropriée et des coefficients piézoélectriques optimaux. Les différences de microstructure, de degré d'orientation et de teneur en oxygène ont été directement reliées aux propriétés piézoélectriques obtenues lors de la comparaison des films réalisés respectivement par PECVD et PVD.

Le diagnostic du plasma par la méthode OES a permis d'identifier plusieurs espèces présentes dans le réacteur de dépôt comme Al, Al^+, N_2, N_2^+, N, à mettre directement en rapport avec la croissance de la couche. Simultanément, d'autres espèces à relier à des sous-produits issus de la décomposition du précurseur comme CN, NH, H, ont été identifiées. Ces résultats sont en accord avec la bande d'impuretés observée par FTIR autour de 2150 cm^{-1} dans les couches d'AlN obtenues par PECVD, laquelle a été attribuée aux espèces CN, Al-H ou Al-N_2 selon la bibliographie. Par ailleurs, il a été possible d'évaluer l'effet favorable de la puissance micro-onde dans la génération d'espèces actives ainsi que d'expliquer l'effet négatif d'un ajout d'hydrogène. En outre, les plus hautes valeurs de pression ont conduit à des températures électroniques et des concentrations d'espèces actives atomiques plus faibles a priori, ce qui pourrait être mis en rapport avec le plus faible développement cristallin observé pour les films orientés <10$\underline{1}$0>. De même, la réduction de la température électronique avec la distance substrat-plasma a été confirmée.

Les couches orientées <10$\underline{1}$0> obtenue par MW-PECVD dans les conditions optimales ont montré une structure non colonnaire avec une taille de grains autour de 20 nm, des valeurs de largeur à mi-hauteur des « rocking-curves » de 11º et des rugosités inférieures à 10 nm. Ces couches n'ont pas montré de réponses piézoélectriques significatives pour les configurations testées. Ce résultat était attendu pour la méthode PFM, conformément au tenseur piézoélectrique du nitrure d'aluminium pour une structure cristalline de type wurtzite. D'autre part l'absence de réponse dans la configuration SAW standard testée n'écarte pas une possible réponse avec d'autres dimensions du dispositif. Le champ électrique au-dessous des électrodes des configurations SAW a été modélisé dans le but de montrer que les couches pourraient donner une réponse pour d'autres géométries, plus complexes mais réalisables. Si ce n'était pas le cas, la cause devrait être recherchée dans un développement cristallin plus faible ou une possible inversion de domaines dans le plan de la surface. Toutes ces raisons peuvent contribuer à l'absence de publications présentant une évaluation des performances de couches orientées <10$\underline{1}$0> insérées dans des dispositifs SAW, bien que cette orientation soit considérée comme optimale par plusieurs auteurs.